I betook myself to the observations of the heavenly bodies; and first of all, I viewed the Moon as near as if it was scarcely two semi-diameters of the Earth distant. After the Moon I frequently observed other heavenly bodies, both fixed stars and planets, with incredible delight; and, when I saw the very great number, I began to consider about a method by which I might be able to measure their distances apart, and at length I found one. And here it is fitting that all who intend to turn their attention to observations of this kind should receive certain cautions. For, in the first place, it is absolutely necessary for them to prepare a most perfect telescope, one which will show very bright objects distinct and free from mistiness, and will magnify them at least 400 times, for then it will show them as if only one-twentieth of their distance off. For unless the instrument be of such power, it will be in vain to attempt to view all the things which have been seen by me in the heavens, or which will be enumerated hereafter.

Galileo Galilei, 1610

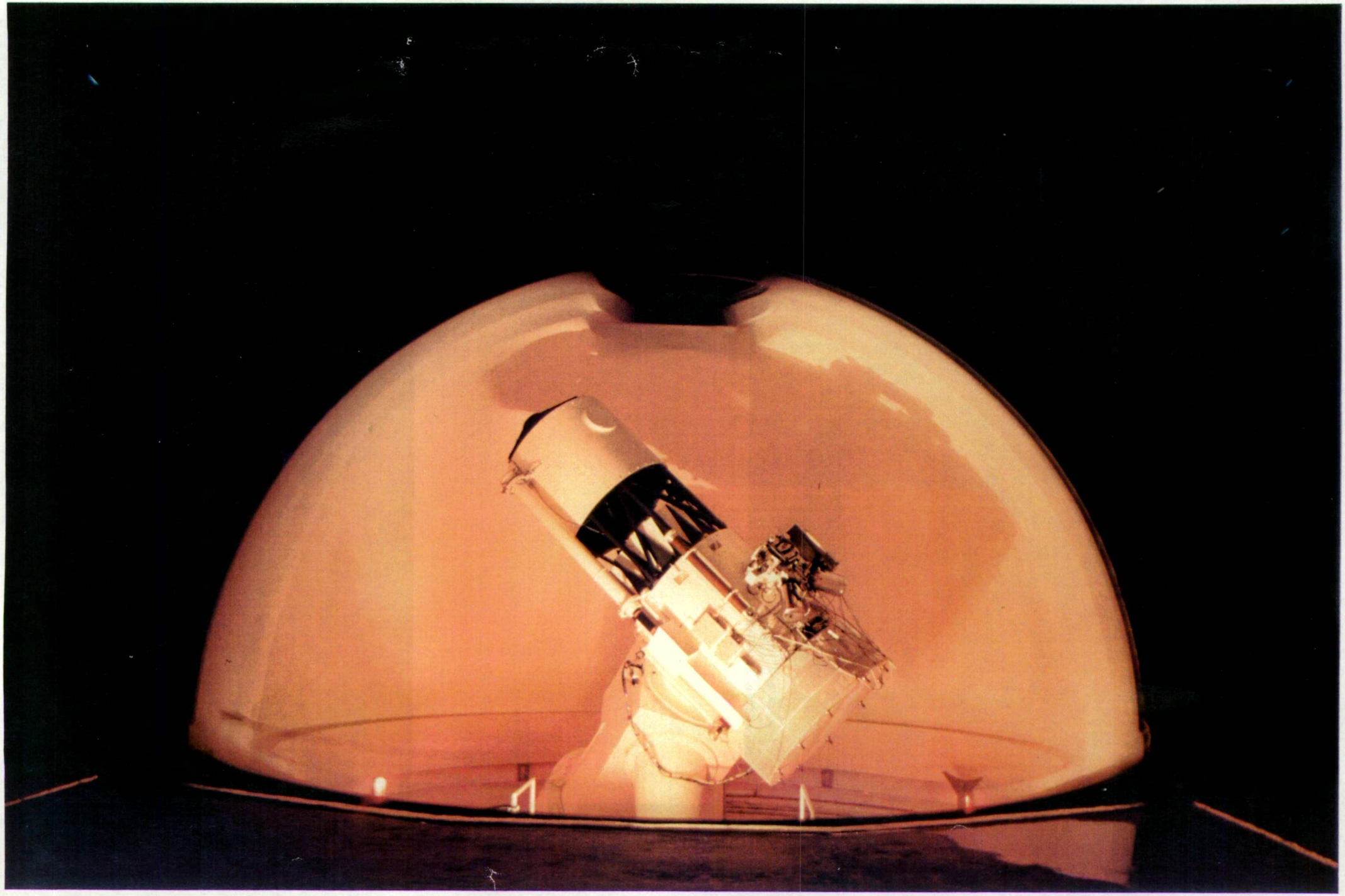

THE DEVELOPMENT AND USE OF A HIGH-SPEED ASTRONOMICAL PHOTOMETER

by

K. M. Hill, B.Sc. (Hons.)
University of Tasmania

A thesis submitted in fulfilment of the
requirements for the degree of
Doctor of Philosophy
at the
University of Tasmania

Hobart
August, 1989

DECLARATION

This thesis contains no material which has been accepted for the award of any other higher degree or graduate diploma in any tertiary institution, and to the best of my knowledge and belief this thesis contains no material previously published or written by any other person, except where due reference is made in the text of this thesis.

(K.M. HILL)

ACKNOWLEDGEMENTS

The research programs reported herein have benefited from the contributions, both large and small, of many co-workers, associates and friends.

I would like to express my sincere gratitude to Dr. R.D. Watson and Dr. M.D. Waterworth for their supervision and support. In particular Dr. Watson for his invaluable discussions relating to the observing programs and for his helpful criticisms of the thesis draft.

I also wish to thank Mr. C.M. Ashworth for his helpful discussions relating to electronic matters, the design and building of the counter boards and his help with some of the observations. As with all things mechanical, parts of a telescope system invariably fail or require design modifications to suit particular needs. For this work I would like to thank Mr. D. Phythian for his care and precision in performing such tasks.

I am also indebted to Dr. D.P. Sharma for extra data on EX Hya, brought by him from India, and his keen interest and help with observations in the latter stages of the EX Hya observing program. I must also thank Mr. S.W. Dieters for the help with the 1986 AAT spectroscopic observations, for interrupting his observing program to obtain the 1987 spectroscopic run on EX Hya, and finally for the many nights he assisted with the Mt Canopus observations. For providing a copy of the FIGARO data reduction software, used to process the EX Hya spectra, I would like to thank Dr. K. Shortridge of the AAO.

I thank Dr. A.B. Giles for the inspiration for the AUSSAT observations (Section 5.3), his assistance with the observations, and for the fruitful discussions we had concerning the results of my analysis of the AUSSAT data. More recently, I would like to thank Mr. P.M. Green for his assistance with the SN1987a observations.

I would also like to acknowledge the contribution of Profs. W.B Hubbard and D.M. Hunten, of the Lunar and Planetary Laboratories of the University of Arizona, for their development of a model of Pluto's atmosphere and its application to the Mt Canopus occultation light curve. I also appreciate the predictions of possible occultation events provided by Mr. M. George.

Finally, I would like to thank my wife and close friends, whom I will not mention by name for fear of missing some, for their moral support and the frequent trips to the beach that were needed to survive a doctorate.

To my parents

ABSTRACT

This dissertation describes the development and implimentation of a computer-based photometric data acquisition system for the Mt Canopus telescope. The high-speed photometric system allows continuous acquisition of data, for up to ~69 min with a maximum sample rate of 9.8 kHz, while providing a real time display of the counts. The system was thoroughly tested with a pulsing LED source and with observations of the Crab pulsar. The results from several observational programs, suited to the system's capabilities, are also presented. The observational programs involved a study of the DQ Her type cataclysmic variable EX Hydrae, a fast photometric study of geostationary spin-stabilised satellites, a monitoring program on SN1987a, and an occultation program which culminated in a successful observation of a Pluto occultation and the detection of an atmosphere on this planet.

The Mark I version of the fast-photometer system was used for the photoelectric study program on the eclipsing cataclysmic variable EX Hya. This program demonstrated the continued secular decrease in the period of its 67 min modulation. The observed rate of change of the 67 min period implies a mass transfer rate of the order of $\sim 3 \times 10^{-11}$ $M_\odot$ yr^{-1} and a magnetic moment around 8×10^{32} G cm^3. Two variations in the eclipse timings are also identified. Firstly, one sees a long-term variation that has been fitted with an ~20 yr period sinusoid. Secondly, one sees a short-term variation which is correlated with the phase of the 67 min cycle. This second variation has been interpreted in terms of the eclipse of an accretion column or arc in the region above the magnetic pole of the white dwarf.

Supplementary to the photometric data, high time resolution spectroscopic data from an eclipse of EX Hya were obtained with the Anglo-Australian telescope. These data are compatible with the general spectral characteristics noted by other workers. The V/R ratio of the spectral lines, around orbital phase $\Phi_{98} = 0$, is consistent with the eclipse of an accretion disk. A sharp peak in the equivalent width of the Balmer lines is seen at the time of the eclipse. It is comparable in width to the X-ray eclipses, and narrower than the optical eclipses. Finally, the accretion curtain model of EX Hya is shown to accommodate, in a qualitative sense, all the observational constraints that must be imposed on any model of the system.

The high temporal resolution attainable with the Mark II photometer system has been amply demonstrated with observations of geostationary spin-stabilised AUSSAT satellites A1 and A2, where features of the order of 1 ms were detected. The satellites were found to exhibit many periodic features. These features were only detected during the satellites' *on* states, which occur near the passage of the equinoxes, and last about one week. When the satellites are in their faint *off* state, no modulation was evident. The spin rate of the satellites was measurable to a few parts in 10^6 in an ~10 min data run. The satellites were also observed during their eclipse by the Earth's shadow. The sensitivity attainable with the Mark II system was demonstrated in a program of monitoring SN1987a. An upper limit of 19^{th} magnitude was placed on any sinusoidal component in the light from SN1987a, from three observations in 1989 (February, March and April). Finally, using the Mark II system, observations of a grazing stellar occultation by Pluto have shown that it possesses an extended atmosphere, whose thickness is comparable to the radius of the planet itself. The occultation light curve is consistent with the effects produced by refraction in an isothermal atmosphere of methane at a temperature of 61 °K.

CONTENTS

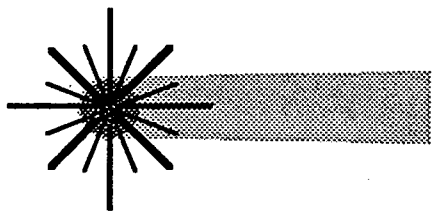

Chapter 1

INTRODUCTION

1.1 Fast Photometry in Astronomy

Astronomical photometry has evolved in step with advances in detector technology from early visual measurements, through photographic measurements, photo-electric measurements with photomultiplier tubes, and most recently to solid state detector measurements using such devices as silicon photodiodes, photodiode arrays, and two dimensional charge-coupled devices. Photographic plates permit integration of light from faint sources and are subject to a more reliable calibration process than are visual measurements. However, they have a limited dynamic range and a non-linear response. Photomultiplier tubes permit only the detection of a single source, but have a larger dynamic range and are linear devices. Also they have much higher quantum efficiencies than do photographic plates. Parallel with the advances in astronomical detector technology have been immense advances in data acquisition and handling techniques, through the development of high-speed digital computers, mass storage devices and data analysis software. They have permitted the full potential of the photomultiplier tube, as a detector in observational astronomy, to be realised. With suitable electronics it has become possible to detect the arrival of individual photons, and hence record the number of photons arriving in a very brief time interval, allowing the study of short-timescale phenomena in optical astronomy

Much of the stimulus to explore the short-timescale domain at optical wavelengths can be traced to the discovery by Cocke et al. (1969) of the 33 ms optical flashes from the

Crab pulsar. Since that time a great variety of stellar phenomena have been examined by fast-photometric techniques, as outlined by Warner (1988). These include the study of stellar occultations by solar system objects, the rapid changes in brightness associated with flare stars, the highly variable light curves of cataclysmic variable stars, the short period and transient features in the light from the X-ray binaries and gamma-ray bursters, some radio pulsars at optical wavelengths, and pulsating stars such as the ZZ Ceti and rapidly varying Ap types.

1.2 Background to this Thesis

The University of Tasmania's 1m telescope (the Mt Canopus telescope) is located close to the city of Hobart. The instrument was conceived in the 1970's and became operational in the early 1980's. It is fitted with a dual channel photometer at a folded Cassegrain focus. It has a TV guiding/finding system employing a 15 cm (f/15) finder telescope with a limiting magnitude of m_v ~12.5 to ~13.5, depending on seeing conditions. A guiding/finding system mounted at Cassegrain focus was installed in 1986, thus increasing the limiting magnitude for acquisition and eliminating differential flexure problems between the finder telescope and the main telescope. A complete description of the original telescope system is given by Waterworth (1980). The frontispiece shows a photograph of the Mt Canopus telescope, obtained by taking a time exposure while rotating the dome with the slit open.

The aim of this thesis was to develop a computer-based photometric data acquisition system for the Mt Canopus telescope, in a form which would permit fast photometric observations to be undertaken, and then to use this system to tackle several observational programs which would be permitted by the system capabilities. The observational programs that were selected involved a study of the DQ Her type cataclysmic variable EX Hydrae, a fast photometric study of geostationary spin-stabilised satellites, a monitoring program on SN1987a, and an occultation program which culminated in a successful observation of a Pluto occultation and the detection of an atmosphere on this planet. The thesis work was undertaken on a half-time basis during the period 1982 to 1989.

The structure of the thesis is as follows. Chapter 2 outlines the development of the fast-photometric system, beginning in 1982. The development of the system proceeded through two stages, referred to in the thesis as the Mark I and Mark II versions. A more recent minor modification, permitting acquisition sample rates as high as 9.8 kHz, is documented in Appendix 1. It must be borne in mind that the options available

in the development of this fast–photometry system necessarily fell within the overall financial constraints of a very small annual budget. This was combined with the limited manpower of one person for telescope and observatory maintenance, and another approximately half-time position for technical support. These restrictions have consequently resulted in the slow development of the system.

Following Chapter 2, the next two chapters of the thesis relate to the photometric program on EX Hya, which was supplemented by data from two short spectral runs on the Anglo-Australian telescope. The study of a cataclysmic variable was decided upon as being consistent with the moderate time resolution capability of the Mark I system, a fact which was dictated by limited computer resources. It was also consistent with the limited photometric quality of the observing site, where only 3 to 4 full nights of photometric quality occur per month. My observations during a 1982 pilot program on V1223 Sgr, to help document the period and phase of its then newly discovered 746 s periodicity, had affirmed the suitability of such a cataclysmic variable study. The choice of the particular object for study , EX Hya, was based on the fact that it was a DQ Her type system with a number of interesting, but not fully understood, observational properties. Further it was a relatively bright southern object, of about 13^{th} magnitude. It could therefore be readily studied at the southerly latitude of Mt Canopus, and would also be visible on the original TV guider/finder telescope attached to the 1 m telescope. Chapter 3 of the thesis is intended to present only a brief review, of the observational aspects of, and binary model for, cataclysmic variables, preliminary to the present photometric study. The results of this photometric study are then set out in Chapter 4, and are discussed in relation to an accretion model for EX Hya.

Chapter 5 presents the results of the programs undertaken with the higher time resolution Mark II version of the photometer system, together with a discussion for the testing procedures of this system and a sample observation of the Crab pulsar. The Mark II version of the photometric system was developed early in 1987, in response to the appearance of SN1987a in the Large Magellanic Cloud, and following the availability of some additional computer equipment. The upper-limit results of the pulsar monitoring program on SN1987a are given in Chapter 5, together with a discussion of the high time-resolution structure in the specular reflection light curves of the geostationary AUSSAT satellites A1 and A2. Additionally this chapter presents the outcome of the 9^{th} of June 1988 occultation of a star by Pluto, which was seen at Mt Canopus, and discusses the resultant model for Pluto's atmosphere. Finally Chapter 6 summarizes the important conclusions from this thesis work.

1.3 Related Technical Work

The work presented in the thesis should be considered in the context of the large amount of instrumental development and equipment testing associated with producing the final working system. This more technical aspect of the work was necessary in light of the restrictions imposed by a very small annual budget and minimal manpower. Thus, in addition to developing the photometer system, and the large amount of related software required for such a system, a considerable amount of time and effort was also necessarily spent in the following general areas normally undertaken by technical staff at professional observatories:

- General telescope maintenance. This included removal and installation of the mirrors for re-aluminizing, implementing minor telescope modifications to improve the telescope's performance, and help with the repairs when equipment failed;
- Input into the design and testing of the Cassegrain TV guider system discussed in Chapter 2. This included modifications to the first version of this system, which resulted in an improved ability to focus objects for both the on-axis and offset guiding positions;
- Installation, repair, and maintenance of the computer system and its associated equipment, such as magnetic tape drive, plotters, printers and terminals;
- Initial testing and setup of the photomultiplier tubes, HV power supplies and pre-amps. The cold boxes for the PM tubes also required periodic maintenance to check for moisture and to ensure that the front window was clean and the heater element was functioning correctly;
- Help with the initial testing and calibration of shaft encoders, which were installed to improve telescope positioning;
- The development of dry-ice making facilities for cooling the PM tubes;
- Observational support for other observers.

Hence in addition to the observational results described directly in the thesis, I see my contribution as being important in having provided a new and useful instrument for general research at the observatory.

1.4 List of Publications

The observations that I have undertaken with the fast-photometry system developed for this thesis have contributed to several publications. These are summarized for convenience in the following list, though they are referenced in the normal manner in the subsequent chapters of this thesis. The thesis contains a detailed discussion of the

material in all of these papers, except the one on V1223 Sgr.

1. "Further Observations of EX Hydrae", K.M. Hill and R.D. Watson: (1984), *Proceedings of the Astronomical Society of Australia*, **5**, 532.

2. "Polarimetry, Photometry and Spectroscopy of the Intermediate Polar V1223 Sgr", D.J. Watts, A.B. Giles, J.G. Greenhill, K.M. Hill, and J. Bailey: (1985), *Monthly Notices of the Royal Astronomical Society*, **215**, 83.

3. "EX Hydrae Timing Data", K.M. Hill, D.P.Sharma and R.D. Watson: (1986), *Proceedings of the International Astronomical Union Symposium No. 118.*, ed J.B. Hearnshaw and P.L. Cottrell, D. Reidel, Dordrecht, 289.

4. "Optical Observations of Geostationary Spin-Stabilised Satellites", A.B. Giles and K.M. Hill: (1988), *Astrophysics and Space Science*, **147**, 359.

5. "Occultation by Pluto", R.D. Watson, K.M. Hill, S.W. Dieters: (1988), *International Astronomical Union Circular*, No. 4612.

6. "Occultation Evidence for an Atmosphere on Pluto", W.B. Hubbard, D.M. Hunten, S.W. Dieters., K.M. Hill and R.D. Watson: (1988), *Nature*, **336**, 452.

7. "Fast Photometry of the Crab, SN1987a and AUSSAT", K.M. Hill, A.B. Giles and R.D. Watson: (1989), *Proceedings of the Astronomical Society of Australia*, **8**, 75.

8. "Supernova 1987a in the Large Magellanic Cloud", S. Dieters, P. Green, K. Hill and R. Watson: (1989), *International Astronomical Union Circular*, No. 4773.

9. "The Eclipses of EX Hydrae", K.M. Hill and R.D. Watson: (1990), *Astrophysics and Space Science*, **163**, 59.

10. "Observations of the 9 June 1988 Occultation by Pluto", R.L. Millis, L.H. Wasserman, O.G. Franz, R.A. Nye, A.C. Gilmore, P.M. Kilmartin, W.H. Allen, R.D. Watson, S.W. Dieters, K.M. Hill, A.B. Giles., G.Blow, J. Priestley, W.S.G. Walker, B.F. Marino, D.G. Dix, A. Page, H.D. Kennedy, J.L. Elliot, E. Dunham, A.S. Bosh, L.A. Young, S.M. Slivan and A.R. Klemola, (1989): *Icarus*, in press.

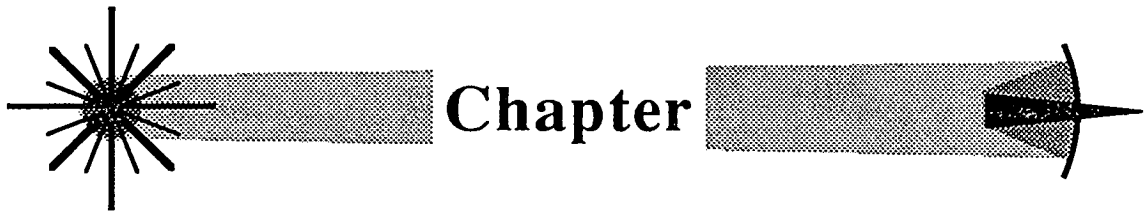

Chapter 2

DEVELOPMENT OF A FAST PHOTOMETER SYSTEM FOR THE MT. CANOPUS 1m TELESCOPE.

2.1 Introduction

The chapter will deal with background details of Cassegrain focus design (Section 2.2), and related details of the Cassegrain TV guider finder (Section 2.3). The design of the Cassegrain photometer is outlined in Section 2.4. Instrument control at Cassegrain is discussed in Section 2.5. The last part of the chapter, Section 2.6, details the hardware and software related to the photometer data collecting system. This was the area of the photometer system design which was implemented by the author while developing a system suitable for fast photometry. Appendix 1 details recent software and hardware developments that allow data to be acquired with a maximum sample rate of 9.8 kHz. Readers wishing only to find out about observational results may omit this chapter entirely and proceed directly to the following chapters.

Figure 2.1 is a photograph showing the arrangement of photometer instrumentation on the telescope. The Cassegrain TV guider/finder is also visible.

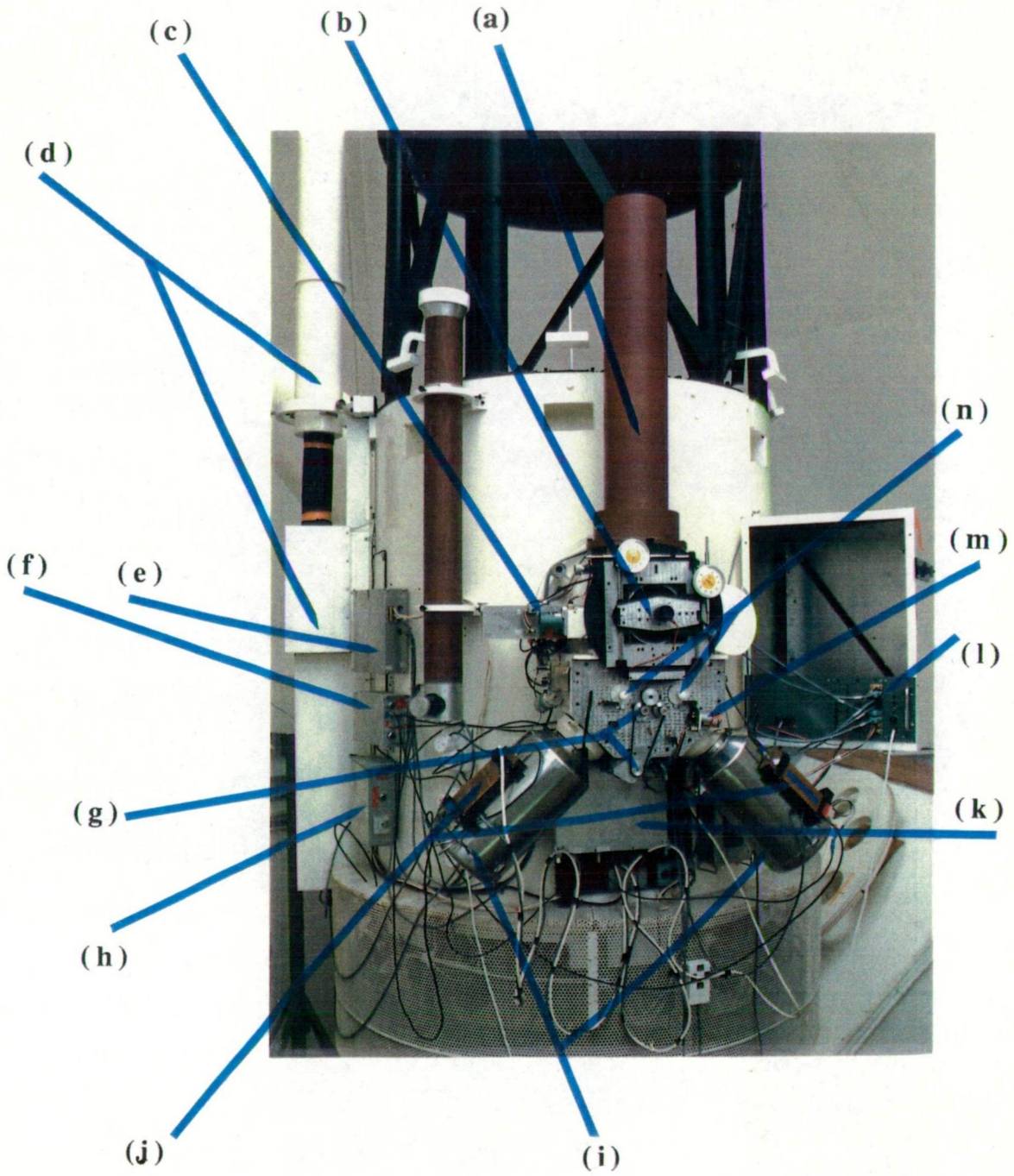

Figure 2.1

(a) Cassegrain TV Guider/Finder.
(b) Eye-piece offset Guider.
(c) Cassegrain TV Guider/Finder Mirror Drive.
(d) Guide Scope Image Intensifier and Camera Assembly.
(e) Filter Wheel Drive and Sensor Electronics.
(f) Photometer discriminators and Line Drivers.
(g) Filter Wheel Drive.
(h) Guide Scope Image Intensifier Power Supply.
(i) Photometer Cold-Boxes.
(j) Photometer Pre-amplifiers.
(k) Photometer H.T. Power Supply
(l) Cassegrain Instrument Control Computer.
(m) N.D. Filter Drive.
(n) Aperture Wheel Controls.

2.2 Cassegrain Design

Possible light paths at the f/11.3 Cassegrain focus of the 1m telescope are shown in Figures 2.2(a) and 2.2(b) . The main features to note are as follow.

The incoming light beam passes through an aspheric Gascoigne corrector lens (L1), which is used to reduce astigmatism in the primary image. The beam may then be intercepted by the mirror (M2) which is used to deflect a section of the primary image into the Cassegrain TV guider/finder system. This mirror is positioned using computer controlled stepping motors and limit switches. It can be located at any position from the optical axis out to the edge of the primary image plane or retracted altogether.

If the on–axis beam is not intercepted by M2 it reaches another mirror (M1). This mirror is placed so as to select the on–axis section of the primary image and deflect it into the photometer. The mirror M1 is mounted on a lever arm so that it can be withdrawn to provide an unobstructed view of the primary image. The arm self–locates such that one side of the mirror is on the optical axis and supplies a beam to the star channel of the photometer and the other side of the mirror provides the beam for the sky channel. Finally, if unobstructed by either M1 or M2, the beam may reach the primary image plane. This section of Cassegrain focus is easily accessible and allows other equipment, such as an eyepiece, offset guider or photographic plate holder, to be attached here. Future equipment such as a low dispersion spectrograph, CCD camera or a third photometer channel for simultaneous comparison star measurements could also be attached at this point.

All of the equipment mounted at Cassegrain focus is fixed on a head which is attached to the telescope by a rotational bearing. This is shown schematically in Figure 2.2(b). The ability to rotate about the optical axis is provided for two reasons. Firstly, if a star happens to be in the sky channel of the photometer, then rotating the head moves the sky channel to another position on the sky. Secondly, if there isn't a star in the field of view of the Cassegrain TV guider/finder system for offset guiding purposes, then by rotating the head it is possible to scan a nearby region of the sky for a suitable guide star.

2.3 The Cassegrain TV Guider/Finder System

Initially object acquisition and guiding for the 1m telescope employed a TV system attached to a 15 cm finder telescope on the side of the main telescope tube. This had

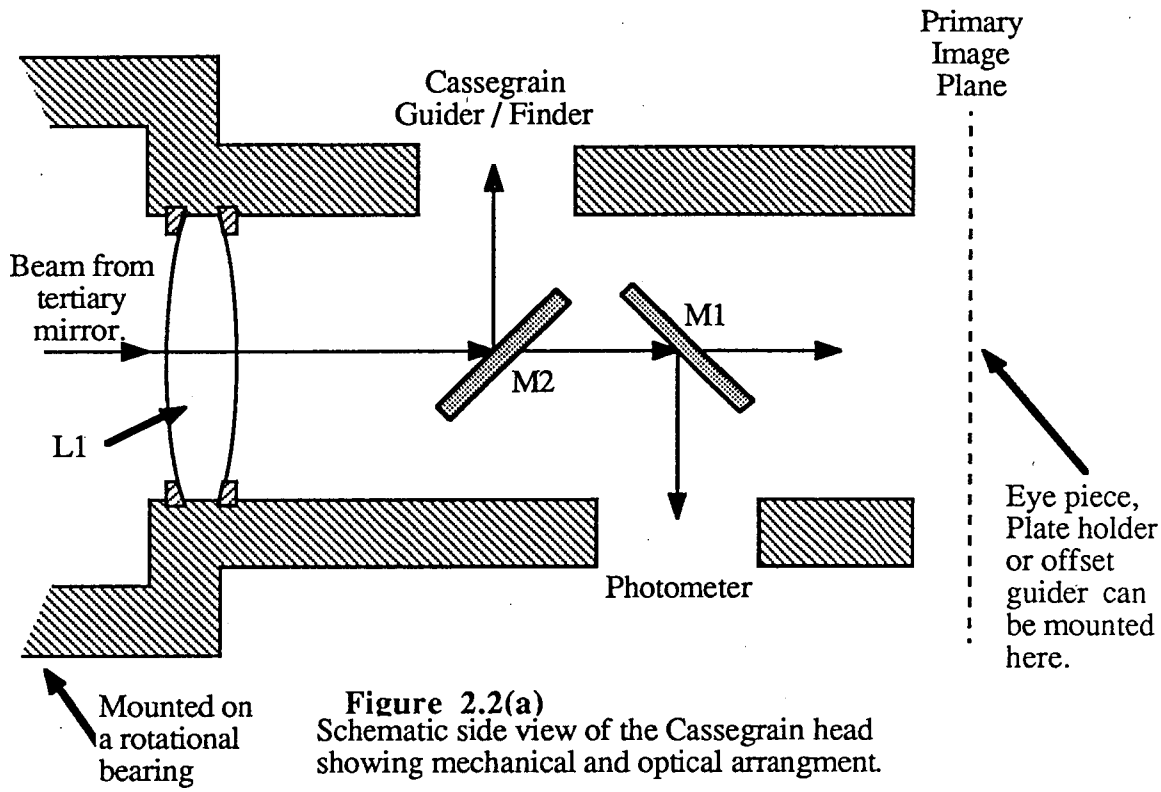

Figure 2.2(a)
Schematic side view of the Cassegrain head showing mechanical and optical arrangment.

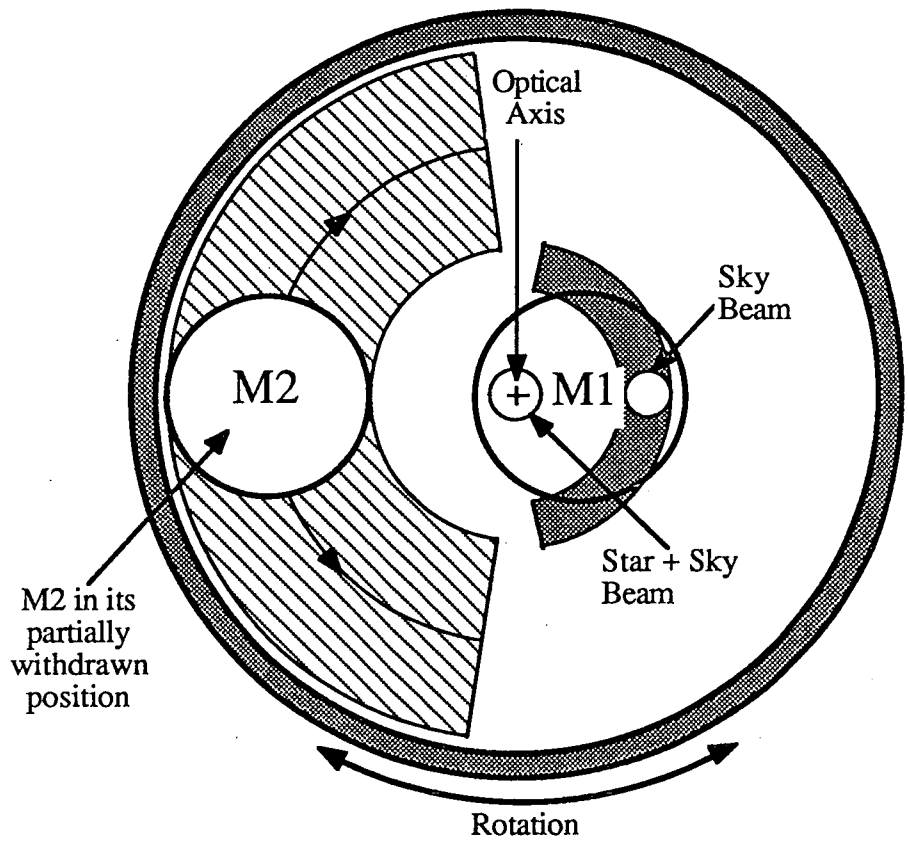

Figure 2.2(b)
Schematic end view of the Cassegrain head detailing M1 and M2 mirror positions

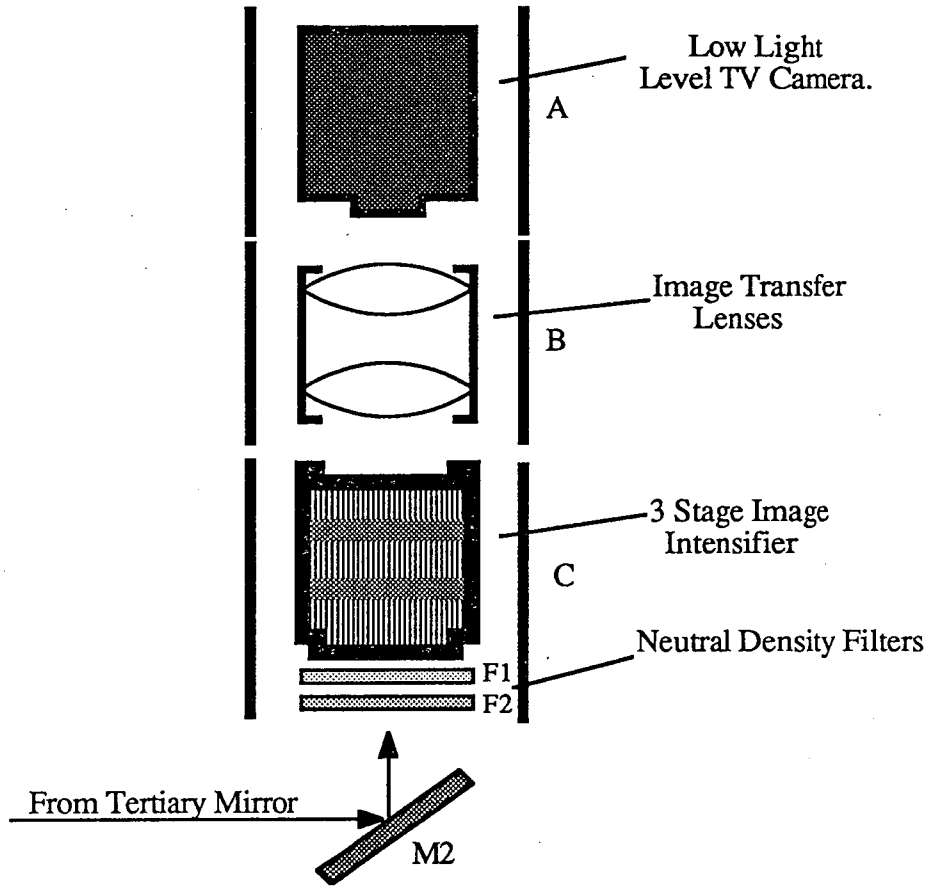

Figure 2.3
The Cassegrain TV Guider/Finder design

two drawbacks. There was a relatively bright limiting magnitude, of between 12.5 and 13.5, depending on seeing conditions, and the existence of differential flexure between the main tube and the finder telescope. Subsequently a new system, better in both respects, was installed at Cassegrain focus. This system is shown in Figure 2.3 .

It consists of a low light level TV camera looking, via transfer lenses, at the output of a three stage image intensifier. The system was constructed in three sections A, B and C, for easy access to the different parts. Each section screws onto the top of the next. This new system enables objects as faint as magnitude 16.7 to be found. Offset guiding for several hours at various positions in the sky has shown no indication of image drift relative to the photometer aperture.

The operation of the Cassegrain TV guider/finder proceeds in the following way. The original 15 cm finder telescope is used to locate the object field using bright stars. The mirror M2 is then placed in its full–in position on the optical axis. In this position the object field is imaged onto the image intensifier as shown in Figure 2.3 . The TV image of the object of interest is then placed in the position corresponding to the photometer aperture on a TV screen. The mirror M2 is partially withdrawn to allow the light from the object to enter the photometer via mirror M1. The new partially withdrawn position of M2 is illustrated in Figure 2.2(b). In moving to this position the mirror M2 is automatically tilted to image the offset field part of the primary image onto the image intensifier.

Once this has been done an offset guide star is chosen from the field, or, if necessary, the Cassegrain head is rotated to change the field to search nearby fields for a suitable guide star. Since the offset field is approximately 4 arc min in diameter there is usually a suitable guide star available on the TV screen without rotating the head. Two neutral density filters F1 and F2 are used for guiding on bright objects. Together they provide either a 10, 100 or 1000 reduction in the light intensity.

The real time display of counts versus time from the photometer is used to define the edges of the photometer aperture accurately on the TV screen. These aperture edges are marked on the screen around the guide star. Once the setup procedure is completed for the object star, and any comparison star needed for variable star photometry, the observation can be commenced. When dealing with a previously unobserved faint object and its comparison stars, the whole procedure takes from 30 to 60 minutes to find and centre them. For bright or known stars the procedure takes 10 to 15 minutes.

2.4 The Photometer Optical and Mechanical Design

The Cassegrain photometer shown in Figure 2.1 is a dual channel system designed to make simultaneous 'sky' and 'star+sky' measurements. Figure 2.4 shows the layout of the system. The photometer design has been described by Waterworth (1980), but a brief description is included here for completeness.

As shown in Figure 2.4, the light is directed into the photometer using mirror M1 of Figure 2.2(b). The beam is split with a mirrored prism to form two beams. An on–axis beam is deflected to the right and an off–axis beam is deflected to the left. Aperture wheels with six equally spaced holes (6.5, 10, 15, 20, 30, and 40 arc sec. diameter) are mounted in the image plane of each beam. The wheels are self–locating and are

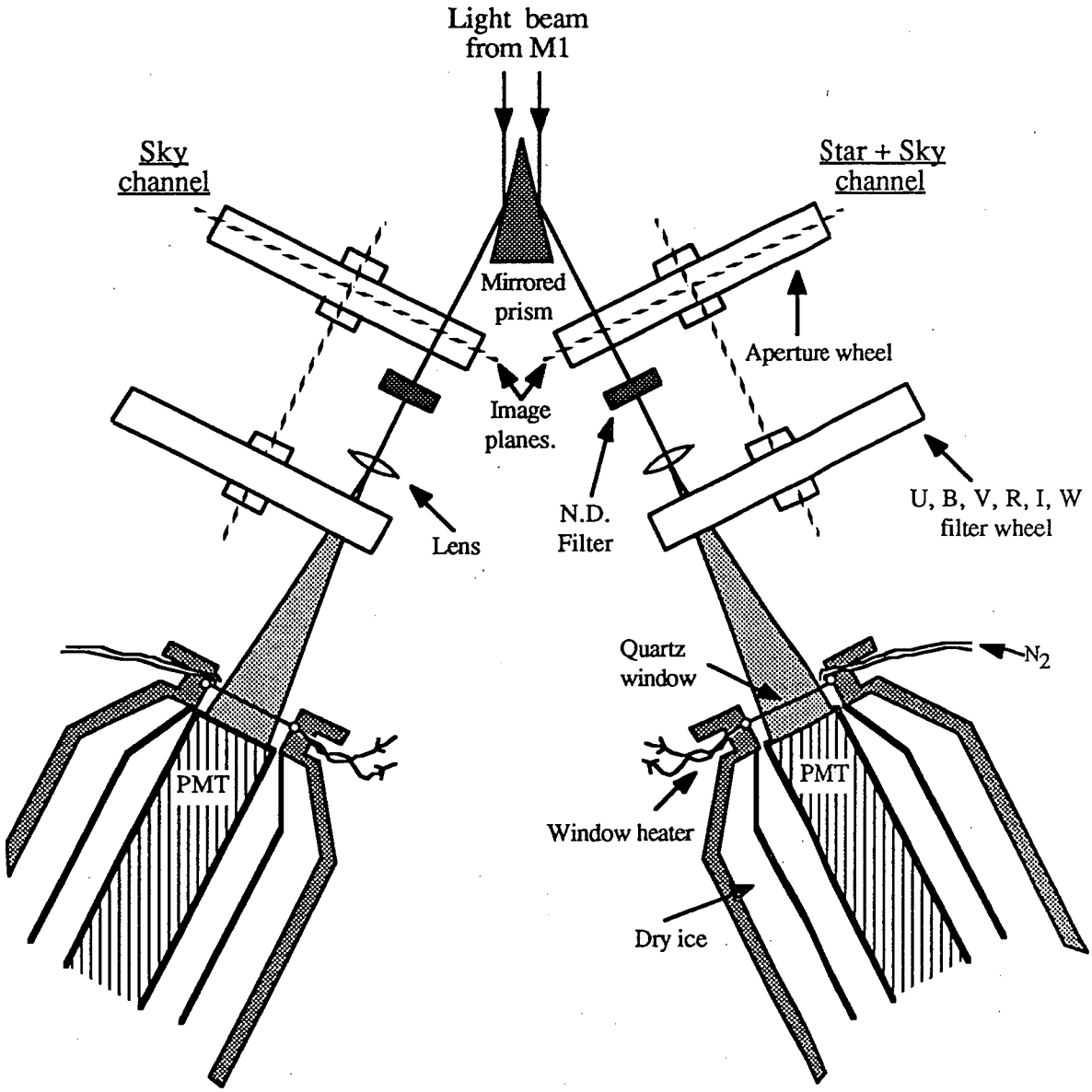

Figure 2.4
The Cassegrain photometer optical and mechanical design.

manually operated from Cassegrain focus. Behind the aperture wheels, neutral density filters are mounted on retractable arms. The sky channel neutral–density filter arm is manually operated from Cassegrain while the star channel one is controlled by computer from the telescope control room.

Lenses (Fabray lens) are used to image the beams onto the photomultiplier tubes by way of filter wheels. Each lens is positioned so that it forms an image of the primary mirror on the photomultiplier tubes. This stationary image helps reduce noise resulting from seeing motion and any sensitivity variations across the surface of the tubes. The filter wheels are similar in construction to the aperture wheels. Five of the six positions available correspond to U, B, V, R and I filters and one is left vacant for white light observations. The filter wheels are operated by computer control from the telescope control room. A heater element surrounds the outer edge of the quartz window on each photomultiplier cold box and a small tube directs dry nitrogen onto the window to prevent fogging.

2.5 Instrument Control at Cassegrain

The Cassegrain photometer and TV guider/finder system have a number of mechanical parts that need to be positioned. In the original system each particular element was manually controlled from Cassegrain focus by the observer. Such a procedure was not satisfactory for two reasons. Firstly, it was time consuming to leave the control room and climb up to Cassegrain focus in semi–darkness, make the changes and return to the control room. Secondly, there are particular telescope positions where it is difficult, or impossible, to reach Cassegrain focus. In these positions it was necessary to move the telescope to make the changes and then move it back to the object.

To resolve these difficulties, when the new Cassegrain TV guider/finder was installed, the photometer was also upgraded by motorising the UBVRI filters and star channel neutral density filter. This enabled the whole system to be operated from the telescope control room. To reduce the number of cables involved in accomplishing this upgrade, a Z80 based microcomputer was installed at Cassegrain focus with appropriate hardware for sensing limit switches and driving DC motors, synchronous AC motors and stepping motors. This Z80 system has the advantage of requiring only one line between the telescope and the control room. Also, new instruments or functions can now be added by simple updates to the eprom–based software. As well as this, devices can be easily interfaced to the data–collecting computer, which is then able to request their status and record it along with the data.

2.6 The Data Acquisition System

In its original form the Cassegrain photometer data acquisition simply relied on the signals from the photomultipliers being fed directly into counters. These counters were started manually by the observer and remained enabled for a preset period of time. At the end of the preset period, the contents of the counters were displayed on a small thermal printer.

Since then the photometer data acquisition system has undergone two major stages of development. These stages were carried out by the author and other technical staff at the University of Tasmania. The essence of these two developmental stages is as follows:

(i) Mark I System
In the early 1980's, a Digital LSI–11/02 computer and Remex floppy disk drive were added to the system. A counter board was designed and built. The counters plugged directly into the LSI–11 Q–Bus and made it possible for the computer, under program control, to start, stop, read the counters, and store the results on floppy disk.

(ii) Mark II System
In 1987 the data acquisition computer was upgraded to a PDP–11/40, with hard disk drives and a magnetic tape unit. A bus interpreter was used to interface the existing Q-Bus peripherals to the PDP–11 Unibus, and new data acquisition software was implemented.

Both these Mark I and Mark II versions of the data acquisition system have been used to obtain the data presented in this thesis and will be described in more detail in the following subsections. All of the data acquisition software for these versions was written by the author.

When following the developmental outline here, it must be remembered that the feasible options were dictated by over–riding financial constraints. These constraints essentially limited equipment to that which was either currently available, or could be obtained on an extended loan basis. During the course of this project the average annual budget for the telescope system was approximately $A5000. This amount had to cover costs of all observing and maintenance done to the telescope, as well as the purchase of any new or replacement equipment.

2.6.1 Mark I Hardware

Figure 2.5 shows the major components of the Mark I version of the photometric data acquisition system. It was constructed around an LSI–11/02 computer with dual 8" Remex floppy disk drives, which were all available to the observatory.

The photometers are operated in pulse–counting mode. Their output goes directly to low noise pre–amplifiers mounted on the outside of their cold–boxes. The outputs from the pre–amplifiers are taken to noise discriminating, pulse shaping and line driving circuitry. This circuitry consists of low–gain amplifiers with hysteresis set to an optimum level for noise rejection, monostable multi–vibrators to produce a square wave, and line drivers. The pulse width from each monostable multi–vibrator is set at ΔT=350 ns. Given a true count rate R_T counts s^{-1}, the probability of coincident counts is given by $\sim R_T x \Delta T$. Thus one percent coincidence occurs at ~28600 counts s^{-1}. To decrease the effect of coincident counts at high count rates it would be necessary to improve the line driver circuitry. This would allow a smaller value of ΔT to be used. However, since the count rate in white light from a magnitude 12 star is of the order of 9,500 counts s^{-1}, (depending on the condition of the mirrors), coincidence is not generally a major problem. For bright objects where coincidence is significant, neutral density filters are available. It is also possible, under most circumstances, to correct the data during data analysis.

The line drivers transfer the signals to the control room along a pair of 50 Ω coaxial cables. At the control room they are fed into dual 32 bit counters. The counters and associated control logic plug directly into the LSI–11/02 Q–Bus. The control logic allows the counters to be enabled, cleared, read or disabled by the computer. Timing is obtained from a frequency standard by way of dividers. The dividers provide either 1.0, 0.1, 0.02 or 0.01 s pulses. The counter board control logic uses these pulses for accurate sample timing. The frequency standard is also used to run the sidereal and solar clocks. The computer can read BCD hours, minutes and seconds using a parallel interface. The solar time was previously set accurately using VNG time signals. The offset between VNG and the solar clock can be measured by examining the VNG signal on a CRO and using the one second clock pulse to trigger the CRO. An accuracy limit of about 5 ms was fixed by the signal travel time delay between VNG and the observatory. A value of 5.16×10^{-9} sec/sec was determined for the long-term drift rate of the frequency standard. It was measured by comparing the 1s pulses from our standard, with the 1s pulse from the Rubidium clock at the Mt. Pleasant radio-astronomy observatory. This value was also found to be consistent with some short-

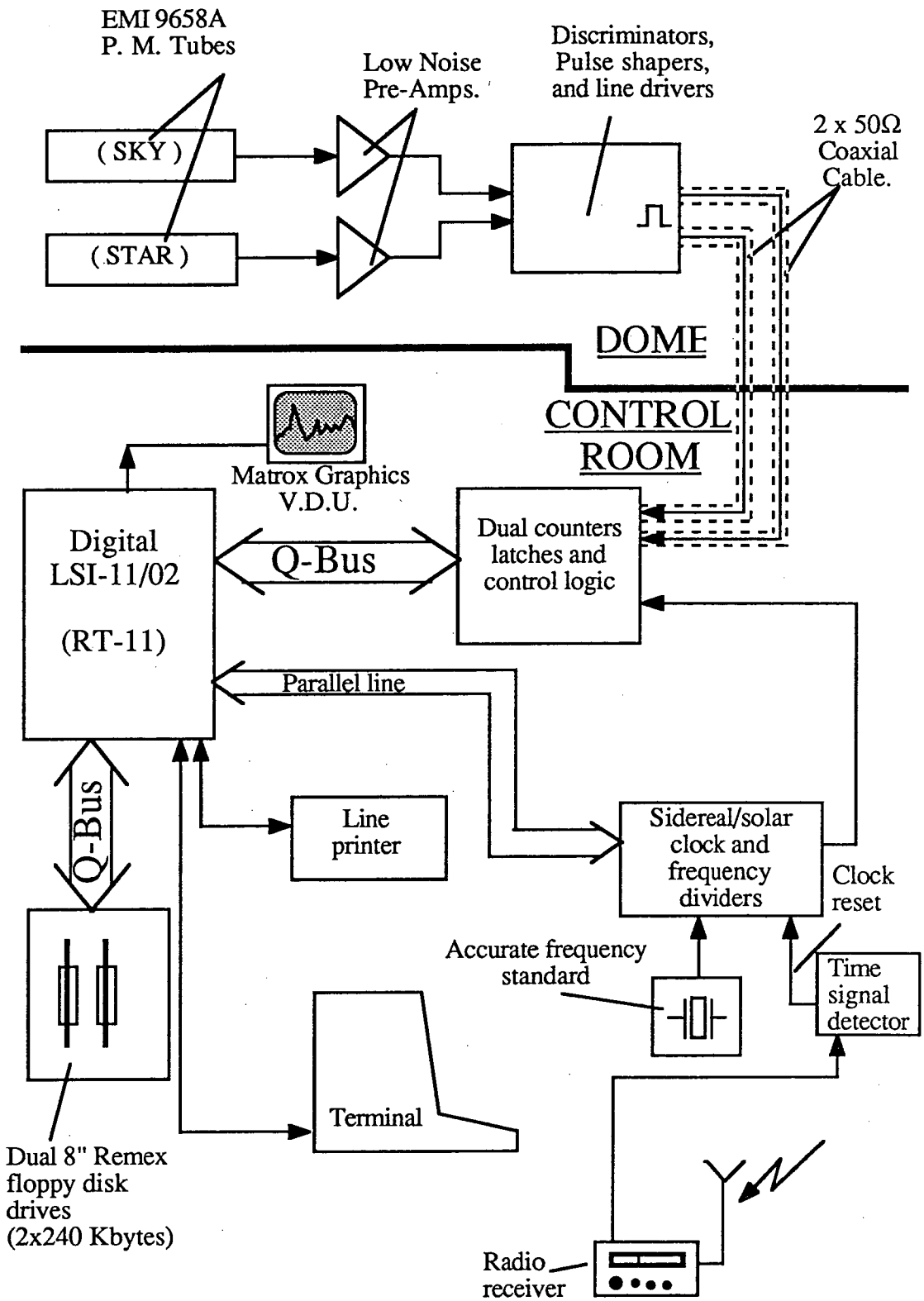

Figure 2.5
The major components of the Mark I data acquisition system.

term spot measurements that were made to check the short-term stability.

When operating, the acquisition system proceeds in the following way. The computer program enables the counters and timing interrupts. Each sample timing pulse then disables the counters, latches the counters into a parallel set of registers, clears the counters and finally re–enables them. This sequence of events results in a 40 ns dead time, which is negligible. The timing pulse is also used to initiate a computer interrupt sequence to read the registers. The whole process continues until the computer program disables the counters and timing interrupts. The absolute start time is obtained by initially reading the solar clock each time there is an interrupt from the counters and delaying data collection until the seconds ticks over. At that point the start time is recorded and data collection is initiated. No other absolute timing information is stored along with the data. The computer stores the counts from both channels of the photometer on the 8 inch floppy disk drive, and uses a Matrox 512x256 pixel graphics board to produce a real time display of the incoming data.

2.6.2 Mark I Software

Two main functions are performed by the data acquisition software. Firstly, it stores the data from the counters, along with other observational information, on floppy disks. Secondly, it provides the observer with a real time display of the incoming data. The real time display of data is used to help define the position of the aperture on the TV guider screen and to monitor the incoming data stream. This monitoring facility provides a sensitive method of detecting guide errors, and cloud and dome obscuration problems.

The major constraint imposed on the Mark I data collecting system by the hardware was the 240K bytes capacity of the floppy disks. This limited the number of continious samples (32 bits x 2 channels) to approximately 30700. At one sample per second this corresponds to about 8.5 hours of data, and at one sample per 20 ms, to only 10 minutes of data. When using high sample rates, like one sample per 20 ms, it is not necessary to store the data in 32 bits, since decreasing the sample time also produces a corresponding decrease in the counts per sample. It transpires that 16 bits is quite sufficient. Hence, to overcome the small disk capacity problem, two versions of the Mark I data acquisition program were made available, one for normal two channel (32 bits) photometry, and another version for high speed single channel (16 bits) photometry. The higher speed version increases the amount of data able to be collected from 10 minutes to 40 minutes with a 20 ms sample time. Apart from this difference,

the two versions of the Mark I programs operate identically. This major storage limitation imposed by the floppy disks was overcome in the Mark II version of the data acquisition system. The Mark II version is necessary if one wishes to acquire useful continuous data streams with sample times of less than 20 ms.

When controlling data acquisition with the Mark I software, commands of the form <esc>n are entered at the computer keyboard. Here n is a number between 1 and 9. The commands initiate the following actions:

(i) **<esc>1**

To close any existing output file and open a new output file. In doing this the operator is prompted for the following file–header information:

a) A data identification comment.
b) The aperture size to be used.
c) The filter to be used (U,B,V,R,I or none).
d) The sampling interrupt period to be used.
e) An interrupt summing factor to be used.

This information is written to the output file along with the current computer date. The program uses the interrupt summing factor to integrate the data from several samples before writing it to the output file. This facility is useful when a particular interrupt sample time is not available. For example, since a 0.5 s interrupt sample time is not available, one would use an interrupt sample time of 0.1 s and a summing factor of 5 to give 0.5 s integrations.

Separate from the file header information, the program also requests a display summing factor to provide a quite distinct integration time for the real time display of data. For example, if data were being accumulated for 0.5 s intervals as above, then it would be possible to have a real time display resolution of 2.0 s by choosing a display summing factor of 20 .

(ii) **<esc>2**

To enable data acquisition. In doing this, the operator is prompted for a run identification comment which is written into the run header part of the output file. Data acquisition is delayed until the next second on the solar clock ticks over, whereupon the solar time is read and recorded in the run header. This delay is necessary to get an accurate value for the start time, since it is only possible to read hours, minutes and seconds from the solar clock.

(iii) **<esc>3**

To disable data acquisition, ending the current run.

(iv) **<esc>4**

To enable the real time display of incoming data.

(v) **<esc>5**

To clear and reinitialise the graphics display. This option is necessary when moving from one source to another. With a display resolution of 1 s, the display buffer would take 512 s to re–cycle. Using this option clears the display buffer immediately.

(vi) **<esc>6**

To disable the counters and interrupts, write any buffered data to the output file, close the output file and return to the RT–11 operating system.

(vii) **<esc>7**

To disable real time graphics display. This option disables the display software, thus allowing smaller sample times to be used than those available with the real time display enabled.

(viii) **<esc>8**

To delete the last data run from the output file.

(ix) **<esc>9**

To swap the real time display between channels. The options available are the star channel, the sky channel, and the difference between them. These options are presented cyclically.

The output file is a Fortran, unformatted, direct access, fixed length (8 bytes) record file. The file format is shown in Figure 2.6. It consists of a file header and several runs of data. Each run is made up of a run header followed by the data. The run header contains an eight character run identification and the start time of the run. This format allows the user to store a whole night's observation in a single file, if space permits. The observer puts each object, or comparison star, in a different run. An alternative is to put all the observations in a single run and manually note the times of events, such as moving to or from comparison stars, or making sky measurements. Using the start

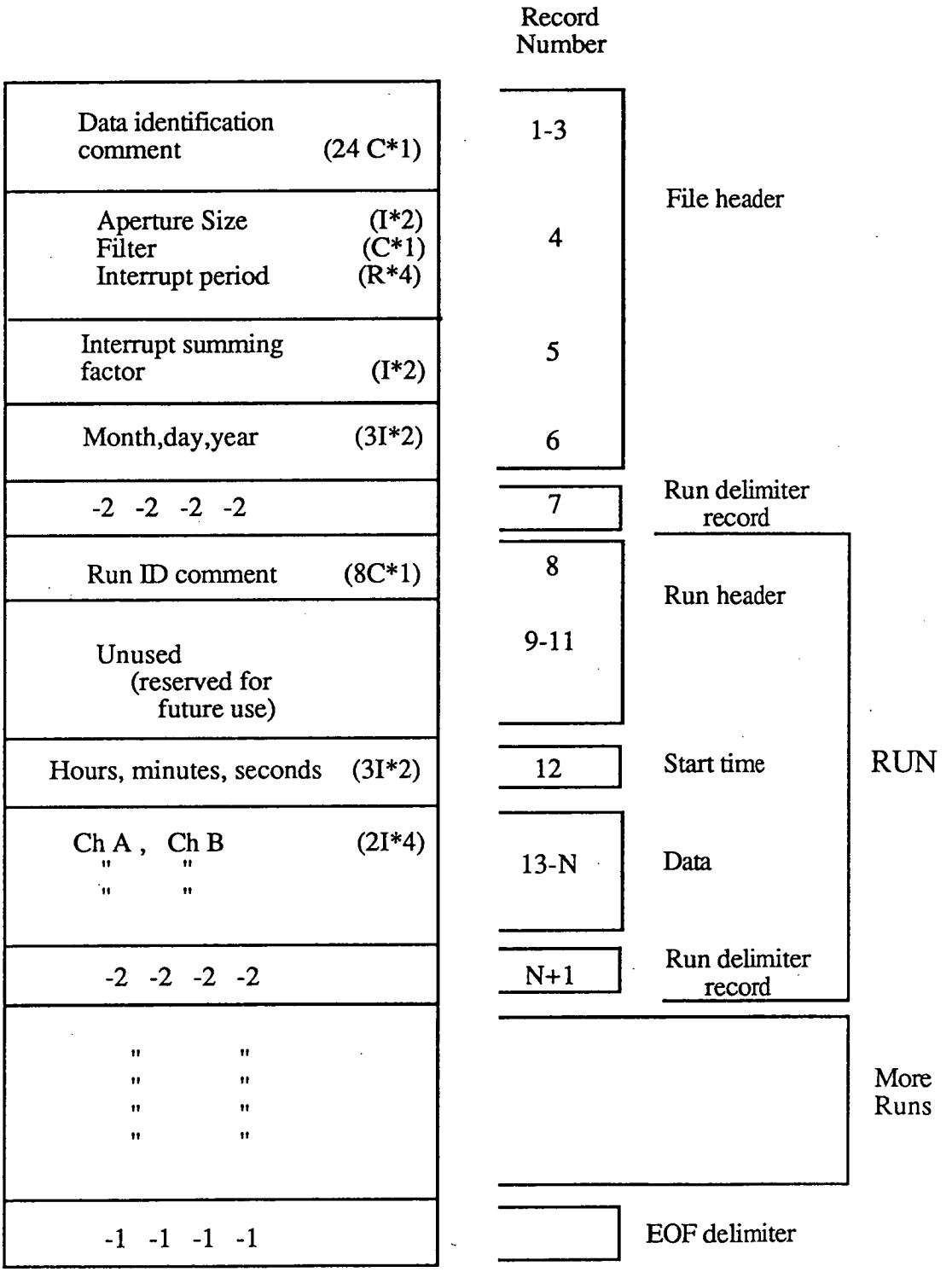

I * 2 = 2 byte integer
I * 4 = 4 byte integer
C * 1 = 1 byte ascii
R * 4 = 4 byte floating point

Figure 2.6
The Mark I data acquisition software file structure.

time from the run header part of the file, it is then a simple operation to extract a particular section of the run. This second technique was found to be more useful when obtaining long sections of data on a single object inter–dispersed with infrequent, short, comparison star and sky background measurements. The file is written using the Fortran WRITE command and hence buffering of the data is left to Fortran I/O system. The data are written in a binary format, this method being more efficient in terms of both space and time.

The data acquisition program is divided into two main parts. The first part consists of a controlling program. This part handles operator requests, the real time display of data, and the writing of data to floppy disk. This section of the program is written in Fortran and its structure is outlined in Figure 2.7. The second part consists of the interrupt initialisation and handling routines. These routines are written in the PDP–11 assembly language Macro–11. The structure of the routines in this part of the program is shown in Figure 2.8

The two parts of the program communicate by way of a common section of memory. This consisting of a large ring buffer, an input pointer which is incremented by the interrupt handling routines as new data arrive, an output pointer which is updated by the control program after it has displayed the data and written it to the disk file, and a buffer overflow error flag which is set by the interrupt processing routines and monitored by the control program. It should be noted that the real time display is never updated while there is unprocessed data in the ring buffer. That is, new data are written to the output file and is only buffered for display until the ring buffer is found to be empty. Only at that point is the real time display updated. This method effectively gives data collection a higher priority than data display. The later requires a few tenths of a second to rescale and update the whole screen.

2.6.3 Mark II Hardware

At the beginning of 1987 the LSI–11/02 was replaced by an available PDP–11/40 computer with 192K bytes of main memory, 2 x RPR02 20M byte disk drives and a half inch 800 bpi magnetic tape drive. The LSI–11 Q–bus peripherals (counter board and Matrox board) were interfaced to the PDP–11 Unibus using an M.D.P. SYSTEMS Inc. bus interpreter. Figure 2.9 shows the structure of this new Mark II computer system.

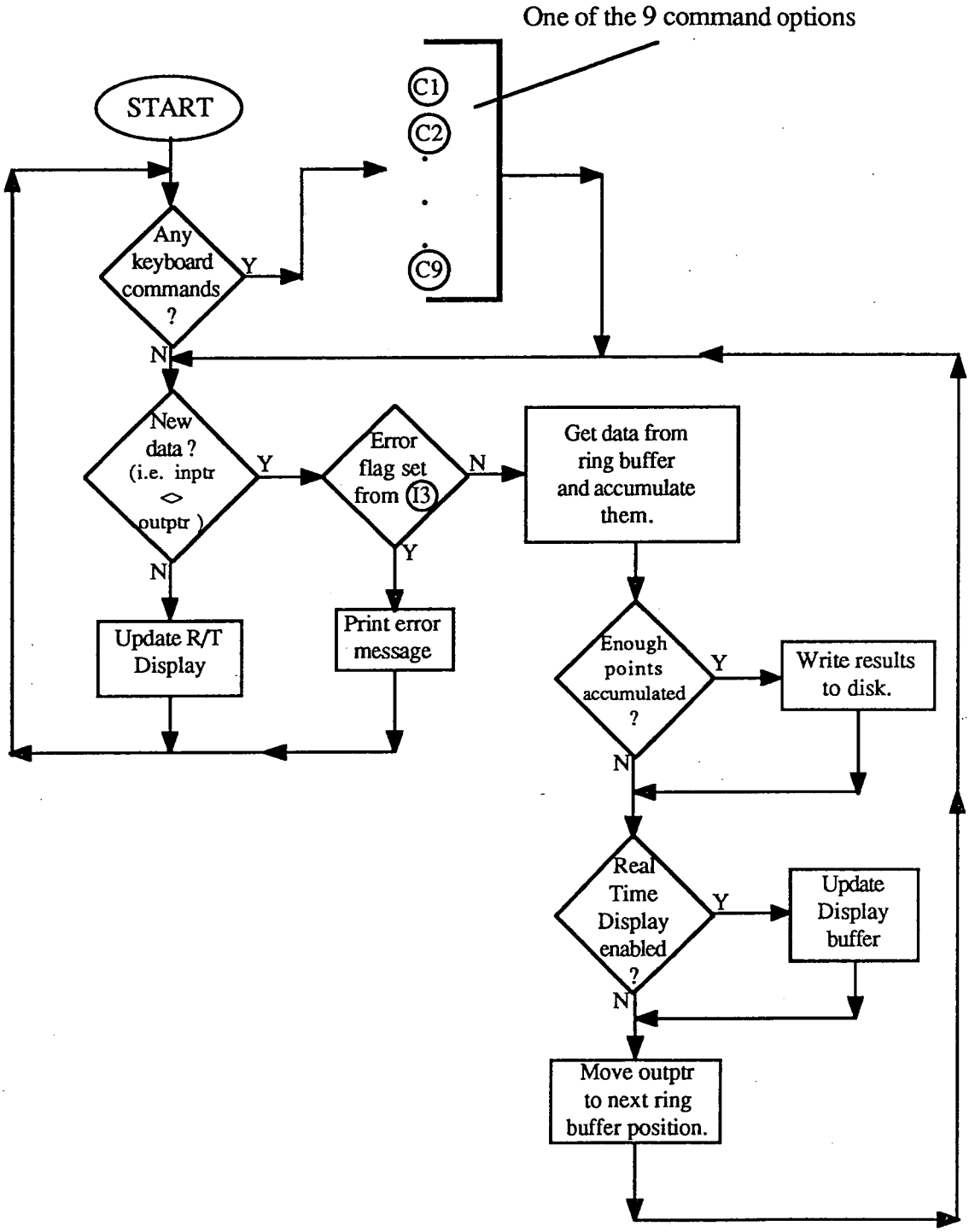

Figure 2.7
The Mark I control program structure.

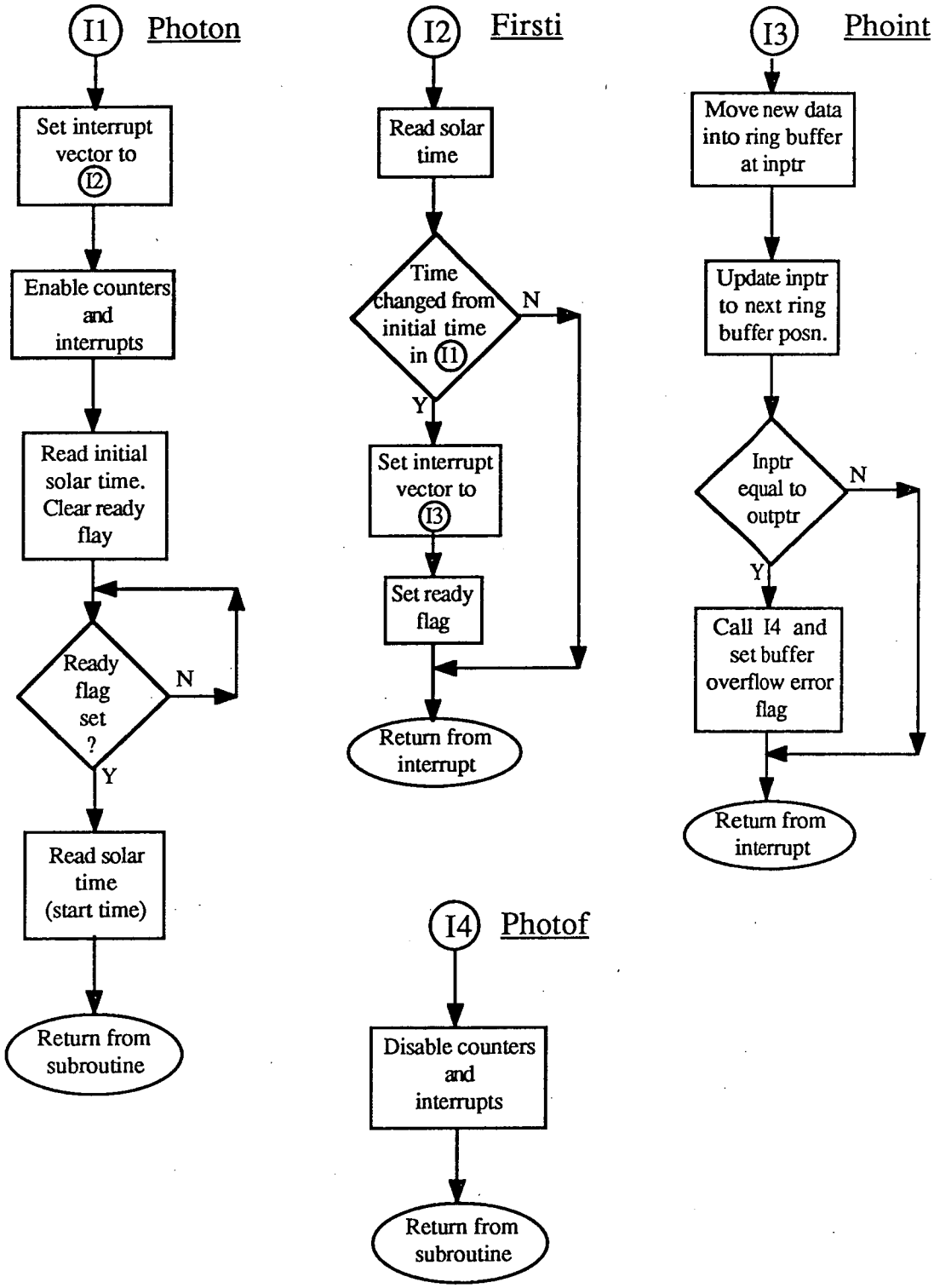

Figure 2.8

The interrupt handling routines associated with the Mark I data acquisition software. The routine Photon enables the counters and interrupts and waits until Firsti has signalled that data collection can commence. Firsti waits until the next solar second ticks over before doing this. All further interrupts are processed by Phoint which handles data collection. The routine Photof is used to disable the counters and interrupts.

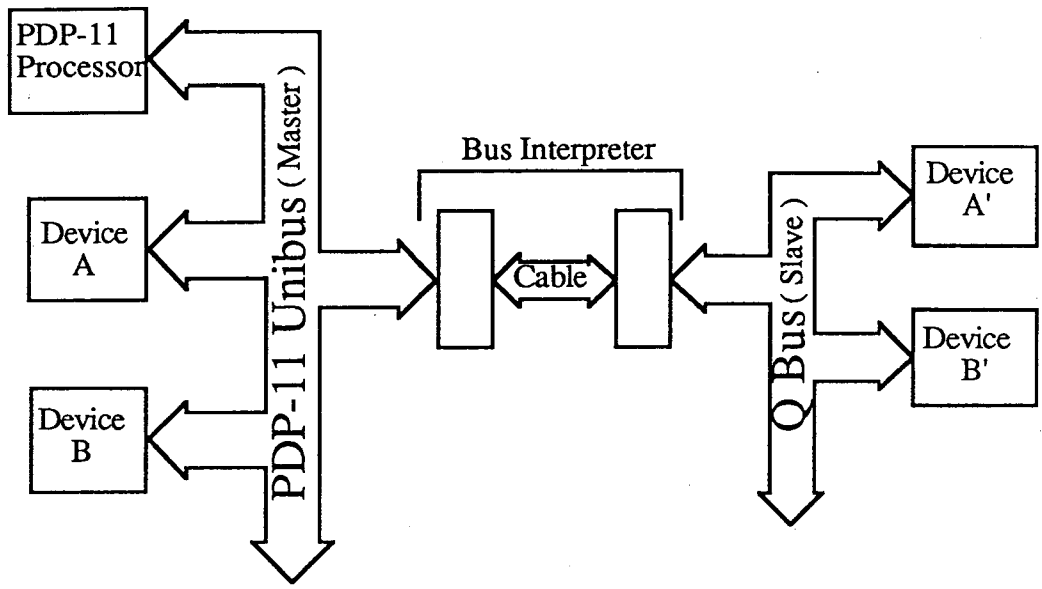

Figure 2.9
The computer configuration used for the Mark II system

The reason for the hardware upgrade was twofold. Firstly, to do high speed photometry of supernova SN1987a a time resolution of less than 1 ms was desirable, and there was a need a need for more disk storage than was currently available on the LSI–11. Secondly, a power supply failure in the LSI–11 caused considerable damage to that computer, necessitating its repair.

Two options were therefore available to us. Either we could repair the LSI–11 and purchase a hard disk drive and controller, or we could use the other observatory computer, a PDP–11/40, previously used for data reduction, and interface the Q–bus peripherals to its Unibus with a bus interpreter. Fortunately an unused bus interpreter existed in the department at the time and was freely available to us. We therefore adopted the second option, because it required little expense, was quick to implement, and provided us with a faster computer which had a magnetic tape drive and hard disk drives attached. At the time of writing this thesis the solar clock has not yet been interfaced to the PDP–11/40; however; this should be accomplished in the near future.

2.6.4 Mark II Software

The Mark II data collecting software was written to operate on the PDP–11/40 based system with a view to doing high speed photometry of the supernova SN1987a. The

proposal was to implement a regular monitoring program for SN1987a, to search for evidence of a rapidly spinning neutron star. Since the spin period might be as small as 1 ms the software would be required to sample at a rate greater than 1 kHz. It was assumed that, at least initially, any modulation would be very weak and it would be necessary to collect as much continuous data as possible.

As already mentioned in Section 2.6.2, for high speed photometry the full 32 bit precision of the counters is unnecessary. Thus, as in the Mark I software, two data acquisition programs have been written. The first program is for two channel (16 bit) photometry. This program has been tested with sample rates up to 2.5 kHz. The second program is used for single channel (8 bit) photometry and will work with sample rates up to 7.5 kHz. For illustration, Table 2.1 shows the time taken to collect 20 Mbytes of data, filling a hard disk, for some sample rates, versus the number of channels and the number of bits per channel.

The Mark II software is capable of much higher data rates than the Mark I versions. There are two reasons for this. Firstly, the data are buffered much more efficiently for the disk and are written asynchronously under DMA control. This improved buffering is achieved by accumulating several disk blocks of data within the program, instead of leaving the buffering to the Fortran I/O system, which is not very efficient. System routines are used for initiating the asynchronous write and detecting its completion. Secondly, the real time display software has been improved. All scaling information is entered into the program by the observer as constants before data acquisition is commenced. In the Mark I software they had been calculated from the incoming data and updated in real time.

Table 2.1

The time in minutes to acquire 20 Mbytes of data for various sample rates as a function of number of channels and number of bits per channel.

		2 channels x 32 bits	2 channels x 16 bits	1 channel x 8 bits
Sample	1.0	43.7	87.3	349.5
rate	2.5	17.5	35.0	139.8
(kHz.)	5.0	8.7	17.5	69.9

The single channel version of the program is a modified version of the dual channel program. The single channel version handles higher sample rates simply because it has only one quarter as many bytes of data to manipulate. Also the code for buffering the data has been improved slightly over the two channel version. It is envisaged that the two channel version will be eventually updated with the same upgraded buffering. This buffering has been optimised by using a single buffer for both input and output. The input routine places new data in a 16K byte ring buffer, and instead of having a separate output buffer, the output routine divides the ring buffer into eight 2K byte blocks. When a block fills up it is written to the output file under DMA control. After the write has been completed, the output pointer is then updated to the next 2K byte block boundary.

As in the Mark I case, the software can be again divided into two parts, consisting of the controlling program and the interrupt processing routines. The interrupt processing routines are virtually identical to the Mark I routines. The only difference is that the section of code dealing with the solar time has been removed. It will be re–inserted when the solar clock is interfaced to the PDP–11/40. The structure of the controlling program is shown in Figure 2.10. This program provides the observer with five options which are initiated by entering the appropriate character on the console keyboard. These options are:

(i) **B** This causes the program to prompt for the number of samples that are to be accumulated per pixel for the real time (RT) display.

(ii) **D** This option allows the observer to set the displays vertical gain/reduction factor.

(iii) **G** This option causes the program to enable the counters and displays the incoming data on the RT display. It does not save the data on disk.

(iv) **S** This option is used as a switch to start/stop saving data to the disk. It can only be used while the program is displaying incoming data (i.e. after the G option).

(v) **P** This option disables the counters and closes the output file if data have been saved to it.

Finally some details about the RT display should be noted. The display resolution is 512 pixels horizontally by 256 pixels vertically. The horizontal and vertical scaling are

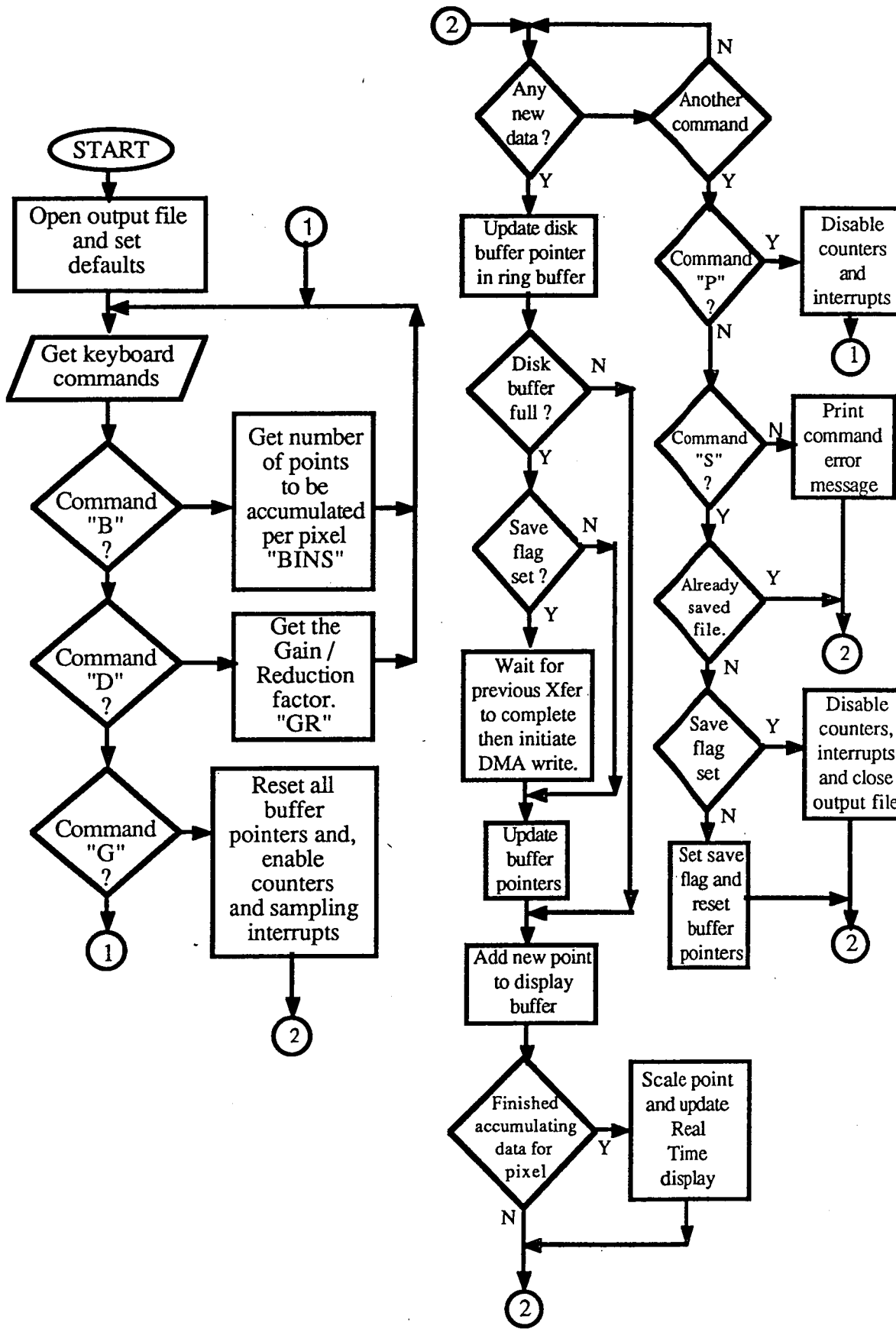

Figure 2.10
The Mark II control program structure.

determined by two parameters that are chosen before data collection is started. The first of these parameters, BINS, is the number of samples that are to be accumulated per pixel for the display. The second parameter, GR, is a display gain or reduction factor. A positive value of GR is interpreted as a reduction factor and a negative value as a gain. For example, GR = 2 reduces the scale by a factor of 2 and GR = –2 increases the scale by a factor of 2. This method has been used as an alternative to using a decimal value, which would be 0.5 and 2 for the above example, since the software avoids floating-point arithmetic where possible to increase program speed.

The horizontal scale is a function of sample time and BINS. For example, with a sample rate of 1 kHz and BINS set to 100, the whole display is updated once every 512 s (10 pixels s^{-1}). The display is updated in a cyclic manner, so the next pixel to be updated after pixel 511 is pixel 0. The vertical scale constant is either BINS/GR for GR > 0 or BINSx(–GR) for GR < 0 . The data to be plotted are divided by this constant, using integer arithmetic, and the result used as the vertical pixel address. If it happens to be greater than 255, say 274, and BINS = 1, then it would wrap around to pixel 18. By setting GR = 2 the 274 would be reduced to 137, hence avoiding the wrap around. If, on the other hand, BINS = 500 and the mean count rate per pixel was 10 counts, with the accumulated counts varying from 4500 to 5500, then all of the data would be plotted in pixels 9, 10 and 11. To improve the vertical resolution, GR could be set to –20. The data would be now plotted between pixels 180 and 220 inclusive, thus improving the display resolution.

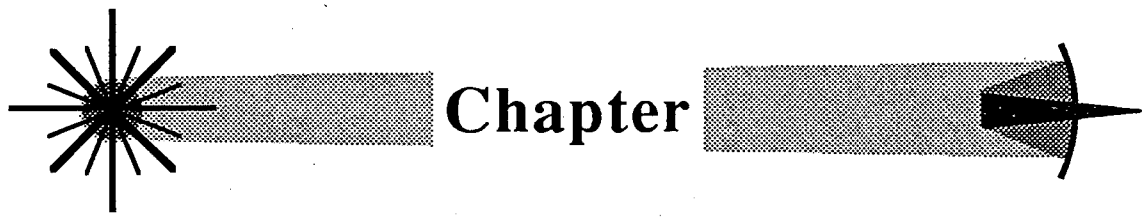

Chapter 3

THE CATACLYSMIC VARIABLES.

3.1 Introduction

This chapter is intended as a breif review of the cataclysmic variable (CV) stars, preliminary to the photometric and spectroscopic observations that are discussed in Chapter 4. The reader who is already familiar with the properties of these stars may wish to proceed directly to Chapter 4.

The first part of this chapter deals with the classification and observational properties of these stars (Section 3.2). Here the important observational features of the classical novae (Section 3.2.1), the recurrent novae (Section 3.2.2), the dwarf novae (Section 3.2.3), and the nova–like stars (Section 3.2.4) are described. The binary model that has been accepted to explain these properties is outlined in Section 3.3 and the remaining sections deal with the chief aspects of this model. In Section 3.3.1 the possible mechanisms that might cause mass transfer between the stellar components in these systems is examined. Some theoretical properties of the secondary component are discussed in Section 3.3.2, and in Section 3.3.3 the properties of simple accretion disks in cataclysmic variables are outlined. The other important sources of luminosity that are considered are the contribution from the hot spot, formed when the stream from the secondary impacts with the disk (Section 3.3.4), and the so–called boundary layer region between the disk and white dwarf surface (Section 3.3.5). In Section 3.3.6 it is noted how the properties of these systems will be substantially modified if the white dwarf possesses a magnetic field. Finally, models pertaining to the outburst

nature of these stars are discussed in Section 3.3.7.

3.2 Observations and Classification

3.2.1 Classical Novae

The classical novae (CN), by definition, have had only one observed outburst. The rise to maximum light is very rapid while the decline is much slower. The pre–novae stars are found from photographic plates to be blue objects that may show slight irregular changes in brightness. The spectra of the novae at minimum light are characterised by emission lines of H I, He I, He II, Ca II and the λ4650 CIII/NIII blend. These are superimposed on a blue continuum. A catalogue of light curves of novae prior to outburst is given by Robinson(1975).

The eruptions of CN range in brightness from 7 to 20 mag. (mean ~12 mag.) in the optical. They then fade by a similar amount, and are observed to cause shells of material to be ejected with velocities between 100 km s^{-1} for slow novae and 4000 km s^{-1} for fast novae. Mass estimates of the ejected material lie in the range 10^{-4} to 10^{-5} M⊙. The optical rise to maximum is of the order of only a few days. The rise is generally very steep, being 7 to 10 mag in the first 24 hours, followed by a slow rise in the last 1 or 2 magnitudes before maximum. At the slow-down point some novae may stop, or even show a decline, before continuing on to maximum. The total energy output from an eruption is $\lesssim 10^{45}$ erg.

The decline rate defines the sub–class of the nova. The *fast* ones take 10 to 20 days to decline 2 mag from maximum, while the *slow* ones take the order of 100 days. The fast novae have brighter absolute magnitudes at maximum than slow novae, but may radiate less total energy. X–ray observations of CN in quiescence have shown that the fast novae seem to be more luminous than the slow ones (Becker and Marshall 1981). If this is the case, it enables the speed class of a nova to be determined well after it has erupted.

The decline in magnitude after maximum is smooth down to ~3.5 mag below maximum. At this point in the decline of a fast novae, rapid quasi–periodic variations can appear with amplitudes of ~1 mag and periods of 1 to 5 days. The slow novae begin this phase with a rapid decline to a transitional minimum which is then followed by a second rise. After this rise the decline continues with less fluctuation. The explanation of the initial sharp drop in light is assumed to be the optical thinning of the ejected shell. At about the same phase in the fast novae the quasi–periodic variations

die away. In both cases, the transition to a slow decline occurs at ~6 mag below maximum. The star then gradually approaches the quasi–stable post–nova state, which approximately corresponds to the pre–nova brightness, and often shows rapid low amplitude changes in brightness. The return to pre–nova brightness usually takes the order of a decade or two. Payne–Gaposchkin (1957) in her now famous book, "The Galactic Novae", presents an enormous amount of observational data (including light curves) for these objects.

The optical variability of CN, however, does not tell the whole story. Ultra–violet (UV) and infrared (IR) observations have shown that, while the visible light declines during the first weeks after the eruption, the UV luminosity rises in such a way that the combined optical plus UV power is approximately constant. The IR characteristics are quite different again, with the fast novae showing little or no black–body IR excess. However the slow novae begin to show an IR excess at about the time the UV luminosity commences to decrease. This excess continues to increase for ~200 to 300 days after the optical maximum, reaching 5×10^4 $L_\odot$ in the case of FU Ser (Geisel et al ,1970). Geisel et al attribute the IR excess to heating of dust grains formed in the ejected material. Two possible mechanisms have been suggested for this heating. It may be collisional warming of the ejected material by interstellar gas. Alternatively, it may be the redistribution of the UV into the IR. Observations made by Gallagher and Holm (1974) have discounted the latter possibility because it predicts a remnant temperature of ~200 000 °K. This was not supported by UV observations they made of FU Ser with the OAO–2 satellite. After reaching maximum, the IR decays with a time constant of the order of 100 – 150 days. Thus the total luminosity of the nova may remain high for much longer than is indicated by its optical–band characteristics.

Gallagher and Starrfield (1978) and Starrfield and Sparks (1987) have presented excellent reviews of the CN systems.

3.2.2 Recurrent Novae

Recurrent novae (RN) resemble the classical novae in that their outburst characteristics are very similar. It is impossible to differentiate between the two from outburst light curves alone, or to identified a recurrent novae from its first outburst. Even between outbursts their behavior is similar. In fact it has been suggested that all novae are recurrent and that the observed ones are just those with the shortest periods. The interval between outbursts ranges from 10 to 80 years and the outbursts range in amplitude from 4 to 8 mag. For RN where more than two outbursts have been observed, the intervals between maxima are not constant but can vary by a ratio as

great as 4:1 . It is, however, quite possible that outbursts have occurred and been missed.

There is strong spectral evidence to suggest that many RN have a giant star for their secondaries. If this is the case, then at minimum light most of their luminosity could be attributed to the giant star. Hence their outburst amplitudes would be similar to those of the CN, for which absolute magnitudes at minimum are much fainter.

3.2.3 Dwarf Novae

Dwarf novae (DN) form the largest of the four sub–classes of CV's, with over 300 known members. They have a rapid nova–like rise to maximum light, but their increase in brightness is only 2 to 6 mag, and they fade back to pre–outburst brightness within 2 to 10 days. The energy liberated during an outburst is typically 10^{38} to 10^{39} ergs, compared with $\sim 10^{45}$ ergs for the CN and RN. The outbursts are repeated quasi–periodically for any particular star. The intervals between outburst range from as little as 10 days to as much as 600 days. Most lie in the range 20 to 50 days. For any particular star the outburst interval varies, but is usually sufficiently constant for a characteristic time–scale to be associated with each star. Unlike the CN and RN, the DN do not show an IR excess on the decline from maximum and there is no evidence for an ejected shell of matter. However, P–Cygni line profiles in the UV are evidence that there is a wind of material moving away from the system during some outbursts. Spectroscopically the DN differ from the CN and RN in that the latter have higher excitation lines and generally their emission lines are stronger. In particular, the λ4650 CIII–NIII blend is present and stronger He II emission is seen. At minimum light the CN and RN tend to be brighter than the DN. The CN and RN have mean absolute magnitudes around $M_V \approx +4.5$ while the DN have $M_V \approx +7.5$. The DN have been grouped into sub–classes U Gem, SS Cyg, Z Cam, and SU UMa according to their outburst characteristics, which are shown in Figure 3.1 and which may be detailed as follows:

(i) The **U Gem** stars are characterised by two distinct forms of outburst which depend on the time spent at maximum. These long and short outbursts and are collectively referred to as *normal* outbursts. The long and short eruptions have a tendency to alternate. The more energetic eruptions tend to be followed by longer intervals of quiescence.

(ii) The **SS Cyg** stars have, in addition to the normal eruptions, another type of eruption. These eruptions tend to be rounded at the peak and have a slow rise to

maximum light. They are referred to in the literature as *anomalous* eruptions.

(iii) The **Z Cam** stars are similar to the U Gem stars in that they have normal eruptions. However, their distinguishing feature is that they can stay at an almost constant brightness for extended periods. These *standstills* almost always occur during the decline from an outburst and at the same point in the decline. They usually last only a few days, but have been known to last as long as several years on rare occasions. The mean energy output during standstill is approximately equal to the mean non–standstill energy output. Typically their outburst period is shorter than average for dwarf novae, being normally less than 50 days.

(iv) The **SU UMa** sub–class, recently defined by Vogt (1980), are also very similar to the U Gem sub–class in that they possess the normal type of eruption as well. However, periodically they undergo an extended outburst, called a *supermaximum*. The supermaxima are 1 to 2 mag brighter than the normal eruptions and generally last longer than the normal outbursts. The super–outbursts have a tendency to be more predictable than the normal outbursts and occur at a rate of one super–outburst per 3 to 10 normal outbursts. The stars that belong to this group also belong to the ultra–short period group, all having orbital periods of less than two hours. DN with outburst periods less than ~30 days fall into either this sub–class or the Z Cam sub–class. The two groups are mutually exclusive, with no SU UMa DN having standstills and no Z Cam stars having supermaxima. Glasby (1970) presents a comprehensive list of schematic DN outburst light curves.

The spectra of dwarf novae in their quiescent state are characterised by broad emission lines on a flat or blue optical continuum. The Balmer lines, He I, as well as He II and Ca II to a lesser degree, are present in the optical region. He II tends to be stronger in the CN and RN. The line width can be attributed to Doppler broadening. The Balmer lines and He I lines are double in systems that are highly inclined. Some DN show the absorption spectrum of G and K main sequence stars. However the secondary is not detected in those with an orbital period less than 6 hours. During a DN eruption the continuum becomes brighter and the lines become relatively fainter. At maximum the emission lines are generally replaced by absorption lines, sometimes with weak central emission on the decline from maximum.

The variation in the light of DN at minimum takes the form of either variability at the binary period or rapid non–periodic fluctuations. The latter is referred to as *flickering*. Many highly inclined DN show a hump in their light curve between orbital phase 0.6

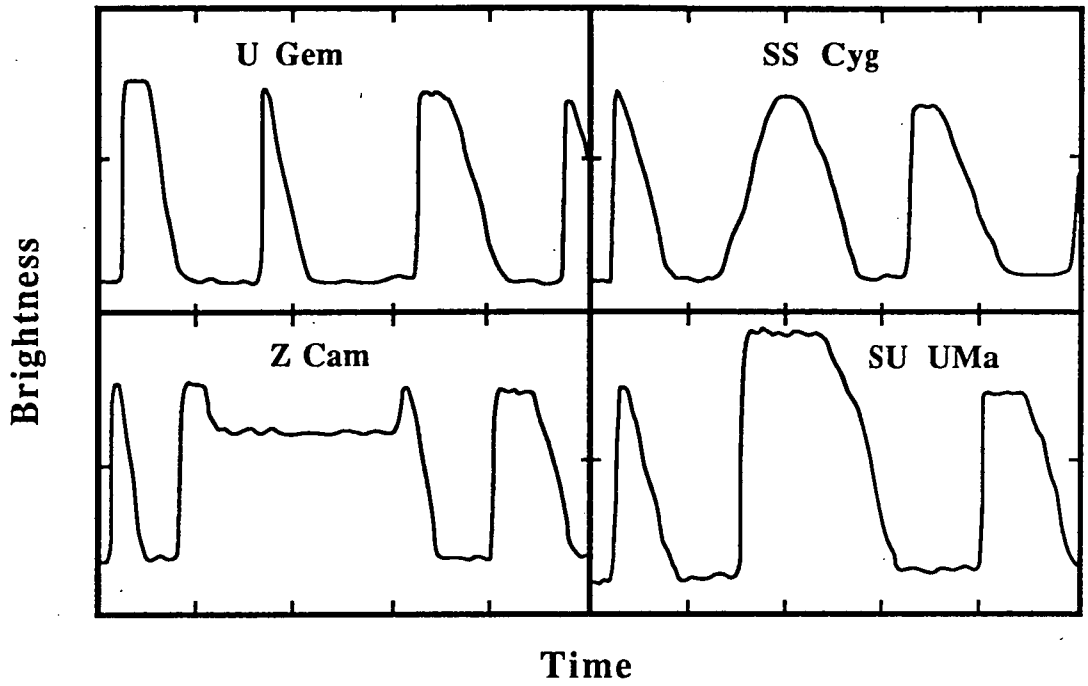

Figure 3.1

Schematic light curves for four sub–classes of dwarf nova. These light curves illustrate the different types of outbursts.

and 0.1. This can contribute up to 50 percent of the light from a system. One of the better known examples of this is the star U Gem itself. Typically flickering shows up as low amplitude ($\lesssim$1 mag) changes in brightness on a time scale that ranges from seconds to tens of minutes. Photometric studies have shown that the amplitude of the flickering is larger in the UV than at longer wavelengths. In systems with a hump, the flickering is generally larger during the hump and is seen to disappear entirely during an eclipse. Some systems, however, show flickering at all binary phases. Power spectra of the light curves reveal a continuous rise in power towards the lower frequencies, with power tending to rise linearly with f^{-1}. Multi–colour observations of eclipsing systems show that the eclipse width is generally longest in the IR and shortest in the UV.

DN begin an outburst with a general reddening and then as they rise to maximum they become bluer (Bailey 1980). The eruption seems to start in the visible part of the spectrum with the UV beginning its increase in brightness after a delay of several hours. Smak (1987) also gives evidence for a second type of outburst that occurs almost simultaneously at all wavelengths. After maximum, the UV and optical wavelengths return to quiescence roughly in step. During the decline from outburst

some DN show low amplitude quasi–periodic oscillations. These usually vary in period, sometimes with a steady drift. At other times the drift is more irregular and with perhaps many periods present at once. Their coherence varies from a few cycles to several hundred cycles. The more coherent cases tend to show an increase in period as the outburst declines. Oscillations are not observed in all DN and on occasions they have failed to be detected in DN that have shown them during previous eruptions. Typically the periods are in the range 10 to 40 s and the amplitudes range from 0.0009 to 0.01 magnitudes.

The hump that is seen at quiescence is only marginally affected by the outburst and its contribution to the total light from the system remains about the same during an outburst. This is evident in U Gem, where the eclipse of the hump–producing feature becomes very shallow during outburst. However, during supermaximum in the SU UMa type stars, the normal hump disappears on the rise to maximum and is gradually replaced with a similar feature that is much brighter than the normal hump (~40 times normal for VW Hydri). This superhump has a period that is 2 to 5 percent larger than the binary period and is even seen in systems with low inclination. On the decline from outburst the amplitude of the super–hump decays more rapidly than the brightness of the star, and eventually the normal hump returns.

Observations of DN with the Einstein X–ray observatory showed them to be low luminosity X–ray sources. In their quiescent state, the ratio of hard X–ray flux to visible flux is approximately unity. However, during outburst the ratio changes so that $L_X/L_V \lesssim 0.06$, indicating that the hard X–ray flux has changed little when compared with the change at optical and UV wavelengths. The soft X–ray luminosity (0.1–0.5 keV), on the other hand, is seen to increase by a factor of ~100 for some DN at maximum. This component has an effective black body temperature of $kT \approx 50$ eV, implying that much of the emission during outburst is in the extreme ultra–violet (EUV) region of the spectrum. The flickering in simultaneous X–ray and optical light curves correlates well, suggesting that they may be related. In eclipsing systems the hard X–ray eclipse is seen to correspond with the optical one.

3.2.4 Nova–like variables

Nova–like variables (NL), unlike stars in the preceding groups, have not been observed to erupt. They show light variations and spectral features similar to the other classes of CV. The nova–like group probably include some historical novae whose outbursts were not recorded, stars that are yet to undergo nova eruptions, and possibly stars similar to the Z Cam stars but in a permanent state of outburst. In general the NL

do not vary as dramatically as the other classes of CV, and are more difficult to recognise. It is not surprising then, that a relatively high proportion of the NL stars are eclipsing systems, since eclipsing systems are much more noticeable. I will also include three other types of CV under the heading of NL objects. Besides the UX UMa stars (that is classical NL variables), there are the magnetic variables, and the VY Scl stars. The magnetic variables encompass the AM Her stars, or *Polars*, and the DQ Her stars, or the *Intermediate Polars*. The properties of these sub–classes are as follows:

(i) The **UX UMa** stars resemble DN near outburst or standstill. Typically they show weak He II and λ4650 emission or absorption. They can have an orbital hump characteristic of the other CV classes, although it is smaller than those in DN with similar inclination. Their flickering characteristics are similar to the DN. Stars belonging to this class have orbital periods greater than 3 hours.

(ii) The **AM Her** stars are recognised primarily by variations, at the orbital period, in their circular and linear polarised light. The fraction of polarisation ranges between 10 and 35 percent and is usually strongest at red and IR wavelengths with the exception of systems with higher than usual magnetic fields (Section 3.3.6.1). These systems don't have eruptions as such, but have *on* and *off* states that may last from weeks to years. The on and off states differ in brightness by 3 to 5 magnitudes. The AM Her objects are the strongest X–ray emitters of all the CV's, with $L_X/L_V \approx 10$. They show broad Balmer, He I, He II and λ4650 single peaked emission lines. When in their off state some of these stars show Zeeman splitting of the emission lines, implying magnetic fields of the order of a few times 10^7 G. In contrast to the DN, the AM Her stars show strong flickering in the red. This tends to be present throughout the whole orbital cycle. The X–ray spectrum of these stars is composed of two parts, a soft X–ray blackbody component and a hard X–ray bremsstrahlung component. Unlike other CV's the soft X–ray flux dominates their X–ray spectrum.

(iii) The **DQ Her** stars have as their defining characteristic, stable, short period, coherent variations in their optical and/or X–ray flux. The period of these oscillations ranges from 33 seconds in the case of AE Aqr to 67 minutes for EX Hya. In some systems three separate periods are seen: a longer period associated with the binary orbit, P_0; a short period variation in the X–ray and/or optical, P_1; and another short period modulation in the optical, P_2. The periods are related by:

$$\frac{1}{P_2} = \frac{1}{P_1} - \frac{1}{P_0}. \qquad 3.1$$

Warner (1982) shows that this relationship is expected if the X–ray/optical periodicity (P_1) is due to the rotation of the primary (see Section 3.3.6.2.). This seems quite likely given the stability of these oscillations ($P/\dot{P} = -2.7 \times 10^6$ yr^{-1} for DQ Her itself). Some of these systems have circularly polarised light in the optical, modulated at period P_1, (~0.6 percent for both DQ Her and AE Aqr). The polarisation is much weaker than that observed in AM Her systems. This indicates that the DQ Her systems have weaker magnetic fields than the AM Her types. It is believed that the primaries in the DQ Her systems possesses fields of $\lesssim 10^7$ G.

Finally, it is worth while noting that many DQ Her stars belong to other CV classes. For example, DQ Her itself is also classed as an ex–nova, EX Hya has dwarf nova outbursts and many are classed as nova-like. Similarly several CN exhibit DN outbursts (e.g. Q Cyg, GK Per). This would tend to support the argument that, for CV's in general, we are looking at similar systems, perhaps at different points in their evolution or with only subtle physical differences.

(iv) The **VY Scl** stars show *high* and *low* states. They stay in their high state most of the time and occasionally dim to a low state, similar to the AM Her stars. However, unlike the AM Her objects, their light is not polarised. In their high state they resemble the UX UMa stars. When they dim, they are more like the DN at quiescence. The low states can last from a few weeks up to many months and are 3 to 5 mag fainter than normal brightness. In their low state, their energy distribution is consistent with that of a hot white dwarf. VY Scl stars are sometimes referred to as anti–dwarf novae because, unlike the DN, they spend most of their time in the high state.

3.3 The Binary Model

The standard model for CV's envisages a binary system in which the primary star is a white dwarf and its companion is a near main sequence G, K, or M star, or in some cases a giant star. I will not include in this discussion the AM CVn stars, which have white dwarf secondaries, as they are fundamentally different. Since the majority of CV's are observed to have short orbital periods ranging from ~82 min to ~16.5 hours (excluding GK Per and T CrB), then by Kepler's third law the distance, a, between the components must be small. We may write this law as

$$a = 3.5 \times 10^{10} \times P^{2/3} \times (M_1+M_2)^{1/3} \text{ cm}, \qquad 3.2$$

where P is the orbital period in hours and M_1 and M_2 are the masses of the component

stars in solar masses. If, for example, a system has a total mass of 1M⊙ and an orbital period of 100 min, then the components will be separated by ~4.9×10^5 km, approximately the Earth–Moon separation.

If the secondary fills its Roche lobe, then material will stream away from it through the inner Lagrangian point (L1). The material lost through L1 will contain orbital angular momentum and, in the absence of a strong primary magnetic field, will form a disk within the Roche lobe of the primary. Viscosity in the disk will eventually cause the material to be accreted onto the white dwarf surface. The infalling stream from L1 forms a hot spot at the impact point with the disk, which manifests itself as the prominent hump seen in the light curves of many CV's prior to eclipse.

If the the magnetic field of the white dwarf is strong enough, then an accretion disk will not form. Instead, the magnetic field will control the flow of matter leaving L1 and form an accretion column. This funnels the material onto the surface of the white dwarf near a magnetic pole. The kinetic energy of the infalling material will be released in a standing shock region above the magnetic pole of the primary. It is also possible for intermediate cases to exist, where the magnetic field of the primary is not strong enough to stop the formation of a disk. However, it is strong enough in the inner parts of the disk to disrupt it and form accretion columns onto the poles of the white dwarf.

The important features of the binary model are illustrated in Figure 3.2. We will now look at the main theoretical aspects of these systems: mass transfer, the secondary, the disk, the hot spot, the boundary layer between the disk and the white dwarf, the effect of a magnetic primary and outbursts.

3.3.1 Mass Transfer

The driving mechanism for many of the features of CV's is the transfer of mass from the companion star onto the white dwarf primary. It is responsible for the formation of the disk, a hot spot on the disk, and accretion columns. Estimates of mass transfer rates, from accretion luminosities of CV's, range from ~$10^{-8.5}$ to ~$10^{-10.5}$ M⊙ yr^{-1}. Ritter (1986) considered several ways to obtain a mass transferring secondary star. He concluded that it is not a self–sustaining process and that nuclear evolution of the secondary, thermal instabilities, or dynamical instabilities could not generate the required results, although nuclear evolution would be important in those systems with secondaries more massive than 1 M⊙. Instead he favoured two mechanisms that drain orbital angular momentum from the system, thus reducing the separation of the components, which in turn decreases the radius of their Roche lobes and causes excess

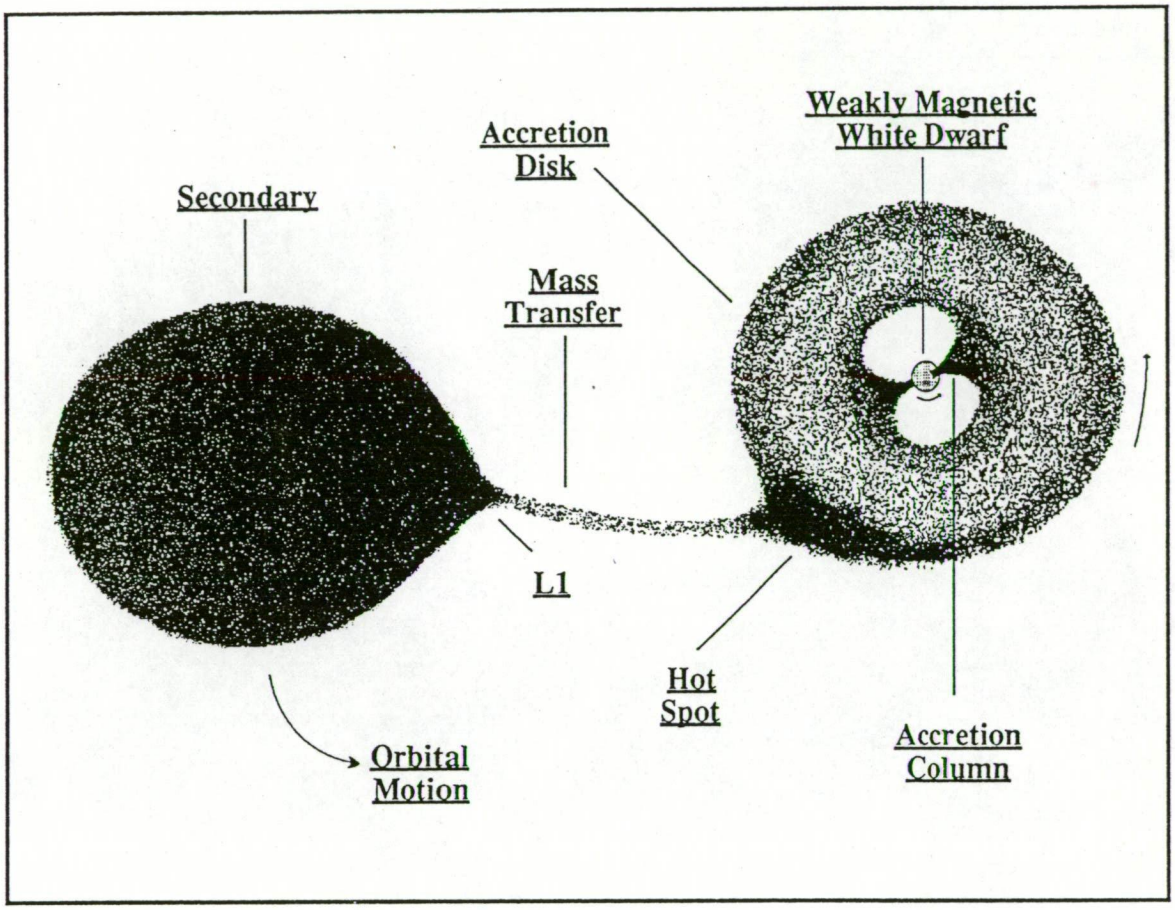

Figure 3.2

Here the important features of the binary model of cataclysmic variables are illustrated. This is a schematic representation only and is not drawn to scale.

mass to spill through L1. The first of these mechanisms is gravitational radiation. It could produce mass transfer rates of about 10^{-10} M⊙ yr^{-1} , which is of the right order of magnitude. The second mechanism is magnetic braking, caused by a magnetically coupled stellar wind emanating from the secondary. It should be noted, however, that recent IUE observations by Cannizzo and Pudritz (1988) are consistent with such a wind emanating from the disk instead of the secondary.

Spruit and Ritter (1983) and Rappaport et al. (1983) have used the two processes to provide a possible explanation for the gap between 2 and 3 hours in the orbital period distribution of CV's. Systems with orbital periods greater than three hours would be driven by magnetic braking. Mass transfer rates of the order of 10^{-9} M⊙ have been estimated for this process. This rate would bring the secondary out of thermal equilibrium, causing the radiative core of the secondary to disappear, and as a consequence, a decay in the magnetic activity. The secondary would shrink inside its Roche lobe and evolve towards thermal equilibrium again. At this point mass transfer would stop and the system would fade without the accretion luminosity. Only when the Roche lobe has decreased, due to gravitational radiation and a much reduced magnetic braking effect, would mass transfer resume and the system become visibly prominent again.

3.3.2 The Secondary Star

The secondary contributes to the luminosity of these systems in the red and IR. Typically it is a near main sequence G,M or K star with central hydrogen burning. However there are also some examples of low mass secondaries that are not hydrogen burning and other systems are known that have giant secondaries. The secondary star is distorted because of the strong gravitational effect of the close primary. This distortion is evident in the IR light curves of some CV's as their projected area varies with the orbital period, and hence causes a modulation of the light from the secondary. Berriman et al (1983), for example, showed evidence for this effect in U Gem.

Warner (1976) used the fact that the secondary must fill its Roche lobe, together with Kepler's law, to derive a relationship for the mean density of the secondary as a function of orbital period only. That is,

$$\rho = 1.43 \times 10^9 \, P_{(s)}^{-2} \quad \text{gm cm}^{-3}. \qquad 3.3$$

Given the existence of a mass–radius relationship for main sequence stars, Equation 3.3 implies a mass–period relationship for main sequence stars in CV's, and

hence a period–luminosity relationship for the secondary. Using these relationships he place the following restrictions on the secondary. Firstly, since a normal main sequence star must have a mass greater than 0.085Mʘ, then the orbital period must be greater than 0.96 hr (for non–degenerate or hydrogen-burning secondaries). Secondly, for orbital periods greater than 10 hours, stars later than F0 would have to be evolved. Thirdly, the period–luminosity relationship predicts that the secondary should only just become visible in systems with orbital periods around 5 hours, and increase in prominence for longer periods. These predictions are essentially in agreement with observations.

3.3.3 The Accretion Disk

Here the physics of accretion disks is outlined. Consider the motion of a thin ring of gas orbiting the primary. Its velocity will be given by

$$V = \left(\frac{G \times M_1}{R}\right)^{1/2}, \qquad 3.4$$

where G is the gravitational constant, M_1 the mass of the primary and R the radius of the ring of gas. The dependence on R implies that the gas in the ring must rotate differentially. The gas will be heated if it possesses any viscosity, the heating energy coming from the gravitational potential energy of the gas. The heated gas will radiate this energy away. The gas on the inside of the ring will lose energy and move down into the potential well of the white dwarf. Gas on the outer side of the ring will be sped up by the faster moving inner material and move out, conserving angular momentum. Hence the original ring will spread out to form a disk.

If the disk is fed mass by the secondary overflowing its Roche lobe, then it will reach a steady state condition with matter flowing through the disk onto the primary. The location of the outer edge of such a disk would be determined by tidal interaction with the secondary, which provides a mechanism for removing angular momentum from the disk and feeding it back into the orbital motion (Papaloizou and Pringle 1977). Mass, and hence angular momentum, could also be lost from the outer edge in the form of a stellar wind. As we have already seen, if the wind is coupled to the secondary, primary, or even the disk, it can carry off enough orbital angular momentum to reduce the separation of the components and sustain a mass transferring secondary.

Pringle (1981), and Bath and Pringle (1985), derived the following important parameters for such an accretion disk. Firstly, the energy radiated in an accretion disk is given by

$$L_{disk} = \frac{G M_1 \dot{M}}{2R_1}, \qquad 3.5$$

where $\dot{M}$ is the accretion rate and R_1 is the inner radius of the disk. This is only half the total energy available from accretion, since the gas at the inner edge of the disk is still rotating at Keplerian velocities and thus the rest of the available energy is in the kinetic energy of the gas.

Secondly, the radial flow of material through the disk is governed by a diffusion equation. This is because the material cannot accrete until it reduces its angular momentum. Changes in the local surface density are on the viscous time scale

$$T_\upsilon \approx \frac{R^2}{\upsilon}. \qquad 3.6$$

Equivalently the radial velocity of material through the disk is

$$V_r \approx \frac{R}{T_\upsilon} \approx \frac{\upsilon}{R}, \qquad 3.7$$

where υ is the effective viscosity of the gas.

Thirdly, each element of the disk will emit a spectrum that can be approximated by a blackbody whose temperature is a function of radius

$$T_e(R) = T^* \times \left(\frac{R}{R_1}\right)^{-3/4} \times \left[1 - \left(\frac{R_1}{R}\right)^{1/2}\right]^{1/4} \qquad 3.8$$

where

$$T^* = \left[\frac{3 G M_1 \dot{M}}{\sigma 8\pi R_1^3}\right]^{1/4},$$

R_1 is the inner radius of the disk and σ is the Stefan–Boltzmann constant. The maximum temperature in the disk, T_{max}, is 0.488xT^*. It occurs at a radius of $^{49}/_{36}R_1$. The minimum temperature in such a disk, T_{out}, would occur at its outer edge. Multicolour observations of the eclipse in BT Mon (Ward and Wade 1985) show that the eclipse lasts longer in the red than in the blue. This indicates that the flux in the red originates from a larger area of the disk than the flux in the blue, which is consistent with the above temperature gradient. The spectrum of a disk described by Equation 3.8 can be approximated by $F_\nu \propto \nu^{1/3}$ for frequencies such that $\frac{kT_{out}}{h} << \nu << \frac{kT_{max}}{h}$, or by $F_\nu \propto \nu^2$ for $\nu << \frac{kT_{out}}{h}$. For the spectrum to

follow the $\nu^{1/3}$ law over a wide wavelength range, a large disk is required in order to possess a large range in temperature. Hence, in the DN at quiescence, the 1/3 spectral index is only ever realised over a small wavelength range, if at all. The UX UMa stars, and DN during outburst, have a $\nu^{1/3}$ disk spectrum over a larger range of wavelengths.

The surface of a disk will possess an optically thin atmosphere and chromosphere, which effect the presence and structure of emission lines. The fact that emission lines are often seen doubled is interpreted as evidence that they arise, due to Doppler broadening, at the surface of a prograde differentially rotating disk (Smak, 1981). The peaks correspond to the projected velocity of gas near the outer edges of the disk, while the wings are derived from the higher velocity material in the inner parts of the disk. The observation that the emission lines are broader and the peaks separated more in eclipsing systems, where the projected velocity of the disk is a maximum, lends further support to their disk origin. In eclipsing systems, the emission line profiles through eclipse also argue for their disk origin, with the eclipse effects seen first in the blue wing and then in the red wing of the emission lines.

The structure of a real disk will be more complicated than in the case above, because of the effect of injecting material into the outer section of the disk from the secondary, tidal effects in the outer regions due to the secondary, possible variations in the viscosity, variation in the mass transfer rate from the secondary, and the effect of irradiation from the central disk region where most of the accretion luminosity originates. However, in spite of all these complexities, some CV's do show the characteristic $F_\nu \propto \nu^{1/3}$ spectrum predicted by simple disk models.

3.3.4 The Hot Spot

Now consider the region on the outer edge of the disk where the gas stream originating from L1 impacts with the disk at free fall velocity and dissipates its excess kinetic energy to form the so called hot spot, or bright spot. As was noted in Section 3.2.3, the hot spot shows up as a hump in the orbital light curve of many CV's. In many systems, though not all, the flickering is correlated with the hot spot. This is particularly noticeable in eclipsing systems, where the flickering is considerably reduced during the eclipse of the bright spot. U Gem and UX UMa are notable examples. Rapid variations in the brightness of the hot spot caused by variations in the accretion rate, inhomogenities in the accretion stream, or even variations in the density of the outer edge of the disk, could all produce the observed flickering.

The hot spot is also a source of hydrogen line emission. This emission is seen as a

single peak, and in systems with large inclinations, its wavelength varies with orbital phase . On trailed spectrograms this variation gives the effect of an S–wave. The S–wave component is usually superimposed on the stationary double–peaked components of the emission lines from the disk.

The geometry of the hot spot can be characterised by three parameters: r_S/a, the distance of the spot from the white dwarf in units of the separation of the two stars; α the angle between the centre of the spot and the line joining the two stars; $\Delta\alpha$ the angular extent of the spot on the disk. Robinson (1976) cites Smak (1971) as having found that, for U Gem, these parameters vary with time since outburst. In particular r_S/a becomes large during eruption and then decreases until the next outburst. The other two parameters increase as r_S/a decreases. The position of the spot in U Gem was found to be consistent with particle trajectories for a stream of gas transferred from the secondary star. A more recent and extensive study of the eclipse structure of Z Cha, by Wood et al., has also found that the position of the hot spot is consistent with theoretical stream trajectories. Perhaps the most important thing that these results demonstrate is that the position of the spot is not fixed but varies considerably, and for a given system it is determined by the inclination of the system, the mass ratio of the stellar components and the radius of the disk.

The luminosity of the hot spot will depend on several factors. The mass of the primary and the size of the disk will determine the size of the gravitational potential well and how far the stream can fall into it, thus determining the amount of energy available at the hot spot. The rate of accretion will determine the rate at which energy is transported to the hot spot. The velocity of the stream relative to the Keplerian velocity of the disk at the point of contact will determine how much energy will be available to heat the gas. The density of the disk and the geometry of the stream will also be important. A dense narrow stream might penetrate into a low density disk, while a diffuse and wider stream may flow above and below a more dense disk. These parameters will vary from system to system and some may even change with time in a specific system.

Warner (1976) found that the shock temperature on the outer edge of the disk ranges from 2×10^6 °K for orbital periods of around 4 hours up to 4×10^6 °K for the shorter period systems. The peak of this radiation lies in the soft X–ray region. Since the spot is optically thick for $\lambda > 1000$Å, the longer wavelength emission will be seen with a temperature ~30 000 °K and a cooling time of ~1 s. The result is that flickering should not occur on time–scales much shorter 1 s in the optical. However, with a disk that is optically thin for wavelengths longer than 1000Å, the cooling time is of the order of

10^{-2} s. This shorter cooling time would result in flickering on shorter time–scales than in the optical.

3.3.5 The Boundary Layer

The other important source of luminosity in these stars is the interface between the disk and the white dwarf surface, the so–called boundary layer. Here the gas, rotating around the white dwarf at its Keplerian velocity of about 3000 km s^{-1}, must slow down to settle on the more slowly rotating primary. The gas at the inner edge of the disk may still contain ~1/2 of the available gravitational energy in the form of kinetic energy. The size of the boundary layer will be the order of the size of the white dwarf. Since ~1/2 the accretion energy is released here its luminosity will be very high. Bath and Pringle (1985) predict that its effective temperature can be as high as six times the maximum temperature encountered in the disk. If this is the case the boundary layer will dominate the spectrum in the EUV and soft X–ray region of the spectrum. If the gas is decelerated rapidly by strong shocks then the temperature of the emitting gas could be as high as ~10^8 °K and result in hard X–ray emission (Pringle and Savonije 1979). Since the initial motion of the disk material is tangential to the surface of the white dwarf, the geometry of the interaction may not be very efficient at producing high temperature shocks. Thus the amount of energy liberated as hard X–rays could be small.

Some X–ray studies have shown CV's to be weaker X–ray sources than one might expect from a strongly shocked boundary layer. Jensen (1985) explains the lower X–ray luminosity by envisaging an optically thick boundary layer with an effective temperature of less than 30 eV. Then, if the neutral hydrogen column density is greater than 10^{21} cm^{-2} in the circumstellar shell, more than 99 percent of the flux would be absorbed. The observed low luminosity hard X–ray flux could be produced in a hot corona with an effective temperature of ~10 keV and formed from gas heated in the boundary layer and inner disk regions. A more comprehensive study by Patterson and Raymond (1985A and 1985B) concludes that the observed EUV/soft X-ray and hard X-ray emission from CV's is consistent with about half the accretion energy being released in the boundary layer.

The gas at the inner edge of the disk still carries a large amount of angular momentum. Bath and Pringle (1985) showed that this angular momentum will be accreted onto the white dwarf and, in turn, cause the white dwarf to spin up. Hence it might be expected that white dwarfs in these systems will be spinning rapidly and hence reduce the amount of energy available at the boundary layer. In general the rotation period of the

primary cannot be measured. However, as we will see in Section 3.3.6.2, if the primary has a weak magnetic field, then the light can be modulated with its rotational period. Rotational periods from 33 s to 67 min have been measured for these stars. In the case of a 0.8 M⊙ white dwarf, the radius of which can be obtained using the mass–radius relationship for white dwarfs, the corresponding surface velocity ranges from ~1300 km s^{-1} to ~11 km s^{-1}. Hence, in the shorter period systems, the surface velocity could be as much as ~1/3 of the Keplerian velocity of the material at the inner edge of the disk, thus reducing the available energy at the boundary layer by ~1/9. Only in systems containing rapidly spinning white dwarfs will the energy available at the boundary layer be reduced significantly.

3.3.6 Systems with Magnetic Primaries

3.3.6.1 AM Her Systems

In systems where the magnetic field of the primary is sufficiently strong ($\gtrsim 10^7$ G), the magnetic field will completely dominate the accretion flow and prevent a disk from forming. In these cases the accreted material will be channelled directly onto the pole/s of the white dwarf and most of the gravitational energy will be liberated in a shock region in the accretion column above the magnetic pole/s. Because the accretion stream hits the primary head–on, it will be very efficient at producing high temperature gas. The shock region, confined by the magnetic field, will be very small. It will be susceptible to obscuration by either the accretion column itself, the secondary star, or even the primary star's surface as it rotates. The magnetic fields are sufficient to have coupled the white dwarf to the companion star and synchronize its rotation period to the orbital period of the system (Lamb 1985, Lamb and Melia 1987). Flickering in these systems can be attributed to inhomogeneities in the accretion column and/or variations in the mass transfer rate.

The spectral characteristics of the shock region are dominated by cyclotron radiation in the IR and optical, bremsstrahlung X–rays in the 10 to 30 keV range, and a blackbody component at EUV and soft X–ray wavelengths. The cyclotron emission from electrons spiraling around the magnetic field lines produces circularly polarised light near the cyclotron frequency. This usually peaks in the red or IR and is given by

$$\nu_b = \frac{eB}{mc} = 2.8\times10^{13}\left(\frac{B}{10^7 G}\right)\ \text{Hz}\,. \qquad 3.9$$

A significant fraction of the visible light is also attributed to the higher harmonics of the circularly polarised cyclotron radiation. In the optical it can show up as peaks equally

spaced in frequency, which can be used as an indirect measurement of the magnetic field strength in these systems. Recent results using this method for several AM Her stars give field strengths in the range 25 to 44 MG (Cropper et al 1989).

The hard X–ray spectrum, with kT~30 keV, is consistent with bremsstrahlung emission from the shock region, while the soft X–ray EUV emission fits an absorbed blackbody, with kT ~15 to 40 ev. To obtain the observed luminosity ratios of $L_{xhard}/L_{xsoft} \approx .1–.001$, a large amount of the accretion energy must be absorbed by the white dwarf and re–emitted as blackbody radiation at EUV and soft X–ray wavelengths. Further away from the shock region in the accretion column, the gas is cool enough to produce a strong emission line spectrum similar to that of the quiescent DN. A notable difference is the presence of strong He II λ4686, with a flux similar to H_β, as well as other high excitation lines. The emission lines are broad, but not doubled as in the CV's with disks. The broadening corresponds to the range of velocities in the free fall gas. There is also a narrow component to the emission lines. This component is thought to come from the side of the secondary facing the white dwarf, and arises from excitation of its atmosphere by radiation from the accretion column. The off states in AM Her systems can be explained as a consequence of these systems not having an accretion disk 'store' of material. Hence changes in the mass transfer rate from the secondary will have an immediate effect on the luminosity of the system.

Good reviews of the AM Her stars have been presented by Liebert and Stockman (1983), King (1983), and Lamb (1985).

3.3.6.2 DQ Her Systems

If the magnetic field strength is $\lesssim 10^7$ G in a CV, then it will not be sufficient to stop the formation of a disk or to synchronise the rotation period of the white dwarf with the orbital period (Lamb and Melia 1987). The distance from the white dwarf at which the disk will be disrupted, and at which the material couples to its magnetosphere, will depend on the balance between the magnetic and gas pressure in the disk. The effect of magnetic coupling is a function of the so–called fastness parameter, introduced by Elsner and Lamb (1977), and is given by

$$\omega_S = \frac{\Omega}{\Omega_k(r_0)} , \qquad 3.10$$

where Ω is the white dwarf's angular frequency, r_0 is the radius of the outer region of

the magnetosphere boundary layer and $\Omega_k(r_0)$ is the Keplerian angular velocity of material in the disk at r_0. From their treatment of disk accretion onto a compact object Ghosh and Lamb (1979) find that

$$r_0 = 0.52\, r_A^{(0)}, \qquad 3.11$$

Here $r_A^{(0)}$ is the characteristic Alfven radius for spherical accretion and is given by Elsner and Lamb (1977) to be

$$r_A^{(0)} = 3.24\times10^8\, \dot{M}_{17}^{-2/7}\, \mu_{30}^{-4/7}\, M_1^{-1/7} \ \text{cm}, \qquad 3.12$$

where μ is the magnetic moment of the white dwarf in units of 10^{30} G cm^3, and M_1 and $\dot{M}$ are in units of solar masses and 10^{17} gs^{-1} respectively. Once the accreting material has coupled to the magnetosphere of the white dwarf, it will be funnelled onto the pole/s of the primary in the same manner as for the AM Her stars. However, because of the weaker fields, accretion may occur over a larger area near the pole than is the case for the AM Her stars.

Because of the similar accretion mechanism, these stars will normally have some similar properties to the AM Her stars, such as high excitation emission lines, hard X–ray emission, and possible weak polarisation effects. They will, however, also display properties associated with accretion disks, such as double emission lines, disk eclipse effects, and possibly light variations associated with the hot spot on the outer edge of the disk. This makes DQ Her variables particularly complex systems to resolve observationally. This will be clearly seen in the Chapter 4 discussion of EX Hya.

Because the rotation of the white dwarf is not coupled to the orbital period, the white dwarf may spin up in a similar manner to CV's without magnetic primaries. The disk couples to the primary at the Alfven radius instead of the radius of the boundary layer, which is just above the surface of the white dwarf. If the magnetic axis and the spin axis are not aligned, then the accretion columns will modulate the X–ray emission at the rotation period of the white dwarf. For systems with prograde disk rotation and $r_0 < r_e$,where r_e is the radius at which the angular velocity of the disk and the white dwarf are the same, this period might be expected to be decreasing, due to the angular momentum accumulated by the white dwarf from the accreted disk material.

Weakly magnetic primaries explain the short period flux modulation and many of the other features of DQ Her stars described in Section 3.2.4. Depending on the orbital inclination of the system and the inclination of the magnetic axis with respect to the rotational axis of the primary, the X–ray emission from the shocked region at the base

of the accretion column can be modulated with the white dwarf rotation period. In the optical, a beat period with the orbital period is sometimes seen. The relationship between the beat period, X–ray period and orbital period is given in Equation 3.1. It is consistent with the X–ray emission being reprocessed in a region fixed in the frame of reference of the orbital motion. This could be in either the region of the disk containing the hot spot or the secondary star itself. The beat period arises because, as the secondary moves around the white dwarf, the white dwarf has to rotate slightly more than one revolution to re–illuminate it. So in one orbital revolution we will see n beat cycles and n+1 X–ray cycles due to white dwarf rotation.

Other side bands have been also observed in these stars. For example, V1223 Sgr has an orbital modulation with a period of 202.4 min, a 12.4 min periodicity in the X–ray associated with the rotation of the primary, and a beat period at 13.2 min. However, it also possesses another modulation at 14.1 min. Warner (1986) shows that it is possible to get sidebands at $(\omega-2\Omega)$, $(\omega-\Omega)$, (ω) and $(\omega+\Omega)$, where ω and Ω are the primary rotation and orbital frequencies respectively. The 14.1 min modulation in V1223 Sgr would be the $(\omega-2\Omega)$ sideband.

In some cases the rotation period is also seen in the optical as well as the X–ray. For example, EX Hya has a 67–min X–ray and optical modulation attributed to the white dwarf rotation period, and no obvious beat period is seen. On the other hand, DQ Her has a 71 s modulation in the optical, but is not detected in the X–ray region, probably because of its high inclination. However, it does show weak circularly polarised light, not synchronised with its 71 second period, but with a fundamental period of 142 s. This can be taken as evidence for a magnetic field, and that the 71 s modulation is related to the rotation of the white dwarf. The 71 s modulation in DQ Her is seen to undergo a 360 degree phase shift during eclipse. This effect is explained if the system has a magnetic primary and the beamed X–rays from the pole are reprocessed in the disk (Petterson 1980).

3.3.7 Outbursts

Finally, we consider some mechanisms for producing outbursts in the CV's. There are two possible sources of energy available in these stellar systems: nuclear and gravitational. Dropping a gram of matter onto a white dwarf releases $\sim 10^{17}$ ergs of energy, while the conversion of a gram of hydrogen to helium releases $\sim 5\times10^{18}$ ergs of energy. It is now generally accepted that the more luminous classical novae ($\sim 10^{38}$ erg s^{-1}) are the result of the nuclear burning of the hydrogen rich layer of accreted material on the surface of the white dwarf. The lower luminosity dwarf novae

eruptions (~10^{34} erg s^{-1}), are thought to occur by a completely different mechanism. It's believed they are powered by the gravitational energy derived from accretion, with outbursts either due to periodic enhancement of the mass transfer rate or variations in the viscosity of the disk. Given the correct conditions either mechanism is capable of powering the RN.

3.3.7.1 Classical and Recurrent Novae

The CN and RN outburst mechanism may be detailed as follows. The hydrogen rich material deposited on the white dwarf accumulates with time. The layer grows in thickness until the bottom reaches a temperature and pressure that is high enough to initiate fusion of hydrogen into helium. For the CN, envelope masses in the range 10^{-4} to 10^{-5} $M_\odot$ are sufficient, while models by Starrfield et. al. (1985) have achieved hydrogen burning with envelope masses of only 10^{-7} $M_\odot$ in luminous white dwarfs (~1$L_\odot$). Once the hydrogen is ignited, the temperature rises rapidly and a thermonuclear runaway reaction occurs. The temperature in the shell reaches ~10^8 °K before degeneracy is lifted. Since the reactions proceed so rapidly and the inertia of the shell prevents its immediate expansion (Gallagher and Starrfield 1978), the temperature continues to rise to $\lesssim 3 \times 10^8$ °K before the shell begins to expand and cool. The reaction rates are found to be very sensitive to the CNO abundances. The more CNO available, the more rapidly energy is released during the early stage of the outburst.

Theoretical models predict that, initially, the outburst will blow some 10 to 50 percent of the accreted envelope off into space at several thousand km s^{-1}. The material that is left returns to hydrostatic equilibrium and continues the hydrogen burning process. The result is the constant UV plateau observed in novae light curves. The luminosity and envelope radius are found to depend on the core mass and envelope mass respectively. Two possible mechanisms operate to end this phase of the outburst. The first of these is mass loss by a radiation–pressure driven stellar wind. The second is dynamical friction caused by the secondary orbiting within the outer radius of the expanded envelope of the primary. Both mechanisms reduce the mass of the envelope so that the remaining material will fall back onto the white dwarf. Without these mechanisms the nuclear burning time for the envelope is many years. This compares with observed times of months to years to return to minimum. After this stage is complete, the accretion disk can begin to re–establish. The system can begin evolving towards another eruption in ~10^4 to 10^5 years, for an accretion rate of ~10^{-9} $M_\odot$ yr^{-1}.

Fast novae are observed to be over abundant in CNO by factors of 20 to 100, when compared with solar abundances. Theoretical models require enhanced CNO

abundances so as to release enough energy into the envelope on a short enough time scale to eject the observed amount of matter with high velocities. However, an over abundance in CNO does not always produce fast novae. For example, the slow nova DQ Her had a high CNO abundance. Theoretical studies by Starrfield and Sparks (1987) have shown that a low mass white dwarf can only produce slow nova eruptions no matter what the CNO abundance is. Therefore they suggest a low mass white dwarf may explain the DQ Her eruption. Work done by MacDonald (1983) suggests that the speed class is a function of the mass of the accreted envelope as well as CNO abundance, and that for low mass envelopes a slow nova outburst can occur even when the CNO abundances are high. They suggest this as an explanation of the DQ Her outburst.

Both thermonuclear runaway on the surface of the white dwarf and accretion events have been used successfully to explain the RN. Starrfield et. al. (1985) were able to demonstrate that an envelope mass as low as $\sim 5 \times 10^{-7} M_{\odot}$, when accreted onto a luminous white dwarf ($\sim 1 L_{\odot}$) of mass 1.38 $M_{\odot}$, was sufficient to trigger a thermonuclear runaway and resulted in an outburst similar to those observed in the recurrent nova U Sco. The recurrence time for such events was less than 10^2 yr, in agreement with observed outburst time scales for these systems. Webbink et al (1987) were able to explain the eruptions of T CrB and RS Oph by the accretion of a burst of mass from a Roche lobe filling giant secondary, while the outbursts of U Sco and T Pyx were shown to be consistent with the thermonuclear runaway model.

3.3.7.2 Dwarf Novae

It is unlikely that thermonuclear energy is the source of DN eruptions, both from an observational and theoretical point of view. Theoretically there is the problem of stopping a thermonuclear runaway reaching the Eddington limit, instead of the typical dwarf nova luminosity of $\sim 10^{34}$ erg s^{-1}, and then turning such a reaction off on the time scale of DN outbursts. Observational evidence from the eclipse in Z Cha during eruptions indicates that outbursts occur in the disk rather than on the white dwarf. A study of the colour changes of SS Cyg and VW Hyi during outburst, by Bailey (1980), found that the eruption occurs first in the optical and is followed several hours later by an increase in the UV. These colour changes are consistent with the outburst starting in the cooler outer parts of the disk and then moving to the hotter inner parts of the disk. Another important clue to understanding the DN outburst mechanism was discovered by Bailey (1975). It is that the outburst decay time increases linearly with the orbital period of the system. The interpretation of this relationship is simply that the

longer period systems, having larger disks, will require more time for the material to diffuse through them.

An obvious way to produce the DN outbursts from accretion energy is to vary the mass transfer rate. There are two ways that this can be achieved. One way is to allow the mass transfer rate to the disk to vary because of instabilities in the secondary. The other way is to have a steady mass transfer rate to the disk, but with instabilities in the disk resulting in the material being accreted onto the white dwarf at a variable rate. Both methods have received theoretical support and the true picture might be a combination of both, or vary from system to system.

If, in the models where the secondary modulates the mass transfer, it does so on a short time, ~1 hour, then a ring is formed as described in Section 3.3.3 and the material will diffuse inward on the viscous time–scale of Equation 3.6. This scenario produces light curves similar to the short eruptions in U Gem stars. By prolonging the increased mass transfer rate it is possible to obtain flat topped outbursts similar to the long outbursts, and by slowly increasing the mass transfer rate it is possible to generate outbursts with a slow rise similar to the anomalous eruptions observed in SS Cyg. It is thought that dynamic instabilities in the secondary might be able to produce a semi–periodic Roche lobe overflow of this nature. Examples of these models are given by Bath (1984), Mantle and Bath (1983), Bath, Edwards and Mantle (1983), and Mantle (1985).

In the variable viscosity disk models, material is lost from the secondary at approximately constant rate. The disk, or part thereof, is unstable and has two viscosity states. During quiescence the disk is in its low viscosity state, and hence the material from the secondary will tend to accumulate in a ring in the outer parts of the disk. Eventually a critical density and temperature is reached, and the disk switches to its high viscosity state. A fraction of the material in the ring will then diffuse through the disk and onto the primary, producing an outburst. According to Cannizzo and Kenyon (1987) an outburst of this nature requires approximately 1 to 10 percent of the material in the disk to be accreted. The temperature and density dependence of hydrogen ionization has been connected with such a disk instability. The onset of the instability is thought to transform the ring from a cool, optically-thin, low viscosity one, with a high cooling rate, into a hot, high viscosity, radiative one and should occur at an effective temperature of $\lesssim 10^4$ °K. However, the exact nature of the viscosity is unknown. The nova and nova–like stars, having higher accretion rates, would have disks that are hotter and denser than those in the dwarf novae, hence avoiding the instability. The disk in these stars would always be in its high viscosity state and result

in steady accretion. The Z Cam stars would be borderline between the nova/nova–like stars and the dwarf novae. A more detailed description of these models can be found in work by the following authors and references therein: Smak (1983), (1984), (1987); Cannizzo and Kenyon (1987); Faulkner Lin and Papaloizou (1985); Meyer and Meyer–Hofmeister (1981).

In summary, it seems to be generally agreed that the outbursts are due to a brightening of the disk, but it is still uncertain whether this is caused by enhanced mass transfer from the secondary or to changes in disk viscosity. It is also worth noting that since the DN eruptions are not nuclear powered, then the material accreted onto the white dwarf should be capable of powering a nova outburst in these systems. Hence the DN and CN classes shouldn't be mutually exclusive. However, nova events from these stars would be much rarer since the lower accretion rates in these systems would result in a correspondingly longer recurrence time

3.4 Conclusion

At first sight the CV's seem to be a somewhat inhomogeneous group of stars, with widely varying properties. However, as has been shown, the simple binary model for these systems is quite successful at explaining the bulk of their characteristics and, in the light of that model, they are a much more uniform group than initially indicated by their properties. This, however, does not mean that our understanding of them is complete. There is still much work to be done, both experimental and theoretical. For example, the exact nature of the types of outbursts (especially in RN), the nature of the emission lines, the cause of the mass transfer process, accurate estimates of the mass transfer rates and disk masses are but a few of the questions needing further detailed work.

From an experimental point of view the task is not a simple one, as will be demonstrated in Chapter 4. We have seen in this chapter that the light from these systems is a combination of many sources, varying on different time–scales. The relative contribution from each source can vary with time as well as from system to system. This is particularly so in the DQ Her systems. The interpretation of these sources would be made much simpler if it was possible to turn them all off, except for the one of interest. This can be partly realised in eclipsing systems, where the eclipse has the effect of turning different parts of the system off, as they go behind the secondary. It is for this reason that eclipsing systems play an important role in the study of the cataclysmic variables and the reason that EX Hya, being one of only three eclipsing DQ Her stars, is an important object to study.

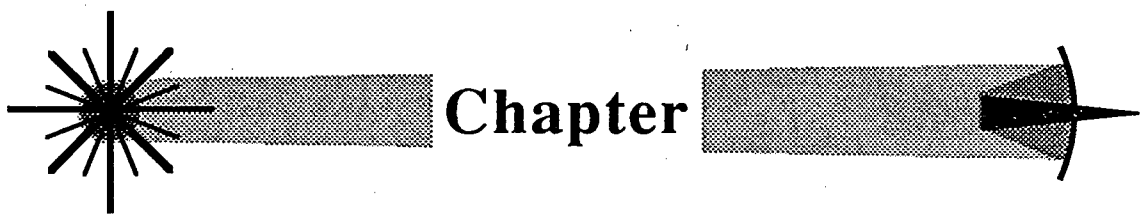

Chapter 4

A SPECTROSCOPIC AND PHOTOMETRIC STUDY OF THE CATACLYSMIC VARIABLE EX HYDRAE

4.1 Introduction

This chapter reports the results of a photometric and spectroscopic study of EX Hya. An overview of the published photometric, spectroscopic and X–ray properties of this star is presented in Section 4.2 of this chapter. Section 4.3 deals with observations of EX Hya using the Mark I photometer system on the University of Tasmania's 1 m telescope. Details concerning these observations and subsequent analysis are covered in Section 4.3.1. The data from the observing runs, along with the results of a time–series spectral analysis are presented in Section 4.3.2. The following three sections then present results obtained when the times of mid–eclipse and 67 min maxima, from these observations, are combined with other published data. The eclipse timing data show a long time–scale variation (Section 4.3.3) and the observed decrease in the period of the 67 min modulation is used to provide estimates of the mass transfer rate and magnetic moment of the white dwarf (Section 4.3.4). The short time–scale variations in mid–eclipse times are seen to be correlated with the phase of the 67 min modulation (Section 4.3.5).

In Section 4.4 the results from two short spectral runs, made on the Anglo–Australian Telescope, are presented. One provides high time and wavelength resolution through a deep eclipse. The other is discussed because it happens to occur close to one of the relatively infrequent outbursts of this star. Details concerning these observations and the related data reduction are discussed in Section 4.4.1. The spectra are presented in

Section 4.4.2, where they are assessed in comparison with results obtained by other authors. The results of the high time resolution spectroscopy during the eclipse are discussed in Section 4.4.3. Finally, in Section 4.5, other observations which relate to the eclipse structure in EX Hya are documented and an accretion model of EX Hya is then examined in the context of those observations.

4.2 An Overview of EX Hydrae

The cataclysmic variable EX Hya is one of the better studied members of this class of variable. In its quiescent state it is one of the brighter dwarf novae, with $m_v \sim 13.0$ to 14.1. It exhibits infrequent outbursts with a mean period of ~574 days (Bateson 1979). Because of their short duration ($\lesssim$4 days), only one such outburst has been observed photo–electrically (Bond et al., 1987), and so far no spectroscopic measurements have been obtained during an outburst. EX Hya was originally suggested as a possible eclipsing system from an observation of its double–peaked emission line spectrum (Kraft, 1962). Further photo–electric and spectroscopic studies confirmed that it was indeed an eclipsing system with a 98 min orbital period (Kraft and Krzeminski, 1962; Mumford, 1964, 1967). When in optical quiescence, it has been found to show relatively strong emission of both hard and soft X–rays, with a flux of ~4 μJ in the 2 to 11 keV range. (Watson, Sherrington, Jameson, 1978; Cordova and Riegler, 1979).

As new properties of this system have emerged, more complex models have been required to explain its behavior. The discovery of a 67 min optical modulation (Vogt et al, 1980), and an accompanying soft X–ray modulation in phase with it, (Kruszewski et al., 1981, 1982), has led to the assigning of EX Hya to the DQ Her sub–class of cataclysmic variables. As we have seen in Sections 3.2.4 and 3.3.6.2, members of this sub–class exhibit properties somewhat between the magnetic AM Her systems and the non–magnetic CV's. Their defining property is an asynchronously rotating, weakly–magnetic, white dwarf primary. EX Hya is unusual in that it and SW UMa are the only two DQ Her stars to lie below the 2 to 3 hr gap in the orbital period distribution of CV's, and as well they are the only two to have dwarf novae outbursts (Shafter et al., 1986). Apart from DQ Her itself and the partially eclipsing system FO Aqr, EX Hya is the only other known member of this class to have an eclipse.

Kruszewski et al. (1981) first suspected that the 67 min period was decreasing with time. This was subsequently confirmed with the accumulation of further data (Gilliland, 1982; Sterken et al., 1983; Hill and Watson, 1984; Jablonski and Busko,

1985; Hill, Sharma and Watson, 1986; Bond and Freeth, 1988) . The 67 min modulation is normally associated with the white dwarf rotation period. Consequently, its period decrease is attributed to the torque applied to the white dwarf when the higher angular velocity inner disk material couples to the magnetosphere. A secular decrease in the 98 min period up to 1976 had led Vogt et al. (1980) to suggest a significant orbital $P/\dot{P}$ term. Further observations since that time have seen a reversal in the original trend (Gilliland , 1982; Sterken et al., 1983; Hill and Watson 1984). Recent results show some indication of a variation on a 20 yr time–scale (Bond and Freeth,1988). There is also some evidence that the optical eclipse wanders back and forth by ~± 20s in time, as a function of the 67 min phase (Hill and Watson, 1984; Jablonski and Busko, 1985). The eclipses are earliest at $\Phi_{67} \approx 0.75$.

Spectrophotometry of EX Hya by Bath, et al. (1980), Sherrington et al. (1980), and Frank, et al. (1981) have revealed the presence of a continuum of the form $F_\nu \propto \nu^{1/3}$, extending from IR to UV wavelengths. Optical spectroscopic studies have been undertaken by Breysacher and Vogt (1980), Cowley et al. (1981), and Gilliland (1982). More recently, extensive data sets of time resolved spectra have been analysed by Kaitchuck et al. (1987) and Hellier et al (1987). The initial X–ray studies have been followed up with further observations by Cordova et. al. (1985), Heise et al. (1987), Rosen et al. (1988) and Beuermann and Osborne (1984,1985, 1988). The X–ray observations have established the existence of a narrow partial X–ray eclipse at higher energies, simultaneous with the optical eclipse. A broad dip, centred before the time of optical eclipse, is seen in low–energy X–ray emission, and the amplitude of the 67 min modulation decreases strongly towards higher X–ray energies.

4.3 Mt Canopus Photometry

4.3.1 Observations and Data Reduction

The main aim of the photometric program on EX Hya was to study its 98 min and 67 min variations. All the photometric data were obtained using the Mark I dual channel photometric system attached to the University of Tasmania's Mt. Canopus 1m telescope. Details of this system were given in Chapter 2.

EX Hya was observed on a total of 17 nights between March 1983 and March 1985. To maximise the signal, all observations were made in white light. The data were recorded with a time resolution of 1 s and later summed into 5 s bins to improve the signal–to–noise ratio. The data from the star+sky channel, (SSC), were corrected for

Table 4.1

Observing Log

Run No.	Date	Start Time (U.T.)	Duration ~hours
1	10–Mar–83	13 11 00	3.0
2	08–Apr–83	12 15 53	5.25
3	18–Apr–83	11 40 01	4.8
4	20–Apr–83	14 47 01	2.2
5	21–Apr–83	13 53 39	1.2
6	18–May–83	12 35 20	3.3
7	Equipment	Failure. Data	corrupt
8	02–May–84	13 54 34	2.4
9	04–May–84	13 01 39	5.6
10	Equipment	Failure. Data	corrupt
11	04–Jul–84	10 28 22	3.5
12	19–Jul–84	11 46 42	2.1
13	23–Jul–84	11 11 06	1.8
14	03–Aug–84	12 18 25	1.4
15	24–Mar–85	15 03 40	3.9
16	25–Mar–85	10 40 31	7.5
17	28–Mar–85	10 50 30	6.5

sky background by calibrating the sky channel, (SC), against the SSC and then subtracting the calibrated SC from the SSC. The calibration was done by observing a section of sky in both the SSC and the SC several times during an observing run. The mean ratio of these observations was then used as the calibration factor. The data were not corrected for extinction, since the primary interest was in the 67 min maxima and eclipse times. A log of the observations is presented in Table 4.1.

The data were reduced using the observatory's PDP–11/40 computer. All data analysis software was written by the author. This software included: a graphics based editor for displaying the data files and removing bad data or locating sections of data at specific times in the data file; programs to perform operations such as addition, subtraction, multiplication and division of data files using a constant or another file as the second operand; a graphics package for driving a Roland DXY–101 plotter; period–search programs for evaluating FFT's; least square period analysis routines; period searching programs using folding techniques; data transmission and communication software.

4.3.2 Properties and Characteristics of the Light Curves

The light curves that were obtained illustrate several features characteristic of this star. These are the large amplitude flickering (~0.3 mag), the 67 min modulation with its highly variable profile, and the sharp eclipses with a duration of ~2 to ~3 min and period of ~98 min. The light curves from several observing runs are shown in Figure 4.1. The 67 min maxima and 98 min eclipse times, predicted from the Bond and Freeth (1988) ephemerides, are marked respectively above and below these light curves. The eclipse profiles shown in Figure 4.2 illustrate the variable nature of the eclipse. They range from being broad flat bottomed 'total–like' eclipses, through to V–shaped 'partial–like' eclipses. Their variable shape may result from changes in the position or structure of the part of the system being eclipsed as well as from the intrusion of flickering.

To follow up suggestions by Gilliland (1982) of a 33.5 min periodicity, and by Cordova et al. (1985) of a 46.4 min modulation in the optical light from EX Hya, a spectral analysis of the data was carried out. Two methods for determining periodicities in gapped data were used. They were, the Q–method described by Warner and Robinson (1972), and a least–squares (LS) method described by Lomb (1975). The Q–method is a folding technique, while the LS algorithm is based on fitting sine waves to the data. The LS method is sensitive to the sinusoidal component of any modulation, similar to the Fourier Transform. On the other hand, the Q–method makes use of all the harmonics of a particular modulation by folding the data at the period of interest. For example, with data consisting of a sine wave with period P, the Q–method will produce peaks at all periods that are an integer multiple of P, while the LS method will produce a peak at the fundamental period only . The spectral resolution obtained using either method is proportional to the time interval covered by the data. For an ~2 yr span of data, the width of any peak in the spectrum would be very small and hence it would be necessary to test many frequencies to ensure that a peak wasn't missed. Large gaps between observations will also produce many alias peaks either side of the real peak. Hence, it was decided not to group all 17 data runs together to perform the spectral analysis. The data from a single run, however, gives very broad peaks, which is not very satisfactory. Thus, given these constraints, it was decided to combine the data from runs 15, 16 and 17 for the analysis. The ~17.9 hours of data, spread over an ~4 day interval, gives reasonable spectral resolution without requiring too many frequencies to be searched. The results of the analyses using both methods are summarised in Figure 4.3.

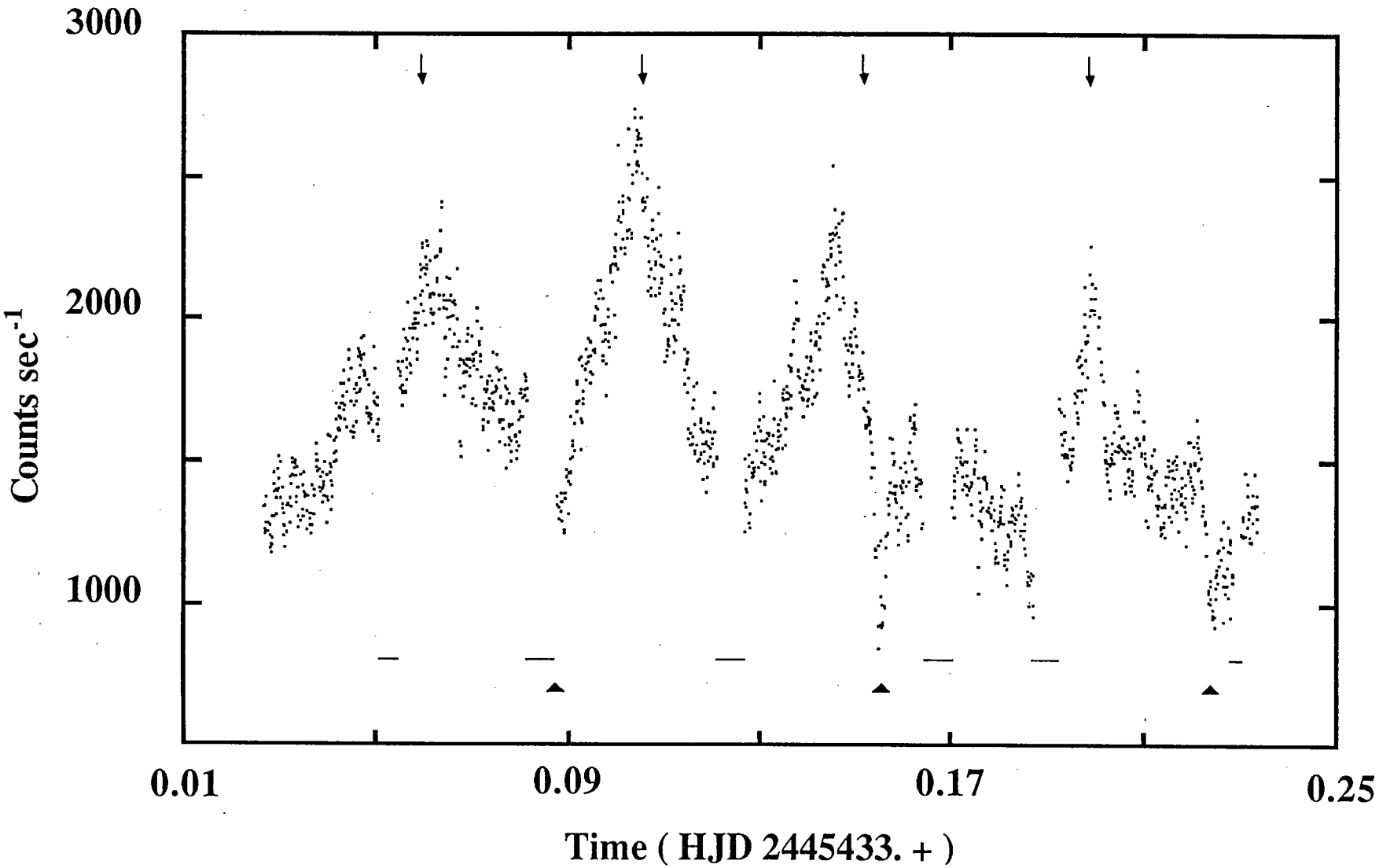

Figure 4.1 (a)
The Light curve of EX Hya, with 10 s integrations, from the 8th of April 1983 run. The arrows above the light curve mark the predicted time of 67 min maximum. The triangles below the light curve mark the predicted eclipse times and the horizontal lines mark interruptions to the data collection.

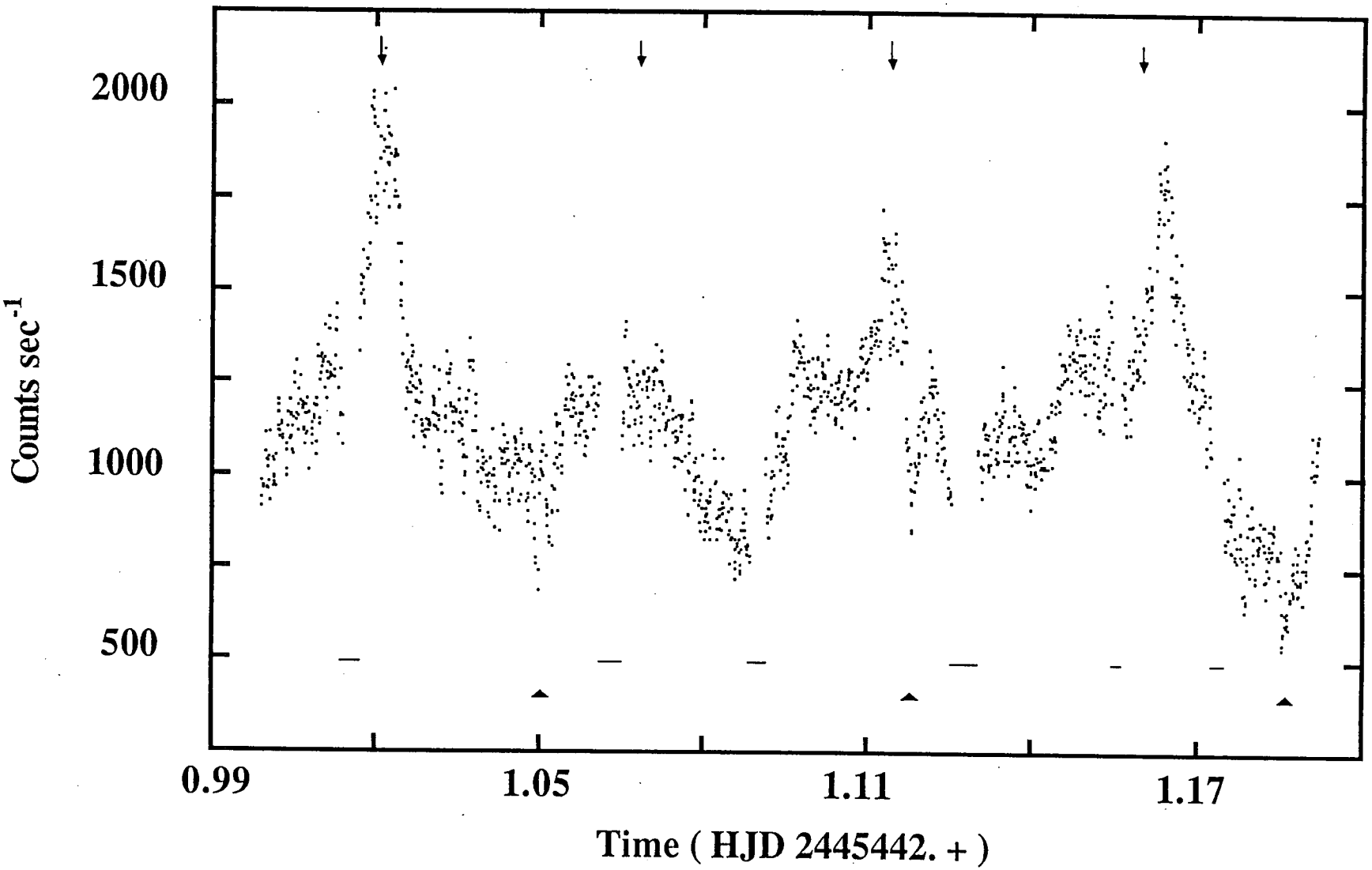

Figure 4.1 (b)
The light curve of EX Hya, with 10 s integrations, from the 18th of April 1983 run. The diagram format is the same as in Figure 4.1 (a)

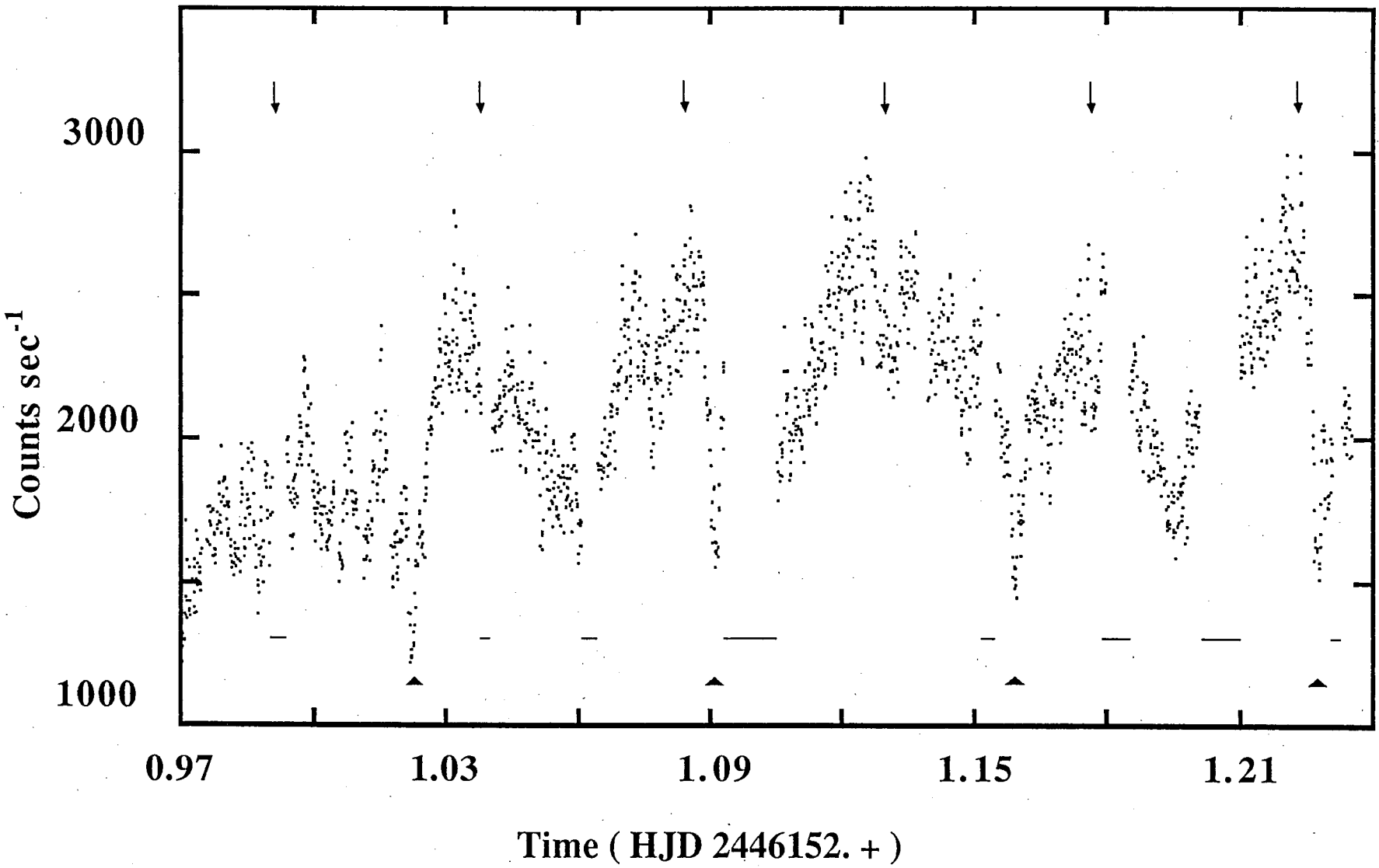

Figure 4.1 (c)
The light curve of EX Hya, with 10 s integrations, from the 28th of March 1985 run. The diagram format is the same as in Figure 4.1 (a)

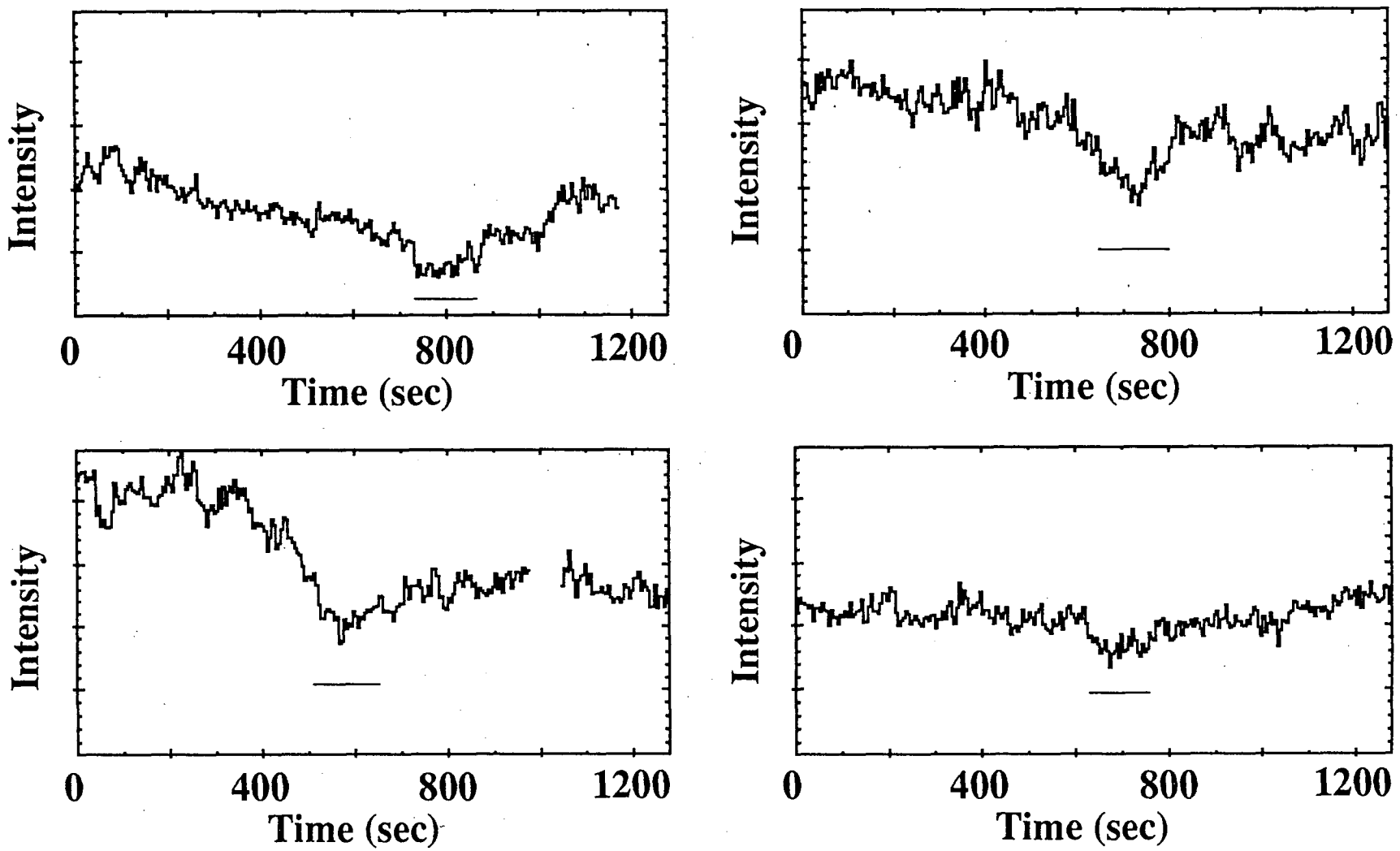

Figure 4.2
The four panels illustrate the variable nature of the eclipse in EX Hya. The horizontal line below each light curve marks the position of the eclipse. The start time for each panel is arbitrary and the data has been plotted with a time resolution of 5 s.

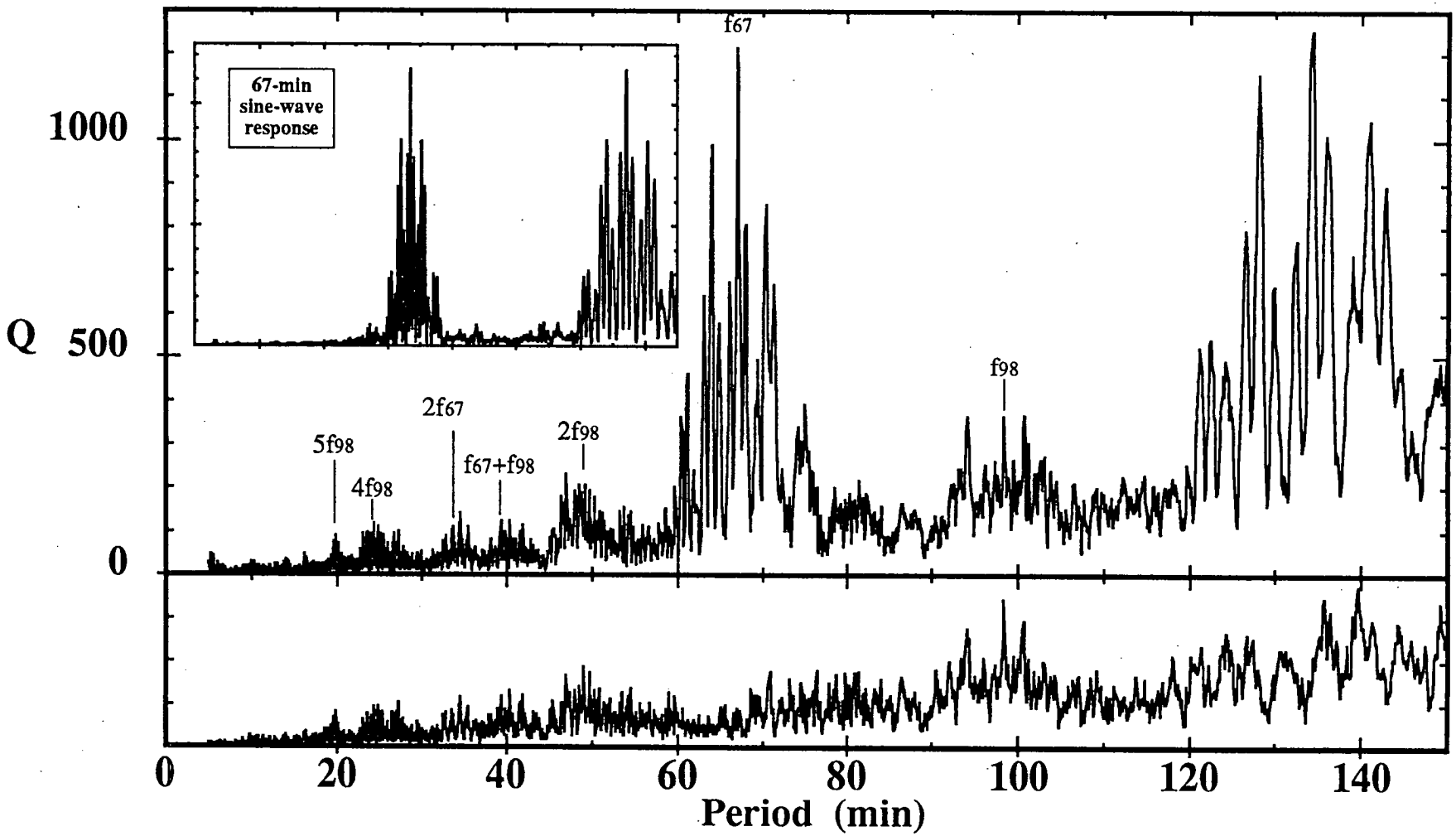

Figure 4.3 (a)
The results of a Q-method analysis of the data from observing runs 15, 16 and 17. The inset at the top shows the Q-method response to a 67 min sinewave with the same sampling pattern as the original data. The periodogram at the bottom of the plot results from removing the best fit 67 min sinewave from the data.

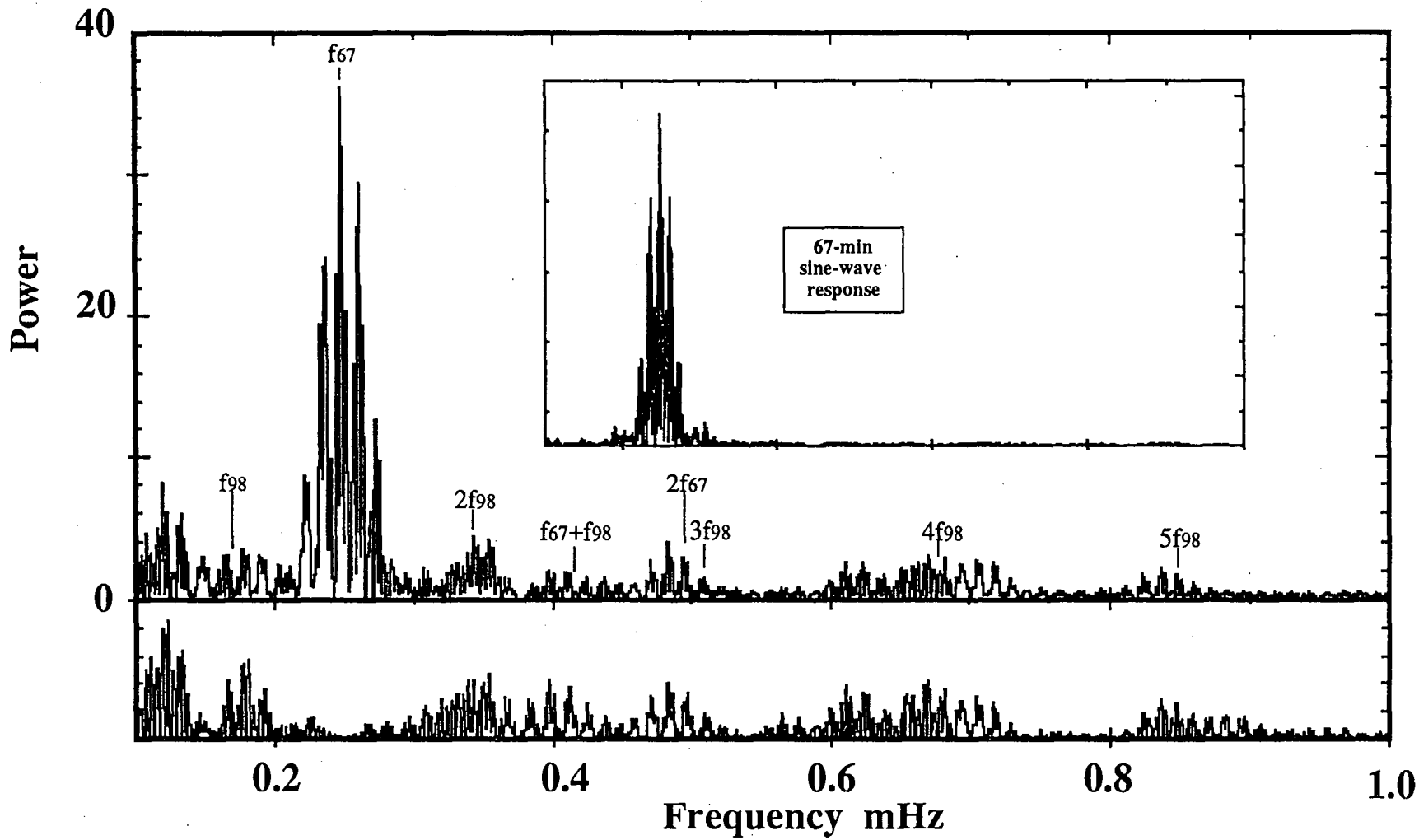

Figure 4.3 (b)

The results of a least-squares spectral analysis of the data from observing runs 15, 16 and 17. The inset at the top shows the response to a 67 min sinewave with the same sampling pattern as the original data. The spectrum at the bottom of the plot results when the best fit 67 min sinewave is removed from the data.

The most striking feature in Figure 4.3 corresponds to the 67 min modulation and its alias peaks, which are attributable to the sampling pattern. The inset in each of the graphs shows the response of each method to simulated data consisting of a 67 min sine wave with the same sampling pattern as in the original data. In each case, the plot at the bottom is the data re–analysed with the best fit 67 min sine wave removed. There is some indication that other periodicites are also present in the data. Small broad peaks are seen near $2f_{98}$, $f_{67}+f_{98}$, $2f_{67}$ or $3f_{98}$, $4f_{98}$, and possibly $5f_{98}$ in both spectra. The orbital frequency, f_{98}, is only clearly present in the Q–method spectrum. This is not surprising since the eclipse is quite sharp and one would expect to see most of this signal at its harmonics when using the LS–method. The peak obtained using the Q–method will be due to all the harmonics of f_{98} and hence much stronger. However, simulations using poisson–distributed noise on a 67 min sine wave with a 2 min base–width eclipse and the same sampling pattern as the original data, produced a much smaller, sharper peak with the Q–method than that observed in the real data. This can be explained if there are other variations at the orbital period. For example an orbital hump that is masked by the larger and highly variable 67 min signal.

To investigate the effects of an orbital hump, as would be produced by a hot spot in the disk, simulated data runs with a broad hump, eclipse, 67 min modulation, and the same sampling pattern as the original data were generated. The hump was modelled by using the positive half of a sine wave centered at $\Phi_{98} = .9$, and a width equal to half the orbital period and a semi–amplitude of 75 percent of the semi–amplitude of the 67 min sinewave. The results of this investigation are shown in Figure 4.4 for both the Q–method and LS–method. In each case the plots show: the results if the simulated data contain a 67 min sinewave and eclipse only; the results if the simulated data also contain the hump feature; and finally the results if the hump in the simulated data is not strictly periodic, but is allowed to move in phase to mimic the variable nature of humps seen in other CV's. Here a random phase shift in the range $\Delta\Phi_{98} = \pm 0.2$ was used.

The points to note in the Q–method results of Figure 4.4 (a) are:
(i) The simulation with the variable hump phase produces a broad feature near $2f_{98}$. A periodic hump and eclipse, or an eclipse alone, does not produce such a feature.
(ii) The broad feature around f_{98} is not produced by an eclipse alone. Some extra modulation is required to produce this feature.

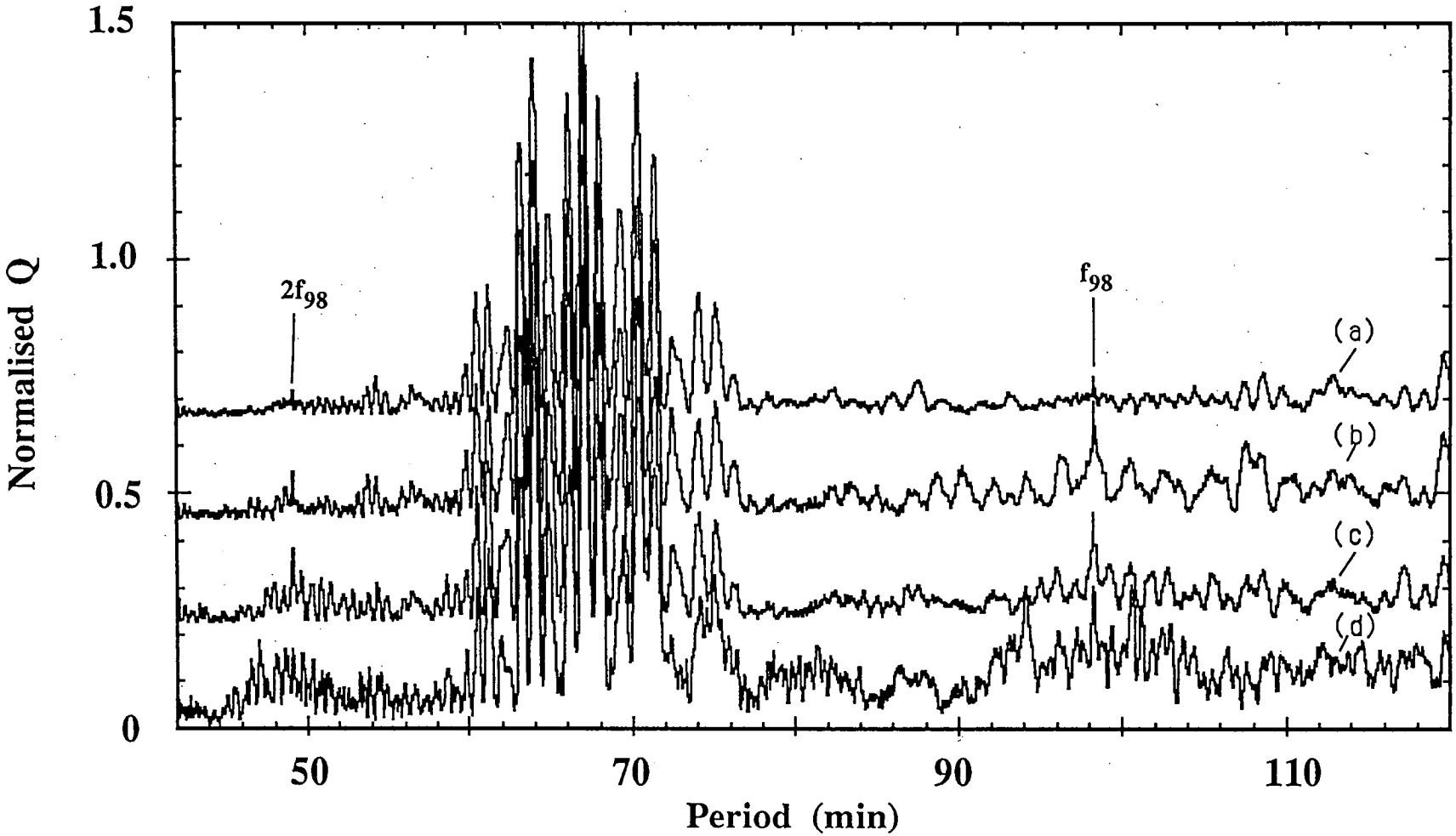

Figure 4.4 (a)

A comparison of the Q-method periodograms of simulated data with that of the EX Hya data. The periodograms have been normalised so that the peaks corresponding to the 67 min modulation have a value of 1 and the individual graphs have been offset vertically for clarity. The simulated data used the same sampling pattern as the EX Hya data. Curve (a) is for poisson-distributed noise on a strictly periodic 67 min sinewave with a 98 min eclipse. Curve (b) also includes a periodic orbital hump prior to the eclipse. In curve (c) the orbital hump has been allowed to wander randomly about its mean position in (c). Curve (d) is for the real data.

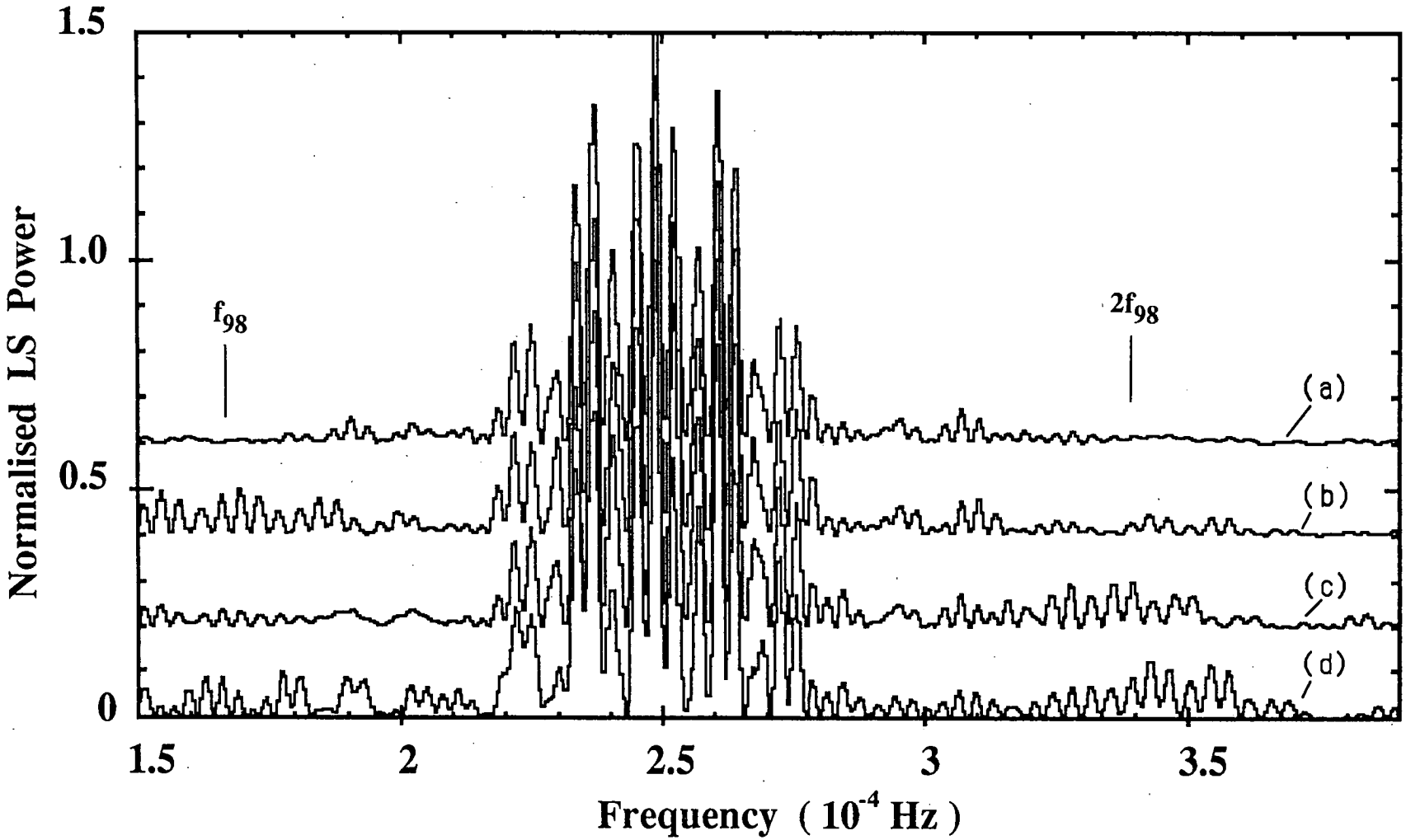

Figure 4.4 (b)

A comparison of the least-squares spectra of simulated data with that of the EX Hya data. The four spectra have been normalised so that the peaks corresponding to the 67 min modulation have a value of 1. The normalisation, offset and layout of the four curves is exactly the same as in Figure 4.4 (a).

The points to note from the LS–method results of Figure 4.4 (b) are:
(i) For a strictly periodic hump, the spectrum obtained using the LS–method produced a broad peak at f_{98} and there is no significant feature near $2f_{98}$. It can be seen from Figure 4.4 that this is not consistent with the spectrum of the real data.
(ii) When the hump is allowed to vary slightly in phase, then the LS–method produces a broad feature around $2f_{98}$ and no significant signal is seen at f_{98}. This is consistent with the real data.
(iii) The simulation with the variable hump shown here does not produce a broad peak centred at exactly $2f_{98}$. This is clearly seen in the LS spectrum. However, other simulations that employed random hump amplitudes and random phases, produced broad peaks whose central frequency wandered around $2f_{98}$. The frequency structure of the broad peak is thus being influenced by the random nature of the hump.

Thus the results of the analysis are not inconsistent with there being a hump component in the light curve of EX Hya. This is not altogether surprising, since the Balmer and He I emission lines have an S–wave component that is attributed to a hump–producing hot spot. The simulated data with a strictly periodic hump is compared with the original data, from run 16, in Figure 4.5. Notice that there is some similarity between the relative depths of the 67 min minima in the simulated data and the minima in the real data. In the simulated data the occurrence of two deep minima followed by a shallow one is due to the 67 min modulation being nearly two–thirds the orbital period, and so this sequence nearly repeats every 3 cycles of the 67 min modulation. A hump would therefore explain some of the variability of the 67 min modulation, sometimes adding to a maximum and sometimes adding to a minimum, as illustrated in Figure 4.5.

It has not been possible to confirm or disprove the existence of a 46.4 min periodicity in the data, as previously seen by Cordova et al. (1985). The Q–method does show a small peak at 47 min, but this is marginally reduced when a 67 min sine wave is removed. It is also worth noting that $2f_{47}$ turns up at f_{94} which is a strong alias peak of f_{98}. The LS–method shows a broad hump in the spectrum around the $f_{46.4}$ and $2f_{98}$ frequencies. The two largest spikes there correspond to $2f_{98}$ and the 47 min peak. If, however, a hump—type feature, whose amplitude and phase are variable, is present, then this type of structure around $2f_{98}$ is consistent with the simulations. To identify a 46.4 min signal beyond all doubt would require better time coverage than is provided by the present data. Several good nights, with as few breaks in the data as possible, are needed to resolve this problem. Similarly the broad peak in both the LS and Q–method spectra near $f_{67}+f_{98}$, which was also noted by Cordova et al. (1985) as

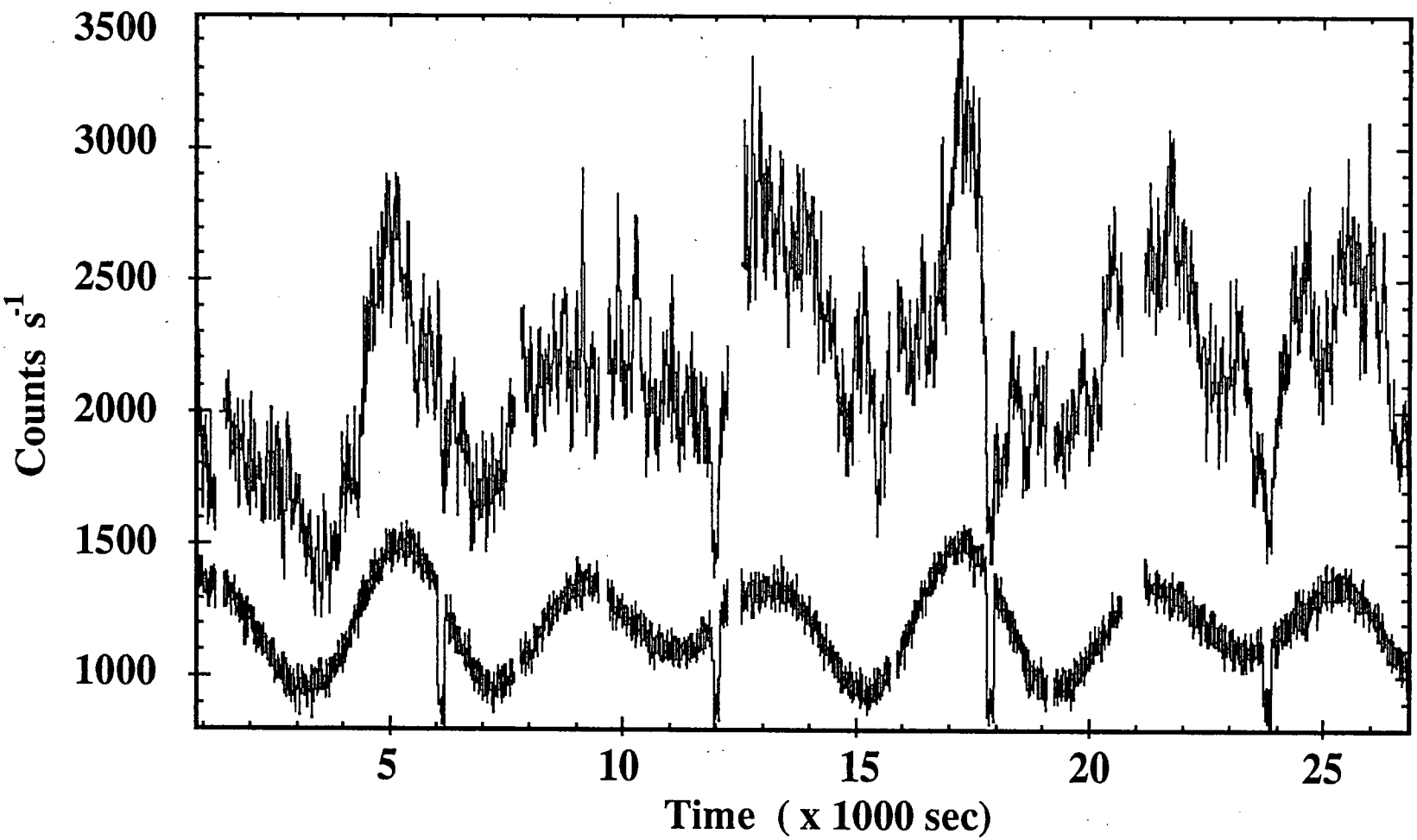

Figure 4.5
The data from run 16 is compared with a simulated set of data containing a 67 min sinewave, eclipse and strictly periodic orbital hump centered on orbital phase 0.9. The light curve of the simulated data has been shifted downward for clarity.

a weak feature in their X–ray data, cannot be confirmed as real. It may be related to the sampling pattern and the random nature of the light curves.

Using both techniques, a periodicity is seen around 33.5 min, as noted by Gilliland (1982). This can be attributed to $2f_{67}$. A smaller fraction of the broad feature in this region of the spectrum may be due to $3f_{98}$. The $2f_{67}$ could possibly be a consequence of only having ~16 cycles of the 67 min period in the data, coupled with the fact that it is highly variable. More extensive sets of data might see a reduction in the size of this peak.

4.3.3 The Orbital Period and Eclipse Timing

A total of 31 eclipses of EX Hya were observed. The mid–eclipse times for these are given in Table 4.2. In this table the Heliocentric Julian Date has been corrected to Ephemeris Time following the discussions of Vogt et al. (1980).

The times in Table 4.2 were combined with all other available published data, as given by Vogt et al. (1980), Gilliland (1982), Sterken et al. (1983), Cordova et al. (1985), Jablonski and Busko (1985) and Bond and Freeth (1988). The resulting ephemeris from the 340 mid–eclipse times, together with 1 σ confidence levels, is

$$\begin{array}{l} \text{ET(mid–eclipse)} = 2437699.94159 + 0.0682338458\,\text{E.} \\ \qquad\qquad\qquad\qquad\quad \pm 5 \qquad\qquad\quad \pm 6 \end{array} \qquad (4.1)$$

The (O–C) residuals, based on the Mumford (1967) ephemeris, for all of the available eclipse times, are plotted in Figure 4.6. It is easy to see from the plot of these residuals why, until 1980, a secular decrease in the orbital period was suspected by other authors. The reversal of the (O–C) drift since 1979 implies that any period change is not a simple one. This long time–scale variation has been fitted with a sinusoid which yields,

$$\begin{array}{l} \text{(O–C)} = 0.00012 + 0.00026\,\text{Sin}\left(\dfrac{360^\circ\,\text{E}}{103000} + 27^\circ\right). \\ \qquad\quad \pm 2 \qquad\quad \pm 3 \qquad\quad \pm 6000 \quad \pm 16^\circ \end{array} \qquad (4.2)$$

This fit is in agreement with that given by Bond and Freeth (1988) and was used to remove the long term trend in the (O–C) values when looking at their short term variability. Since the data correspond to only one cycle of this sinusoid, a ~20 yr periodicity cannot be claimed to be present. Several cycles would be necessary to confirm such a result. However, it is worth noting that the time–scale of this variation

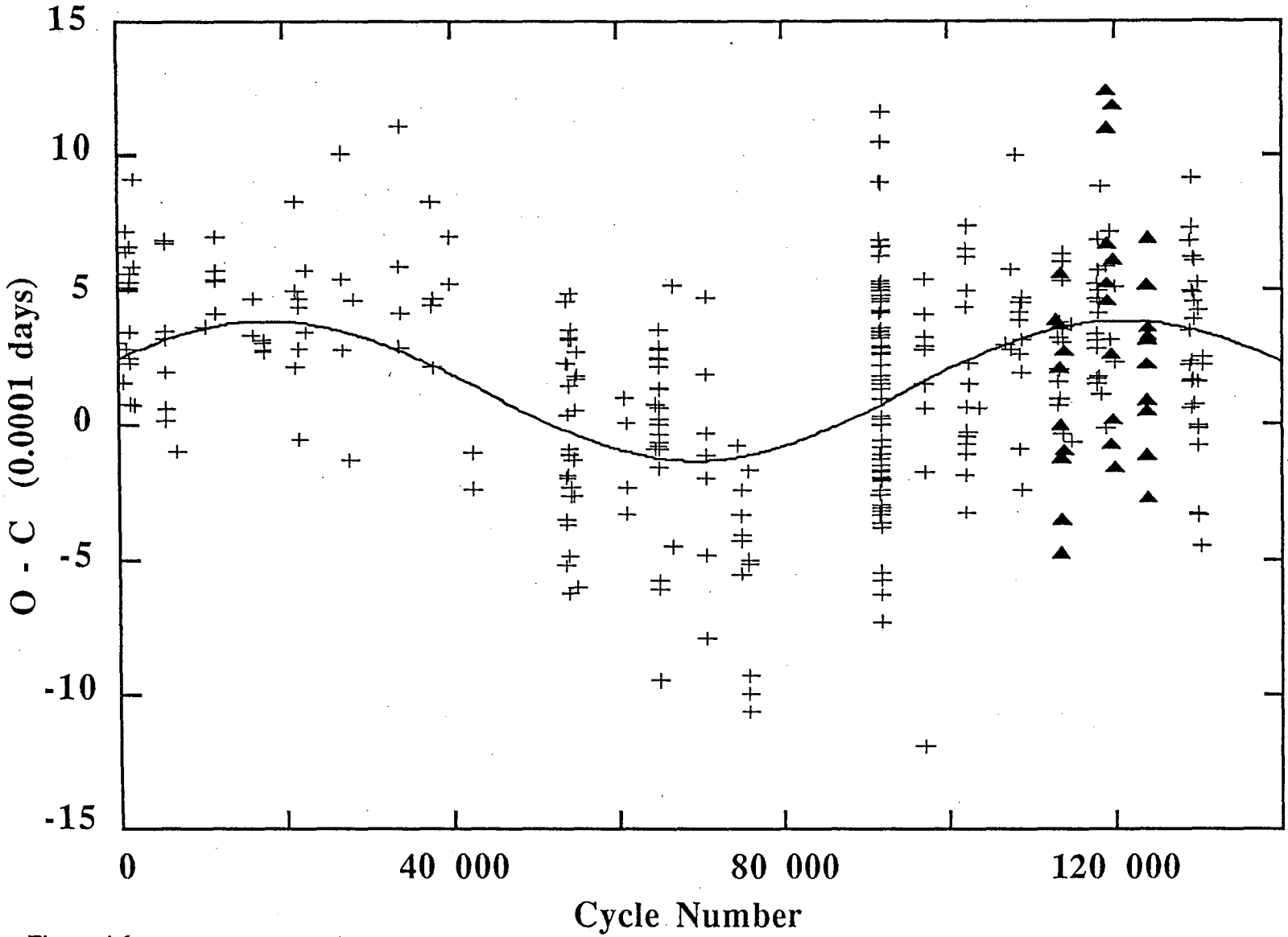

Figure 4.6
The O-C residuals, in units of 10^{-4} d, versus cycle number for the eclipse minima of EX Hya. The residuals are based on the elements of Mumford (1967). The solid line is a least squares sinusoidal fit and the points marked with triangles are from this work.

Table 4.2

Heliocentric Times of Mid–Eclipse

HJD (2440000+)	E	HJD (2440000+)	E
5404.1571	112909	5856.0694	119532
5433.1563	113334	5871.0133	119751
5433.2247	113335	5871.0821	119752
5443.0500	113479	5875.0385	119810
5443.1188	113480	5885.0687	119957
5443.1860	113481	6149.2023	123828
5445.1649	113510	6149.2704	123829
5446.1204	113524	6150.0214	123840
5473.0728	113919	6150.0890	123841
5473.1414	113920	6150.1574	123842
5823.1132	119049	6150.2259	123843
5823.1820	119050	6153.0229	123884
5825.0924	119078	6153.0921	123885
5825.1600	119079	6153.1600	123886
5825.2283	119080	6153.2282	123887
5856.0015	119531		

is similar to period variations seen in some other CV's. Warner (1988), has proposed a model for these quasi–periodic variations, where solar–type cycles result in changes in the radius of the secondary and subsequently lead to variations in the orbital period. Warner estimates that the radius of the secondary in EX Hya would only have to change by a factor of $\Delta R/R \approx 5 \times 10^{-7}$ to produce the observed (O–C) amplitude of 0.00026 d.

4.3.4 The 67 Minute Period

Thirty three maxima of the 67 min modulation were observed and these times are listed in Table 4.3. When combined with all other available published data, as summarised by Hill and Watson (1984), Hill, Sharma and Watson (1986), and the recent results by Bond and Freeth (1988), 374 times of 67 min maximum result. These give the following ephemeris :

$$\mathrm{HJD(max)} = \underset{\pm 50}{2437699.89027} + \underset{\pm 12}{0.0465465506}\,E - \underset{\pm 6}{7.7\times10^{-13}}\,E^2. \quad (4.3)$$

The quoted errors are 1 sigma confidence levels. A statistically significant quadratic term, first suggested by Gilliland (1982), continues to be present in the data at the ~12 sigma level. This may be seen in the Figure 4.7 plot of the (O–C) residuals as a

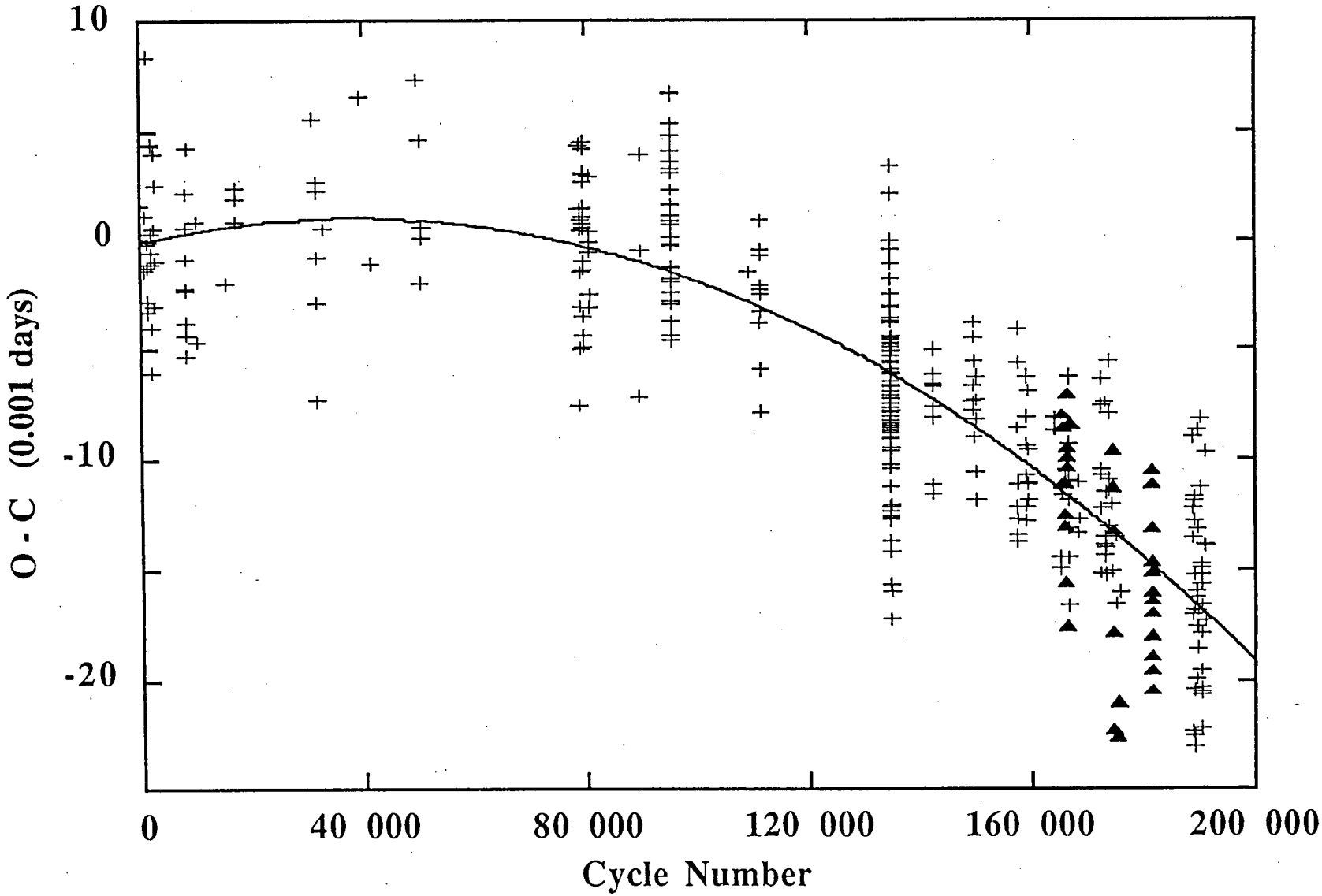

Figure 4.7
The O-C residuals in units of 10^{-3} d, versus cycle number of the 67 min modulation of EX Hya. The residuals are based on the elements of Vogt et al. (1980). The solid curve is the least squares quadratic fit and the points marked with triangles are from this work.

Table 4.3

Heliocentric Times of 67 min Maximum

HJD(max) (2440000+)	Cycle Number	HJD(max) (2440000+)	Cycle Number
5404.064	165516	6153.180	181610
5404.110	165517	6153.126	181609
5404.154	165518	6153.032	181607
5433.058	166139	6150.247	181547
5433.104	166140	6150.201	181546
5433.148	166141	6150.149	181545
5433.199	166142	6150.098	181544
5443.021	166353	6150.055	181543
5443.068	166354	6150.009	181542
5443.115	166355	6149.266	181526
5443.164	166356	6149.219	181525
5445.155	166399	6149.168	181524
5473.092	166999	5875.008	175634
5823.154	174520	5855.969	175225
5825.075	174561	5825.253	174565
5825.118	174562	5825.213	174564
6153.224	181611		

function of 67 min cycle number. In this diagram, the Vogt et al. (1980) ephemeris is used and the present quadratic fit is shown. The short term scatter of (O–C) values in Figure 4.7 can be attributed to observational errors introduced by the strong flickering activity. In the context of the DQ Her model of EX Hya, the decreasing 67 min period may be interpreted in terms of the spin–up of the compact magnetic primary as it acquires angular momentum from infall of disk material. Following Pringle (1975), a value of $P/\dot{P} = -3.8(\pm 0.3)\times 10^6$ yrs is deduced from this ephemeris. The observed $P/\dot{P}$ may be used to argue that the primary is a white dwarf and not a neutron star, as noted by Warner (1985). He points out that the accretion model of Ghosh and Lamb (1979) implies values of $P/\dot{P}$ of this order of magnitude, if the primary is a white dwarf, but a system with a neutron star primary would give a value of $P/\dot{P}$ about two orders of magnitude smaller.

Using the accretion theory developed by Elsner and Lamb (1977) and Ghosh and Lamb (1979) and employing a similar method to Bond and Freeth (1988), the $P/\dot{P}$ value provides a way of estimating the mass transfer rate in EX Hydrae. For a white dwarf primary of mass M_{wd}, radius R_{wd} and rotational angular frequency ω_{wd}, its angular momentumn is given by

$$L_{wd} = I_{wd}\,\omega_{wd}$$

and hence

$$\frac{dL_{wd}}{dt} = I_{wd}\dot{\omega}_{wd} + \dot{I}_{wd}\omega_{wd} = N. \qquad 4.4$$

Where N is the torque applied to the white dwarf due to accretion. For accretion in the presence of a magnetic field Ghosh and Lamb (1979) give

$$N = n(\omega_s)N_0. \qquad 4.5$$

Here N_0 is the rate of angular momentum transfer caused by material crossing the outer radius, R_{orb}, of the magnetospheric boundary layer. It is given by $N_0=(G\,M_{wd}\,R_{orb})^2\dot{M}$, where $\dot{M}$ is the mass transfer rate. The $n(\omega_s)$ term describes the magnetic coupling of the disk material to the magnetosphere of the white dwarf. Ghosh and Lamb (1979) found that $n(\omega_s)$ can be characterised by only the so-called fastness parameter ω_s, which is defined by

$$\omega_s = \frac{\omega_{wd}}{\omega_{orb}},$$

where ω_{orb} is the Keplerian angular frequency at R_{orb}. They find that $n(\omega_s) \approx 1.39\{1-\omega_s[4.03(1-\omega_s)^{0.173}- 0.878]\}(1-\omega_s)^{-1}$, to within five percent for $0 \leq \omega_s \leq 0.9$.

Since the moment of inertia of the white dwarf can be written as

$$I_{wd} = r_g^2\, R_{wd}^2\, M_{wd}, \qquad 4.6$$

where r_g is the radius of gyration. For a white dwarf Ritter (1985) gives

$$r_g = 0.452 + 0.0853 \log(1-M_{wd}/M_{ch}), \quad 0 \lesssim M_{wd} \lesssim 0.95M_{ch}$$
$$r_g = 0.275, \quad M_{wd} = M_{ch}.$$

Taking the derivative of I_{wd} with respect to M_{wd} gives

$$\dot{I}_{wd} = (1+2\alpha+2\beta)\, r_g^2 R_{wd}^2 \dot{M}, \qquad 4.7$$

where $$\alpha = \frac{d\ln(R_{wd})}{dM_{wd}} \quad \text{and} \quad \beta = \frac{d\ln(r_g)}{dM_{wd}}.$$

Subsitution then gives

$$\dot{M} = \frac{r_g^2 R_{wd} M_{wd}\dot{\omega}_{wd}}{n(\omega_s)(GM_{wd}R_{orb})^{1/2} - (1+2\alpha+2\beta)\, r_g^2 R_{wd}\omega_{wd}} \qquad 4.8$$

Hence, given the mass, radius, rotation period and the rate of change of period for the white dwarf, along with the effective radius (R_{orb}) at which the orbiting material couples to the magnetic field of the white dwarf, we can estimate the mass accretion rate. In this context, Eggleton's (1983) representation of the mass–radius relationship

for white dwarf stars can be used to obtain the radius of the primary, given its mass; i.e.

$$R_{wd} = 7.8\times10^{8}\left(\left[\frac{M_{wd}}{M_{ch}}\right]^{-2/3} - \left[\frac{M_{wd}}{M_{ch}}\right]^{2/3}\right)^{1/2}, \qquad (4.9)$$

where M_{ch} is the Chandrasekhar limiting mass, and is taken to be 1.44 Mʘ. For EX Hya the masses of the component stars have been measured spectroscopically by several authors and values in the range 0.5 to 1.4 Mʘ and 0.13 to 0.25 Mʘ have been obtained for the primary and secondary stars respectively (Breysacher and Vogt 1980; Cowley et al. 1981; and Gilliland 1982). More recently, Hellier et al. (1987), using an extensive data set, give 0.78 Mʘ as a best estimate of the mass of the white dwarf. However, the mass could be as little as 0.62 Mʘ, or as great as 0.99 Mʘ. Hellier et al. were also able to remove the components of the emission lines associated with the hot spot and the 67 min modulation, and thus obtain emission–line profiles that could be attributed solely to the disk. The maximum velocity, given by half the base width of the Balmer lines, is ~1250 km s^{-1}. If this is attributed to the Keplerian velocity, V_{orb}, of material at the inner edge of the disk, where the material couples to the magnetosphere of the white dwarf, then one can use it to estimate R_{orb}. The boundary region should be quite small, Ghosh and Lamb (1979) estimate the width of the magnetosphere boundary layer to be ~0.04 R_{orb}. Based on the estimate of R_{orb}, the Hellier et al. mass information used in Equation (4.9), and the present P/$\dot{P}$ data, values of $\dot{M}$ were calculated via equation (4.8). These are presented in Table 4.4. Using the

Table 4.4

Results of Mass Transfer Rate and Magnetic Moment Calculations.

	Based on best white dwarf mass estimate	Range limits determined from white dwarf mass range	
M_{wd} (Mʘ)	0.78	0.62	0.99
R_{wd} (cm)	7.15×10^{8}	8.5×10^{8}	5.5×10^{8}
R_{orb} (cm)	6.6×10^{9}	5.3×10^{9}	8.4×10^{9}
ω_{orb}	1.9×10^{-2}	2.4×10^{-2}	1.5×10^{-2}
$\dot{M}$ (Mʘ yr^{-1})	3.1×10^{-11}	4.3×10^{-11}	1.9×10^{-11}
$\dot{M}$(g s^{-1})	1.9×10^{15}	2.7×10^{15}	1.2×10^{15}
μ(G cm^3)	8.1×10^{31}	6.1×10^{31}	1.0×10^{32}

subsequent value of $\dot{M}$ it is also possible to make an estimate of the magnetic moment of the white dwarf using Equation (3.11) and (3.12). In this context R_{orb} will be a reasonable approximation to the outer region of the magnetospheric boundary layer, (r_o in Equation 3.11). Magnetic moment estimates are therefore also given in Table 4.4.

The mass transfer rates derived in Table 4.4 are also consistent with the independent estimate made using Pattersons (1984) empirical relationship between orbital period and mass transfer rate. This relationship is given by,

$$\dot{M}= 5.1(+3,-2) \times 10^{-10} \; P_4^{3.2\,(\pm 0.2)} \; M\odot \; yr^{-1}, \qquad (4.8)$$

where P_4 is the orbital period in units of 4 hours. For EX Hya it predicts a mass transfer rate $\dot{M}= 3\ (+2.5,-1.6)\times 10^{-11}$ $M\odot$ yr^{-1}. The values obtained for the magnetic moment of the white dwarf are also consistent with the DQ Her model for EX Hya. Lamb and Melia (1987) conclude that for white dwarfs with $10^{31} \lesssim \mu \lesssim 10^{33}$ (G cm^3) a DQ Her system will result, and that for magnetic moments in the range $10^{32} \lesssim \mu \lesssim 10^{35}$, the systems will be DQ Her systems that evolve into AM Her systems. If this is the case, then the spin-up of the primary in EX Hya, away from synchronism, is not consistent with the orbitally synchronised primaries in AM Her systems. It would therefore be expected that $\mu \lesssim 10^{32}$ G cm^3, as is indicated by the estimates in the Table 4.4.

4.3.5 Eclipse Time Residuals and the 67 min Modulation

An important effect, first noted by Hill and Watson (1984), and independently by Jablonski and Busko (1985), is the correlation of the eclipse (O–C) residuals with Φ_{67}, the phase of the 67 min modulation. A plot of this effect, using all of the 340 eclipse times, is shown in Figure 4.8. The figure was generated by removing the ~20 yr sinusoidal fit to the long term trend of the (O–C) residuals. The revised residuals were then plotted against the phase of the 67 min modulation corresponding to the mid–eclipse time. The quadratic ephemeris of Bond and Freeth (1988) was used to determine the 67 min phase. The maximum difference between that ephemeris and the one given by Equation 4.3 corresponds to a phase difference of only $\Delta\Phi_{67} = 0.02$. In Figure 4.8 a least–squares sinusoidal fit is also shown. The semi–amplitude of this sinusoid is 17 ±2 s. It has a mean level of –6 ±1.5 s relative to the Mumford (1967) ephemeris. The formal fit to the phase of the sinusoid, 0.02 ±0.02 rad., is not significantly different from zero. Also shown in Figure 4.8 is a histogram of the

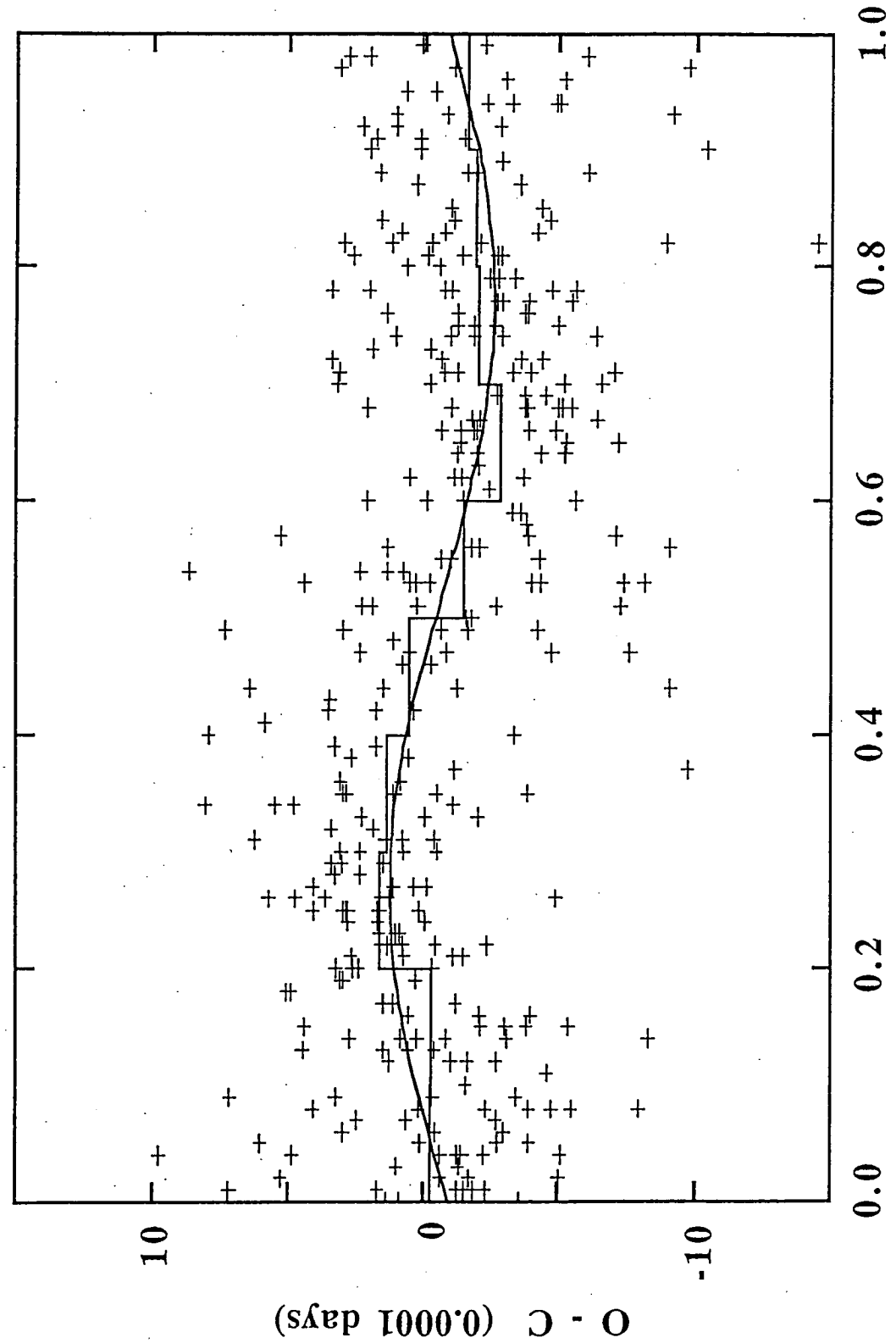

Figure 4.8
The correlation of eclipse (O-C) with the phase of the 67 min modulation. The ~20 yr sinusoidal variation in the (O-C) data was removed from the residuals before plotting them with respect to the 67 min cycle. A least squares sinusoidal fit is shown, as well as a histogram giving the average values in 0.1 phase bins.

average values in each of the 0.1 phase bins along the Φ_{67} axis. An F–test confirms, at greater than the 99.99 percent level, the statistical significance of the improved fit gained by using a sinusoidal model for the data over a simple mean fitted to the data. The semi–amplitude of the sinusoid fitted here is little different from the earlier estimate of 20 s given by Hill and Watson (1984), which was based solely on the eclipse timings of Sterken et al. (1983), but is only about half of the 35 s value suggested by Jablonski and Busko (1985).

A sinusoidal variation, such as the one shown in Figure 4.8, may in principle be produced by systematic effects on the way mid–eclipse times are measured on the rising and falling branches of the 67 min modulation. Jablonski and Busko(1985), however, estimate a maximum semi–amplitude of 3 s for such an effect. If this is indeed the case, then the timing difference between eclipses at $\Phi_{67} = 0.25$ and $\Phi_{67} = 0.75$ is intrinsic to the system. In the context of the DQ Her model, this may be interpreted as implying that the majority of the eclipsed optical flux comes from a source, locked to the white dwarf rotation, which shifts back and forth perpendicularly to the line of sight by $\sim 10^4$ km each 67 min. The eclipses are later at $\Phi_{67} = 0.25$ and earlier at $\Phi_{67} = 0.75$.

The phasing of the sinusoid in Figure 4.8 is important, since it implies the geometric location of the majority of the eclipsed optical flux at times of 67 min maximum and minimum. This is because a white dwarf, rotating in a prograde sense with respect to the orbital motion, will carry any rotationally–locked eclipsed structure from the orbitally preceding–side of the star at $\Phi_{67} = 0.75$, through the side nearest the observer at $\Phi_{67} = 0$, and onto the orbitally–trailing side at $\Phi_{67} = 0.25$. Prograde white dwarf rotation in EX Hya must be considered highly probable in view of the observed decrease in the 67 min period, which is due to accretion from the surrounding disk. Such disks normally have prograde motion. Thus the data in Figure 4.8 implies that the majority of the eclipsed optical flux originates on the near side of the white dwarf at $\Phi_{67} = 0$, and, correspondingly, on the far side at $\Phi_{67} = 0.5$. The most recent discussions of models for the EX Hya system identify the eclipsed structure with accretion columns or arcs in the region above the magnetic poles of the white dwarf.

4.4 Anglo–Australian Telescope Spectroscopy

4.4.1 Observations and Data Reduction

Spectroscopic observations were obtained using the 3.9 m Anglo–Australian Telescope, at Siding Spring New South Wales, on the nights of 26th July 1986 and 21st February 1987. The objective was to obtain a short series of time–resolved spectra through a single eclipse of EX Hya. These observations were fitted between spectra of other cataclysmic variables, which constituted the principal observing program.

The spectroscopic data were acquired using the Royal Greenwich Observatory (RGO) spectrograph which is mounted at the cassegrain f/8 focus of the AAT (Robinson 1985). Figure 4.9, adapted from Robinson (1985), details the RGO light paths at cassegrain focus. The spectrograph can be configured in several ways, so it can be used by different auxiliary equipment. The modes that are relevant to this work concern the placement of the Newtonian flat and dichroic mirror. With the Newtonian flat in place, the light beam is deflected to the collimator and then back past the Newtonian flat and onto the grating, camera and detector. The detector that was used in this configuration was the Image Photon Counting System (IPCS). This is a two dimensional detector that counts individual photon events by means of an image intensifier optically coupled to a continuously scanning television camera. The positions of the photon events are recorded in digital memory. Using the dichroic mirror instead of the Newtonian flat allows simultaneous observations at blue wavelengths with the IPCS and at red wavelengths with the Faint Object Red Spectrograph (FORS). The FORS attaches to the bottom of the RGO spectrograph, sharing the same dekker, slit and shutter. The FORS is a collimator–less spectrograph with dispersion by a grism and uses a GEC CCD as the detector.

On the night of 26th July 1986, spectra were acquired simultaneously in the blue region, $\lambda\lambda$ 4000 – 5000 Å, using the RGO spectrograph with the IPCS, and in the red region, $\lambda\lambda$ 5600 – 8500 Å, using the FORS. The IPCS spectra were obtained with the 1200 B grating which gives a reciprocal dispersion of about 0.5 Å per pixel and a corresponding resolution of 1.3 Å. The FORS is a low resolution spectrograph, which has a reciprocal dispersion of about 10 Å per pixel and a correspondingly lower resolution. A Cu–Ar arc spectrum taken before and after the stellar spectra was used for wavelength calibration. The spectra acquired on the night of 21st February 1987 were only in the blue region, using the RGO spectrograph Newtonian flat and IPCS

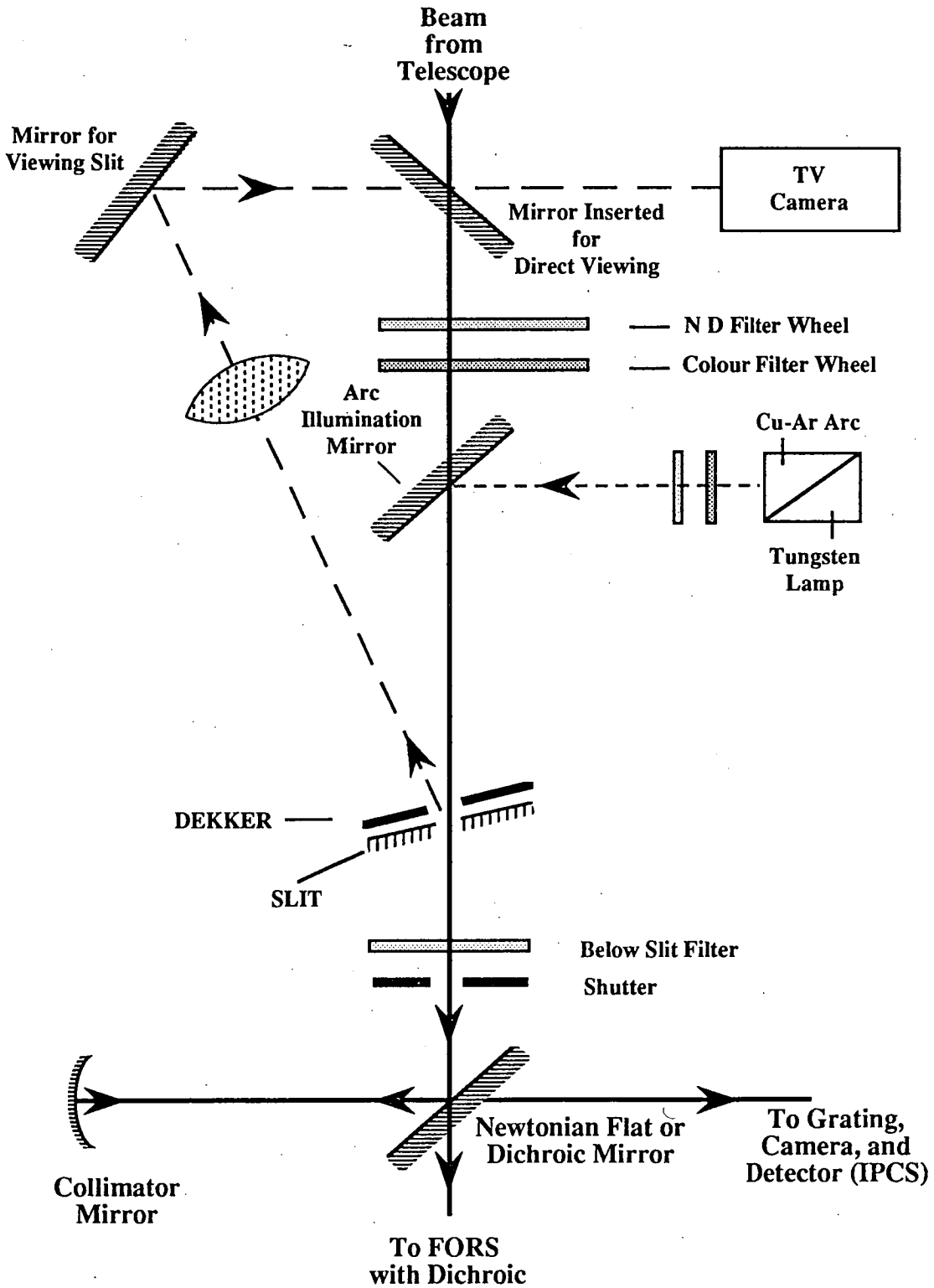

Figure 4.9

The light path for the RGO spectrograph adapted from Robinson (1985).

detector in the same configuration as for the earlier night, and covering $\lambda\lambda$ 3950 – 4900 Å. Flux standards were obtained on both occasions.

The data from the 26th July 1986 run were recorded using the 'normal' AAT IPCS and FORS acquisition software. Here the IPCS and FORS data were acquired by two independent software packages. To make an observation, in both cases, one simply specifies the exposure time and then directs the software to begin the exposure. However, the FORS acquisition software controls the shared shutter and hence controls the real exposure time. To synchronise the data acquisition it is simply a matter of starting the IPCS exposure before the FORS and finishing it later than the FORS. This is accomplished by setting the IPCS exposure time to be a little longer than that for the FORS and then initiating the IPCS exposure before the FORS exposure. At the end of an exposure the IPCS spectrum is written to tape and the FORS spectrum is written directly to the disk on the VAX computer. After the spectra have been written out, another observation can be commenced. In both cases the spectra are stored in a two dimensional data structure, with one wavelength dimension and one spatial dimension corresponding to slit position. Since the object star occupies only a few channels of the slit dimension, the sky background spectrum is obtained in nearby channels for subtracting from the star spectrum.

In the case of the 26th July 1986 data, spectra were obtained over a 17 min timespan, but, because EX Hya was the first object observed for the night, and acquisition was not achieved until a few minutes prior to the predicted eclipse time, the data did not adequately establish pre–ingress conditions. It was previously decided to sacrifice some time resolution for the extra spectral coverage gained by using the FORS. The spectra were limited to 120 s integrations because of the long read–out time, ~60 s, for the FORS system. Hence this spectral run is of little use in detailing changes during the eclipse. However, the sum of all the spectra for that run is presented here as Figure 4.10, with a brief discussion of them in Section 4.4.2, because these spectra preceded, by just over one day, a well–documented outburst of EX Hya (Bateson et al. 1986, Bond et al. 1987). The spectral run commenced at JD 2446637.890. At this stage EX Hya had an $m_v \approx 13.2$. At some time between JD 2446639.20 and JD 2446639.85 the outburst occurred, taking EX Hya to $m_v \lesssim 9.7$.

The data from the 21st February 1987 run were obtained using the area spectroscopy software (ASPECT) package. This software package allows for continuous data acquisition from the IPCS with programmed telescope motion if desired. The continuous data acquisition is achieved by dividing the IPCS external memory into two

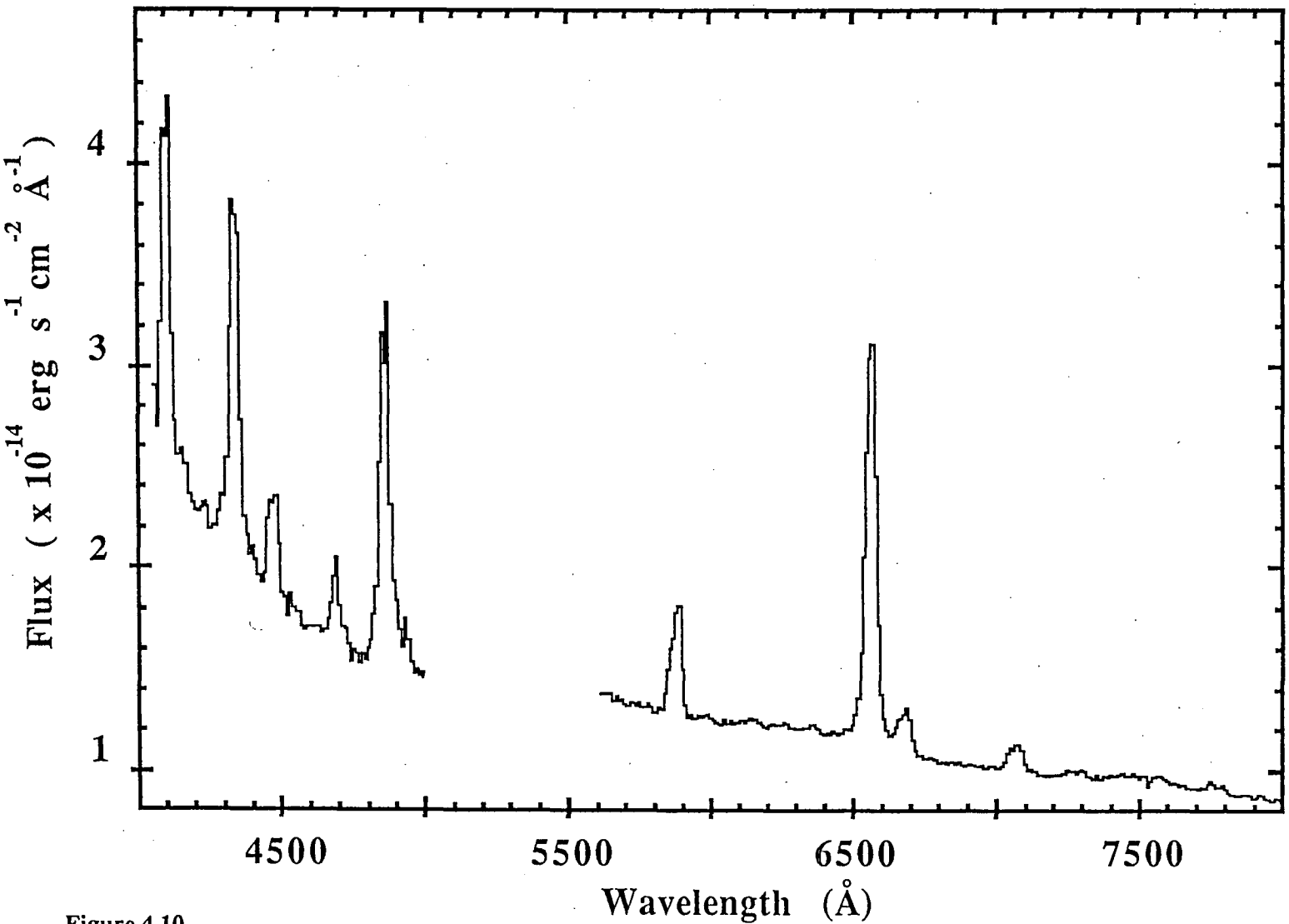

Figure 4.10
The spectrum of EX Hya obtained with the IPCS and FORS systems over a 17 min time period beginning at JD 24466637.890. For consistency, the IPCS spectrum has been convolved to the lower resolution of the red spectrum obtained with the FORS, so the strong line doubling present in EX Hya is not visible in this plot.

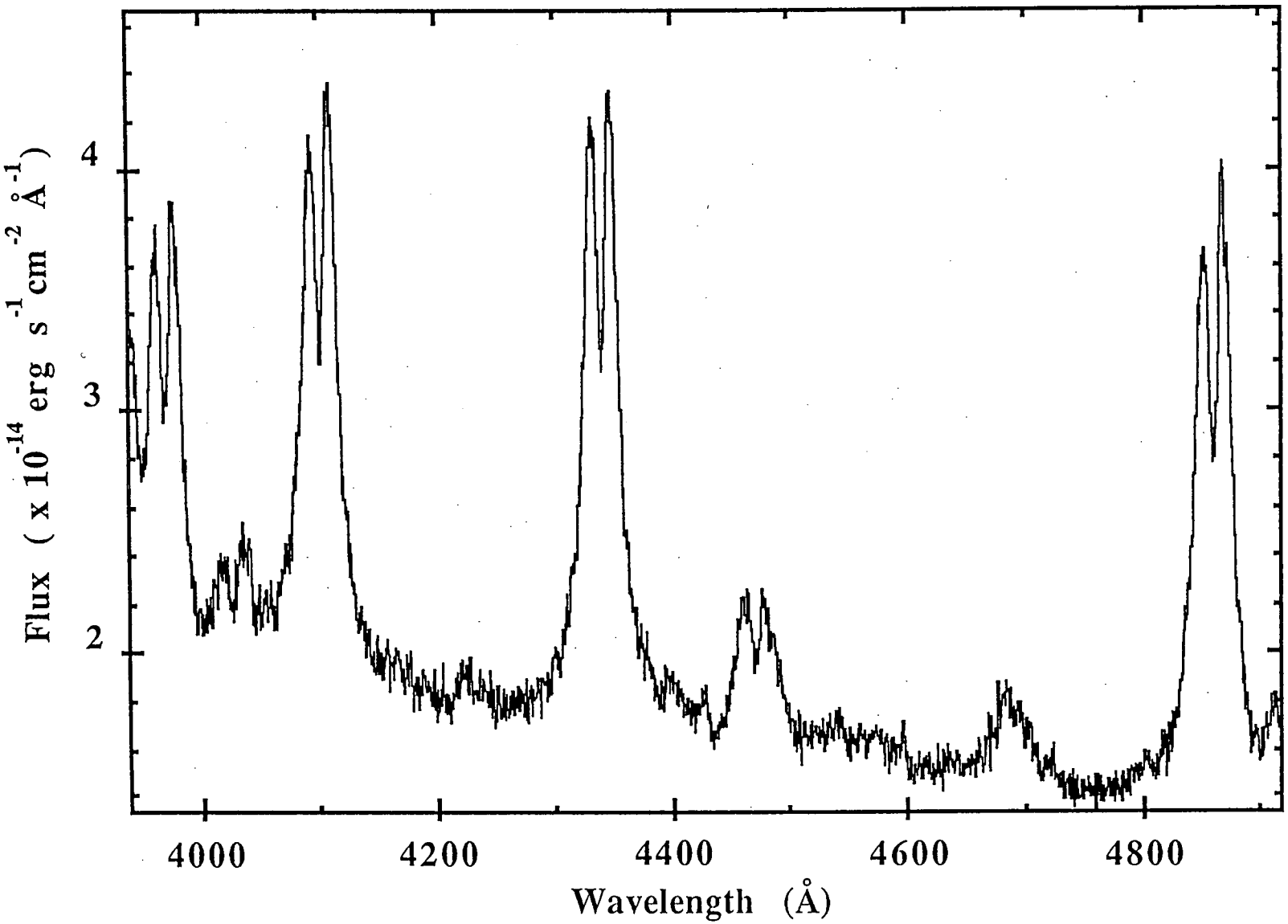

Figure 4.11
The spectrum of EX Hya obtained with the IPCS system over a 63 min time period beginning at JD 2446848.226.

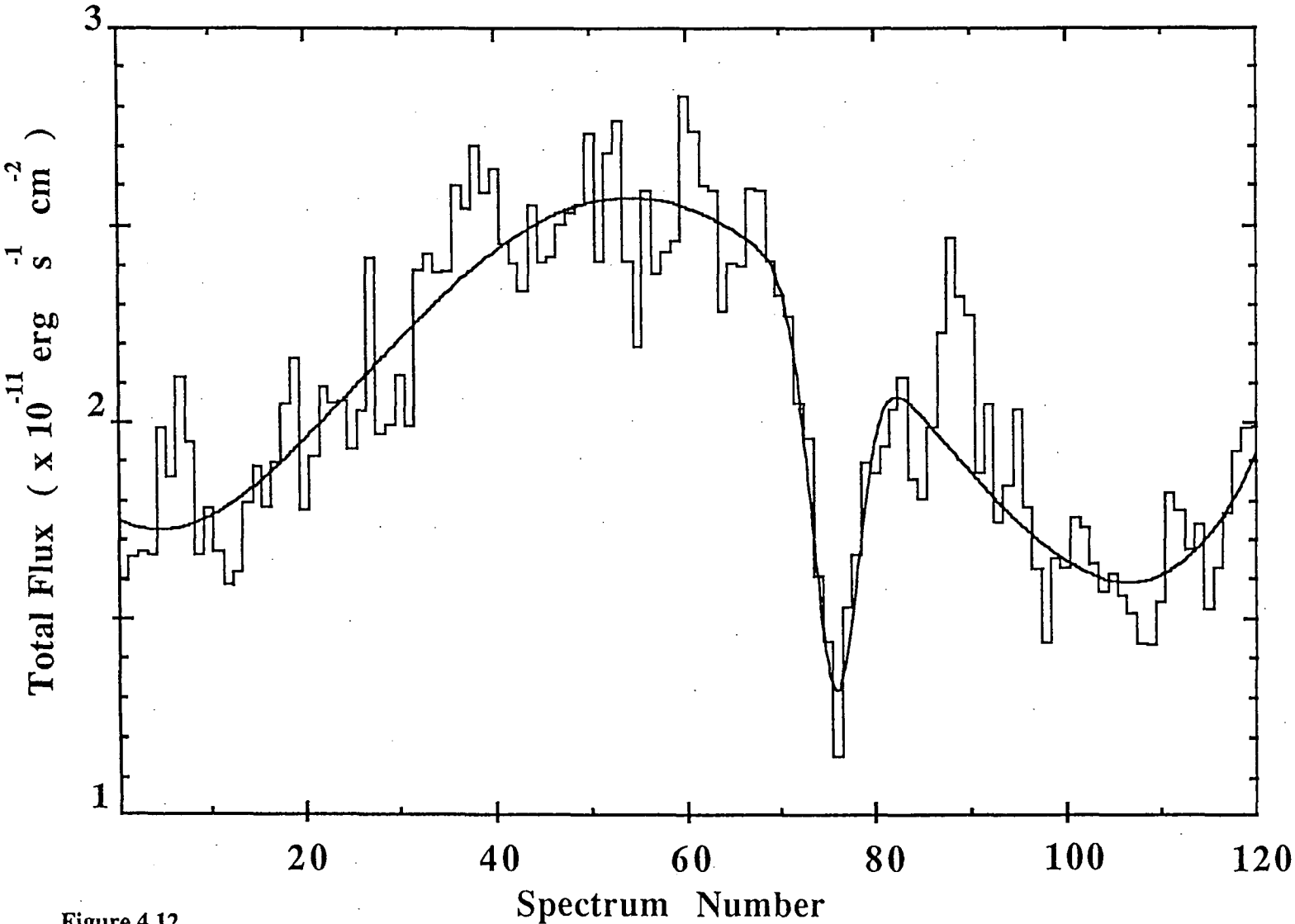

Figure 4.12
The integrated IPCS flux (λλ 3950-4900 Å) as a function of 30 s spectrum number, for the spectral run beginning at JD 2446848.226. Dead-time gaps of ~60 s occurred after spectrum numbers 30, 60 and 90, but are omitted here. A polynomial function has been fitted to the 67 min modulation and a Gaussian to the eclipse region.

sections. Data are collected in one half while the contents of the other half are being written to disk. The number of spectra to be obtained is specified at the beginning of the run. At the end of each run the accumulated spectra are copied from the disk to tape and then the next run is commenced. Each data run results in a three dimensional data structure with one wavelength dimension, one spatial dimension corresponding to slit position, and the other dimension being time.

For the 21st February 1987 data, four 15 min runs were completed over a 63 min timespan beginning at JD 2446848.226, thus covering almost one complete cycle of the 67 min modulation. A single, well–observed, eclipse occurred some two–thirds of the way through this set of data. The integration time for each spectrum was set at 30 s. Every 15 min there is an ~1 min dead–time as the accumulated IPCS spectra were read to tape. The eclipse is located midway through a 15 min data block, so no useful eclipse information was lost due to the ~1 min dead–time gaps. The grand sum of all spectra for this night is presented in Figure 4.11, with no corrections for velocity variations having been made. The nature of the eclipse is seen in Figure 4.12, where the integrated flux ($\lambda\lambda$ 3950–4900 Å) in each 30 s spectrum is plotted as a function of spectrum number. The 67 min modulation is clearly visible in this figure and a least–squares polynomial fit to this variation is shown. Its phase at the time of eclipse is $\Phi_{67} = 0.16$.

Involving, as it does, the study of a single eclipse, the data presented here are considerably more limited than those presented in the most recent studies of Kaitchuck et al. (1987) and Hellier et al. (1987). However, the spectra here are of higher resolution in both wavelength and time than the Kaitchuck et al. data, which were acquired with a wavelength resolution of 2.7 Å and a time resolution of 230 s. While the Hellier et al. data have similar wavelength and time resolutions to the present data, their signal to noise is lower, having been obtained on a 1.9 m telescope.

Data reduction was performed using a package, called FIGARO, written by Keith Shortridge of the AAO. FIGARO is written to run on Digital's VAX series of computers. It is a system of interconnected programs that are callable from the Digital Command Language (DCL) on the VAX. The package contains a large range of analysis programs for interactively manipulating and performing arithmetic on arrays of up to three dimensions. It includes programs for doing wavelength calibration, atmospheric extinction corrections, atmospheric band removal using a B star calibration spectrum, and flux calibrations. The system is also able to display the data on a variety of display devices. More details on this system are available in manuals

from the Anglo–Australian Observatory and Cohen (1987) gives a brief description of its history and the design philosophy used in its development.

While at the AAO, doing preliminary data reduction, I obtained a copy of FIGARO from Keith Shortridge and installed it on the University of Tasmania Physics Department VAX 750 computer. Subsequent analysis of the data was performed at that site. The data were converted to flux above the atmosphere using extinction tables for the AAT site, included in FIGARO, and the spectroscopic standards HD140283 (Oke and Gunn, 1983) and L745–46 (Oke ,1982) for the 1986 and 1987 runs respectively. The smooth spectrum star HD184711 was used for removing atmospheric bands from the FORS spectra.

4.4.2 General Spectral Characteristics

The low–resolution pre–outburst spectrum in Figure 4.10 shows the typical emission line features of EX Hya. As well as the Balmer lines, the He I lines λλ 4026, 4471, 4921, 5015, 5875, 6678, 7065 Å and the He II line λ 4686 Å are readily visible. Several other weaker features are present, including O I λ 7773 Å, as studied by Friend et al. (1988). The continuum slope in the region λλ 4500–7000 Å is similar to that for the EX Hya spectrum in the Williams (1983) catalogue, though less steep than indicated by the spectro–photometry of Bath et al. (1980). The absolute fluxes in the continuum of Figure 4.10 are some 20 percent stronger than those in the Figure 4.11 data. However, with the limited data runs here, this may simply be attributable to the effect of any individual flares, or the 67 min flux modulation, rather than any pre–outburst condition. There is also the suggestion in Figure 4.10 of a more rapidly rising flux in the H_δ region compared to Figure 4.11. This may also not necessarily relate to the pre–outburst condition, since the U–B colours, in non–magnetic cataclysmic variables at least (Bailey, 1980), redden in early pre–outburst changes. However, since DQ Her systems have either no recorded outbursts or outburst only rarely (Ritter, 1984), nothing is known about outburst properties of these systems. The shorter–wavelength enhancement in Figure 4.10 is, however, probably a real effect. Further support for this is to be gleaned from the fact that it is absent in the 120 s mid–eclipse spectrum of that data run. No such change in continuum slope was seen during the eclipse observed in the 1987 data run. Thus the eclipsed structure may have been stronger in the blue when the Figure 4.10 data were acquired.

All of the high–resolution spectra from the 21st February 1987 run, summed in Figures 4.11 and 4.12, are shown individually using false colour images in Figure

4.13.1 and Figure 4.13.2. Here the spectral resolution resolution has been reduced to 2Å/pixel to increase the signal to noise ratio. The final flux calibrated spectra are shown in Figure 4.13.2., whereas in Figure 4.13.1 a linear fit to the continuum part of each spectrum has been removed to illustrate the emission line variations more clearly. Enlarged sections around H_β and H_γ are also presented in both Figures, to show the line structure in more detail. The spectra clearly show the line–doubling in the Balmer lines and He I λλ 4026, 4471 Å seen in other studies. The doubling is more prominent in Figure 4.11 than in other published spectra of a similar wavelength resolution (Gilliland, 1982; Hellier et al. 1987). This is presumably in part due to the particular range of phase of the S–wave emission in the data, which is clearly seen in Figure 4.13.1 (b) and (c) . This S–wave component of the line emission, as documented by Kaitchuck et al. (1987) and Hellier et al. (1987), moves rapidly from its blue to red extremes at phases just prior to and during the eclipse. For the remainder of the phases covered by the data, it is located near its blue or red extremes. The prominence of the line–doubling may also be partly due to non–disk emission components being relatively weaker in this data run, since the time–resolved spectra show a much stronger doubling than the corresponding time–resolved spectra of Hellier et al. Near phase $\Phi_{98} = 0.85$, the line doubling gets particularly strong in the present data. The fluxes in the central dips of the Balmer lines fall to as low as 30 percent of the peak fluxes, and in the He I lines they reach down to the continuum level. Also seen clearly in Figure 4.11 is the absence of line–doubling in the He II λ 4686 Å emission, indicating a different originating location for its flux compared with H I and He I emission. The absolute values of the continuum fluxes in Figure 4.11 are comparable with those in the total spectra given by Gilliland (1982) and Hellier et al. (1987), as are the line fluxes. The Kaitchuck et al. (1987) fluxes are larger by about a factor of two.

The detailed wavelength structure of each of the major emission lines is shown more clearly in Figures 4.14 and 4.15. The Balmer line twin peaks correspond to a velocity separation of 1000 to 1200 km s^{-1}. Similar values are noted by Breysacher and Vogt (1980), Cowley et al. (1981), and Hellier et al. 1987). Correcting for the 70 km s^{-1} orbital velocity variations measured by Hellier et al., before forming the grand sum spectrum, changes only slightly the structure of the line profiles in Figures 4.14 and 4.15. Emission in the wings of the Balmer lines is detectable out to velocities of about 3500 km s^{-1}. Gilliland (1982) and Hellier et al. (1987) determine similar values. The close similarity of the velocity structure of H I and He I lines is evidenced by comparing the λ 4471 Å line of Figure 4.15 with the Balmer lines in Figure 4.14.

Figure 4.13.1

A time resolved false colour image of the calibrated IPCS spectra beginning at JD 2446848.226. Each spectrum in this image has had a linear fit to it's continuum removed, so as to display the emission line variations in more detail. The spectral resolution has been reduced to 2 Å per pixel to increase the signal-to-noise ratio. Panel (a) shows the entire data set, while panels (b) and (c) show the spectra around H_β and H_γ in more detail. The effects of the 67 min modulation, eclipse, and line doubling are seen clearly in these images.

Figure 4.13.2

A false colour image of the original flux calibrated data used to generate Figure 4.13.1. The layout for this figure is the same as for Figure 4.13.1

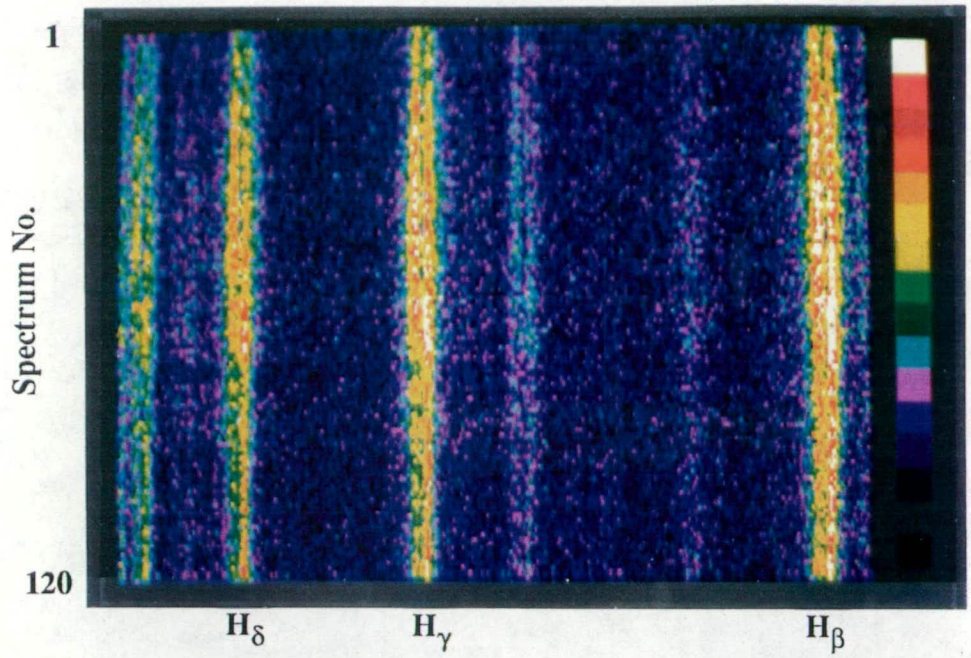
1
Spectrum No.
120
H_δ
H_γ
H_β

(a)

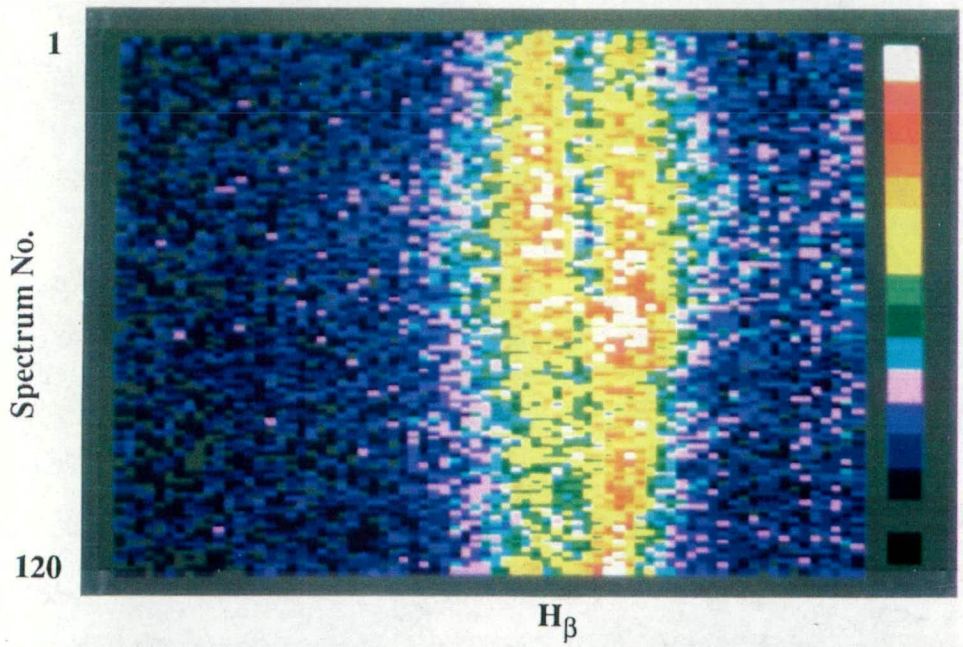
1
Spectrum No.
120
H_β

(b)

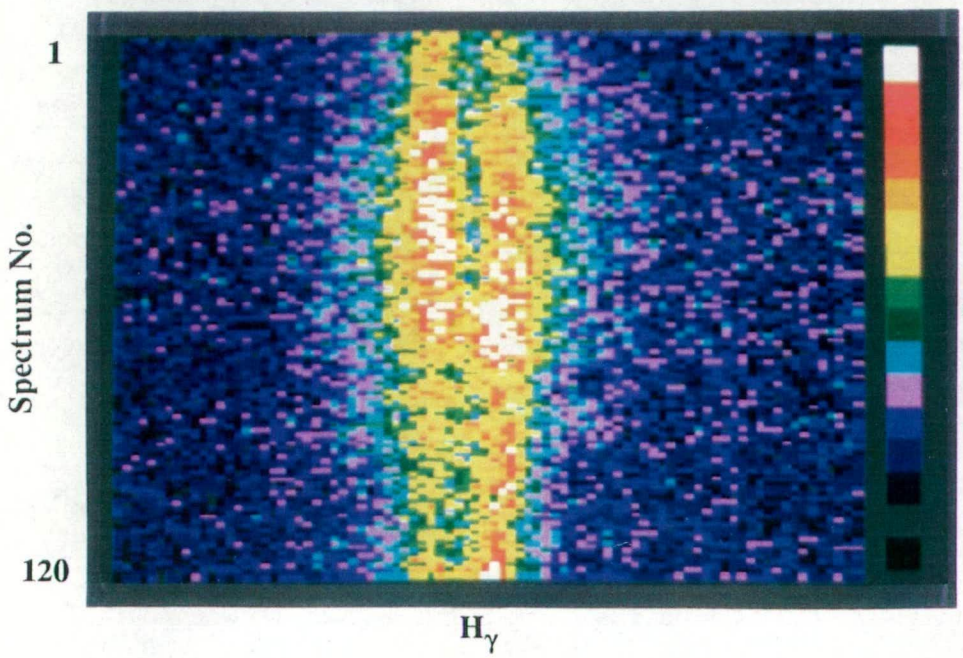
1
Spectrum No.
120
H_γ

(c)

Fig. 4.13.1

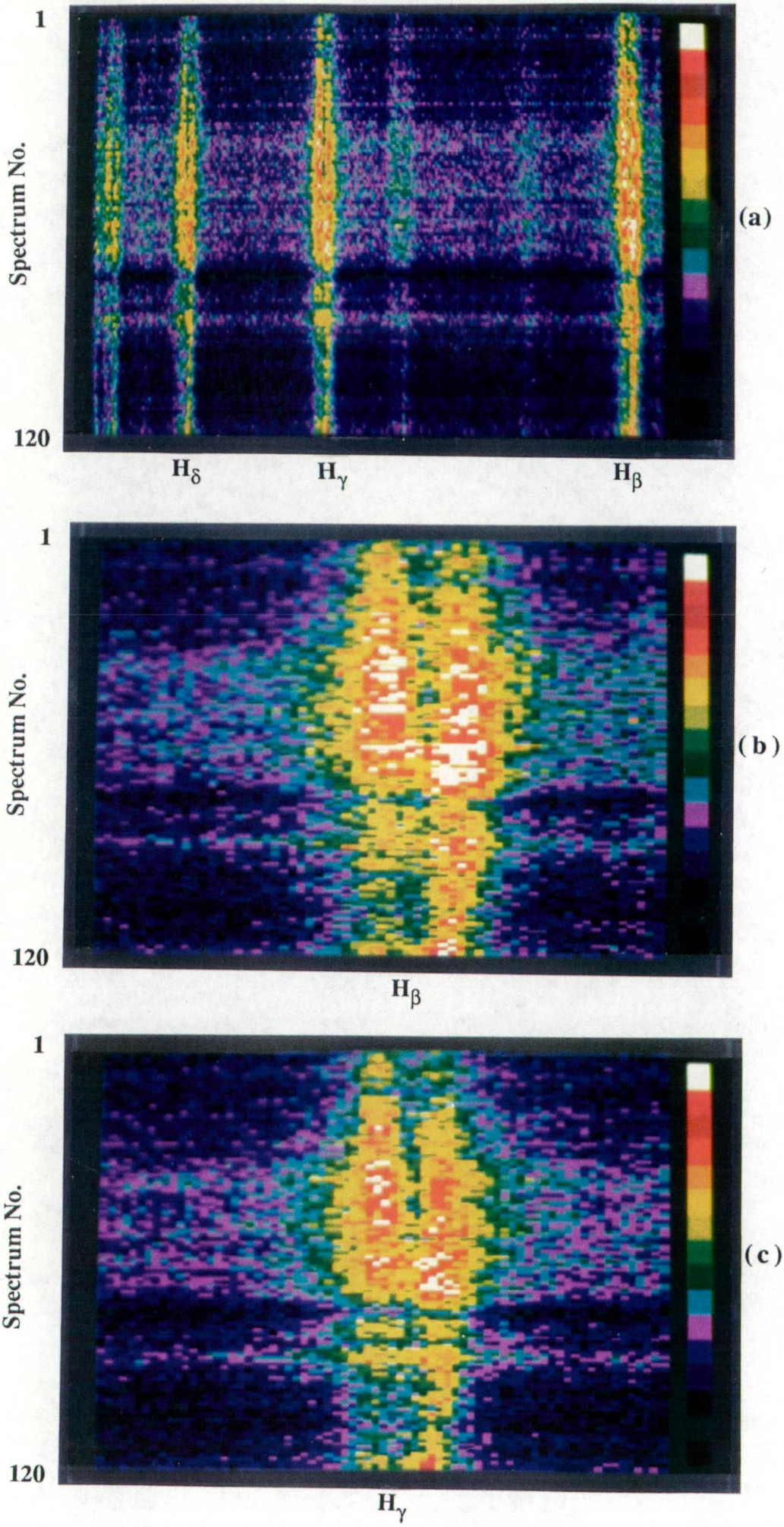
1
Spectrum No.
120
H_δ
H_γ
H_β
(a)
1
Spectrum No.
120
H_β
(b)
1
Spectrum No.
120
H_γ
(c)

Fig. 4.13.2

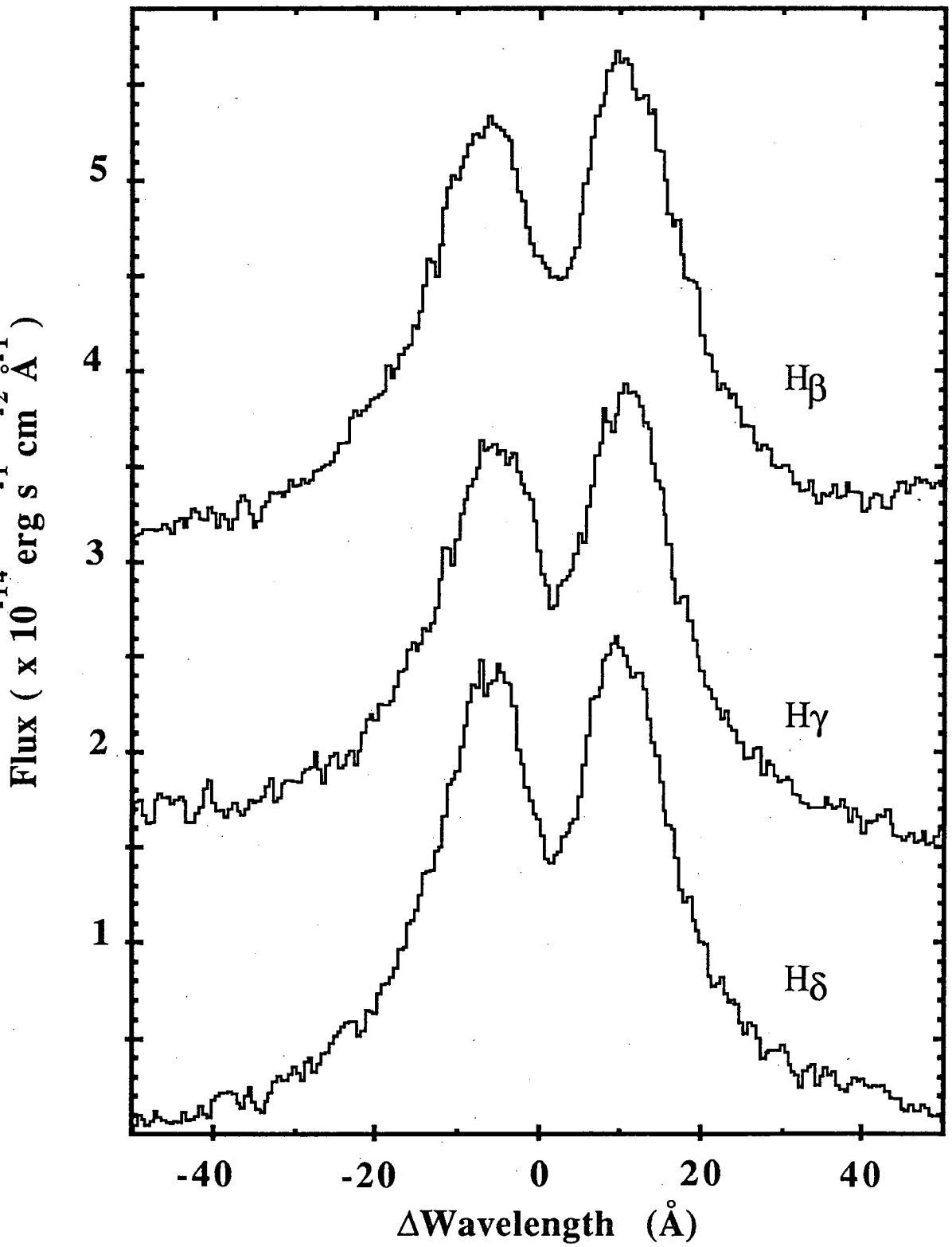

Figure 4.14
Details of the wavelength structure of the hydrogen lines H_β, H_γ and H_δ for the spectral run beginning at JD 2446848.226. The zero point on the horizontal axis is the nominal rest wavelength of the line. The zero point on the vertical axis is the continuum flux level near H_δ. The H_β and H_γ lines have been shifted vertically for clarity.

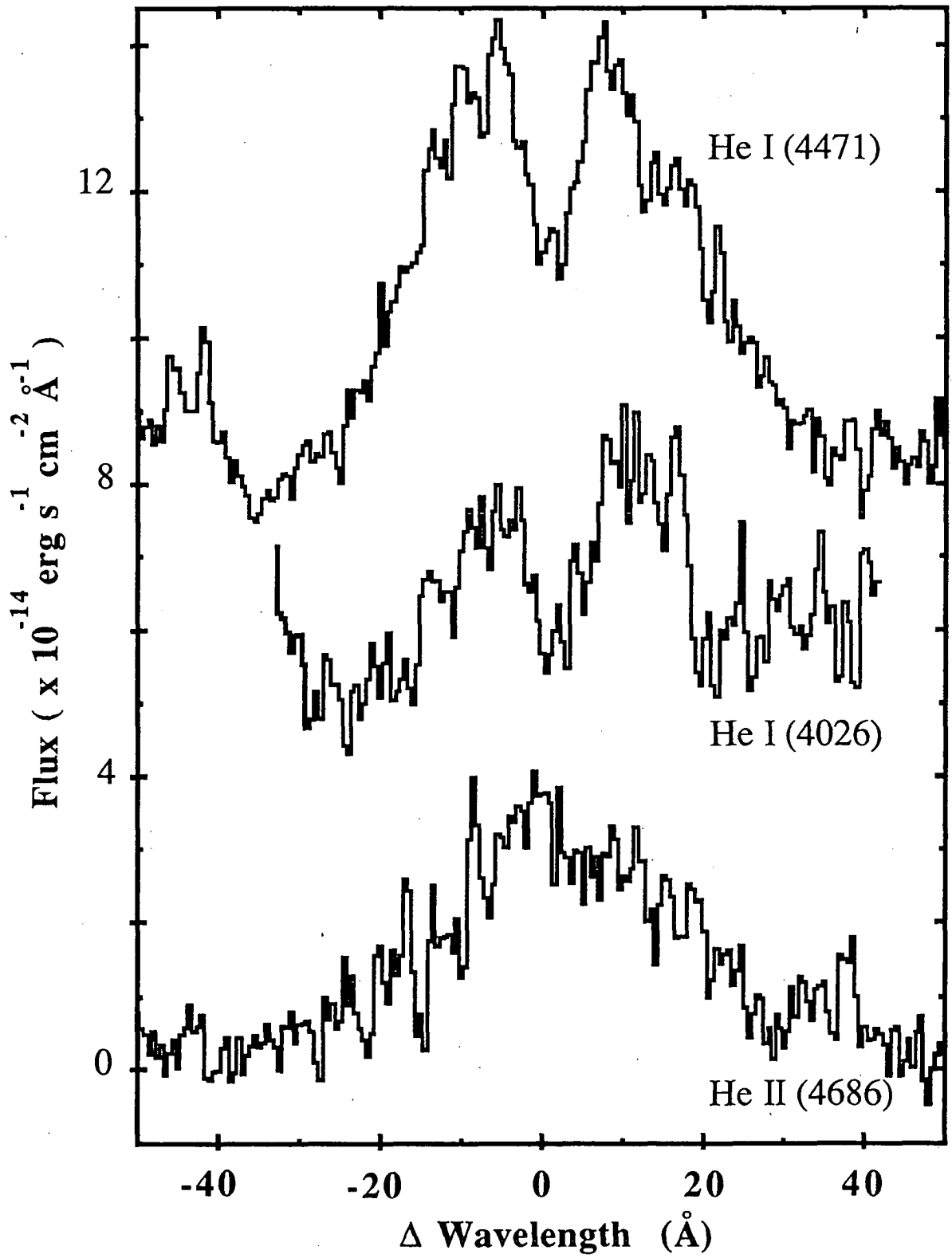

Figure 4.15
Details of the wavelength structure of the helium lines He I λ4471 Å, λ4026 Å and He II λ4686 Å for the spectral run beginning at JD 2446848.226. The zero point on the horizontal axis is the nominal rest wavelength of the line. The zero point on the vertical axis is the continuum flux level near He II λ4686 Å. The He I lines have been shifted vertically for clarity.

The He I λ 4026 Å line is blended in the wings of H_δ and H_ε, so the velocity structure in its wings is not discernible. It is also worth noting that the high velocity emission extremes of He II λ 4686 Å are similar to those of the Balmer lines, even though the low velocity structure is clearly quite different.

The large data set of Hellier et al. (1987) has enabled these authors to determine the properties of three components in the emission lines. These are: (i) the double–peaked component of constant flux coming from the disk; (ii) the single–peaked S–wave component seen in the H I and He I lines, whose radial velocity varies with an amplitude of ~600 km s^{-1} on Φ_{98}, and which is identified with enhanced emission where the gas stream from the secondary interacts with the disk; (iii) the 67 min modulated emission, which contributes about one third of the phase–averaged Balmer line fluxes and is very broad, presumably originating in the high–velocity accretion region close to the white dwarf primary. The 67 min modulated source produces the observed Φ_{67} dependence of emission line equivalent widths and the weaker Φ_{67} modulation of the ratio of violet to red (V/R) line strengths in the far wings of the Balmer lines, as documented by Hellier et al. Both the equivalent width dependence and this V/R modulation with Φ_{67} have their maxima at $\Phi_{67} \approx 0$. In the V/R case, this implies accretion flow of the line–emitting region is mainly directed towards the observer at this phase, though not in a highly collimated fashion. The V/R ratio for the complete Balmer lines is however dependent on Φ_{98} because of the S–wave emission. We see the violet peak higher from the beginning of the data run at $\Phi_{98} \approx 0.6$ to $\Phi_{98} \approx 0.9$. The red peak then becomes higher until the end of the data run at $\Phi_{98} \approx 0.2$. This is in agreement with the results of other workers (Breysacher and Vogt, 1980; Cowley et al. 1981; Gilliland, 1982; Hellier et al., 1987). Kaitchuck et al. (1987) also report that emission line widths vary with Φ_{67}, having a maximum width near $\Phi_{67} \approx 0$. This variation is clear in the present data run, as can be seen in Figure 4.13.1 (b) and (c).

Table 4.5 gives the observed Heliocentric Julian Date for the mid–eclipse and 67 min maximum of the 21st February 1987 data run, as was displayed in Figure 4.12. The data have been corrected to Ephemeris Time. Cycle numbers and (O–C) residuals are also given. For the eclipse, these are based on the ephemeris of Mumford (1967), and for the 67 min variation they are based on the most recent quadratic ephemeris of Bond and Freeth (1988).

Table 4.5

Observed Heliocentric Ephemeris Times

	HJD (2446848+)	E	(O–C) (x .0001 d)
67 min max.	0.2501	196543	–9
Mid–eclipse	0.2573	134073	–5

4.4.3 Spectra through Eclipse

The eclipse phenomenon in EX Hya can be studied with a view to probing the geometry of the accretion flow around the white dwarf primary. The eclipse of the optical and hard X–ray flux in EX Hya is quite sharp. However, there is also a much broader *eclipse effect* detectable in the emission line V/R ratio for a range $\Delta\Phi_{98} \approx \pm 0.15$ either side of the sharp eclipse in the broadband flux. This latter effect was first commented on by Cowley et al. (1981), and more clearly demonstrated by Hellier et al. (1987). The effect involves a reduction of V/R relative to the general trend for phases prior to eclipse, as the secondary obscures the approaching half of the disk flow. After $\Phi_{98} = 0$ the receding half of the disk flow is then obscured, and the V/R level rises above the general trend for a certain time. Similar effects have been seen in DQ Her (Young and Schneider, 1980), HT Cas (Young et al., 1981) and Z Cha (Marsh et al., 1987) and have been attributed to the accretion disk in these systems.

An indication of this broad eclipse effect can be readily seen in the 21st February 1987 data, even though only a single data run is involved. This is shown in Figure 4.16 where the average V/R ratio for the Balmer lines H_β, H_γ and H_δ has been plotted as a function of the 30 s spectrum number for the data run. Here the V/R ratio for each spectral line was determined by dividing the line at a wavelength which was taken as the rest wavelength, appropriately corrected for the gamma velocity ($\gamma = -180$ km s^{-1}) and the orbital velocity ($K_1 = 70$ km s^{-1}) determined by Hellier et al. (1987), and then calculating the fluxes in the violet and red halves separately before taking the ratio of these values. The data have been summed into 10x30 s = 300 s bins to reduce the noise in Figure 4.16. Clearly, the histogram in Figure 4.16 shows a generally decreasing trend over the length of the data run. This is to be expected because of the V/R dependence on Φ_{98} documented by Hellier et al. (1987). Their sinusoidal fit to V/R has a maximum value at $\Phi_{98} \sim 0.6$. Since the data run begins at $\Phi_{98} \sim 0.6$ and

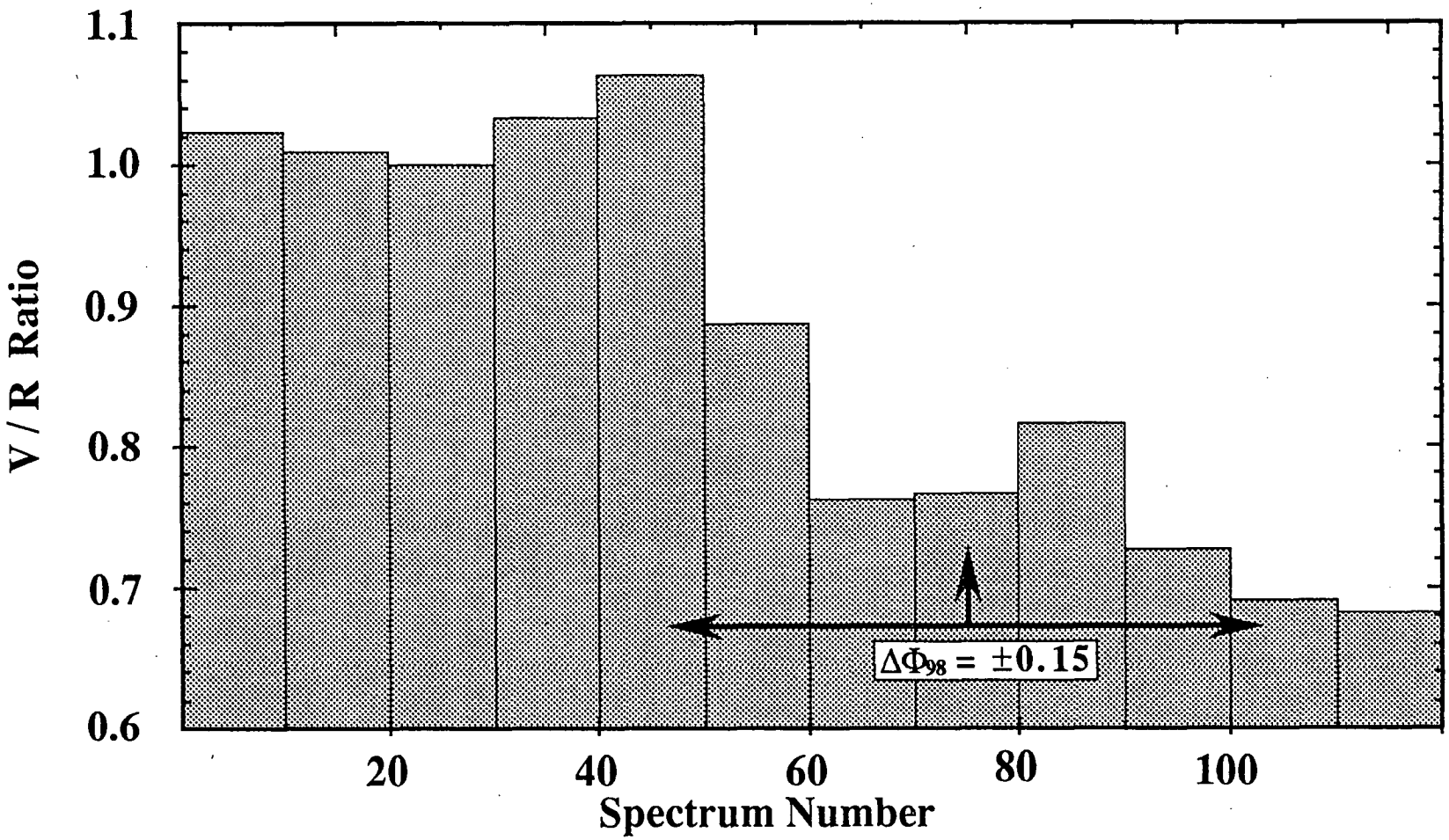

Figure 4.16
The average V/R ratio for the Balmer lines H_β, H_γ and H_δ as a function of 30 s spectrum number for the spectral run beginning JD 2446848.226. The V/R ratio is determined as discussed in the text, and the 30 s spectra have been summed into 10x30 s = 300 s bins to reduce the noise. The mid-eclipse location is marked with an arrow.

ends at $\Phi_{98} \sim 0.2$ a decreasing trend for V/R over the whole of the data run is predicted. The indication of the eclipse effect in Figure 4.16 is the interruption of this decreasing trend by a broad dip preceding the eclipse, and a slight relative enhancement following it. The general shape of the V/R plot here is consistent with the better determined results of the larger Hellier et al. (1987) data set.

The details of the spectral changes occurring through the sharp eclipse in the 21st February 1987 data are shown in Figure 4.17, as a function of 30 s spectrum number, for the block of 30 spectra centred on the eclipse. In panel (a) of this figure, the shape of the eclipse in the continuum flux is shown. For this plot, a smooth continuum was fitted to each 30 s spectrum and this was then integrated over the wavelength range $\lambda\lambda$ 3950 – 4900 Å. The shape of the eclipse in panel (a) is similar to that for the eclipse of total flux in Figure 4.12. In the latter, a Gaussian fit with a FWHM value of 2.8±0.3 min is applicable. This compares with a FWHM of 2.6±0.3 min noted by Rosen et al. (1988) from the optical data of Warner and McGraw (1981), and a similar value noted by Beuermann and Osborne (1988) from their own data. Thus the eclipse observed here appears typical in its duration.

In panel (b) of Figure 4.17 the sum of the equivalent widths of the Balmer lines H_β, H_γ and H_δ is shown through the eclipse. Clearly a sharp peak in equivalent width occurs at the time of eclipse, as was also noted by Hellier et al. (1987) in their data. The smooth curve in panel (b) is a Gaussian fit on top of a quadratic background fit. The equivalent width background is decreasing with time in the vicinity of the eclipse as the 67 min flux modulation is passing from maximum to minimum. The Gaussian fit has a FWHM of 1.9±0.3 min. It is worth noting that this is comparable to the 1.8±0.4 min FWHM of X–ray eclipses reported by Rosen et al. (1988) who suggest that the hard X–ray eclipse may be narrower than the corresponding feature in the optical band. Beuermann and Osborne (1988) find similarly shorter (1.8 to 2.2 min) FWHM values in the Gaussian fits to their hard X– ray data, but are equivocal about this implying an event shorter than the optical eclipse because of the non–Gaussian shape of their X–ray eclipses. In summary, therefore, it can be concluded that the equivalent width peak in the Balmer lines is similar in duration to the X–ray eclipses, and these both may be somewhat shorter in duration than the optical eclipses.

The existence of an equivalent width peak in Figure 4.17(b) implies that the eclipsed structure, at least in its inner confines, has a region of relatively stronger optical continuum emission vis–a–vis the Balmer line emission, than do the other emission sources. The height of the Gaussian fit in this figure is 50±7 Å. This compares with

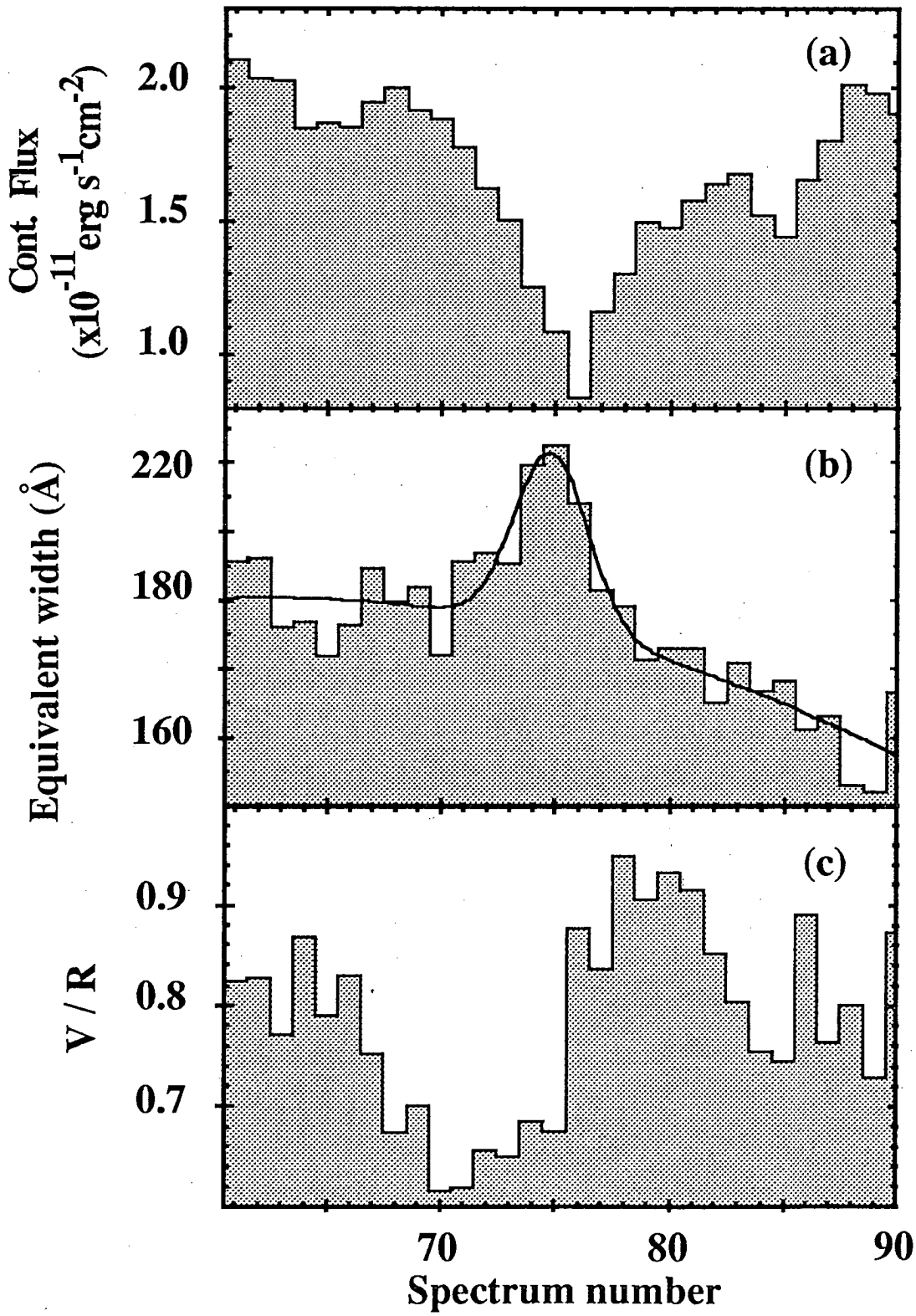

Figure 4.17
Details of the changes occuring through the EX Hya eclipse which was observed during the spectral run that began at JD 2446848.226. Panel (a) gives the integrated flux changes ($\lambda\lambda$ 3590-4900 Å) under the continuum. Panel (b) gives the sum of the equivalent widths of H_β, H_γ and H_δ. Panel (c) gives the average V/R values for the same three lines. The horizontal axis is the 30 s spectrum number.

the 20Å peak reported by Hellier et al. (1987) for H_β alone. Thus a fractional increase of 30 percent in equivalent width at mid–eclipse is seen in both studies. Also the eclipse depth here is close to the average eclipse depth in the Hellier et al. data. The depth of the Gaussian fitted to the total flux eclipse in Figure 4.12 is ~0.55 mag. The average B–band eclipse depth shown in Figure 5 of Hellier et al. is ~0.5 mag. Using either the Hellier et al. data or the present data one can infer the flux change in the Balmer lines and in the continuum emission at mid–eclipse. The inferred drop in the Balmer line fluxes is 20 to 25 percent, compared to the much larger inferred drop in continuum fluxes of between 40 to 45 percent in average eclipse conditions.

Figure 4.17(c) gives the average V/R value for the Balmer lines H_β, H_γ and H_δ for the block of 30 spectra surrounding mid–eclipse. The time of the rapid reversal in V/R, as with the time of the equivalent width peak in Figure 4.17(b), agrees with the mid–eclipse time to within one 30 s spectrum bin. Except for a vertical axis offset, the shape of the V/R plot here is very similar to the plot of comparable data by Hellier et al. for H_β alone. These authors satisfactorily fit a model of a Keplerian disk to their V/R data.

It would be desirable to examine a plot analogous to Figure 4.17 for the He I and He II lines as well as the Balmer lines. For He I λ4471 Å there is a suggestion of an equivalent width peak similar to that in Figure 4.17(b), but for He II the statistics are too poor for any conclusions to be drawn.

4.5 The Accretion Curtain Model of EX Hydrae

From Hellier et al. (1987), Rosen et al. (1988), and the preceding discussion in this study, the most important observational constraints which have to be considered when developing a model of the accretion geometry and of the eclipsed structure in EX Hya may be summarized as follows:

(i) The quasi–sinusoidal X–ray modulation at 67 min is in phase with the 67 min optical modulation and has an amplitude which decreases strongly with increasing X–ray energy. It is not detected significantly above 6 keV.

(ii) The partial X–ray eclipses, which are in phase with the optical eclipses, have a depth which increases with increasing X–ray energy, at least up to 6 keV. The eclipses are not visible below about 2 keV, and show a gradual ingress and egress.

(iii) Both X–ray and optical eclipse depths are dependent on Φ_{67}, being deepest at $\Phi_{67} \sim 0$.

(iv) Optical emission line flux varies in phase with, but more strongly than, the 67 min optical continuum modulation. Hence equivalent widths vary with Φ_{67} and have maximum values at $\Phi_{67} \sim 0$. The line widths similarly vary with Φ_{67}.

(v) The far wings of the Balmer lines have a V/R ratio which modulates weakly with Φ_{67} and has a maximum value at $\Phi_{67} \sim 0$.

(vi) There is some eclipse of the Balmer emission line fluxes but this is considerably smaller than the eclipse of the optical continuum flux.

(vii) Mid–eclipse times modulate with Φ_{67}, implying the majority of the eclipsed optical flux orbitally–precedes the primary at $\Phi_{67} = 0.75$, moving to the near side at $\Phi_{67} = 0$ and then to the orbitally–trailing side at $\Phi_{67} = 0.25$.

Recent accretion models which have been proposed for EX Hya are the 'accretion curtain' and the hybrid 'absorption/occultation' models, both considered by Rosen et al.(1988), and the AM Her configuration proposed by Heise et al. (1987). The absorption/occultation variant, which requires an X–ray contribution from both poles, has difficulties explaining the observed Φ_{67} dependence of eclipse depth [point (iii)]. The AM Her variant encounters difficulties with the strong evidence for the existence of an accretion disk, in terms of observed line–doubling and the V/R eclipse effect noted in Section 4.4.3. Hence here the discussion is limited to the accretion curtain variant, which appears to fit quite comfortably with points (i) to (vii), at least in a qualitative sense.

The accretion curtain model envisages the disruption of the accretion disk at perhaps 10 R_{wd} above the surface of the white dwarf primary (Hellier et al., 1987). Accretion occurs on a circular arc near each magnetic pole, but its rate varies with azimuthal angle around the pole and is greatest from the side of the disk towards which the pole is currently pointed. This is shown schematically in Figure 4.18. For the inferred mass accretion rate of EX Hya, the X–ray emitting regions extend about 1 R_{wd} above the surface of the white dwarf (Rosen et al., 1988). If $i \sim 78°$, as deduced by Hellier et al., then the inner hole of the disk is sufficiently wide to allow the possibility that the X–ray emitting regions above both poles are visible.

The component of optical emission associated with the 67 min modulation is assumed to originate in the accretion curtain, but presumably over a more extended region than does the X–ray emission. Beuermann and Osborne (1988) point out that heating of the accretion curtain, in its optically thick sections, occurs preferentially on its concave interior side ④. The heating is due to absorption of low–energy photons from the X–ray emitting regions ①. This is shown schematically in Figure 4.18, where it is also clear that the best aspect to view this enhanced optical emission is when the observer is looking at the inner side of the accretion curtain leading below the orbital plane towards the lower pole at the instant that this pole is on the near side of the white dwarf. It is reasonable to assume that this configuration corresponds to the optical 67 min maximum, as indicated in Figure 4.18, provided the inner hole of the disk is sufficiently wide to permit this enhanced optical emission to be seen. It will be argued, in a subsequent paragraph, that this is indeed the case.

The 67 min X–ray modulation is envisaged to occur in the Figure 4.18 accretion curtain model as follows. When the upper pole faces away from the observer, both X–ray emitting regions are seen through the lowest density of the accretion curtain ③, as is clear in Figure 4.18. This corresponds to the maximum in the X–ray flux. Because of the height of the X–ray emitting regions, occultation by the white dwarf surface has only a minimal effect in this configuration. Conversely, when the upper pole points towards the observer, the line of sight from both X–ray emitting regions passes through the highest density regions of the accretion curtain ②, giving the minimum X– ray flux. At this juncture, any significant occultation of the lower X–ray emitting region by the white dwarf surface will act to decrease the X–ray flux further. The energy dependence of the X–ray modulation [point (i)] follows naturally from the increasing cross–section of the photo–electric absorption process with the decreasing energy of the X–rays. Thus the quasi–sinusoidal X–ray modulation at 67 min is mostly a reflection of the varying density of the accretion curtain along the line of sight as the white dwarf rotation proceeds.

The 67 min optical modulation experiences a similar contributing effect from the varying density of the accretion curtain. At X–ray maximum the lower pole is nearest to the observer, which is also the configuration that is expected to correspond to optical maximum, so that X–ray and optical modulations will be in phase [point (i)]. In this configuration the enhanced optical emission on the inner side of the accretion curtain leading to the lower pole is seen through the lowest density of that accretion curtain material which is heading towards the upper pole. Similarly, any emission from the high density accretion region leading to the upper pole, which is then on the far

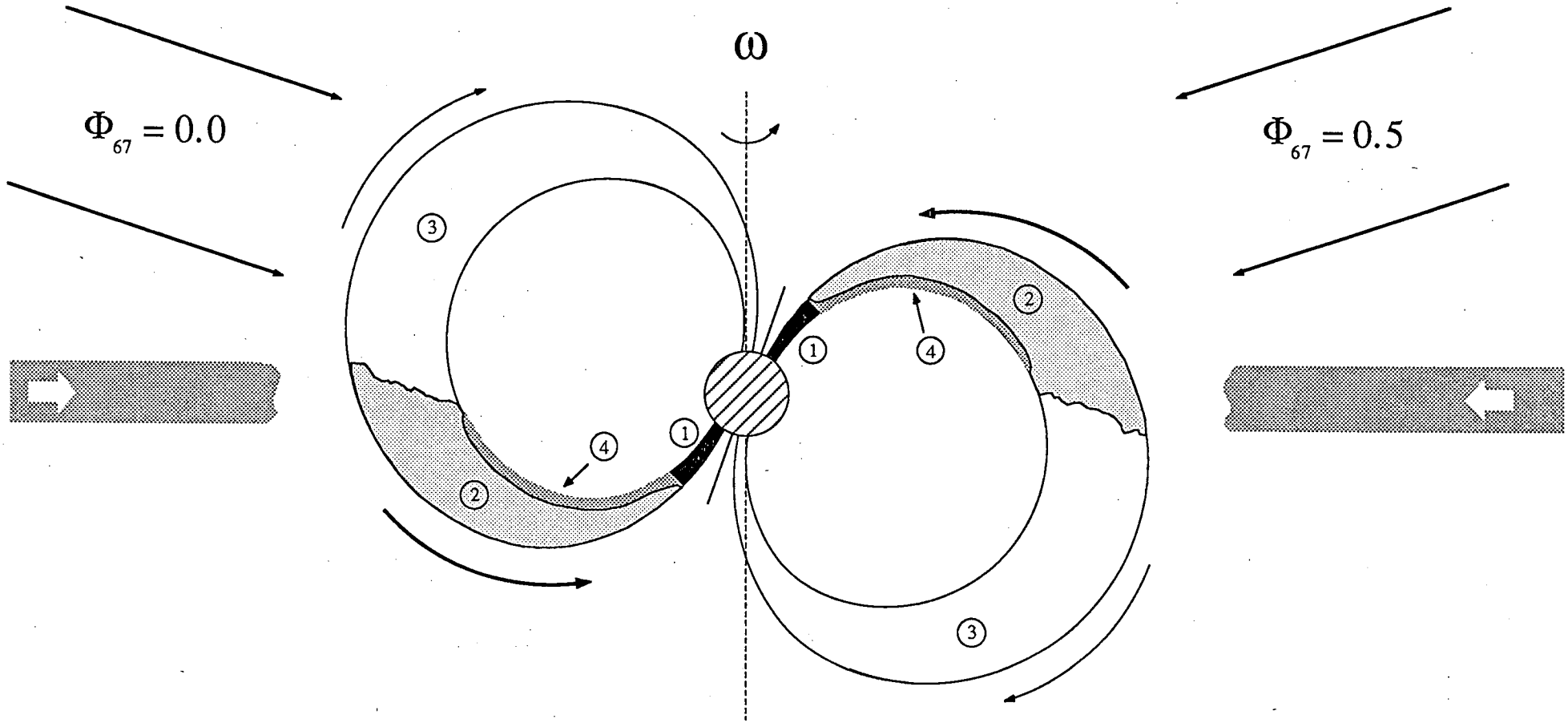

Figure 4.18
A schematic of the region around the white dwarf primary in EX Hya, assuming the accretion curtain model. The observer's view at $\Phi_{67} = 0$ and 0.5 is indicated with arrows. The highest accretion flow occurs from those sections of the disrupted disk which are closest to the magnetic poles at any instant. X-ray heating of the accretion flow occurs preferentially on the concave interior side. The dimensions of the X-ray emitting regions are ~ 1 R_{WD}. The disk is disrupted at ~ 10 R_{WD} above the surface of the primary.

side from the observer, only has to penetrate a region of low density in the accretion curtain. Conversely, when the configuration labelled $\Phi_{67} = 0.5$ in Figure 4.18 applies, the region of enhanced emission on the inner side of the accretion curtain leading to the upper pole is hidden from the observer. At the same time, the corresponding emission from the accretion curtain leading to the lower pole has to penetrate the highest density part of the accretion curtain leading to the upper pole. Thus this configuration will give the minimum optical flux. In the accretion curtain model it would also not be at all surprising if the 67 min modulation of the optical emission line fluxes was greater than that of the optical continuum [point (iv)] because of the larger optical depth of the accretion curtain in the lines. As well, an observed line width maximum at $\Phi_{98} \sim 0$ [point (iv)] is plausible if the inclination of the magnetic axis to the rotation axis is such that the regions of optical emission are travelling more nearly along the line of sight to the observer in the $\Phi_{67} = 0$ configuration than in the $\Phi_{98} = 0.5$ configuration.

To explain the observed partial X–ray eclipses [point (ii)], two possible eclipse geometries are envisaged by Rosen et al. (1988). These are as follows:

(a) The observed X–ray emission comes principally from the upper pole and the eclipse occults part of the tall emission column above this upper pole.

(b) Both poles contribute significantly to the observed X–ray emission and the eclipse occults the X–ray emission from the lower pole only. The X–ray emission region of the upper pole escapes the eclipse altogether.

Beuermann and Osborne (1988) suggest that the observed central depths in the X–ray eclipses may be more readily accommodated in case (b). One can also argue in favour of case (b) on general grounds based on the properties of the optical eclipses. This argument may be developed in the following manner. If it is reasonable to assume that the optical emission in the accretion curtain arises from a region which is more extended radially above the white dwarf surface than is the region of X–ray emission, then both case (a) and case (b) eclipse geometries leave the region of optical emission above the upper pole largely unocculted by the secondary at eclipse. Hence it can be concluded that the observed optical eclipses are occultations of the emission in the accretion curtain leading to the lower pole only. Thus the optical emission region leading to the lower pole is not totally obscured by disk material. By implication, the X–ray emission from the lower pole, which is closer to the white dwarf, is also unlikely to be heavily obscured by the disk, favouring a case (b) eclipse geometry.

A further consequence of the region of optical emission above the upper pole being largely unocculted at eclipse may be deduced as follows. The depth of the optical eclipses is dependent on Φ_{67} [point (iii)], reaching mid–eclipse fluxes which are just below the minimum flux of the 67 min modulation, and which are approximately independent of the 67 min phase. Hence it can be inferred that the optical emission in the upper polar region is very little modulated with Φ_{67} and essentially all the 67 min optical modulation arises from the emission leading to the lower pole. A substantial non–modulated optical flux is of course still permitted from the emission region leading to the upper pole. This deduction concerning the upper pole optical emission is at least qualitatively plausible in terms of the Figure 4.18 model.

The identification of the eclipsed optical structure with the emission region leading to the lower pole is consistent with the location of the eclipsed optical flux inferred from the Section 4.3.5 discussion of eclipse timings [point (vii)]. From Figure 4.18 it can be seen that the optical emission region leading to the lower pole is indeed on the near side to the observer at $\Phi_{67} = 0$, and will give earlier eclipses at $\Phi_{67} = 0.75$ and later eclipses at $\Phi_{67} = 0.25$. A back and forth shift of $\sim\pm$10,000 km perpendicular to the line of sight and parallel to the orbital plane, as noted in Section 4.3.5, is plausible in terms of Figure 4.18 provided the magnetic dipole axis of the white dwarf is not highly inclined to the rotation axis. The constraint here is that the radius of a white dwarf with a mass ~0.8 M$\odot$, as deduced for EX Hya by Hellier et al. (1987), is R_{wd}~7000 km. Since the height of the stand–off shock marking the beginning of the X–ray emitting region probably has a similar value, the optical emission region is likely to be most significant at radial distances $\lesssim$14000 km from the white dwarf centre.

The fact that V/R for the far wings of the Balmer lines implies that the motion of the high–velocity line–emitting regions is mainly directed towards the observer at $\Phi_{67} = 0$ [point (v)] is not necessarily in conflict with the deduced importance of the optical emission region leading to the lower pole in Figure 4.18. Two factors must be considered in this regard. Firstly, it is to be recalled that a substantial non–modulated flux is still permitted from the optical emission region leading to the upper pole. It is this region which is the presumed source of the V component of the far wing emission at $\Phi_{67} = 0$. Secondly, at $\Phi_{67} = 0$ the hotter concave interior of the emission flow leading to the lower pole is visible. This will have weaker Balmer line fluxes per unit continuum flux than any emission arising from the cooler outer side of the emission flow which leads to the upper pole. Thus this assists in increasing V/R at $\Phi_{67} = 0$. A lower relative strength of Balmer line flux to optical continuum flux in the flow to the lower pole also qualitatively fits with observed eclipse properties [point (vi)]. I would

also expect that the He II flux would be substantially occulted at mid–eclipse, though some may remain from the unocculted region above the upper pole. However, the statistics in this data set are not adequate to resolve this matter.

The energy dependence of the depth of the partial X–ray eclipses [point (ii)] is attributable, in a case (b) eclipse geometry, to the photo–electric absorption process in the accretion curtain. Rosen et al. (1988) point out that higher energy X–rays are less absorbed, so the X–ray emission region near the lower pole produces deeper eclipses at these energies when it is occulted. The extended nature of the X–ray emitting columns (~1 R_{wd}) ensures that the X–ray eclipses are not instantaneous, but have a gradual ingress and egress [point (ii)]. The Φ_{67} dependence of the partial X–ray eclipse depth [point (iii)] can be qualitatively understood in case (b) eclipse geometry, according to Rosen et al., if the lower pole contributes proportionally more than the upper pole to the total X–ray flux at 67 min maximum than at 67 min minimum. Provided this is the case, all of points (i) to (vii) have been qualitatively accommodated by the accretion curtain model. In addition, it is not unreasonable to expect that this model might give shorter X–ray eclipses than optical eclipses at all Φ_{67}, as noted in Section 4.4.3, particularly if the magnetic axis of the white dwarf is not highly inclined to its rotation axis. Finally, a note of caution should be sounded in relation to the mid–eclipse X–ray fluxes. These, like the mid–eclipse optical fluxes, are reported to be approximately independent of 67 min phase. However, unlike the optical case, Figure 4.18 would suggest that the X–ray flux from an unocculted upper pole, as one has in case (b) eclipse geometry, might be significantly modulated with Φ_{67}.

4.5 Conclusion

The photo–electric observations of EX Hya continue to show a secular decrease in the period of the 67 min modulation, with $P/\dot{P} = -3.8 \times 10^6$ yr, consistent with a white dwarf primary. The observed rate of change of period implies a mass transfer rate of the order of $\sim 3 \times 10^{-11}$ $M_\odot$ yr^{-1} and a magnetic moment around 8×10^{31} G cm^3. Eclipse timings identify a long term variation, on a time–scale of ~20 yr, which is consistent with solar–type cycles in the secondary star, and short term variations, correlated with Φ_{67}, which may be interpreted in terms of an eclipse of an accretion column or arc in the region above the magnetic pole of the white dwarf.

A short spectroscopic run on 21st July 1986, which preceded an outburst of EX Hya by a little over 1 day, shows enhanced flux in the blue region of the spectrum. This enhancement was not present in a spectrum during the eclipse in the same run. There is

no direct evidence to relate this feature to the outburst. However, a second spectroscopic run did not show a decrease in the blue flux during eclipse.The latter run, on the 21st February 1987, gives high time resolution data which are consistent with the general spectral characteristic features found by other authors. The velocity structure of the Balmer and He I emission lines are seen to be very similar. The wings of the He II λ4686 emission line are similar in their structure to the Balmer and He I lines. However, the low velocity structure of the He II line is single peaked and quite different to that of the other emission lines. The V/R ratio, near orbital phase $\Phi_{98} = 0$, is consistent with the eclipse of an accretion disk. The Balmer lines at the time of the eclipse show a sharp peak in equivalent width. This feature is comparable in width to the X–ray eclipses, and is attributed to the inner region of the eclipsed structure where there is a stronger optical continuum emission and/or weaker Balmer line emission.

The photometric, spectroscopic, and X–ray data on EX Hya have been discussed in terms of an accretion curtain model. It appears that this model, in a qualitative sense at least, is consistent with these data. In this accretion curtain model, an accretion disk is formed but is disrupted by the magnetosphere of the white dwarf at ~10 R_{wd}. Unlike accretion in AM Her type systems, where the accreting matter is confined to tight columns, accretion in EX Hya may occur over a large range of longitudes around the magnetic poles. Further spectroscopic and photometric observations, especially during outburst† , will no doubt shed more light on the nature of this interesting object.

† Footnote: In a paper which arrived subsequent to the completion of this thesis, Hellier et al. (1989) have reported the results of photometric and spectroscopic studies of EX Hya during two recent outbursts.

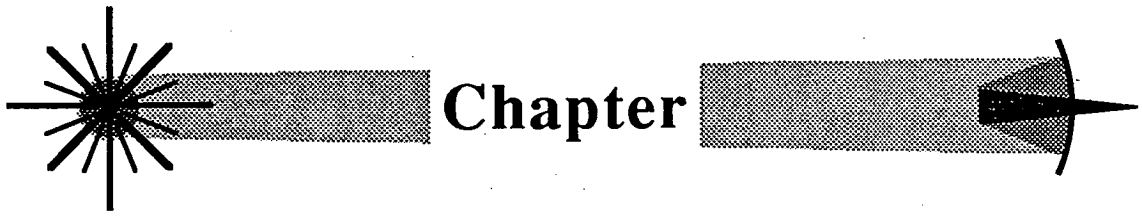

Chapter 5

ULTRA–HIGH SPEED PHOTOMETRY WITH THE MARK II SYSTEM

5.1 Introduction

This chapter covers a range of topics related to data acquired with the Mark II (ultra–high speed) photometer option. Section 5.2 covers testing of the system using periodic signals, and a brief discussion of the Fourier techniques used to search for any periodic structure in the data.

In an attempt to find a convenient periodic source in the sky, observations of the first two AUSSAT satellites were undertaken (Section 5.3). However, the satellites proved to be interesting sources in their own right, and the resulting observations and data analysis are discussed in Sections 5.3.1 and 5.3.2 respectively. The results of the analysis are interpreted in terms of the satellite design and the solar reflection geometry in Section 5.3.3. Since the satellites are above the Earth's equator they are eclipsed by the Earth's shadow during the passage of the equinox. In Section 5.3.4, the observations and results from one such eclipse are presented.

Perhaps the most famous source of rapid stellar pulsations is the Crab pulsar. It has become a standard test source for high–speed photometry and, even though it only just attains enough altitude to be seen at Mt Canopus, some data runs were acquired on it. These runs are discussed in Section 5.4. The initial impetus for upgrading the photometer system to its Mark II version came from the appearance of the supernova in the Large Magellanic Cloud, SN1987a. In Section 5.5, the observations on this object

are presented (Section 5.4.1), and their subsequent analysis (Section 5.4.2) have allowed an upper limit to any pulsed fraction of the light from the remnant to be calculated.

Finally, in Section 5.6, ultra–high speed photometry is considered in relation to stellar occultations, and the results of a grazing stellar occultation by Pluto, using the Mark II system, are presented. These observations indicate the presence of an extended atmosphere on Pluto, and are detailed in Section 5.6.2. A model of the Pluto atmosphere, based on the Mt Canopus data and developed by W.B. Hubbard and D.M. Hunten of the Lunar and Planetary Laboratory of the University of Arizona, is discussed in Section 5.6.3.

5.2 System Testing and Periodic Signal Analysis

The initial Mark II photometer data acquisition system discussed in Chapter 2.6 has undergone many minor upgrades since its implementation. After each upgrade it was necessary to test the system thoroughly to ensure that it was functioning correctly. This sub–section describes the methods used to test the acquisition hardware and software, as well as some of the period analysis software.

The first stage in testing the acquisition software and hardware was to replace the pulses from the photomultipliers with a periodic signal. To ensure that the periodic signal and sample timing were synchronised, a square–wave, derived from the frequency standard used for sample timing, was employed. Its frequency was chosen so that it would divide exactly into the sample frequency. For example, a 50 Hz signal could be fed into the counters and data acquired at 2.5 kHz. The acquisition program under test was then allowed to collect data for ~30 to 60 min. If all was working as it should, then the acquired data consisted of a periodic sequence of zero count samples followed by a sample containing one count. In the above example one would expect 49 samples containing zero counts followed a sample containing one count. The data file was then examined for any discrepancies. Generally each upgrade would be tested at a sample rate of 5 kHz and count frequencies of 50 Hz, 1 kHz, and 2.5 kHz.

After the acquisition system had passed this first stage of testing, the whole system was tested using a pulsing light emitting diode (LED) driven from a Rockland frequency generator. The Rockland has a high stability crystal reference with an oven controlled temperature. Its frequency stability, as a function of temperature, is $\pm 2 \times 10^{-10}$ parts per °C, and it has an ageing rate of 1 part in 10^9 per ay. The LED

frequency was chosen to be substantially less than the sampling frequency, so that the signal was well sampled. The LED itself was mounted in the offset guider eye–piece and relied on its light being scattered into the photomultiplier tubes. The amount of light entering the photomultiplier tubes could be controlled by the distance the LED was inserted into the offset guider eye-piece, a potential divider on the LED, or by changing the size of the aperture. Recently a more elaborate system has been installed. This consists of a LED mounted at the top of the telescope to the side of the secondary mirror, together with electronics for producing constant amplitude pulsations. In this new system, the light from the LED enters the photomultipliers after passing through all of the telescope optics, in a similar manner to star light. This particular system may also be used to make relative measurements of the telescope efficiency.

Data runs acquired using the LED were returned to the Physics Department for analysis. The department's computer system initially consisted of a VAX 750, but has recently been upgraded with the addition of a faster Micro–VAX 3500 with more memory than the VAX 750. The data runs were subject to three types of analysis: (i) a period search using a Fast Fourier Transform (FFT) program based on one given by Bergland and Doland (1979); (ii) a period search using Warner and Robinson's (1972) Q–method technique; (iii) a pulse profile study using the period obtained from the Q–method analysis in a superimposed–epoch folding program. The last of these three analyses can also be used to obtain an estimate of the limiting sensitivity of the system.

The results from one of the LED data runs are shown in Figure 5.1. For this run the telescope was also pointing at a bright star to increase the mean count rate to a level which was comparable with SN1987a, 200 to 300 hundred days after its eruption. The LED frequency was set at 81.729 Hz. The pulse width of the signal driving the LED was estimated, using a CRO, to be between 2 and 3 ms. The sample rate used for this run was 2.5 kHz. The plots in Figure 5.1 are derived from the analysis of a single 512K point data segment, consisting of approximately 209 s of data. The first and second harmonic of the periodicity are clearly seen in the 512K point FFT in Figure 5.1(a). The Q–method periodogram, for the same data, appears in Figure 5.1(b). The Q–method provides a better estimate of the frequency of the signal than the FFT, and that estimate was used to fold the data for the pulse profile in Figure 5.1(c). The peak frequency, obtained by fitting a Gaussian to it, is 81.728906±7 Hz. This value of frequency was used, in preference to the nominal 81.729 Hz, when folding the data, since it will account for any frequency offset between the Rockland and the frequency standard used for sample timing. In this example the nominal and fitted values are in good agreement. The pulse width from Figure 5.1(c), of between 6 and 7

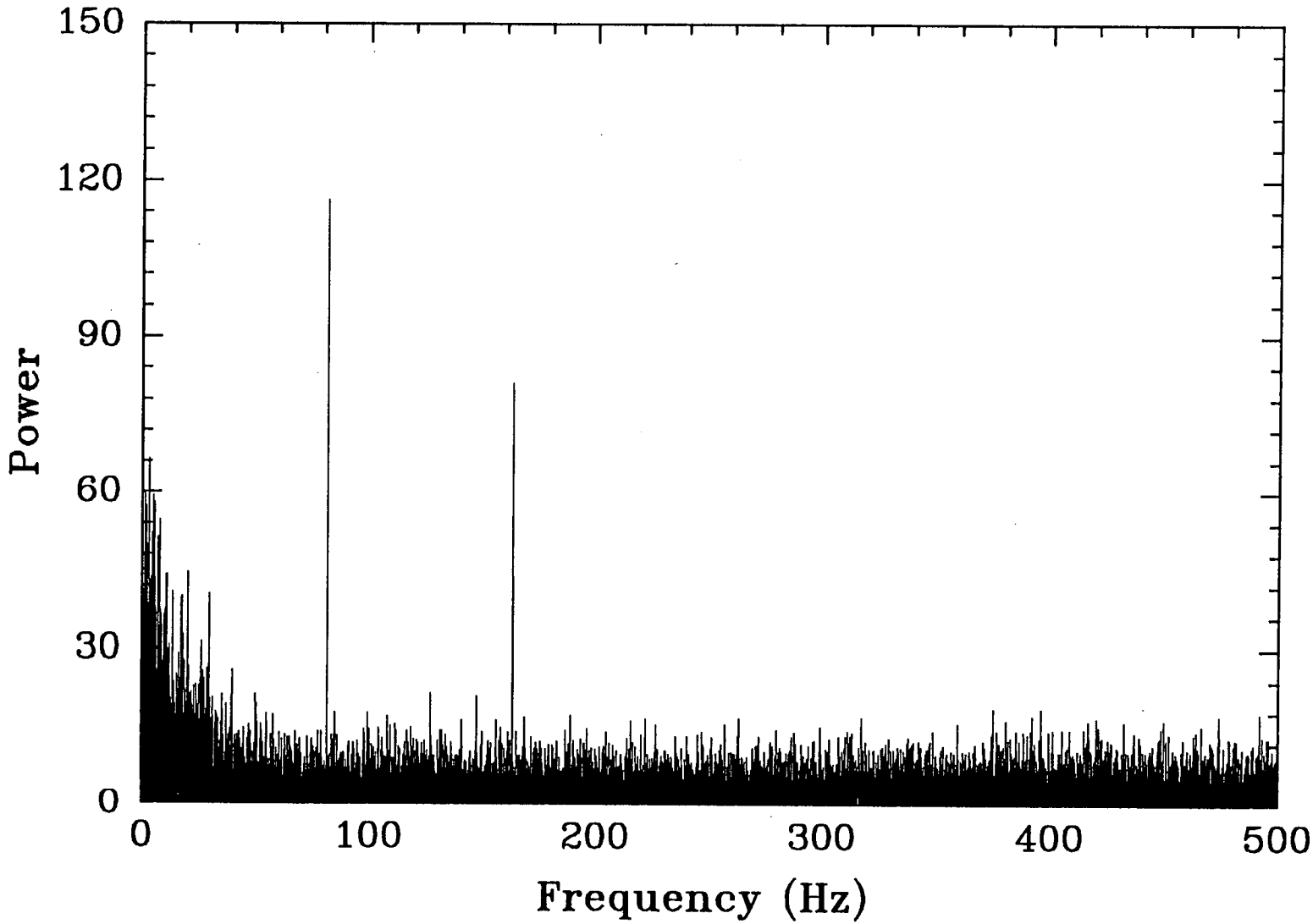

Figure 5.1 (a)

An example FFT obtained when using a pulsed LED test signal.

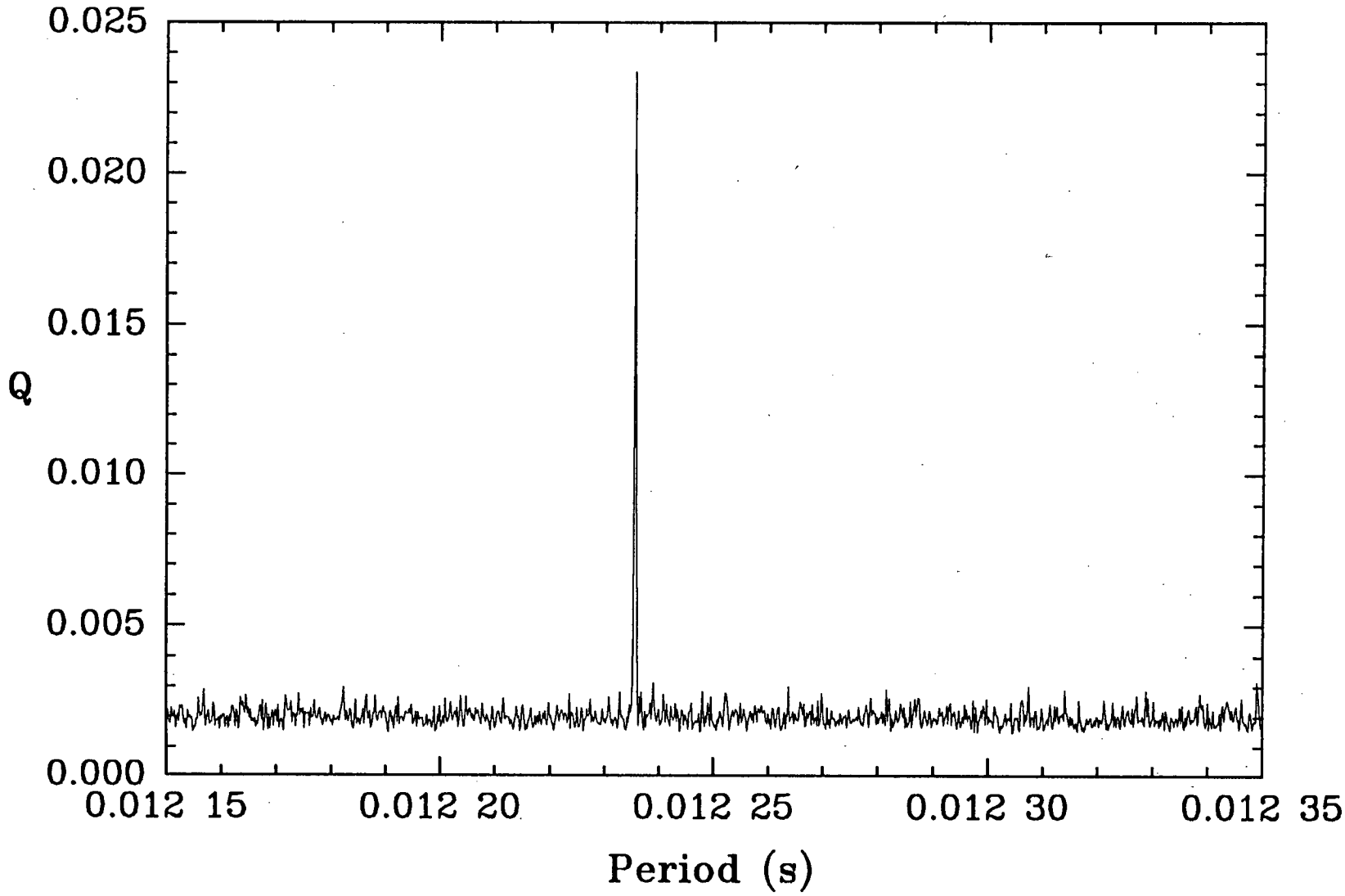

Figure 5.1 (b)

The Q-method periodogram for the same data set used to produce Figure 5.1 (a)

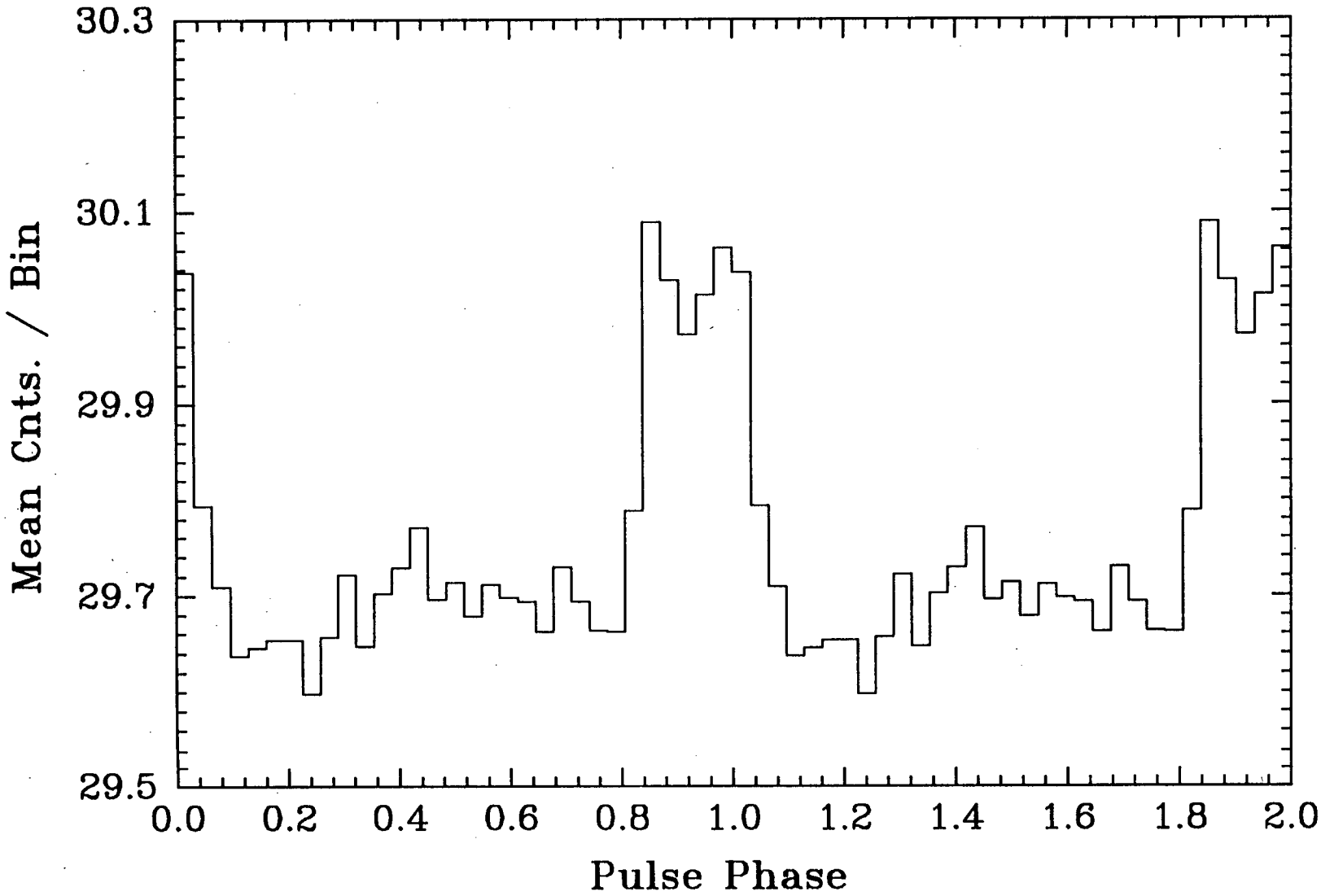

Figure 5.1 (c)
A light curve of the LED data phase-folded at the best Q-method period.

bins, corresponds to between 2.3 and 2.8 ms. This agrees well with the estimate from the CRO. The total pulsed flux in this run, estimated from the folded pulse profile, is ~0.2 percent of the mean unpulsed flux level. Results such as in Figure 5.1 imply that the system is working well.

At this juncture it is worth noting, without entering into too much detail, a few points, which are relevant to the observations presented in this chapter, concerning the analysis of the photometric data for periodic signals. The FFT method is probably the most efficient method for searching large data sets for faint periodic signals (van der Klis, 1988) . The problem is one of resolving a small signal above the spectral noise, which will be due mainly to counting statistics. Ideally, when looking for a monochromatic signal, one would take a single transform of the whole data set to obtain the largest signal–to–noise ratio. However, time and computer resources may make this impracticable, or the signal may not be monochromatic and hence a single transform will not obtain the best signal–to–noise ratio. In either case the data can be divided into segments, the FFT of each segment calculated and a mean FFT obtained. In calculating the mean FFT of K data segments each of N points, the variance, relative to one of the single FFT's, is reduced by a factor K. A further improvement can be gained by averaging the FFT's of overlapped data segments. In this procedure the data segments comprise points 1 to N, N/2 + 1 to 3N/2, N + 1 to 2N and so on, giving 2K–1 data segments. Since the overlapped data segments are not statistically independent, the variance is not reduced by a factor of 2K–1, but by a factor of ~9/11(2K–1) (Press et al., 1986). An example of the improvement obtained from using overlapped data segments is shown in Figure 5.2. This figure displays the distribution of powers in an average FFT obtained from overlapped and non–overlapped data segments. The non–overlapped distribution was obtained from 10 data segments of 64K points from the LED data used in Figure 5.1, and the non–overlapped distribution was calculated using 19 overlapped segments of the same data. The reduced scatter of the powers present in the resulting average FFT is clearly evident in this figure and would aid in the detection of any faint signal. This overlapped–data–segment technique was therefore employed in the relevant data analysis sections discussed in this chapter.

Following the Lewin et al. (1988) and van der Klis (1988) discussion of Fourier techniques in relation to photon counting data, power spectra evaluated in Sections 5.2, 5.4, and 5.5 have been normalised in the following way:

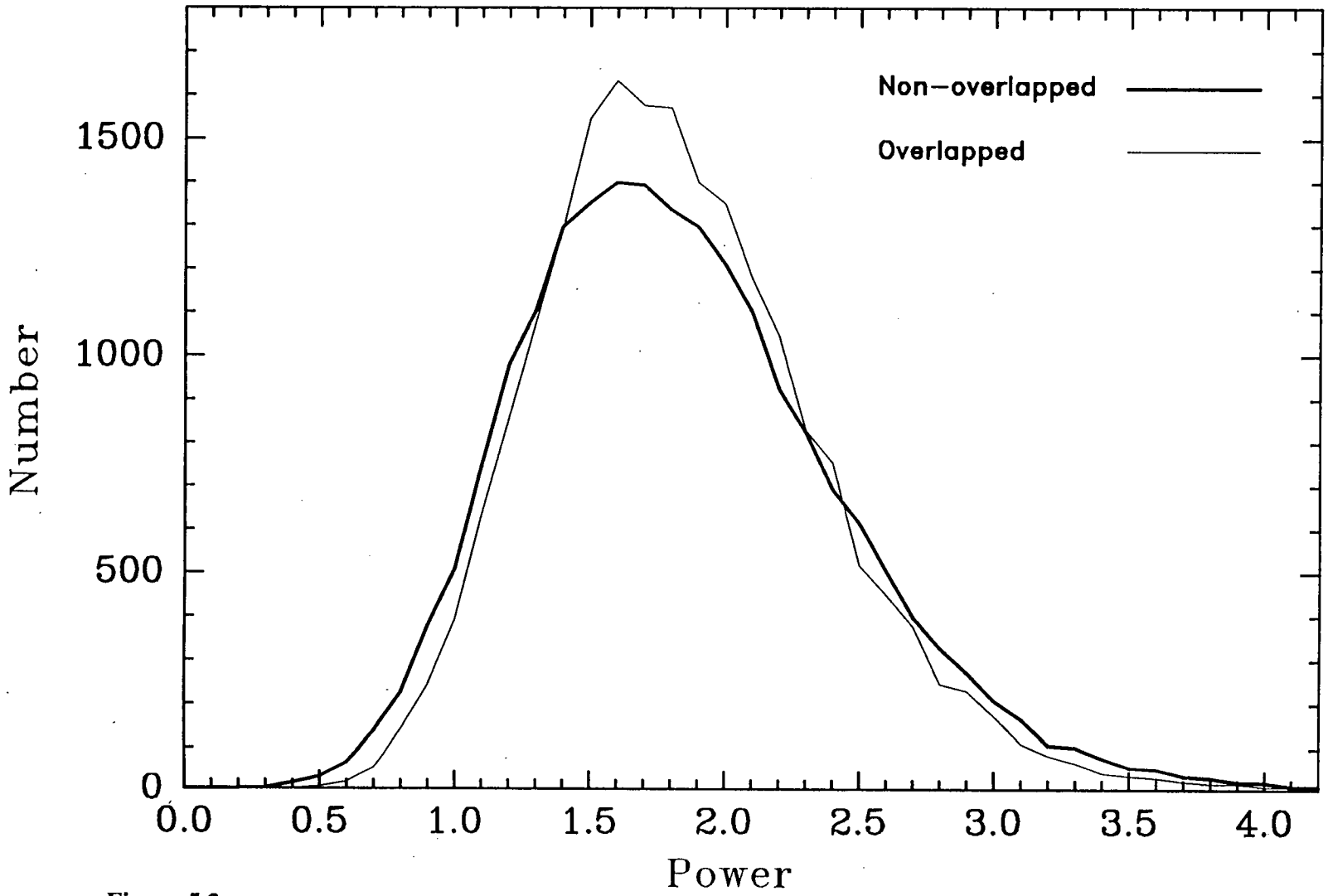

Figure 5.2
A comparison of the distributions of power in an average FFT for overlapped and non-overlapped data segments. Note the reduction in the number of high and low power values when using overlapped segments compared with the non-overlapped case.

$$P_j = \frac{2 \mid a_j \mid^2}{N_{ph}}, \qquad (5.1)$$

where the a_j are the complex Fourier amplitudes and N_{ph} is the total number of photons in the transform. With this normalisation, Poisson–distributed counts will result in a mean spectral power $<P_j,\text{noise}> = 2$. A sinusoidal signal, $X_k = A \sin(2\pi f_j t_k)$ with $t_k = \frac{kT}{n}$ (k=0 to n–1), of duration T, sampled at n consecutive bins of duration $\frac{T}{n}$, will cause a spike P_j at frequency f_j in the power spectrum, with

$$P_j = \frac{N^2 A^2}{2 N_{ph}}. \qquad (5.2)$$

Note that, in Figure 5.1, the mean power between ~400 Hz and ~1250 Hz, $\sim<P_j,\text{noise}>$, is ~1.89 and not 2 as predicted. This discrepancy can be at least partially explained by dead–time effects (Lewin et al., 1988) resulting from coincidences due to the high mean count rate present in this particular run. The Lewin et al. paper notes that the mean power will be depressed by a factor of $(1–\mu T_s)$, where μ is the observed mean count rate and T_s is the duration of a single event. More support for this line of argument is obtained from the observation that runs with lower mean count rates result in values of $<P_j,\text{noise}>$ much closer to 2. For the Figure 5.1 run $\mu \approx 7.5 \times 10^5$ c s^{-1} and T_s is ~350 nsec (Section 2.6.1), hence a value of $<P_j,\text{noise}>$ around 1.94 would be expected. This is still larger than the observed 1.89 value and could possibly indicate some other effect producing a non–Poisson count distribution at high count rates or some other dead–time effect requiring a larger value of T_s.

Another point to note is the effect on a peak in the FFT of a signal that has a frequency that is not exactly at one of the Fourier frequencies f_j. In this case the power at f_j, the nearest Fourier frequency, will be reduced in amplitude by a factor of $\left(\frac{\sin(\pi x)}{(\pi x)}\right)^2$, where x is the fractional difference between f_j and the true frequency of the signal, in units of the Fourier frequency. To illustrate this effect, consider a signal , P_s, whose frequency lies half way between f_j and f_{j+1}, corresponding to the case x=0.5. In this case the power from the signal will be distributed equally into the peaks at f_j and f_{j+1}, increasing them by $0.405 \times P_s$. In this example, either reducing or increasing the length of the FFT produces a larger peak in the power spectrum than would otherwise be the case. If the number of points in the FFT is reduced by a factor of 2, and hence x=0.25, then the power in the peak due to the signal will be $0.95 \times P_s$. If the number of points is

doubled, and hence x=0.0, then the power in the peak due to the signal will be P_S. So it is possible to get a larger peak, and hence a better signal–to–noise ratio, from a shorter length FFT, depending on the frequency of the signal. Hence it is worthwhile, in any effort to detect faint signals, to analyse the data with the longest convenient length length FFT, and then re–analyse with overlapped data segments of half the original size.

5.3 Observations of Geostationary Spin Stabilised Satellites

In addition to the tests described in Section 5.2,it was decided to investigate the possibility of using spin stabilised geostationary satellites to provide a more convenient and reliable calibration standard in the sky. It was also felt that such observations would make a good test for the difficulty expected in finding the earliest optical evidence for a pulsar in the SN1987a supernova remnant, as will be discussed in Section 5.5. It was decided to work with the first two Australian AUSSAT communication satellites. AUSSAT A1 was launched by STS 51–I on the 27th of August 1985 and AUSSAT A2 by STS 61–B on the 27th of November 1985. These two craft are examples of the Hughes HS376 design and, externally, are almost identical except for the despun antenna section. Their basic structure is illustrated in Figure 5.3. In the event, observations of the two AUSSAT satellites proved to be of more interest than simple test objects for the photometer system, and the observations yielded useful information on the satellites themselves.

5.3.1 Observations

The observations of the AUSSAT satellites were made on a number of nights during 1987 and a journal of the observations is given in Table 5.1.

Initially it was not certain how difficult it would be to locate the AUSSAT satellites. A short exposure plate had been taken by the UK Schmidt telescope, at the request of AUSSAT Pty., to cross–check the positions of A1 and A2 with positions derived from the main ground station antenna. This plate covered both objects and suggested $m_V \approx 13$, which is in rough agreement with the general comments of Taylor (1986). In Run 1 AUSSAT A1 was found, but a search for AUSSAT A2 failed to find it. In hindsight, the magnitude of A1 was between $m_V \approx 13.5$ and $m_V \approx 14$, which is at the limiting magnitude of the TV system on the finder telescope, and A2 may have been missed in a small raster scan search using the main telescope Cassegrain TV acquisition system. On subsequent occasions, with the exception of the specular

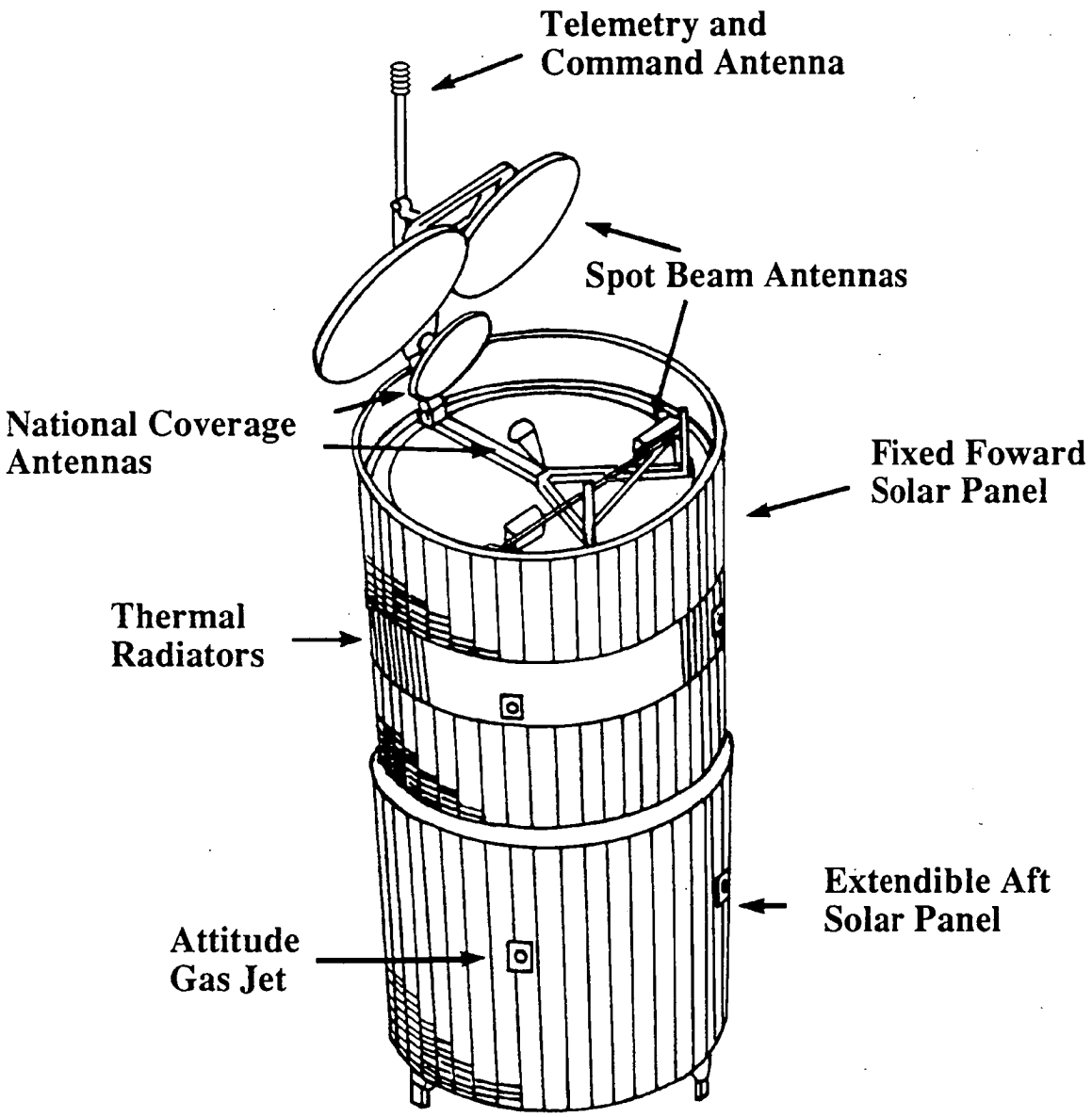

Figure 5.3
A schematic of the AUSSAT spacecraft with the aft section deployed. This is the standard Hughes HS376 model. In general the solar cells are placed in vertical strips and the individual rectangular cells are oriented with their long axis around the satellite circumference.

Table 5.1

Observation Log of AUSSAT A1 and A2 During 1987.

Run No.	Date	Offset (days)	State	AUSSAT	Comments
1	Feb 25	–37.35	OFF	A1	Located
2	Apr 04	–2.63	ON	A1	White light, 1ms, 15 min data run
			ON	A2	" " " "
3	Apr 24	+19.65	OFF	A1	UBVRI + White, 1ms, 10 min data runs
4	May 06	+31.65	OFF	A1	White, 1ms, 10 min data runs x 6
5	Jun 04		OFF	A1	Photographs taken
6	Sep 01	–4.85	ON	A1	White, 1ms, 10 min data run
			ON	A2	" " " "
7	Sep 04	–1.85	ON	A1	White, 1ms, eclipse, video
			ON	A2	" " " "
8	Sep 07	+1.15	ON	A1	Spot measurement due to clouds
9	Sep 08	+2.15	ON	A1	White, 1ms, 10 min data run, Video
			ON	A2	" " " "
10	Sep 13	+7.15	OFF	A1	Located, Cloud
11	Oct 29	+54.15	OFF	A1	Located
			OFF	A2	Located
			OFF	A3	Located

reflection periods, we found both satellites to be at a similar faint magnitude. After their initial location, the local hour angle and declination of both satellites was noted, and in later runs little effort was required to find them.

It is important to realise that, since the satellites are approximately stationary, the telescope tracking drive was switched off for the observations. The satellites do however move in a 2' to 3' long ellipse on the sky, with a period of 24 hours. The shape and orientation of this elipse changes throughout the year, and depends on the station keeping strategy adopted by the ground controllers. The effect is therefore predictable. Since this movement can amount to 15" to 20" per hour, continuous observations were restricted to ~10 min. For this type of operation clearly no offset guide stars can be used! For those who have done any observational astronomy it is a strange experience to see a stationary target object with the field stars continually drifting past. On the first attempt at using the fast photometer system to observe the two spacecraft (Run 2), they were surprisingly bright on the TV. An ~1.1 s spin modulation was visible on the real time display of counts from the photometer. In fact the spin modulation could also be seen directly as the image of the satellite pulsed in

comparison to stars that drifted passed on the TV screen. At the time of Run 2, the reason for the increase in brightness, which will be refered to as an *on* state, when compared with that in Run 1, was not clear. Further observations were prevented by a long period of bad weather and a full moon. On the next observing run (Run 3), three weeks later, A1 was in its original faint *off* state. Analysis of extended data sets of this run has revealed no detectable modulation in the *off* state. The original aim of having access in the sky to a permanent calibration source for the fast photometry system had not therefore been realised.

The observations of the satellites in 1987 clearly showed that the bright *on* states occurred near the equinox passages of the Sun. At around this time the alignment of the sun, satellite, and observatory are such that a direct reflection of the sun, from the satellite, is possible. In retrospect the specular reflection episodes are not surprising, since Taylor (1986) reports that some geosynchronous spacecraft have been seen to produce a naked eye flash prior to eclipse. Analysis of the data during the *on* states of the satellites will now be discussed.

5.3.2 Period Searches and Data Analysis of Specular Reflection Episodes

A section of the real time data, from the 4th of September 1987, binned into 5 ms bins, is presented in Figure 5.4 as an example. This shows about four and a half complete spin periods of AUSSAT A1 and illustrates the reason why the spin modulation was clearly visible on the TV image during the specular reflection episodes. Here the peak to peak amplitude is around 1.5 mag. The data were also subjected to a FFT analysis using the overlapping–data–segment technique described in Section 5.2. Figure 5.5 shows the mean 64K point FFT for ~9 min of continuous data obtained on AUSSAT A1, again on 4th of September. This span of data represents ~480 complete rotations of the satellite. The ~0.93 Hz rotation frequency, f_0, is detected but does not have the greatest amplitude. The largest amplitude occurs at $4f_0$ (at $2f_0$ on some other nights) which is not surprising in view of the phase folded light curve for the same data, which is shown in Figure 5.6. A phase folded light curve for a comparison star of similar brightness to AUSSAT A1 is also shown in this figure. The comparison star data are folded at the spin period of AUSSAT A1 and is offset to the sky background level for the AUSSAT data. Since the comparison star has no periodicities, its curve it is just subject to statistical variations and is therefore an indication of the noise level in the AUSSAT A1 light curve. The sharp 'flashes' and the slower large modulation in

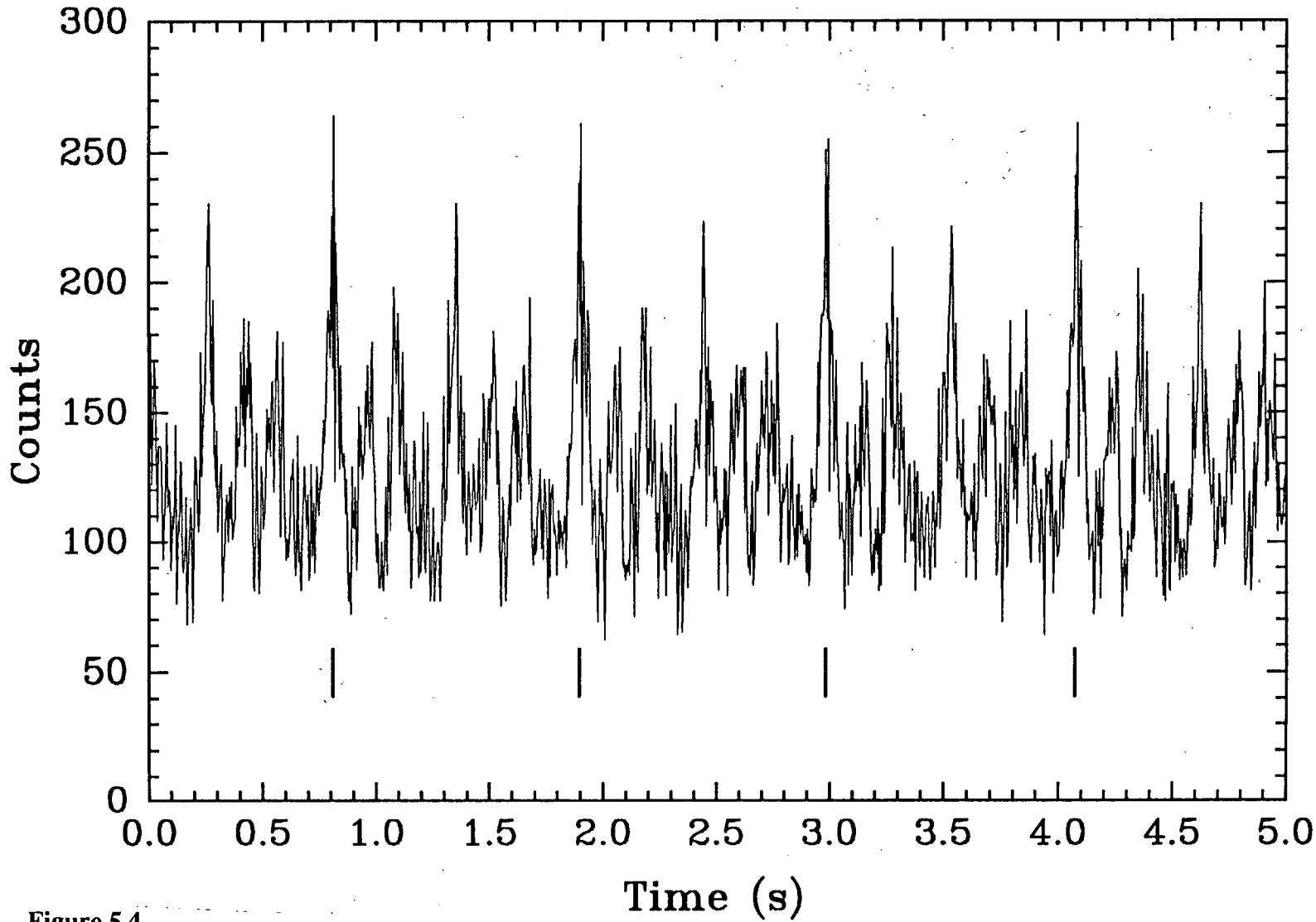

Figure 5.4
The real time light curve of AUSSAT A1 on the 4th September 1987, with a time resolution of 0.005 s. About four and a half spin periods are shown, although the complicated profile suggests that there are more. The ticks below the light curve mark the ~1.07 s spin period.

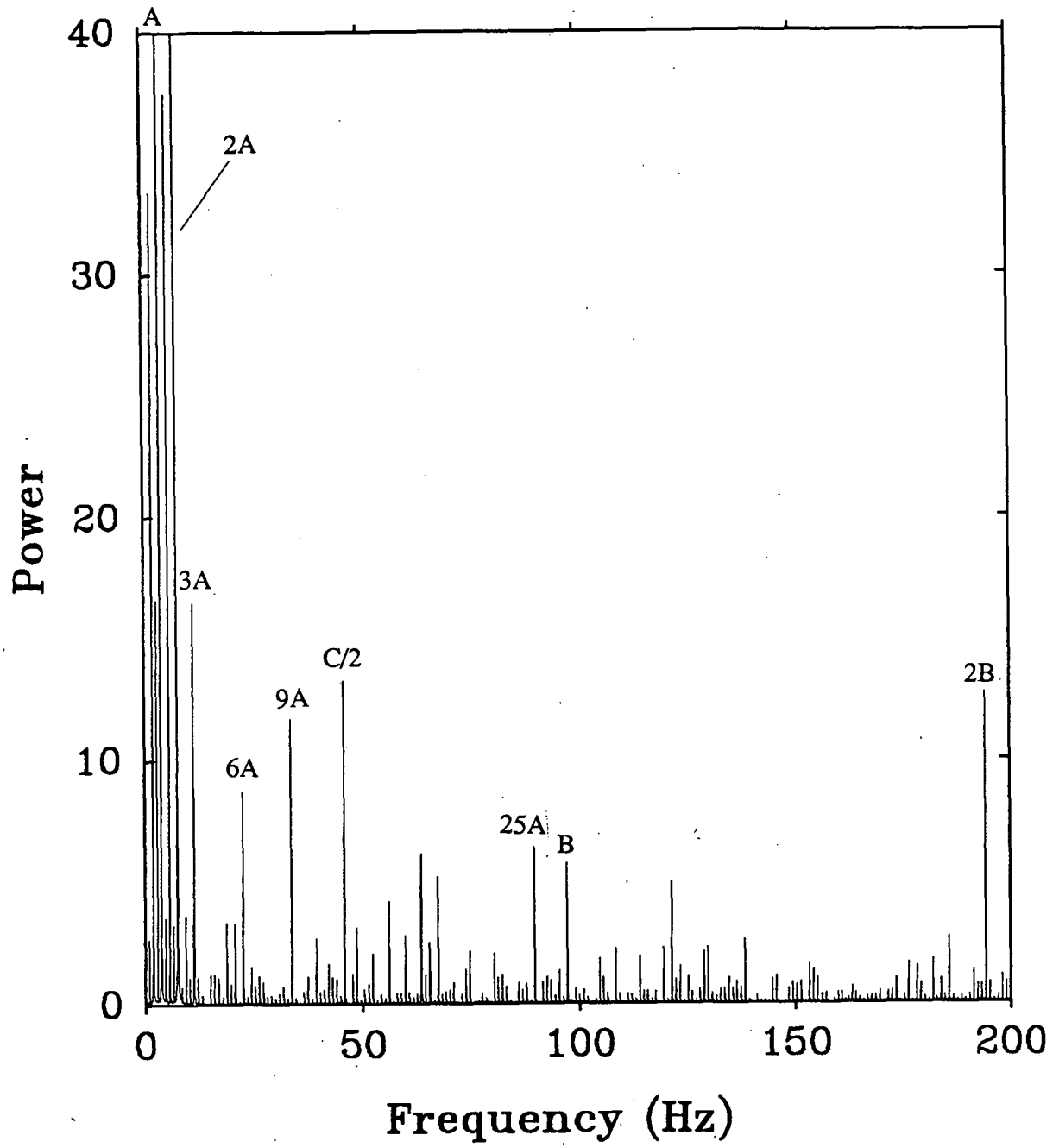

Figure 5.5
The FFT spectrum of AUSSAT A1 on the 4th September. The spectrum consists of a number of low-frequency spikes which include the ~0.93 Hz spin period, the 90 and 95.5 Hz solar cell reflections and all their associated harmonics and beat frequencies. The noise level in the FFT is lost along the zero axis. Peak A corresponds to $4f_o$, the largest peak for this run. Peak B is from the 104 cell section and peak C/2 results from the 180° symmetric, 98 cell section of the satellite. Some of the low-frequency components have been cut off at the top of the figure.

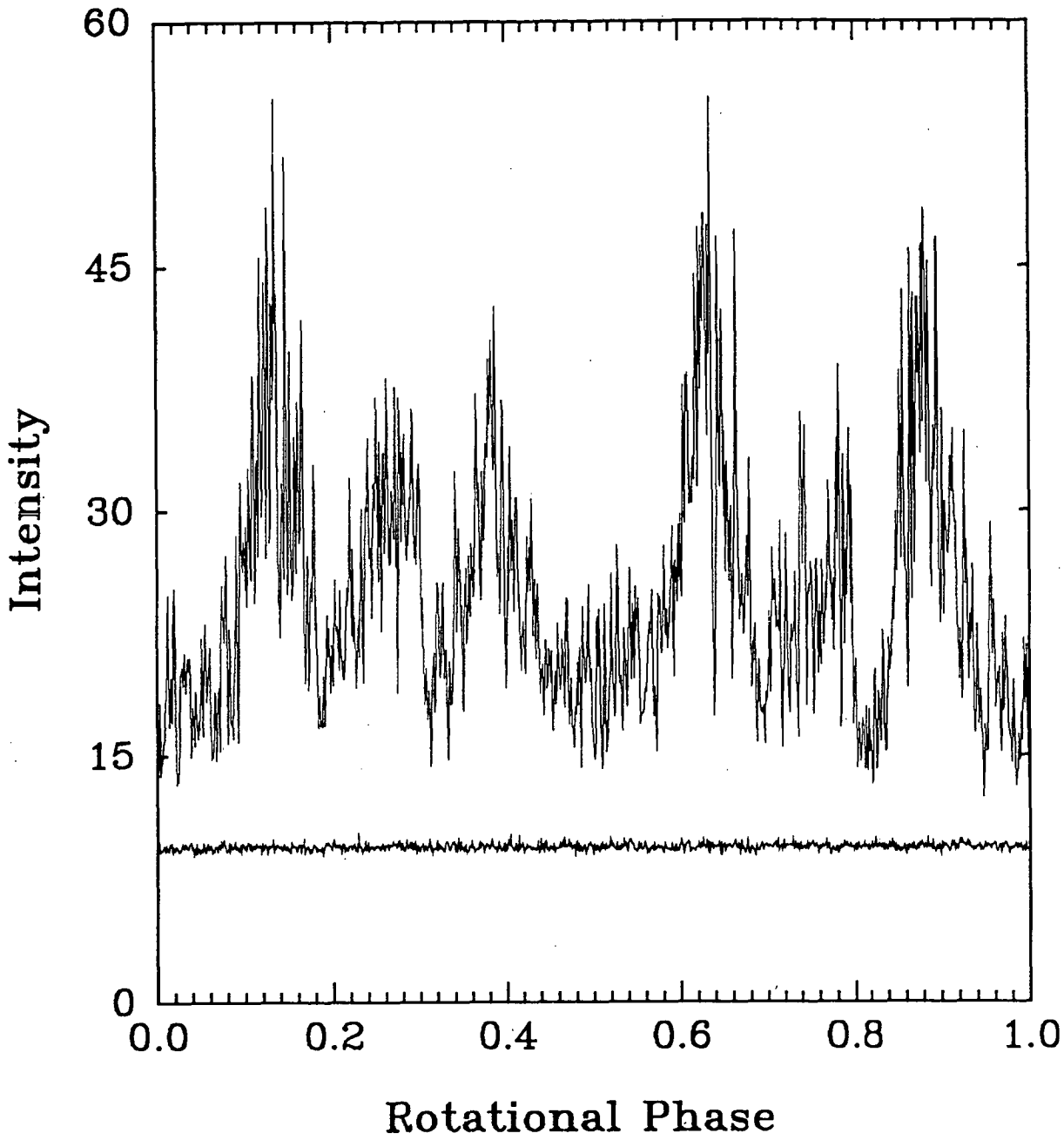

Figure 5.6
This shows the folded light curve of AUSSAT A1 at the derived spin period on the 4th September 1987. The time resolution is 0.001 s. The noise level is indicated by the lower trace. This was obtained by folding the data for a star of similar brightness to AUSSAT at the same spin period and offsetting it to the background sky level.

the AUSSAT A1 folded light curve are clearly very significant, with the noise level in the Figure 5.5 FFT lost along the frequency axis .

All of the white light data for the *on* nights in Table 5.1 have been examined to determine the exact values of f_0 for both AUSSAT A1 and A2. This was done using the Q–method of Warner and Robinson (1972) to search a small range of trial periods near the known spin rates. An accurate value of f_0 is required to phase fold the ~480 spin periods in each data set. Once this is done a final trim to the derived spin period can be made by inspection of a diagram like that in Figure 5.7. This figure shows two almost identical light curves which cover spin phases 0.7 to 1.0 only. One curve is a fold of the first minute of data from a ~9 min run and the second curve is a fold of the last minute. The slight phase shift results from folding with an incorrect spin period. When this shift is reduced to zero using cross–correlation techniques the best fit spin period has been obtained. Monitoring one of these satellites for a few hours should enable the spin period to be measured to better than one part in a million. Table 5.2 lists the derived spin periods for the nights during 1987 on which good data were obtained. Corresponding values, given by Edwards (1987), are measured by on–board sun sensors but are not logged to the ground to a particularly high accuracy. The values shown in table 5.2 are for the apparent spin periods, and are not corrected for the alias introduced by the satellite's 24 hour orbital period.

The phase folded light curves and FFT's for AUSSAT A1 and A2 on four nights during 1987 are shown in Figures 5.8(a) to 5.8(d). The light curves of the two satellites have similarities in form, but are surprisingly different in detail considering

Table 5.2

Spin Periods of AUSSAT A1 and A2 during 1987

Date	Time EST	Satellite	Spin Period (s) Ground	On–board
Apr 4	22	A1	1.0866240	1.0865
		A2	1.0812600	1.0812
May 6	22	A1	Not Detected	1.0834
Sept 1	23	A1	1.0704950	1.0706
		A2	1.0899680	1.0901
Sep 4	22	A1	1.0706795	1.0706
		A2	1.0901455	1.0901
Sep 8	23	A1	1.0706235	1.0706
		A2	1.0901400	1.0901

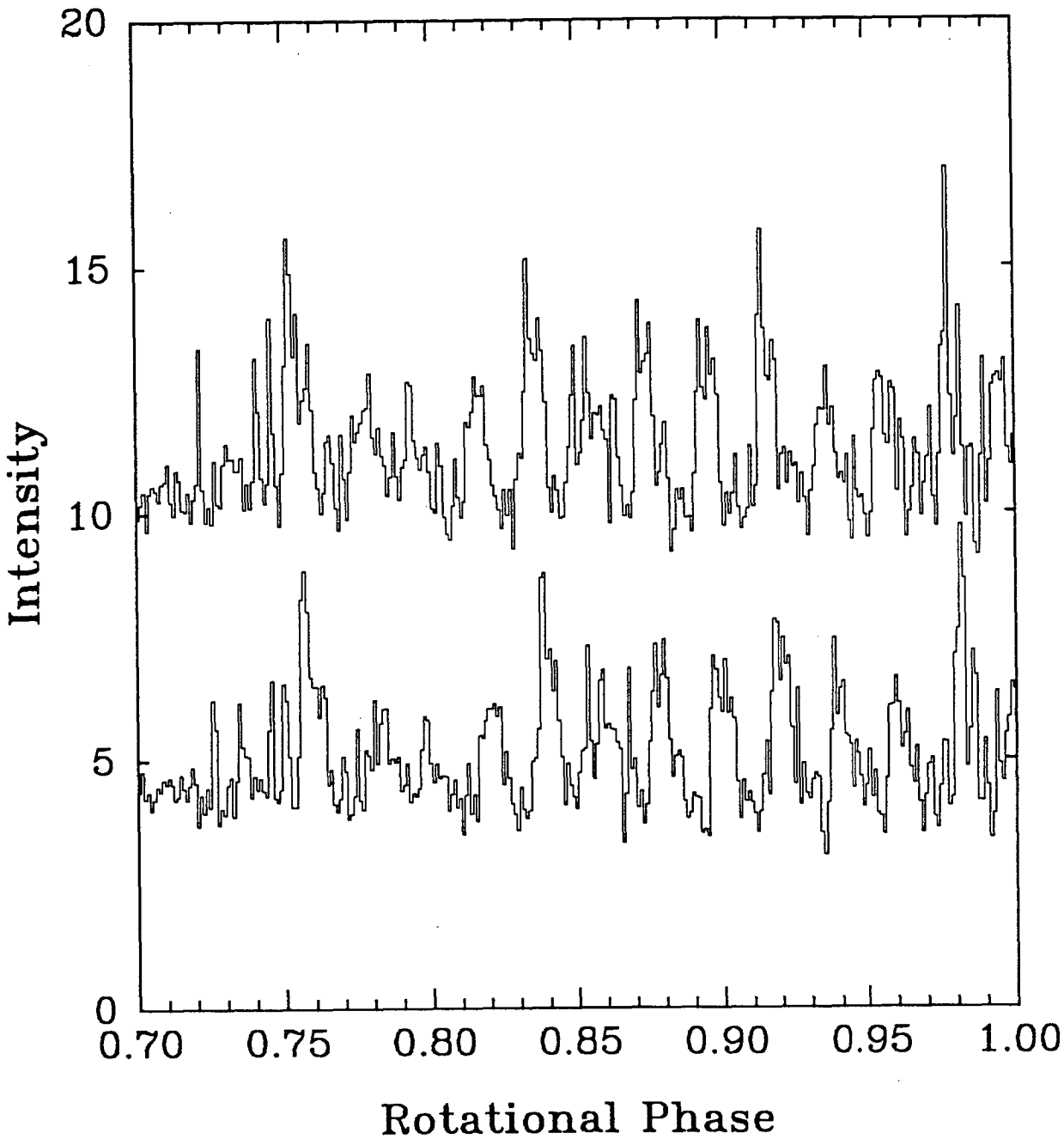

Figure 5.7
The phase folded light curves for the first and last minute of data from the ~9 min AUSSAT A1 run obtained on the 4st September 1987. The data is folded at a period of 1.0707050 s instead of the correct value given in Table 5.2. The one ten millionths of a second difference is responsible for the slight phase shift between the two curves. The top trace has been displaced in intensity to avoid confusion.

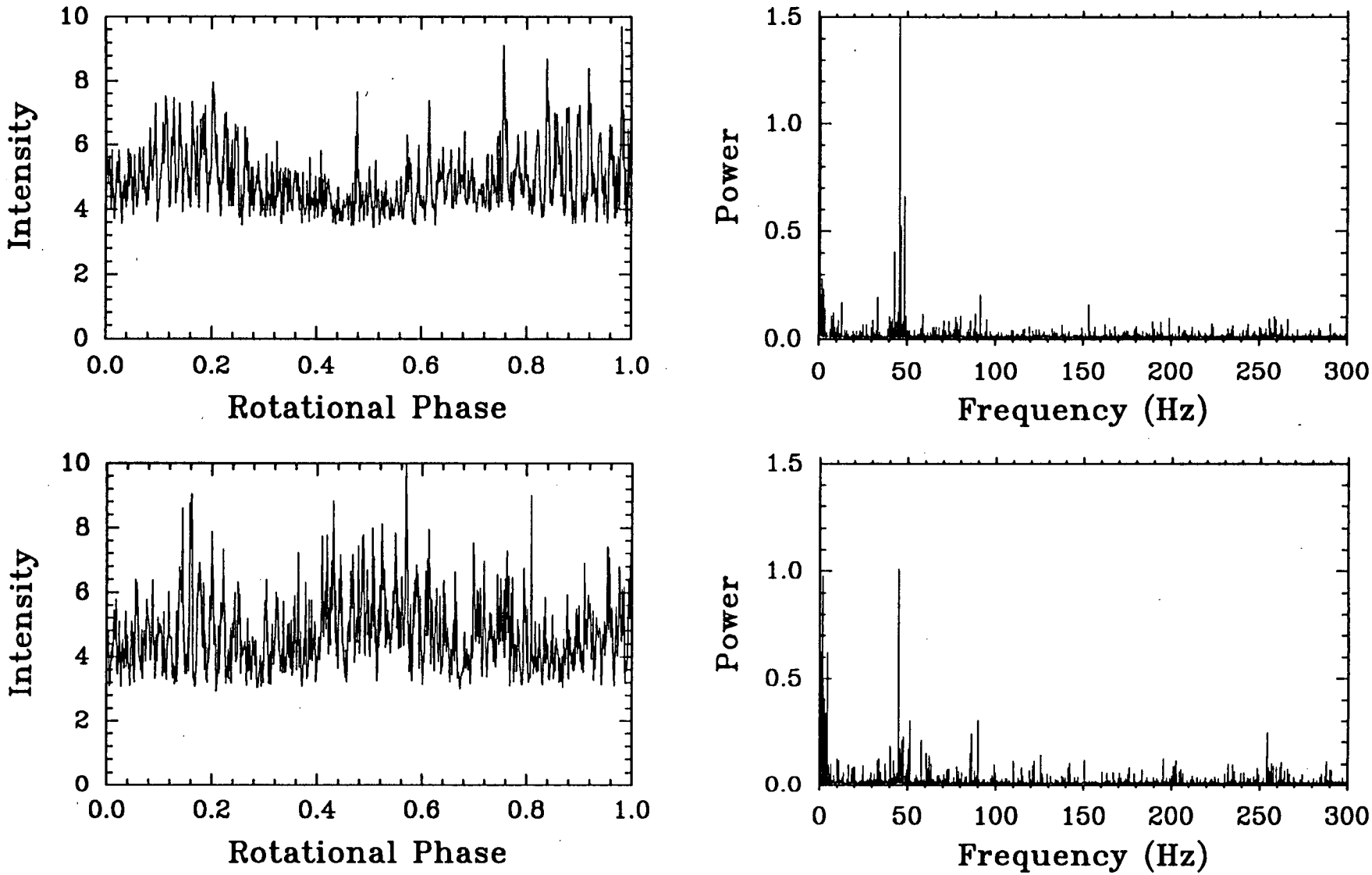

Figure 5.8 (a)
The phase folded light curve and corresponding FFT for AUSSAT A1 on the 1st September 1987 are shown in the upper two panels of this figure. The lower two panels show the data for AUSSAT A2 on the same night. This night is marked as point (a) on Figure 5.9.

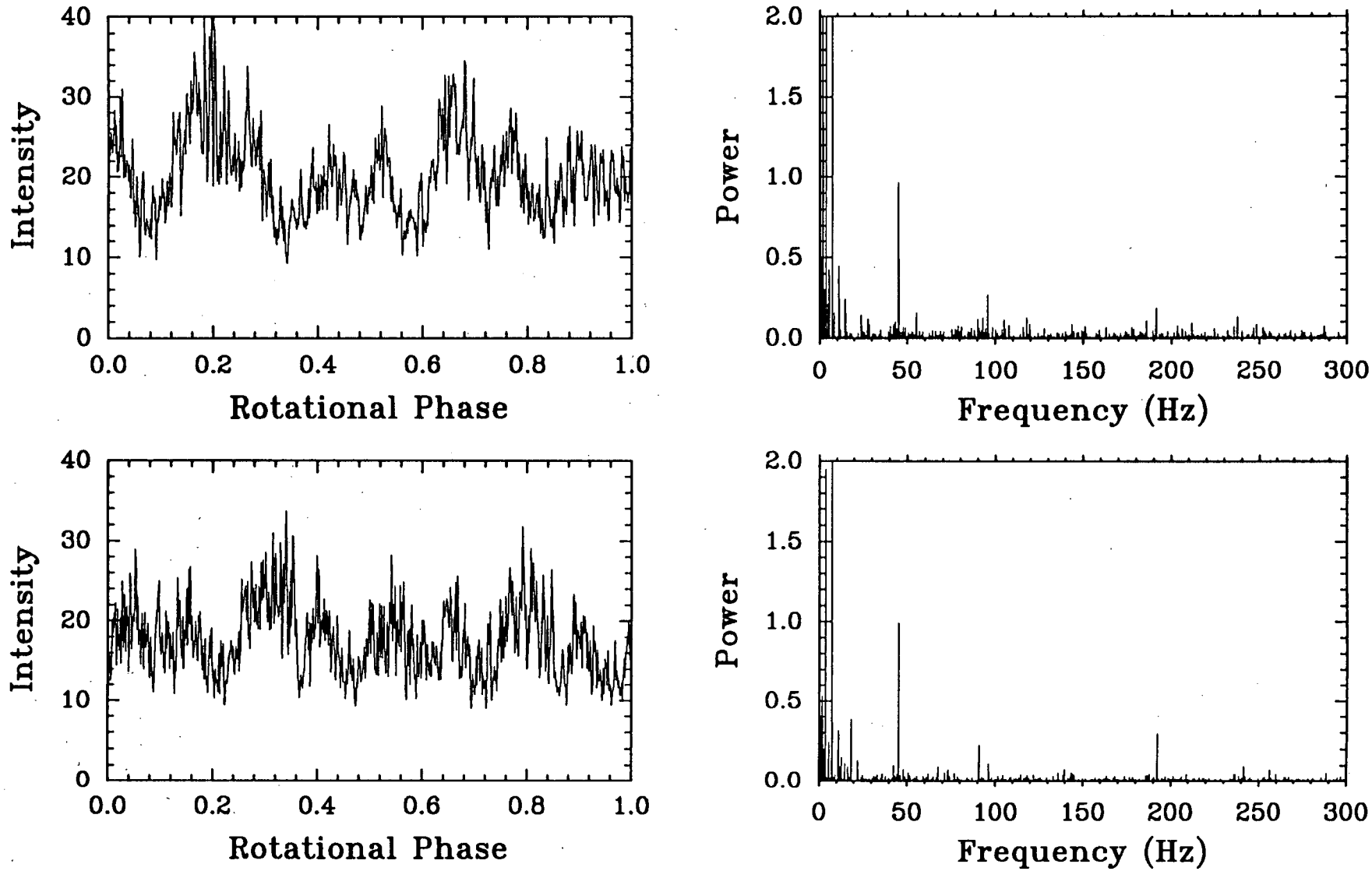

Figure 5.8 (b)

The AUSSAT A1 and A2 light curves and FFT's for the 4 th April 1987. The format of this figure is the same as that of Figure 5.8(a). This night is marked as (b) on Figure 5.9 The data in this figure has been phase shifted to approximately match that in Figure 5.8 (d). The two curves are very similar even though they are separated in time by about five months.

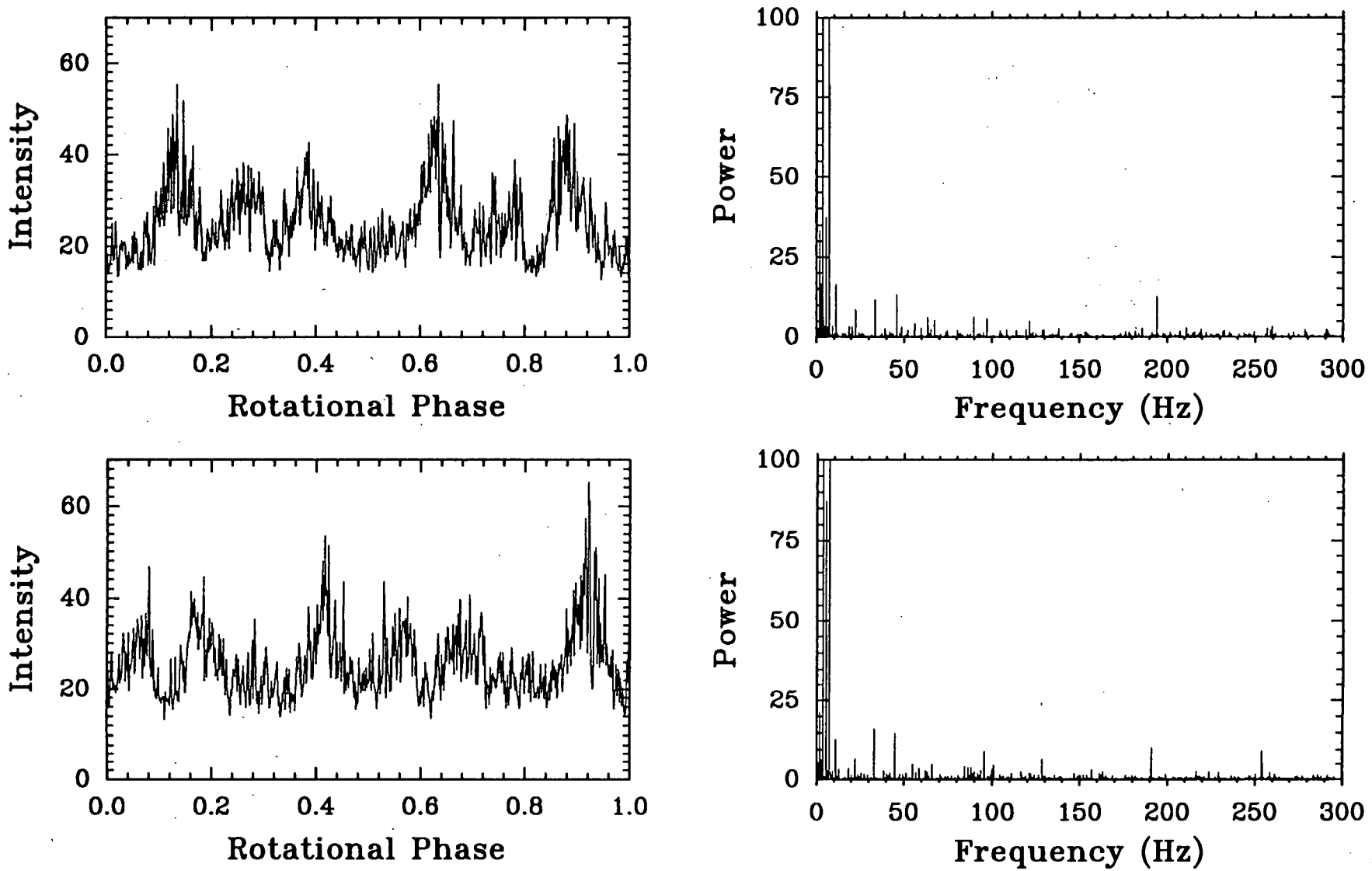

Figure 5.8 (c)
The AUSSAT A1 and A2 light curves and FFT's for the 4th September 1987. The format of this figure is the same as that of Figure 5.8(a). This night is marked as point (c) in Figure 5.9.

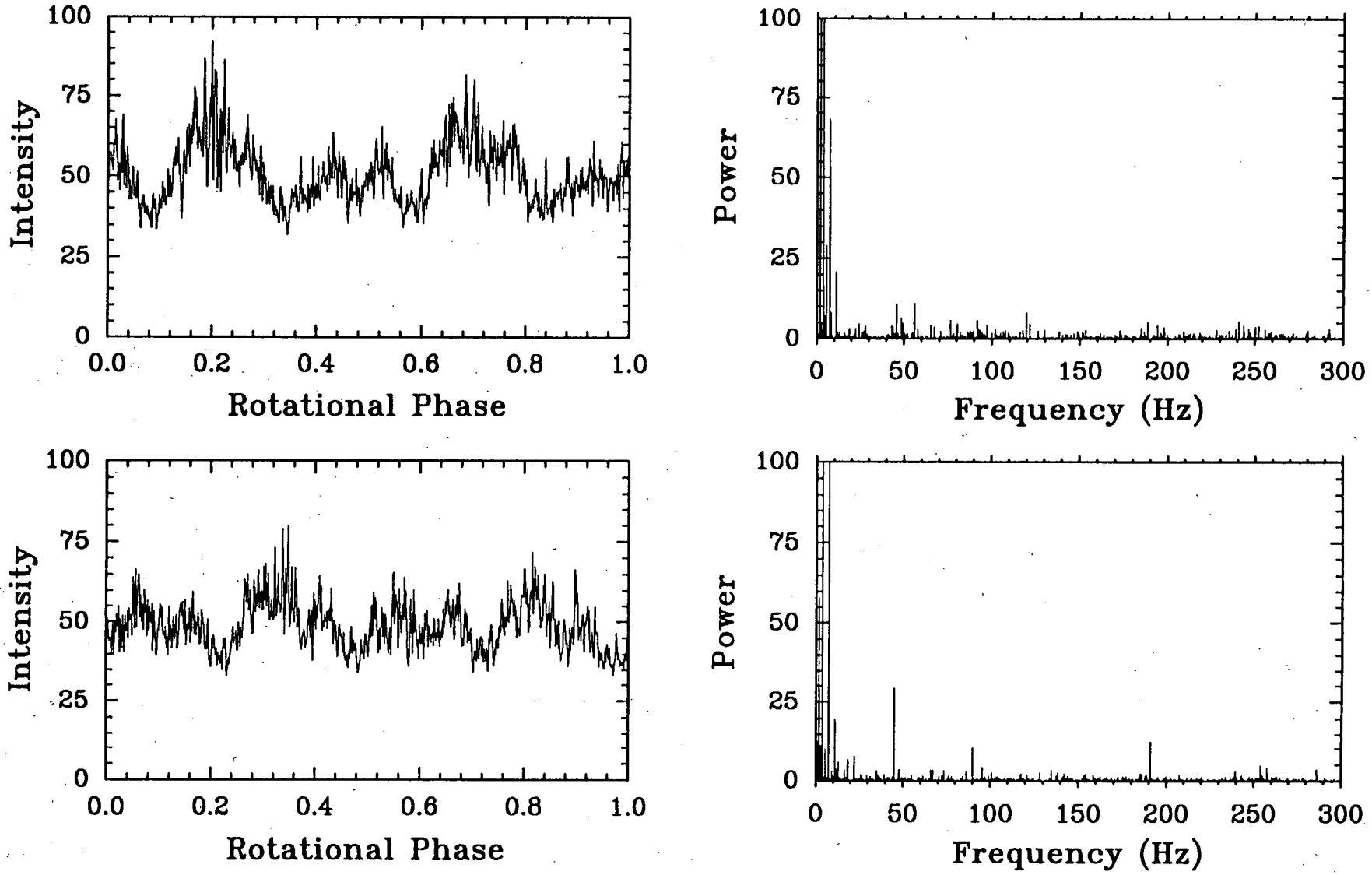

Figure 5.8 (d)
The AUSSAT A1 and A2 light curves and FFT's for the 8th September 1987. The format of this figure is the same as that of Figure 5.8(a). This night is marked as point (d) on Figure 5.9.

the two spacecraft are almost identical. The FFT spectra in Figure 5.8 have been truncated at 300 Hz in order to show the low frequency structure more clearly.

Finally it should be re–iterated that no evidence of any periodic modulation was found in the satellite light intensities when they were in their *off* state. FFT processing of ~1 hour of data, from AUSSAT A1 obtained on the 6th May, confirmed that the spikes so evident in the *on* mode were not detected down to a limit of ~0.5 percent of the mean intensity. In particular there was no significant signal at the expected f_0 of ~0.923 Hz or its harmonics. The data were also folded at the on–board sensor spin rate, but this yielded no evidence of any spin period modulation. The sharp 'flashes' would of course been smeared out over the ~1 hour time span of the data when using the limited accuracy on–board sensor folding period.

5.3.3 Satellite Features Detected

The most notable feature of the FFT's in Figures 5.5 and 5.8 are the sharpness and number of the spikes, at least when compared with more conventional astronomical objects. The sharp definition suggests that what we are seeing is some precisely defined flashing quality more in the nature of an artificial beacon. This is quite clearly the case although the beacon qualities of the spacecraft are simply a coincidental by–product of its design. So what are we seeing and how does it come about? Basically it is not too complicated and can be almost completely understood in terms of simple geometry.

The outer surface of the AUSSAT satellites is covered with ~16,000 solar cells. The precise arrangement of these cells gets quite complicated as there are three main regions, several different cell sizes, and strips of filler cells to maximise coverage of the available surface area. A detailed description of the solar cells on the AUSSAT spacecraft is given by Gorian and Henry (1986). An good approximation to their exact layout is that the deployed aft section has 98 rows of cells around its circumference and the forward section has 104 rows of cells (see Figure 5.3). Large peaks related to these exact multiples of f_0 were noted in the FFT of the 4th April even before the detailed drawings of the solar cell distribution were obtained from Hughes. The typical cell size is 2.3 cm x 6.5 cm with the long axis aligned around the circumference of the satellite. Since each revolution of the satellite occurs in ~1.08 s the reflections from the length wise strips of 98 and 104 cells occur at frequencies of ~90 and ~95.5 Hz. Both these frequencies, together with their harmonics and beat frequencies, are clearly present in the FFT spectra. Since the filler strips on the deployed array are located such as to give

this section a 180 degree symmetry, the peak at 90 Hz is weaker than the one at 45 Hz. A plot of the folded light curve, such as Figure 5.6, is therefore showing many of the individual flashes from the solar cells. Note that each spike in the folded light curve of Figure 5.6 is real and repeatable since, as Figure 5.7 shows, a folded light curve for the first and last minute of an ~9 min run look almost identical.

On the forward section of the satellite there are also several thousand small thermal radiator mirrors, as can be seen in Figure 5.3. There are 8 rings of 285 mirrors around the circumference of this part of the satellite. The ~266 Hz frequency from these mirrors can also be seen in some FFT's. It should also be noted that the slower brightness modulation of the satellites as they spin often seems to be dominated by the beating of the 90 Hz and 95.5 Hz frequencies. This gives rise to the six broad peaks of intensity within the rotation light curve, as is seen in Figure 5.6. It is this aspect of the modulation which is so readly visible in the real time image on the Cassegrain TV guider screen.

5.3.4 The Reflection Geometry

Calculations of optimum specular reflection geometry for geostationary satellites is quite straight foward, even though the orbital motion and positional correction strategy for satellites like the AUSSAT ones are quite complex (Edwards and Hope, 1987; Hope et al., 1986). From the point of view of the ground–based observations, the main relevant fact is that the spin axes of the spacecraft are maintained parallel to that of the Earth, and so the perspective of a particular satellite does not change for a fixed observatory location. From Hobart, at a latitude of ~42.9 deg south, geostationary satellites appear north of the celestial equator at a declination of around 6.6 deg, a value which is only slightly dependant on hour angle. Sunlight incident on the satellite surface from a declination of ~+6.6 deg will therefore be reflected directly towards the latitude of Hobart. The sun has a declination of +6.6 deg twice during the year. This occurred on April 7th and September 6th in 1987. Quite by chance the first photometry run (Run 2) occurred very close to the first of these dates.

The length of time spent in the *on* state was not known to us, though we assumed it would probably be no longer than a couple of days. In an effort to determine the length of the *on* interval for AUSSAT A1, it was observed on every possible occasion as September 6th 1987 approached. Another run of bad weather frustrated attempts to obtain a good coverage, and on the first clear observation, September 1st, the satellite was already in its *on* state and relatively bright. An estimate of the brightness of A1 on

all the nights it was observed is plotted in Figure 5.9, about the expected optimum specular reflection date. The coverage is not very good, but the data are reasonably well fitted by a Gaussian curve centered 0.4 ± 0.1 days later than expected. The small offset may be due to poor photometry since cloud was present on some nights. The Gaussian curve in Figure 5.9 has a half–height width of about 5 days and a base width of about 10 days. Unfortunately it was only possible to obtain a quick reading for the brightness of AUSSAT A1 through a gap in the clouds near the predicted optimum date on September 7^{th}, and no light curve was possible. It was estimated to have been between 8^{th} and 9^{th} magnitude at this time. AUSSAT A2 gives a similar curve to that in Figure 5.9, but there was no spot measurement for September 7^{th}. The lack of points near peak brightness for this satellite may have been responsible for a somewhat broader Gaussian fit with a lower peak height than that for the A1 fit. The Gaussian fit parameters for both satellite light curves are given in Table 5.3.

The folded light curves vary quite a lot from night to night through a specular reflection episode, as is shown in Figures 5.8 (a) to 5.8 (d), but are very repeatable over a period of a few minutes. Note, however, that the folded data for the 4^{th} of April is very similar to that for the 8^{th} of September. To emphasize this, the light curve in Figure 5.8 (b) has been phase shifted to approximately match the one in Figure 5.8 (d). Although points (b) and (d) in Figure 5.9 are on opposite sides of the Gaussian fit, they are also from opposite equinox passages. Hence the reflection geometry is similar on both occasions. This supports the expectation that the reflection intensity is similar if the geometry is similar. The relative phasing of the other light curves in Figure 5.8 is completely arbitrary.

The reasons for the night to night changes and differences between AUSSAT A1 and A2 light curves is not clear. These variations may be due to a number of combined

Table 5.3

Gaussian Fit Parameters for the Specular Reflection Episode of AUSSAT A1 and A2 during September 1987.

Gaussian Parameter	A1	A2
Centre (days)	0.4±0.1	0.3±0.1
Width (HWHM days)	2.6±0.1	2.8±0.2
Height (counts)	27100±900	22300±1200

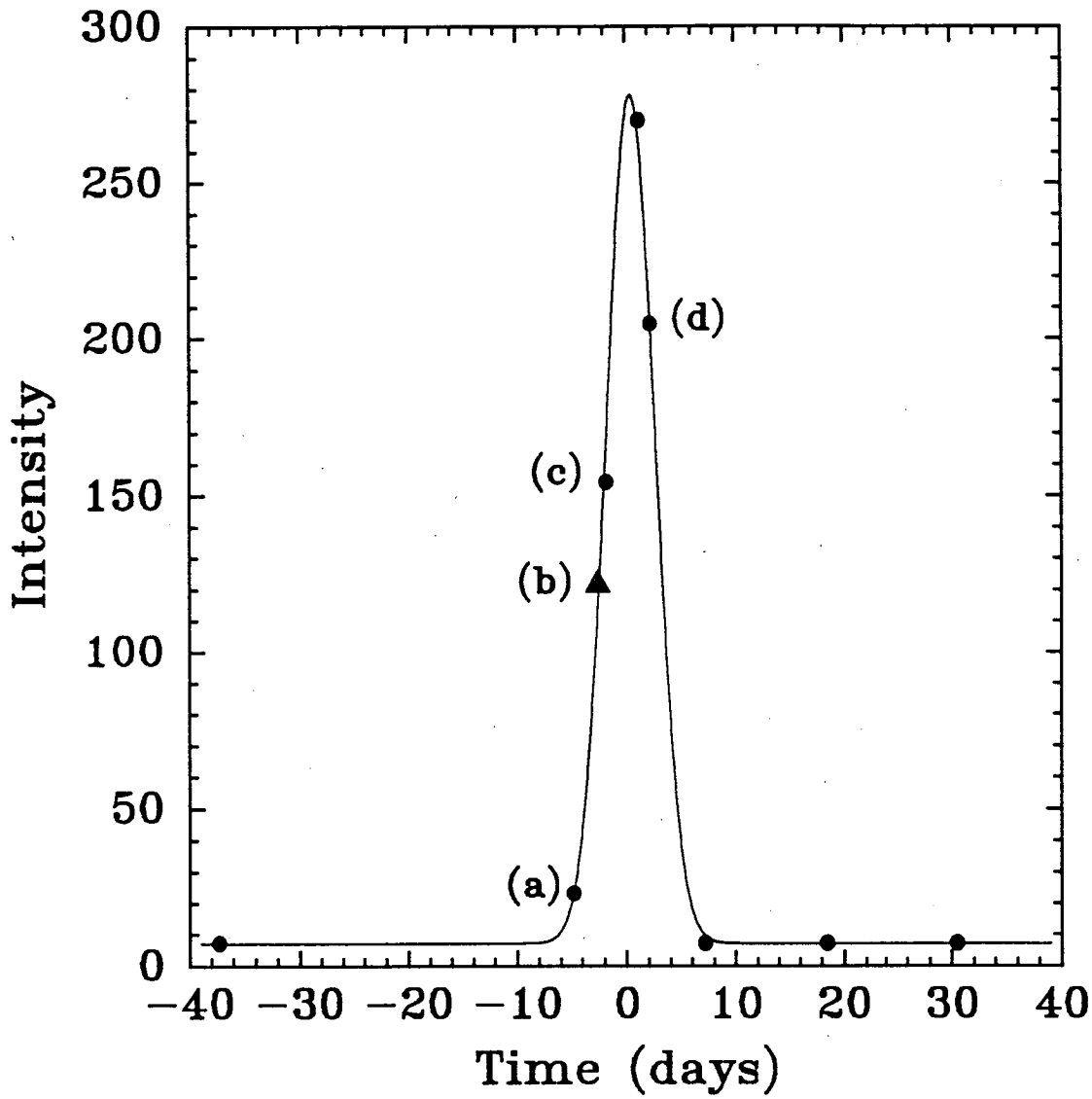

Figure 5.9
The uncalibrated measured brightness of AUSSAT A1 plotted relative to the expected date of maximum brightness. The dots are for the September data and the triangle is for the 4th April 1987 data. Points (a) to (d) refer to the data shown in Figures 5.8(a) to 5.8(d). The unlabelled point near the peak is a spot measurement as clouds prevented light curves being obtained.

effects since the reflections will be very sensitive to small changes in the angle of incident sunlight. Regions on the outer surface of the satellite may depart from a perfectly cylindrical geometry, or the fixed and deployed sections may not be quite optically parallel. Small random orientations of the mirrored tiles and solar cells can also be expected, since they are only fixed in an adhesive matrix and their exact orientation does not effect their operation. The two satellites orbital drift north or south of their mean positions will also be different. As well, the spacecraft will exhibit a small nutation effect, since their spin axes cannot be aligned perfectly with the Earth's axis. Further observations may assist in determining the relative importance of all these factors.

5.3.5 Satellite Eclipse Observations

The *on* mode of the satellites also coincides with their Earth eclipse season, so care must be taken not to try to find the spacecraft when they are near the anti–Sun hour angle. The eclipse season lasts for about 25 days either side of the two equinoxes. As noted by Taylor (1983), at the ~36,000 km distance of the satellites, the radius of the Earth's shadow is ~8.7 deg and its penumbra region extends to ~9.2 deg. Since the satellites are approximately stationary, it is an easy matter to measure their immersion light curve, but the emmersion light curve is harder, as a small pointing correction may be necessary due to the slow orbital drift of the satellites. The drift can always be estimated if the satellite position has been monitored for the previous half hour or so. An example immersion eclipse is shown in Figure 5.10. For Hobart this event was some way from a central event. It lasted ~38 min compared with a maximum possible duration of ~70 min. The eclipse proceeds very rapidly since the angular change in the position of the Sun, as observed by the spacecraft, is the usual Earthbound rate of 1 solar diameter every 2 min. The ingress duration for the Figure 5.10 eclipse is lengthened by a factor of ~2 over the minimum duration, since the position angle of immersion is ~327 deg. The two panels in Figure 5.10 illustrates how the sharp flickering features in the satellite light curve are lost when a long integration time is used. For this eclipse, the immersion occurred with the sun's rays passing tangentially through the Earth's upper atmosphere over southern–central Russia.

5.4 Observations of the Crab Pulsar

The Crab pulsar was first identified as an optical source of pulsations by Cocke, Disney and Taylor (1969). Since then it has become a standard test source for ultra–high speed photometry. Although it is an ideal test source, the latitude of the Mt.

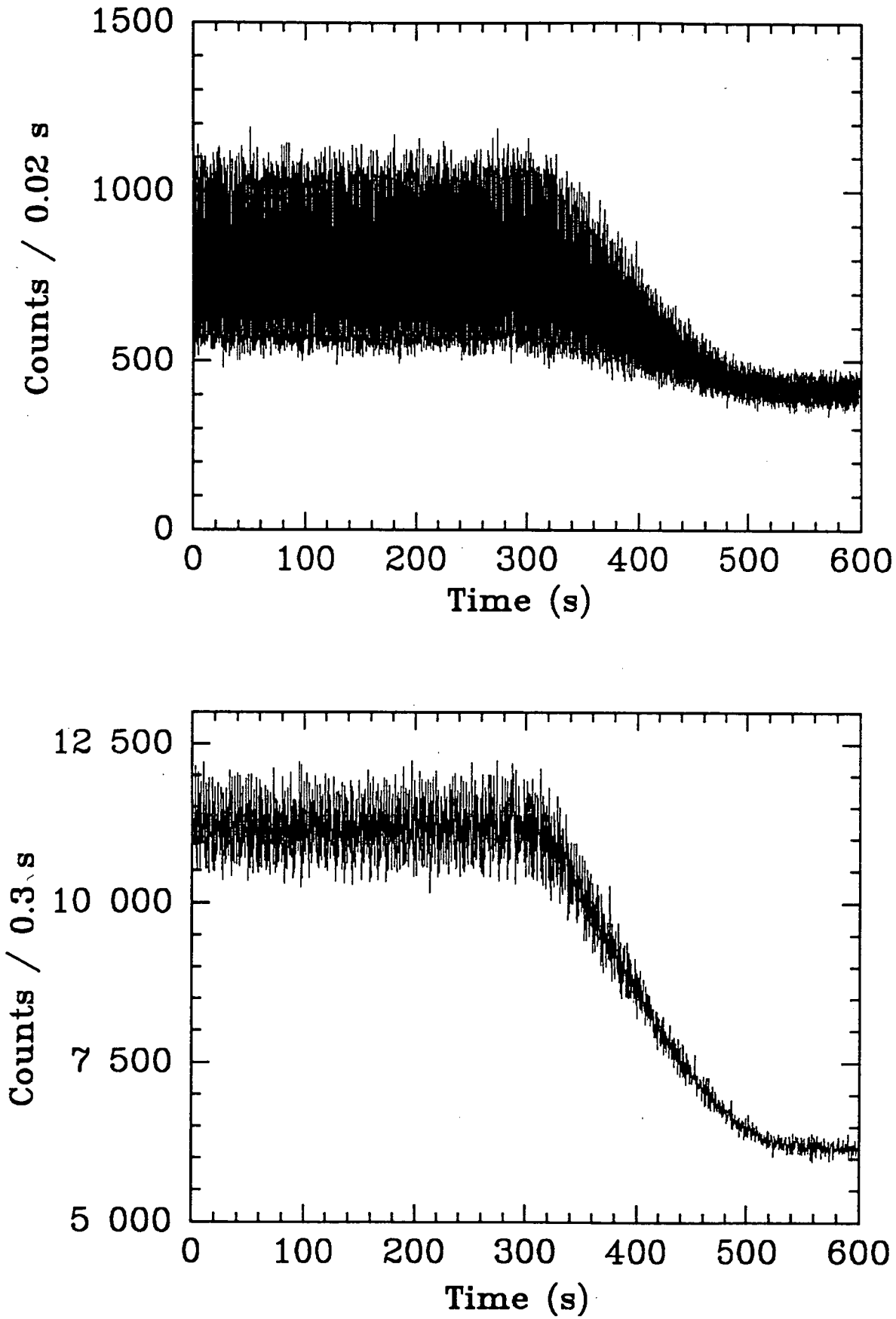

Figure 5.10
The eclipse light curve for AUSSAT A1 going into the Earth's shadow on the 4th September 1987. The sunlight illuminating the satellite passed through the upper atmosphere over southern Russia. The two panels illustrates how the sharp flickering features are smoothed out when the integration time is increased.The slight ripple prior to the eclipse is a beating effect between the data binning and spin period

Canopus Observatory, ~42.9 deg south, coupled with the northern declination of the pulsar, means that the observing season is very limited. The Crab never attains an altitude of more than ~25 deg above the horizon, so is only visible through a large air mass at Mt. Canopus. A test observation on the Crab pulsar therefore represents a strong challenge to the telescope and photometer system. On the night of the 24th of November 1987 two data acquisition runs were made on the Crab. The data for both runs were acquired using a 2.5 kHz sample rate. A 40" aperture was used to minimise seeing effects and guide correction errors. The first run was ~20 min in duration and was of only mediocre quality because of less than perfect sky conditions at the low altitude of the Crab, and the presence of some minor guide errors. The second run, of ~28 min duration, was more successful, and the results of the analyses of the data from that run is presented in Figure 5.11.

The presence of the pulsar was clearly evident in both runs, as revealed by the presence of many spikes in the FFT's of the data sets. A single 4096K point FFT of the second data run is shown in Figure 5.11(a). Note that not every point in the FFT spectrum has been plotted in Figure 5.11(a). Instead, the maximum power from each consecutive group of 256 frequency bins has been plotted. Hence the mean spectral noise in Figure 5.11(a) appears to be at a power level of around 15, whereas the mean power level was measured to be ~2.1 and its variance was ~4.3. The minimum powers in consecutive groups of 256 frequency bins extend almost down to the zero axis.The power spectrum shows a fundamental peak corresponding to the ~33 msec rotation period of the pulsar and at least 9 other peaks due to its harmonics. The most pronounced peak is the 1st harmonic. This is due to the presence of two optical flashes per rotation of the pulsar. The Q–method periodogram, shown in Figure 5.11(b), was also computed, and provides a better estimate of the fundamental frequency. The best period estimate, obtained by folding the first and last few minutes of the data at the best Q–method period, and then using cross–correlation techniques to provide a final period adjustment, is 0.03334312 ±6 s. This period was then used to phase fold the data and produce the phase folded light curve presented in Figure 5.11 (c). The mean un–pulsed light level, estimated from Figure 5.11 (c) is ~2.985 counts per bin. The pulsed light, averaged over a complete cycle, is ~1.95×10^{-2} counts per bin. Hence, the pulsed fraction of the total light in the data run is ~0.6 percent, where the un–pulsed contribution is due to , un-pulsed pulsar, nebular, sky background, and dark current counts.

The light curve in Figure 5.11 (c) is consistent with other published optical light curves of the Crab pulsar. The obvious similarities are : (i) a two–peaked profile; (ii) the larger

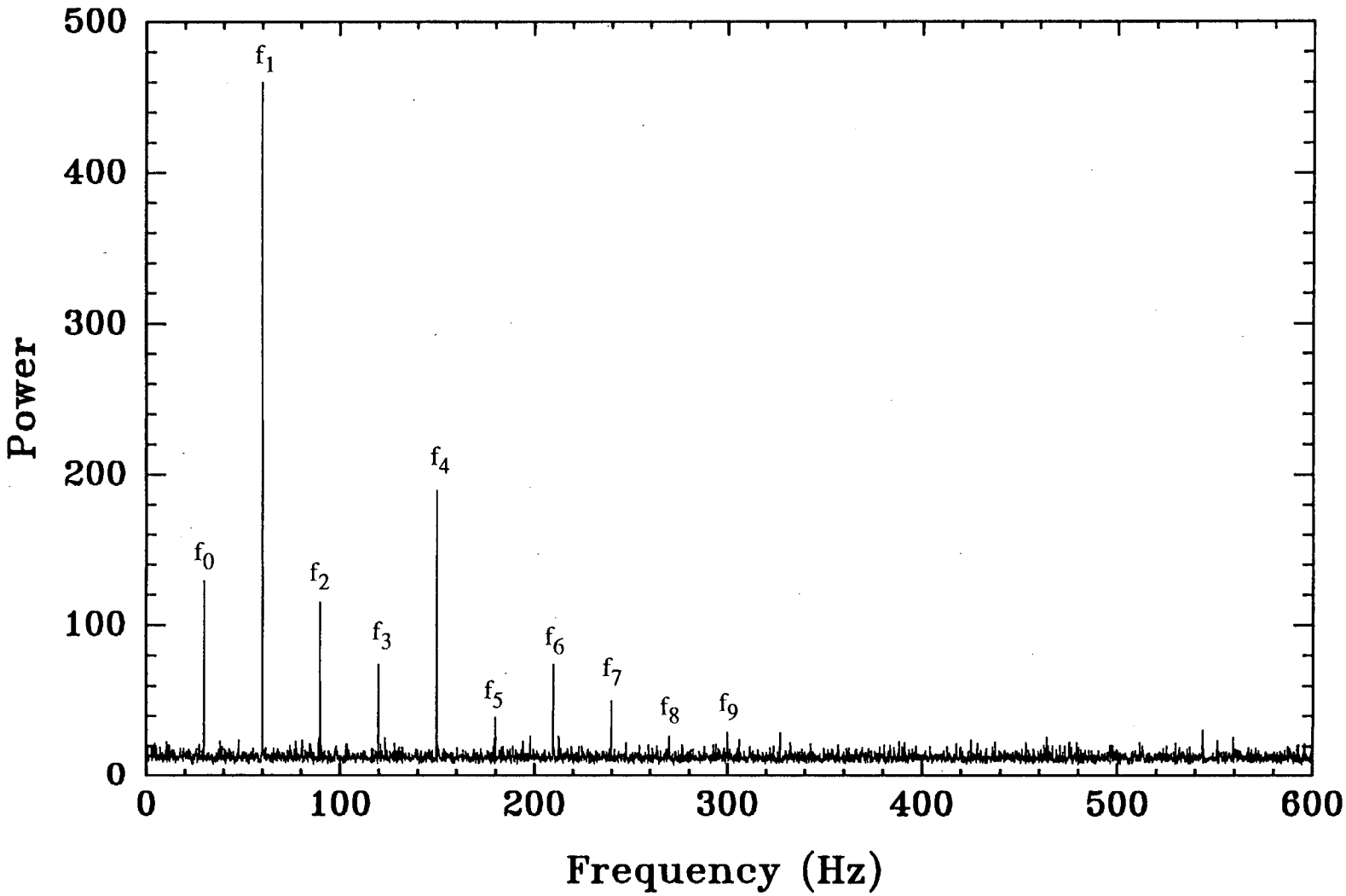

Figure 5.11 (a)
A single 4096K point FFT spectrum of ~28 min of data obtained on Crab pulsar. The data were acquired at 2.5 kHz. The FFT has been truncated at 600 Hz to illustrate the lower frequency structure in more detail. Not all of the FFT spectrum points have been plotted. Instead only the maximum power from each consecutive group of 256 points has been plotted.

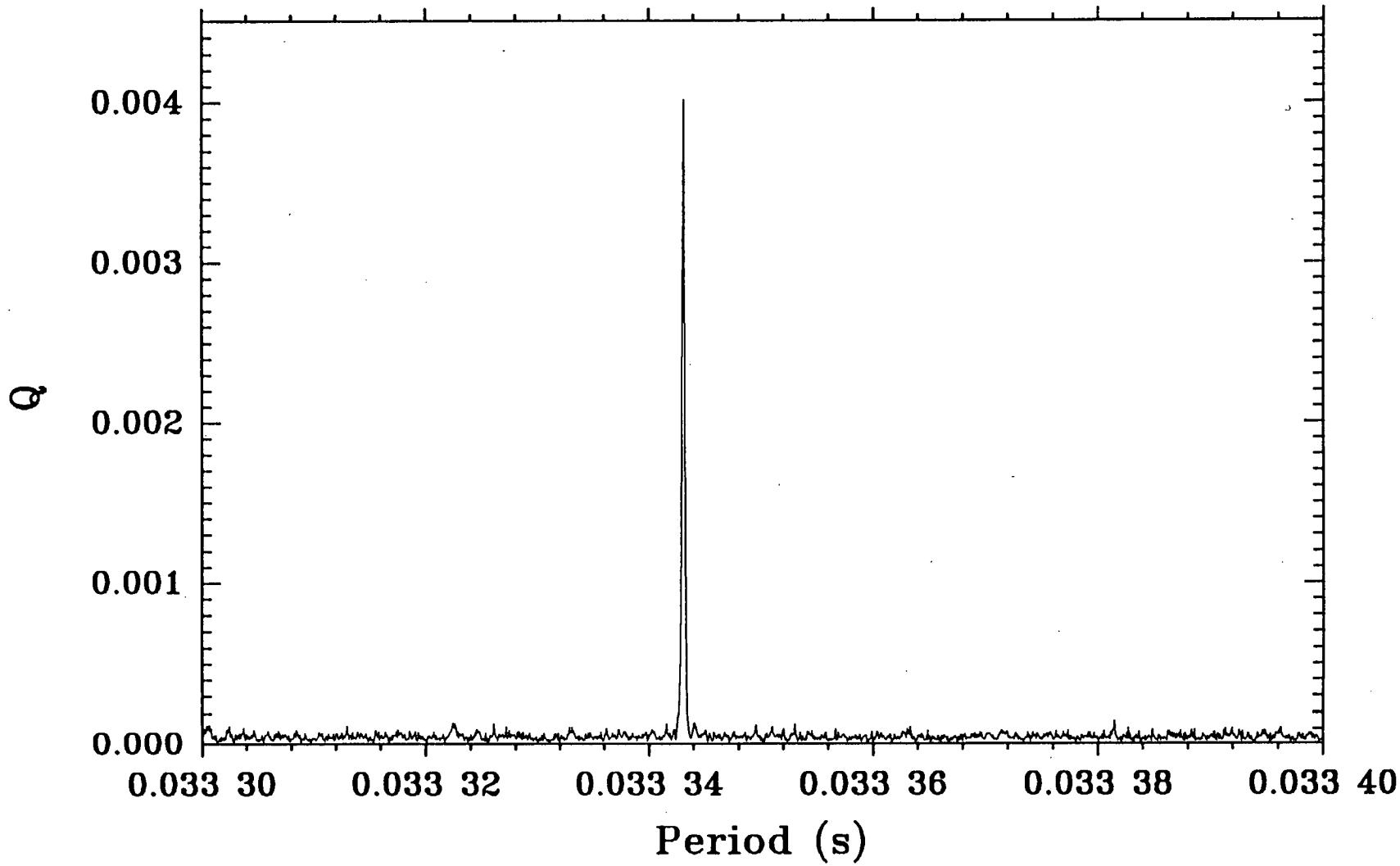

Figure 5.11 (b)
The Q-method periodogram for the same data set used to produce the FFT in Figure 5.11 (a). Here the period range has been restricted to periods around the fundamental peak.

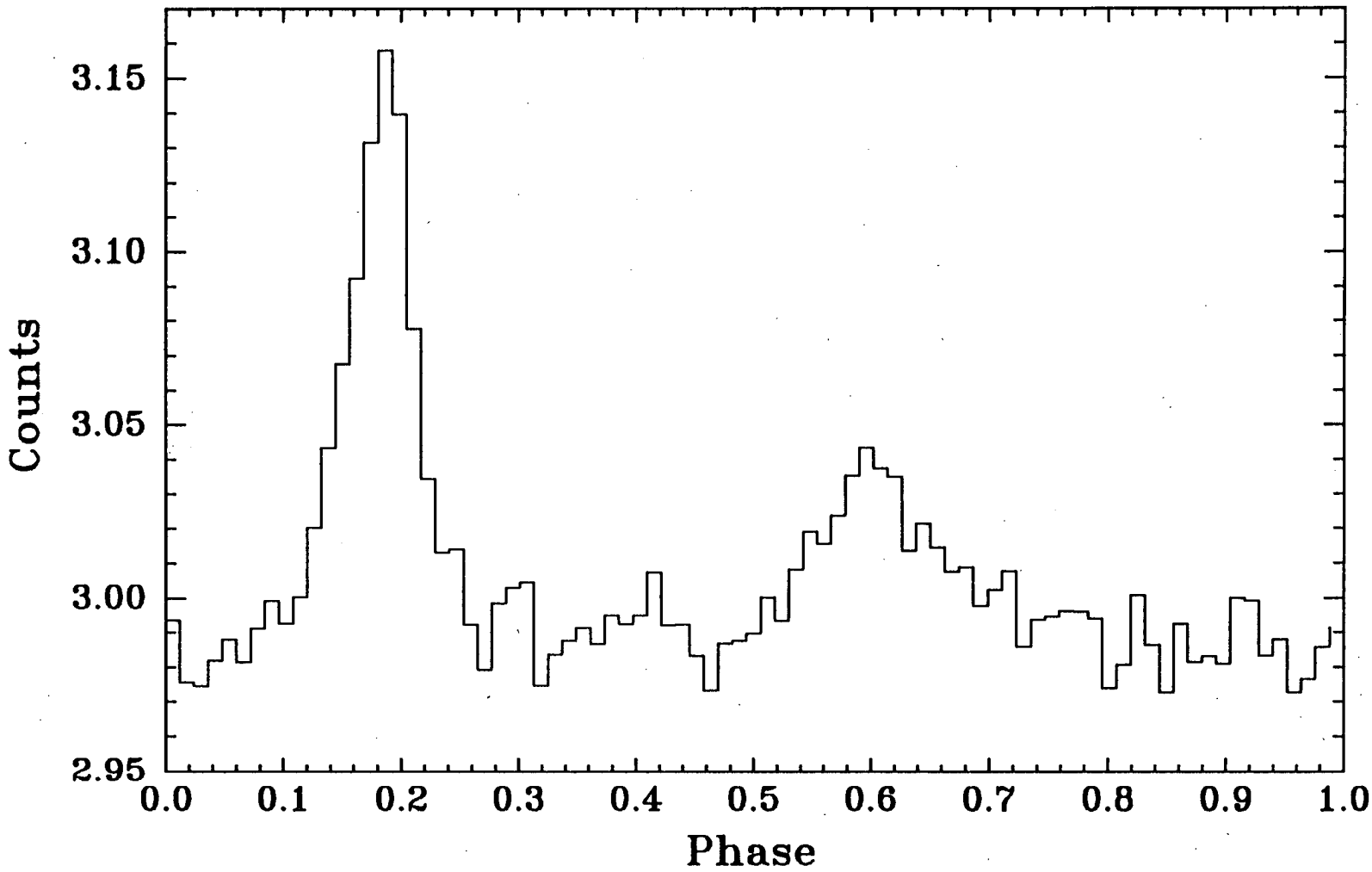

Figure 5.11 (c)
The phase folded light curve of the Crab pulsar obtained from ~28 min of data acquired on the Mt Canopus 1.0m telescope. Here each bin corresponds to ~0.4 ms and the vertical axis represents the mean number of counts per bin.

peak has a slightly more extended rise and sharper fall time while the reverse is true for the smaller peak; (iii) the two pulses are not separated equally in phase, with the main pulse to interpulse phase difference, measured from the peak separation in Figure 5.11 (c), being $\Delta\Phi \approx 0.42$. The observation presented here is undoubtedly the most southerly ground–based optical detection of the Crab's pulsation. The results indicate that the photometer system is quite clearly capable of detecting much fainter pulsating sources than the Crab pulsar.

5.5 Ultra–high Speed Photometry of SN1987a

The beginning of 1987 heralded a rare event for astronomers. On the night of the 23rd February 1987 the first naked eye supernova appeared since the one seen by Kepler in 1604. Its appearance (IAUC 4316) naturally led immediately to speculation as to whether or not a rapidly spinning neutron star might have formed at the centre of the remnant. Some workers, such as Arnett (1987), expect that such a remnant should exist. An event as rare as this presents itself as a unique opportunity for supernovae studies. However, the far southern declination of SN1987a also meant that the many observatories at northern latitudes would have a restricted observing season, if they could see SN1987a at all. The latitude of the Mt. Canopus observatory, on the other hand, meant that the supernova could be observed from there all year round. Being a small observatory with limited equipment, man–power, and funds, it was decided that our best contribution to the observations of SN1987a would be in the form of high–time resolution photometry. So, immediately upon hearing the news of the occurrence of SN1987a, I began upgrading the photometry system, as discussed in Chapter 2.6.3 and 2.6.4, with the intention of looking for any early signs of a pulsar in the SN1987a remnant. This section details the observations and results of the supernova observing program thus far.

5.5.1 Observations

Since the supernova explosion, 39 ultra–high speed photometry runs have been performed, resulting in the accumulation of $\sim 1.25 \times 10^5$ s of data. A journal of the observations is presented in Table 5.4. The data have been collected through broad–band colour filters, and, in the early stages, a neutral density filter with 10 percent transmission. The primary purpose of the filters in these observations was to keep the total photon count–rate down to approximately $\sim 10^5$ Hz, thus avoiding any significant losses due to coincident counts in the counting circuitry. The data were acquired using the 'two channels x 16 bits' acquisition software until around the end of 1987. From

Table 5.4

Journal of SN1987a Observations

Run	Date	Start Time (AEST)	Duration (s)	Sample Freq.(kHz)	Filter
1	10–MAR–87	20:12	1600	2.5	I+ND
2	11–MAR–87	00:51	1680	2.5	I+ND
3	13–MAR–87	21:41	1680	2.5	U+ND
4	13–MAR–87	22:46	1680	2.5	I+ND
5	13–MAR–87	23:47	1680	2.5	B+ND
6	14–MAR–87	03:26	1680	2.5	B+ND
7	Run aborted	just after	start	due to bad	weather
8	23–MAR–87	23:56	1680	2.5	B+ND
9	31–MAR–87	22:30	1680	2.5	B+ND
10	31–MAR–87	23:52	1680	2.5	I+ND
11	23–APR–87	21:32	1680	2.5	U+ND
12	23–APR–87	22:40	1680	2.5	I+ND
13	01–JUL–87	23:01	1680	2.5	B+ND
14	03–SEP–87	~23:00	250	2.5	V+ND
15	15–OCT–87	~23:00	1580	2.5	V+ND
16	25–OCT–87	~23:00	1680	2.5	V+ND
17	20–NOV–87	21:48	1680	2.5	V+ND
18	10–DEC–87	22:18	1680	2.5	B+ND
19	17–DEC–87	00:09	2880	5.0	B+BD
20	14–FEB–88	21:30	1680	2.5	B+ND
21	14–FEB–88	22:43	2820	5.0	B+ND
22	25–FEB–88	22:27	2600	5.0	B
23	02–MAR–88	21:58	4000	5.0	V+ND
24	09–APR–88	22:31	8160	2.5	B
25	03–JUN–88	21:24	7180	2.5	V
26	13–JUL–88	23:05	1800	2.5	R
27	12–AUG–88	21:25	2500	2.5	R
28	31–AUG–88	22:57	7190	2.5	R
29	04–OCT–88	22:21	8160	2.5	Clear
30	08–NOV–88	20:47	4500	2.5	"
31	05–DEC–88	22:34	3400	2.5	"
32	15–DEC–88	23:00	8160	2.5	"
33	16–DEC–88	01:00	7200	2.5	"
34	14–JAN–89	21:52	8160	2.5	"
35	11–FEB–89	22:06	3360	6.0	"
36	12–FEB–89	00:18	3360	6.0	"
37	12–FEB–89	02:14	3360	6.0	"
38	01–MAR–89	22:29	4560	9.0	"
39	04–APR–89	22:03	4560	9.0	"

then until March 1989 the 'single channel x 8 bit' acquisition software was used. These options within the Mark II version of the acquisition software are refered to in Chapter 2.6.4. The last two runs have used a new dual–counter 'single channel x 4 bit' acquisition package, which is described in Appendix 1, since it has only very recently been implemented. The data from each run was analysed using standard fast Fourier techniques.

5.5.2 Results and Discussion

Any pulsed component in the light from SN1987a was not expected to be visible for some time after the initial explosion. As of April 1989 the present observations have not shown any evidence of a pulsar at the centre of the remnant. In early days the debris and dust resulting from that explosion would tend to hide any pulsar. Woosley and Phillips (1988) note that the optical depth due to electron scattering is expected to remain large for about two years following the explosion. It is not surprising therefore that the early runs show no sign of any periodic structure in the light from SN1987a. The results of a single 4096K point FFT of the data from Run 12, only a little over 1 month after the supernova appeared, is shown in Figure 5.12. Not all of the 2048K spectral points have been plotted in Figure 5.12. Instead, the lower plot is the average of consecutive 512 spectral points, and the upper plot is the maximum power in the same 512 points. The minimum of each of the consecutive 512 frequency bins has not been plotted, but lies along the zero axis.

In Figure 5.12, three large spikes around 82, 164 and 246 Hz result from the calibration LED described in Section 5.2. It was decided to leave the LED system turned on during some of the early runs as a check to ensure that the system was functioning correctly. The increase in power at low frequencies is attributable to seeing, transparency, and tracking effects. Clearly there are no significant spikes in the spectrum, apart from the LED, from frequencies around 40 Hz up to 1250 Hz. The low frequency section of this spectrum is presented in Figure 5.13 to show it in more detail. It is not obvious from the plot in Figure 5.13(a) whether or not any of the very low frequency spikes are significant. To resolve this matter the spectrum has been normalised with respect to the mean and then re–plotted as Figure 5.13(b). This is justified, since the power distribution in each 512 point bin can be approximated by a chi–squared distribution whose standard deviation is equal to the mean. Hence, the plot in Figure 5.13(b) is effectively a plot of the number of standard deviations the maximum power in the consecutive 512 frequency bins was above the mean power.

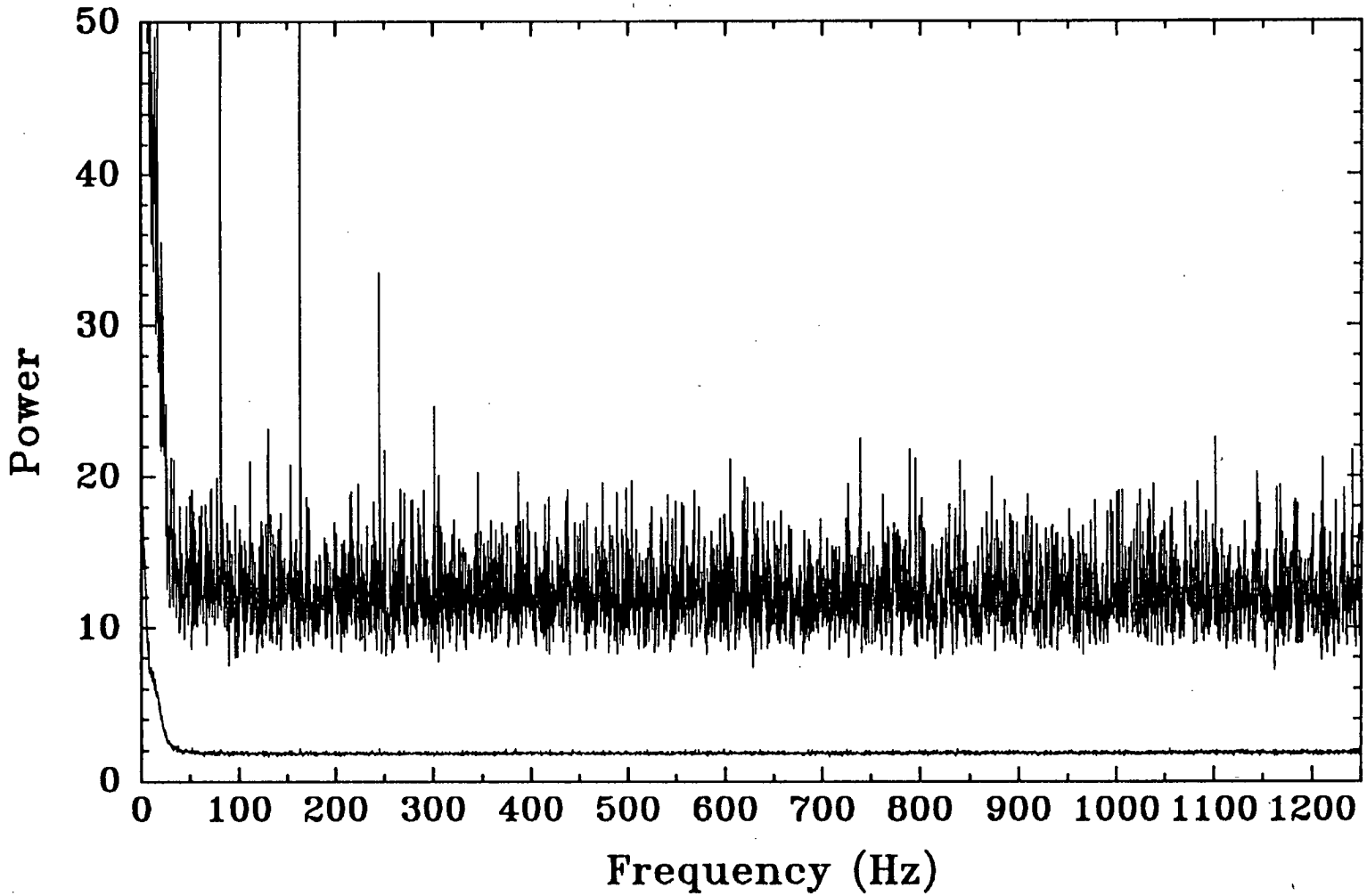

Figure 5.12

The FFT power spectrum of ~1678 s of data from SN1987a on the 23rd of April 1987. The data were acquired with a sample rate of 2.5 kHz. The spectrum is the result of a single 4096K point transform. The lower curve is the mean power of each consecutive 512 spectral points and the top curve is the maximum taken from each of the 512 points. The minimum powers have not been plotted, but lie along the zero axis. The spikes near 82, 164, and 246 Hz are due to a calibration signal from a LED. No other significant spikes are present.

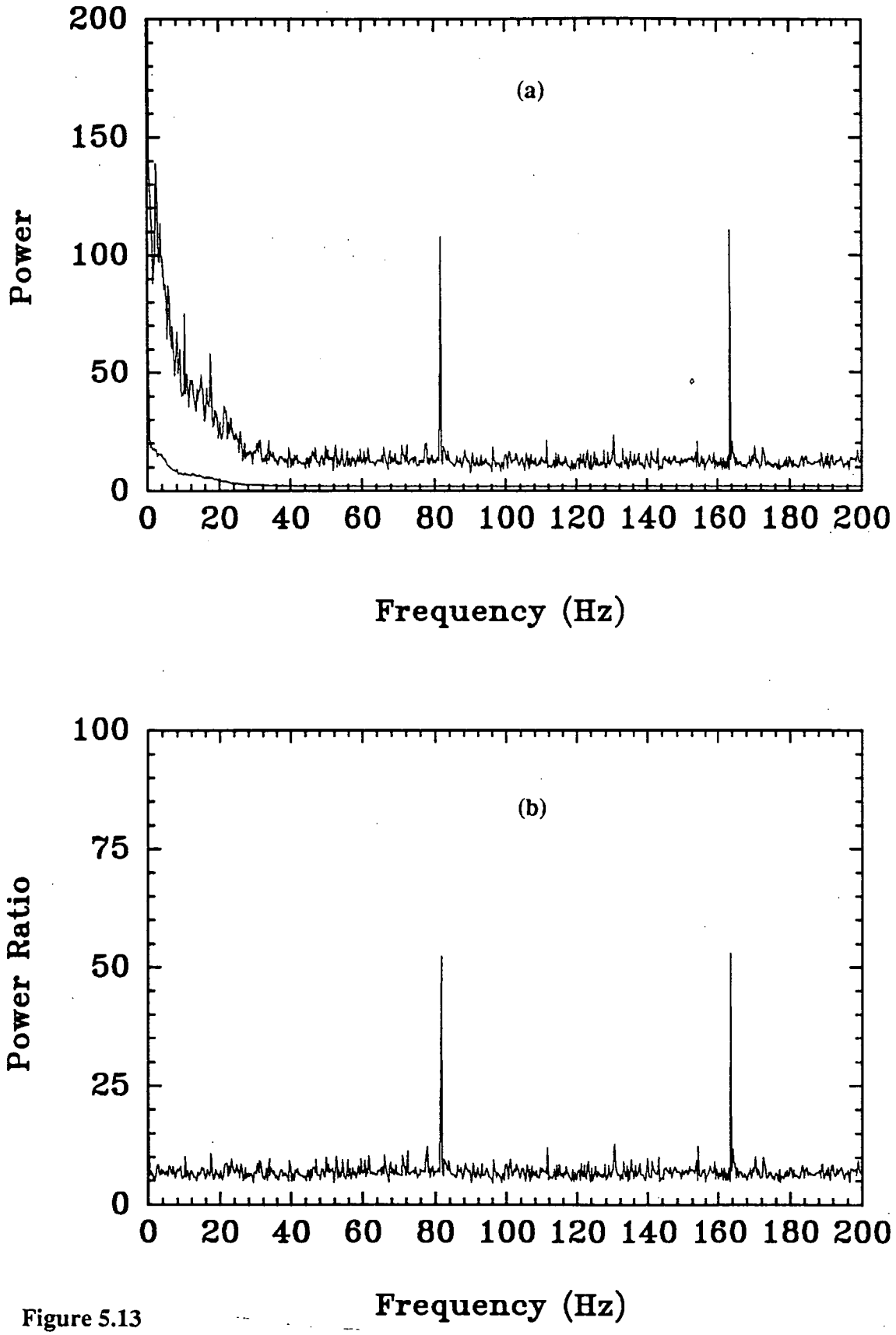

Figure 5.13
Panel (a) shows the low frequency part of the spectrum from Figure 5.12 in more detail. To determine whether or not any of the very low frequency spikes were significant, and remove the effect of increasing power at the very low frequencies, the upper plot in panel (a), representing the maximum power, has been normalised with respect to the lower plot in panel (a), which represents the mean power. The result is shown in panel (b).

Figure 5.13(b) indicates that none of the spikes in the very low frequency part of the Figure 5.13(a) spectrum are significant.

For the Figure 5.12 data, a conservative estimate of the sensitivity, to the presence of any sinusoidal signal in the data, can be obtained using Equation 5.2. Given that the largest noise peak in the power spectrum between 30 Hz and 1250 Hz has a value of ~24, and that the mean count rate for this run is 47.0 counts per sample, then the maximum power corresponds to an amplitude of $\sim 2.3 \times 10^{-2}$ counts per sample, or 0.05 percent of the mean supernova count rate. This is equivalent to a modulation with an integrated flux 8.3 mag fainter than the supernova. The I magnitude of the supernova at around this time was ~2.3 (Suntzeff and Haumy, 1987). This places an upper limit to any modulation in the I band for Run 12 at $m_I \approx 10.6$. Similar calculations may be undertaken for other runs.

The first, as yet un–confirmed, evidence for a rapidly rotating pulsar at the centre of the supernova remnant was reported by Middleditch et al. (1989). This evidence has been detailed fully by Kristian et al. (1989), who discuss a periodic signal at a frequency of 1968.629 Hz in observations from the 18th of January 1989. If this modulation is interpreted as the rotation frequency of the pulsar, then the SN1987a pulsar would be rotating at about three times the frequency of any other known pulsar. In an effort to verify this result, data were acquired at 6.0 kHz on observing Runs 35, 36, and 37, thus increasing the Nyquist frequency of the Mt. Canopus observations from 1250 Hz to 3000 Hz. After developing new acquisition software and hardware that could acquire the data at an even higher rate (Appendix I), the data in the last two runs reported here were acquired at a sample rate of 9.0 kHz, further increasing the Nyquist frequency to 4.5 kHz, well above the suspected pulsar spin rate.

The results of the FFT analysis of Runs 35, 36 and 37 are presented in Figure 5.14. The plot represents the average of 24 x 4096K point FFT's of overlapped data segments (8 FFT's from each run). The Figure 5.14 spectrum is presented in a similar manner to the one in Figure 5.12. Blocks of 512 frequency points have been grouped together in the spectrum, and the average power in each block is seen as as the central band of the three bands appearing in the power spectrum. The maximum and minimum power values for each block of frequency points respectively generate the upper and lower data bands in the figure. There are no significant features in this spectrum up to 3000 Hz. To place a 90 percent confidence level upper limit to the amplitude of any modulation, the method described by Lewin and Paradijs (1989) has been used. To

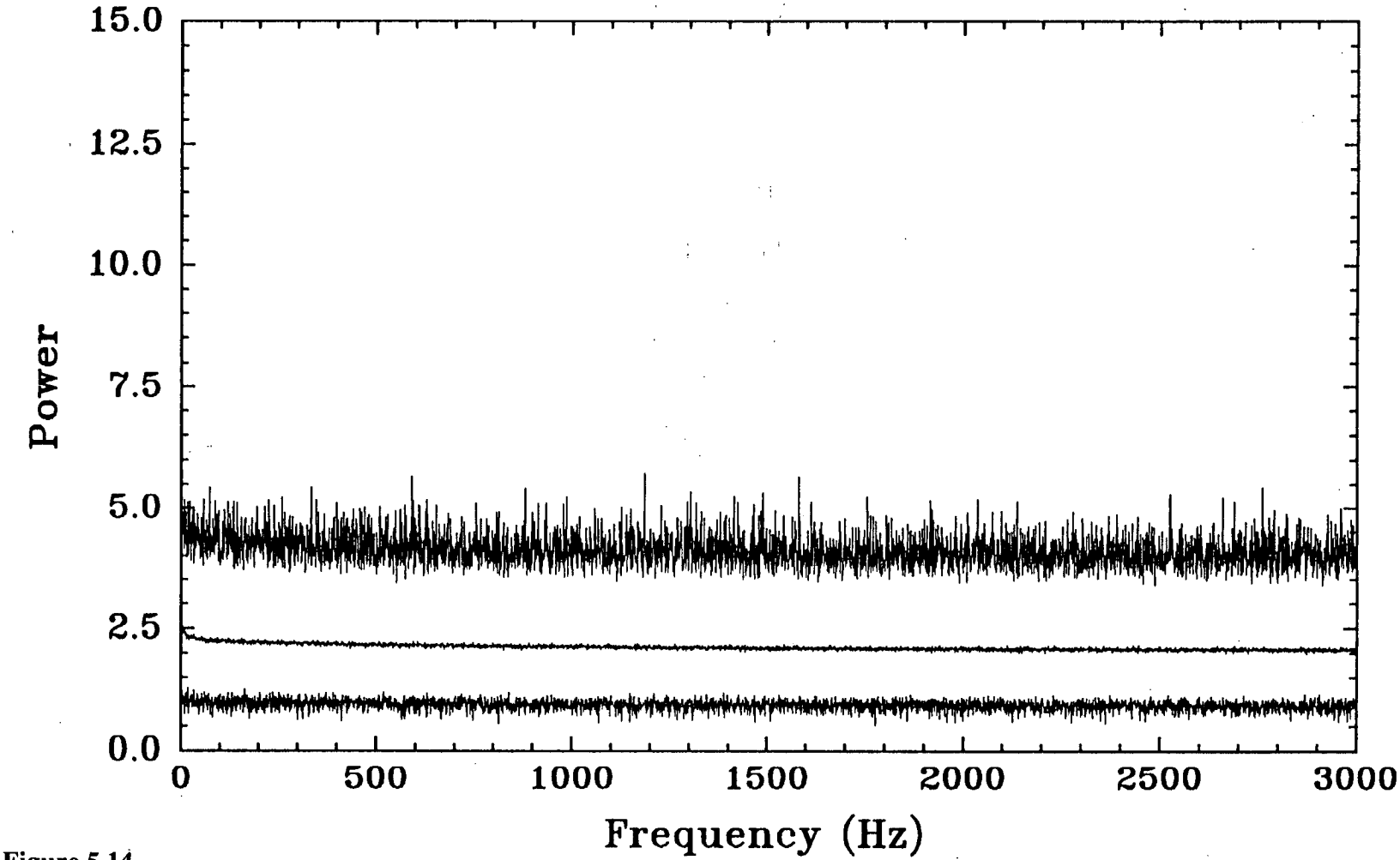

Figure 5.14

The FFT power spectrum of SN1987a data from the 11th of February 1989. The raw data consisted of ~157 min of samples obtained at 6.0 kHz. The spectrum is the average of 24 x 4096K point transforms of overlapped data segments. The spectral points have been grouped into blocks of 512 points for plotting. The mean power in each block appears as the central band in the spectrum. The maximum and minimum values for each block appear as the upper and lower bands. No significant peaks are present.

use this method it is necessary to obtain the cumulative probability distribution of the FFT powers in a frequency interval of interest. It is possible to use either a theoretical chi–squared distribution or, if enough spectral points are available, the distribution can be obtained directly from the FFT spectrum itself. The later method was used here. The probability distribution for the Figure 5.14 data, in the frequency interval 1500 Hz to 3000 Hz, is shown in Figure 5.15. In this case there is no significant change in the distribution when the frequency interval is extended to lower frequencies. The distribution is used to obtain the power value, P_{exceed}, that is exceeded 90 percent of the time by the noise. For this distribution $P_{exceed} \approx 1.45$. The power level corresponding to the 90 percent confidence upper limit is then defined by,

$$P_{ul} = P_{max} - P_{exceed}, \qquad 5.3$$

where P_{max} is the highest power in the range of interest. The maximum power between 1500 and 3000 Hz in Figure 5.14 is 5.6. Given that the mean count rate over the 3 runs was 0.69 counts per sample, and using Equation 5.2, a 90 percent confidence upper limit, for the amplitude of any sinusoidal component in the detected light, of 1.2×10^{-3} counts/sample is obtained. This corresponds to 1.7×10^{-3} of the mean light level. If the frequency interval is narrowed to ±20 Hz either side of the Middleditch et al. (1989) period, then the 90 percent confidence limit reduces to 1.5×10^{-3} of the mean light level, or 7.1 mag fainter than 'SN1987a + background'. The background contributed ~20 percent of the counts to the data in Runs 35, 36, and 37, and so the 90 percent confidence upper limit to any sinusoidal component of the modulation ± 20 Hz either side of the Middleditch et al. period is reduced to ~6.8 mag fainter than the supernova. On this particular night the supernova V magnitude, estimated from the extrapolation of a visual light curve given by Berki et al. (1989), was around 12.1. Thus the upper limit to any modulation in the light from the supernova for these runs would be around magnitude 19. Kristian et al. (1989) estimate their detected periodic signal to have had an integrated flux in the magnitude range 18.0 to 19.0.

The results of the FFT analysis of Run 39 are presented in Figure 5.16. This plot represents the average of 17 x 4096K point FFT's and is presented in a similar manner to power the spectrum in Figure 5.14. No significant peaks are present and the 90 percent confidence upper limit ±20 Hz either side of the Middleditch et al. (1989) period was calculated to be ~18.6 mag., given that the supernova was at ~13.0 mag. at the time.

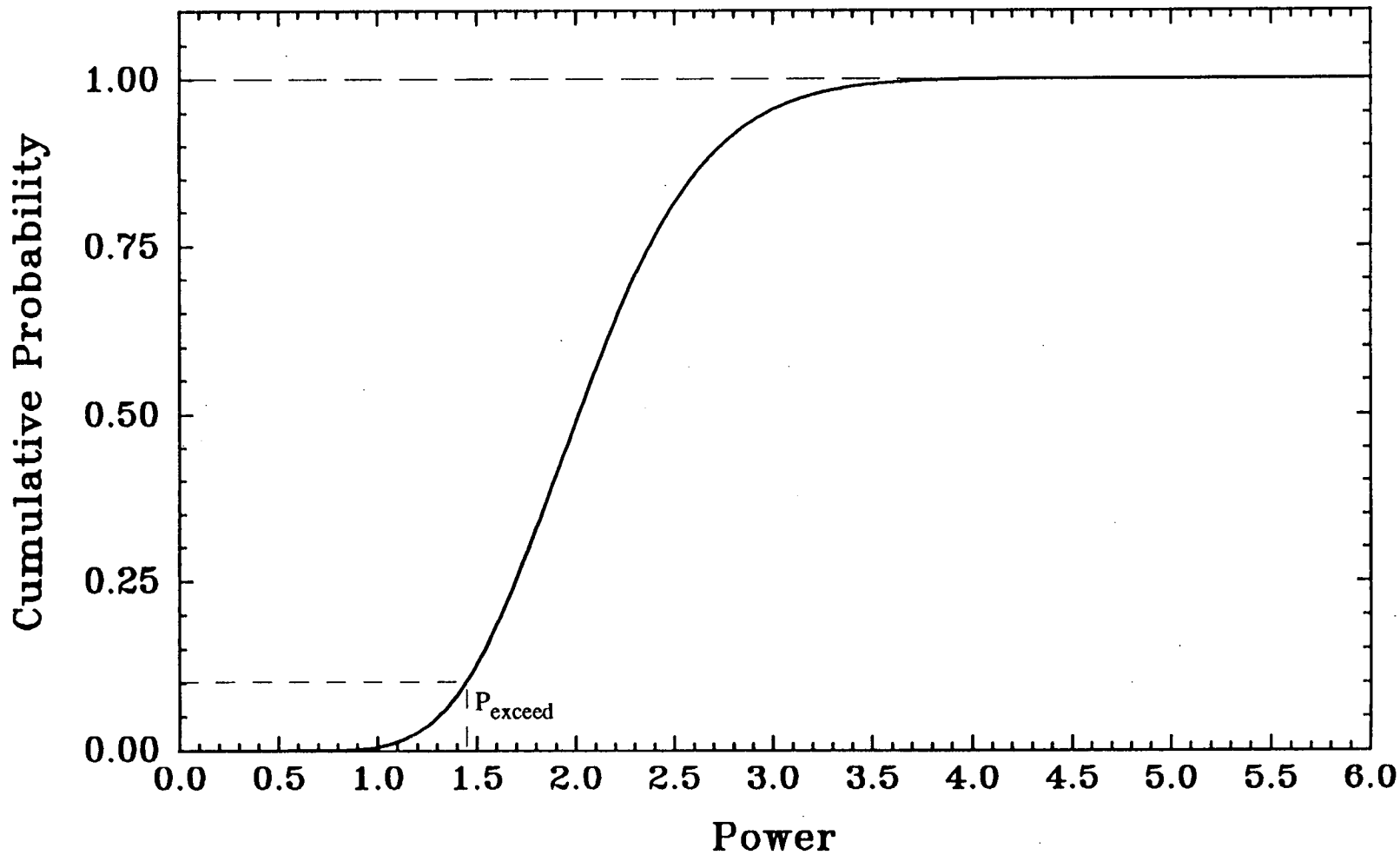

Figure 5.15
The cumulative probability distribution from the Figure 5.14 FFT powers in the frequency interval interval 1.5 kHz to 3.0 kHz. P_{exceed} is the value of the power that is exceeded 90 percent of the time.

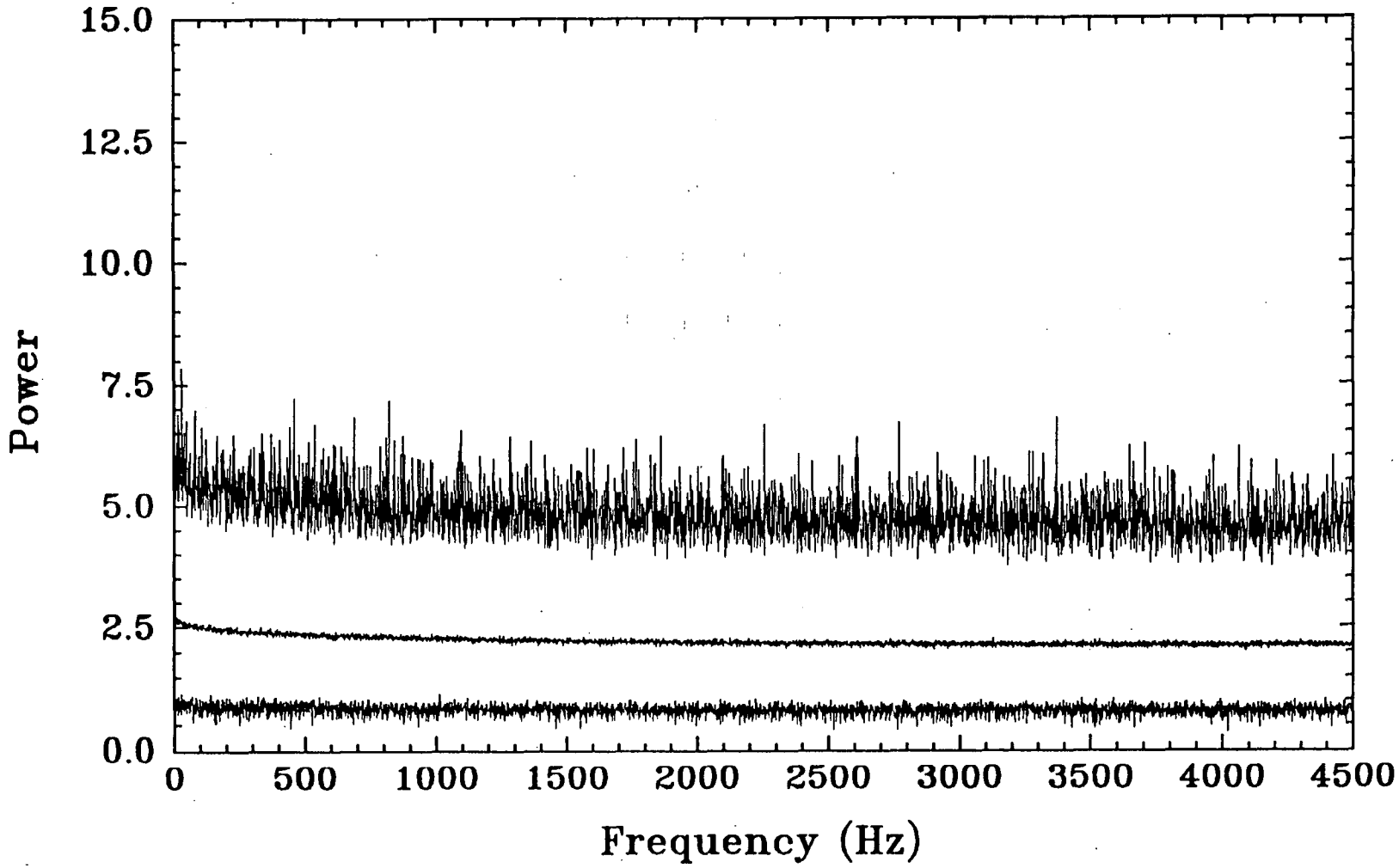

Figure 5.16

The FFT power spectrum of SN1987a data from the 4th of April 1989. The raw data consisted of ~70 min of samples obtained at 9.0 kHz. The spectrum is the average of 17 x 4096k point transforms of overlapped data segments. The spectral points have been grouped into blocks of 512 points. The mean power in each block appears as the central band in the spectrum. The maximum and minimum values for each block appear as the upper and lower bands. No significant peaks are present.

One interesting aspect of the spectrum in Figure 5.16, unrelated to the supernova, is the non–zero slope of the spectrum at high frequencies ($\lesssim$100 Hz). Unlike the spectrum in Figure 5.12 this rise is not attributable to atmospheric or aperture effects. A closer inspection of the data reveals a non–Poisson component in the distribution of counts. This particular run had a mean count rate of 0.16 counts per sample and so the probability of getting, say, 10 counts in one sample is given by,

$$\frac{0.16^{10} \times e^{-0.16}}{10!} = 2.6\times10^{-15}.$$

That is, even given the large number of samples (4.07×10^{7}), we would not expect even a single sample to contain 10 or more events. However, such events are present. In fact there were 60 events that contained as many as 15 counts, which is the maximum count that can be stored in 4 bit data. The largest number of counts that one would expect to see in a single event, with the above mean, would be 5, or 6. The excess events in the 6 to 15 counts range amounted to only 0.018 percent of the total flux. These large counts could possibly result from cosmic ray events in the photomultiplier tube, the non–Poisson dark current, natural radioactivity, or afterpulses in the photomultiplier tube. The manufacturer's notes on photomultiplier tubes state that afterpulses occur between 300 ns and 3 μs after the initial pulse. Simulated data consisting of a Poisson component with an extended tail at high count rates, similar to the observed distribution, was unable to reproduce the sloping spectrum. It simply raised its mean power level. However, when a fraction of the large counts (counts>4) was allowed to increase the count rate of the following sample, a spectrum very similar to the real data resulted. This would seem to indicate that the large pulses, perhaps due to cosmic rays, either tend to produce afterpulses or cause the pre–amplifier to ring. The effect is also noticeable in the Figure 5.14 spectrum, although to a lesser degree. This is presumably since the mean photon count rate is higher, and hence the Poisson component is larger, compared with the constant cosmic ray background and dark current components. In either case these are small effects and will not change the supernova results. However, in general, by acquiring data with a high sample rate, it would be possible to remove these spurious counts from the data, using their Poisson probability as the rejection criterion.

It is worth noting that, while the Middleditch et al. (1989) period remains unconfirmed, two points lend strong support to their observations. Firstly, observation of other stars immediately after the observation of SN1987a, using the same equipment, did not reveal any pulsations. Secondly, a variation in the detected

frequency in SN1987a, over the eight hour observing period, is fitted reasonably well by a sinusoid only when the data is corrected for the Doppler shift of the Earth and its motion around the Sun. If the pulsation is real, then a possible reason for negative results since the January 18th detection is that the original detection was made through a temporary hole in the debris around the pulsar, and that hole has subsequently closed. Further observations are required to resolve this problem and perhaps confirm the Middleditch et al. result. The relatively bright stars within a few arcseconds of SN1987a will eventually determine our limiting sensitivity. As the supernova fades their contribution to the number of detected photons will increase. However, it is possible that, even though the supernova light as a whole is decreasing, when the debris begins to clear, the contribution of any pulsed source may increase sufficiently to be visible above the background stars. Hence SN1987a will continue to be monitored at around 1 to 2 month intervals.

5.6 Observations of a Grazing Stellar Occultation by Pluto

The usefulness of ultra-high speed photometry is not restricted to observations of rapidly spinning objects, such as the optical counterparts of the X–ray and radio pulsars, or the white dwarfs in DQ Her systems. Events much closer to Earth requiring high–time resolution measurements are stellar occultations by solar system objects. These events are particularly suited to measuring the dimensions and positions of solar system bodies, and also sometimes yield data on the occulting star. The occultation converts the problem from one of angular resolution of the telescope to a simple matter of timing.

5.6.1 Stellar Occultations

Since an occultation observation consists of measuring the amount of light transmitted past the solar system object, then the limiting resolution is determined principally by diffraction effects in the cases of lunar or asteroidal occultations, or by refraction effects in the case of occultations by planetary bodies with atmospheres. In the diffraction limited cases the resolution is limited by the Fresnel scale. It is thus possible to obtain stellar dimensions with orders of magnitude improvement over direct means of measurement. The basic limitation, at least as far as stellar diameter measurements are concerned, is the apparent brightness of the star in question. The high–time resolution needed for such work restricts measurements to the brighter stars, since at low count rates photon noise will dominate the data.

Lunar occultations have the advantage of being fairly numerous, since the Moon sweeps out a considerable area of sky each night. However, this advantage is partially offset by the bright background of scattered moonlight. Nather (1970) notes that, for an ~9^{th} mag star, the resulting light curve is so noisy, due to statistical fluctuations in the background, that it is of little value. Such a high background would require the use of neutral density filters in the case of our photon counting circuitry. Asteroidal occultations offer slightly more potential, since such observations are not subject to the high lunar background light levels. Another advantage is the greater distance to the asteroid, which results in a larger fringe separation at the Earth. However, this last point must also be considered against the potentially larger velocity of the asteroid shadow at the Earth, when compared with a lunar shadow velocity of ~1 km s^{-1}. For example, a recent occultation of the star SAO158222 by the minor planet 241 Germania, which at the time was approximately 10^3 times more distant than the Moon, and hence had a fringe spacing of ~32 times that of a similar lunar occultation, had an apparent motion of ~6.4 "h^{-1}. This meant that its shadow crossed the Earth with a velocity of ~3.3 km s^{-1}. When combined, these two effects result in a factor of ~9.6 increase in resolution over a similar lunar occultation. However, gains in resolution of 2 to 3 are more common. The major drawback associated with asteroidal occultations, except for a few of the larger asteroids, is that the asteroid's shadow, projected onto the Earth, is the same dimension as the asteroid itself. Although this allows the dimensions of the asteroid to be measured with some degree of accuracy, especially if several observations are made at different positions in the path, it necessarily means that the path width of the shadow is small, and has a high probability of missing fixed observatories. The large distances associated with the asteroids also means that small errors in their predicted position and motion can result in the predicted shadow path being many asteroid diameters from the actual shadow path. With all this in mind, I have made observations of a dozen or so asteroidal occultations predicted for the New Zealand / South Eastern Australia region, that could have had shadow paths close to Mt Canopus observatory. However, in all cases so far observed , the shadow has missed the observatory.

Planetary occultations have the advantage that their shadow path is much wider than the path of the shadow for asteroidal events, and hence the probability that an event will occur for a particular location is increased considerably. Planetary occultations, on the other hand, are of little value in determining stellar diameters. In the case of planetary occultations, the immersion and emergent light curves are dominated by atmospheric refraction effects (Baum and Code, 1953; Goldsmith, 1963; Wasserman

and Vevaerka, 1973; French et al., 1978). The initially parallel rays from the star are fanned out as they pass through the planet's atmosphere, and hence one observes a gradual reduction in the light from the star instead of the sharp transition characteristic of lunar and asteroidal events. Hence, planetary occultations provide a method of probing the atmospheres of planets, giving information on dimensions, temperatures, pressures and composition (Kovalesky and Link, 1969; Freeman and Lynga,1970).

5.6.2 Observations of the P8 Event

The remainder of this section deals with the observation of an occultation of a star by Pluto, using the Mt. Canopus telescope and the Mark II data acquisition option. Mink and Klemola (1985) published a list of 10 possible Pluto occultations, P1 to P10, between 1985 and 1990. The initial predictions indicated that the event P8 was a particularly good candidate, and would be visible from the northern Pacific. However, in the months prior to the event, refined predictions indicated that the occultation would be visible from the North Island of New Zealand and most of Australia (Wasserman et al., 1988). Last minute predictions were provided by R.L. Millis of Lowell Observatory and G.L. Blow of Carter Observatory. On the night of the 9th of June 1988 the P8 event, when Pluto occulted a 12th mag star, provided the first confirmed stellar occultation data for this remote object. The event was observed at 12 sites (5 visual) in Australia and New Zealand, and also by the Kuiper Airborne Observatory ~5500 km south of Hawaii (IAUC 4611, 4612 and 4620). Table 5.4 presents the details of the sites that observed a dimming of the star during the occultation event (Blow, 1988). The most northerly and southerly sites constrain the size of Pluto, and analysis of the combined data gathered from these sites will provide a direct measurement of Pluto's size and shape..Figure 5.17 shows the approximate path of Pluto's shadow as it crossed the Earth, as seen from Pluto's perspective. The sites that acquired a photometric record of the event are also shown in this figure. The number besides each location corresponds to the site number in Table 5.4

The Mt. Canopus observations of the P8 event were made in unfiltered light through a 30 arcsec aperture, which included Pluto, Charon and the occulted star. The data were acquired at 1 kHz and summed later to obtain a light curve with an acceptable signal–to–noise ratio. Over–sampling the data in this way ensures that as little information as possible is lost. It is a simple matter to sum consecutive samples to recover the data with a lower time resolution. The occulted star and Pluto–Charon were observed with the same system, at the same airmass, again on the 3rd of July 1988. This second observation was to allow the 9th of June data to be corrected for the

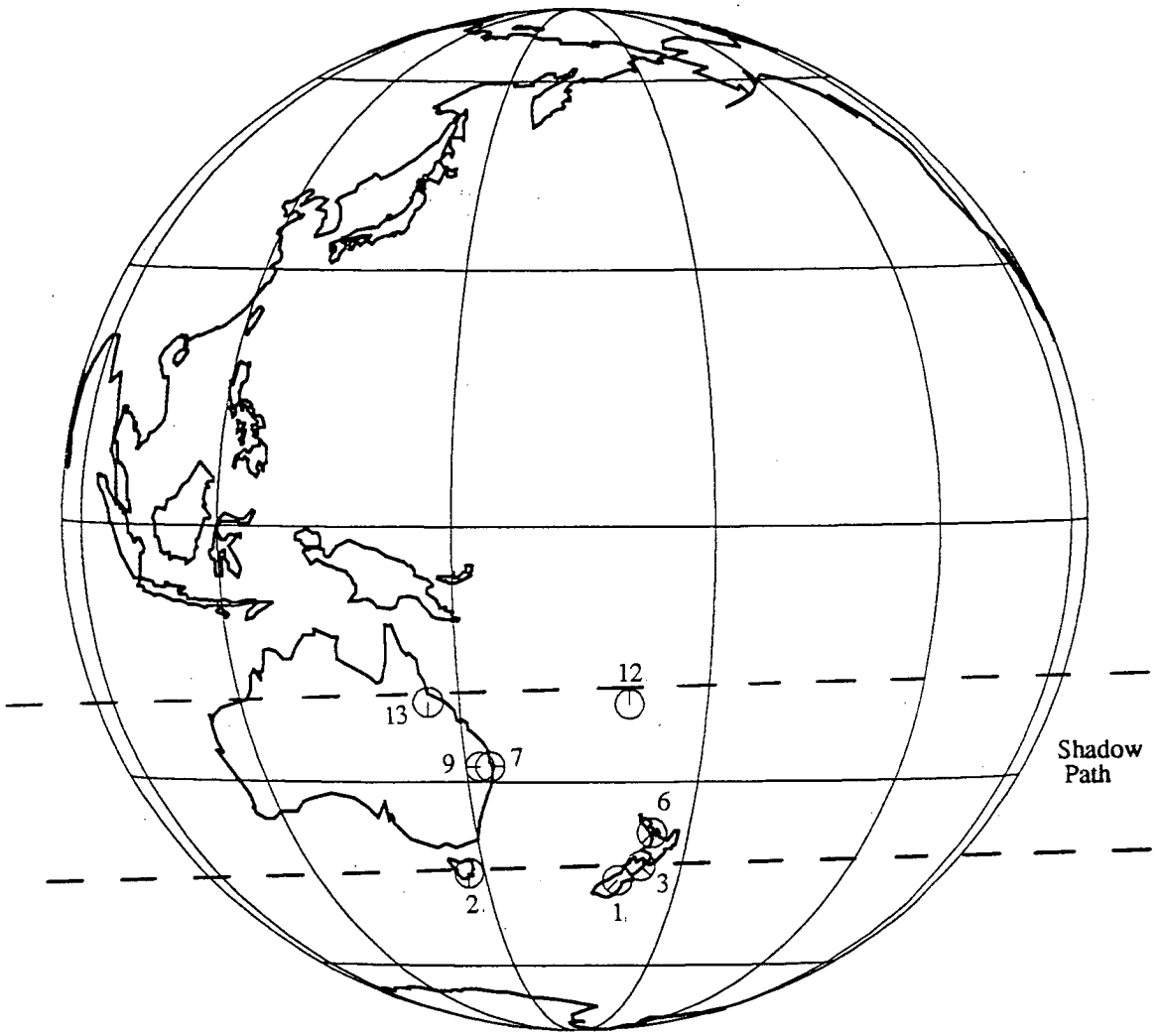

Figure 5.17
The path of Pluto's shadow as it crossed the Earth's surface for the P8 event, as seen from Pluto's perspective. The sites that acquired a photometric record of the event are shown with circles. The number beside each site corresponds to the site numbers in Table 5.4.

Table 5.4

Ground Based Observing Sites that Detected the P8 Event

Site no.	Location	Long. ° ' "	Lat. ° ' "	Telescope Size,detector
1	Mt John(a), NZ	170 27 53.8	–43 59 14.7	0.61, photometer
	Mt John(b), NZ			0.61, photometer
	Mt John(c), NZ			1.0, photometer
2	Mt Canopus, Tas	147 25 53.1	–42 50 57.3	1.0, photometer
3	Black Birch, NZ	173 48 13.0	–41 44 55.9	0.41, photometer
4	Lower Hutt, NZ	174 56 03.7	–41 12 48.3	0.35, visual
5	Tawa, NZ	174 48 52.9	–41 10 34.0	0.20, visual
6	Auckland, NZ	174 46 37.9	–36 54 28.0	0.50, photometer
7	Mt Tamborine, Qld	153 12 47.7	–27 58 20.7	0.32, photometer
8	Witches Falls, Qld	153 10 45	–27 56 30	0.33, visual
9	Darling Downs, Qld	151 51 32	–27 47 58	0.35, photometer
10	Woodridge, Qld	153 05 43.5	–27 38 18.7	????, visual
11	Nebo, Qld	148 44 04	–21 44 05	0.25, visual
12	K.A.O.(Ingress)	170 40 12	–20 25 06	0.9, CCD
	K.A.O.(Egress)	170 29 48	–20 14 48	
13	Charters Towers ,Qld	146 15 40	–20 00 30	0.36, photometer

background light from Pluto–Charon. The 'Star/Pluto–Charon' count ratio from the 3rd of July observation was 0.206. However, assuming Pluto's regular brightness variation, it was 0.141 mag fainter on the 3rd of July. After correcting the 'Star/Pluto–Charon' ratio for this change, it becomes 0.234 ±0.004. This is in good agreement with the KAO white light CCD band value of 0.234 ±0.002., measured on the 9th of June (Elliot et al., 1989). The corrected Mt Canopus occultation light curve of the P8 event is presented here in Figure 5.18. The light curve is in units of unocculted stellar flux, summed to a time resolution of 1 s. The smooth curve drawn through the data was obtained by heavily filtering the light curve. Figure 5.18 immediately reveals two important results. Firstly, the stellar signal displays a gradual diminution, characteristic of the presence of an atmosphere, rather than the abrupt change that is expected for an occulting body without an atmosphere. Secondly, during the occultation, the stellar flux fell to only just below half of its unocculted value and displayed a rounded minimum, indicating the grazing nature of the event.

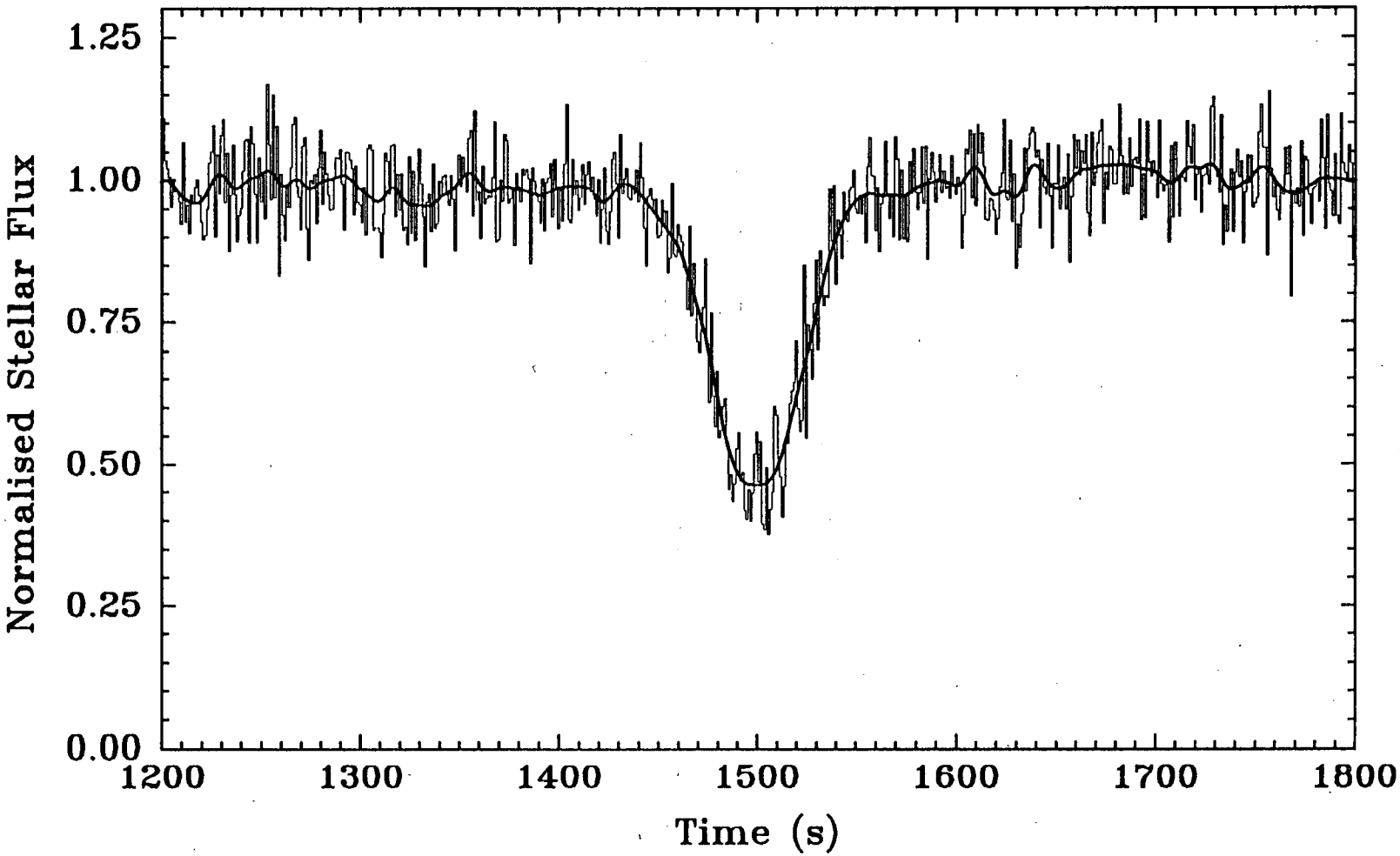

Figure 5.18
The Pluto occultation light curve for the P8 event on 9th of June 1988, as a function of the fraction of transmitted stellar flux. The data have been plotted with a time resolution of 1 s, and start at 10:15:00 UT.

5.6.3 Results and Discussion

For the Mt. Canopus site, at the time of the P8 event, one second of time corresponded to a Pluto displacement, relative to the star, of 18.26 km (Hubbard et al., 1988). Thus the observed ~115 s duration of the occultation in Figure 5.18 corresponds to a chord length of ~2100 km at Pluto. This is comparable to the radius of the solid planet, R_p=1142 ±9 km (Tholen and Buie, 1988). The long duration of the event is even more astonishing when one considers that the Mt Canopus chord was slightly outside the limb of the planet (Hubbard et al., 1988). A schematic of the Pluto–Charon configuration at the time of the occultation, and showing the extent of Pluto's atmosphere based solely on the Mt Canopus chord length, is presented in Figure 5.19. The Pluto–Charon configuration is based on the system moving at 2.95 " h^{-1} with a position angle of 269 deg, and with Charon ~0.52" to the south of Pluto and leading Pluto by 3 to 4 min of time (Blow, 1988). The Mt Canopus result confirms the early predictions by Trafton (1980), and Hunten and Watson (1982), that Pluto may have a substantial atmosphere.

In Figure 5.18 there is some indication that the ingress, at least in the early stages, is somewhat more extended than the egress. This asymmetry also exhibits itself in the Mt John and Auckland data, but its presence in the Black Birch data is uncertain due to telescope guiding problems during the egress. If this effect is real, then it may indicate an asymmetric distribution of the mass in Pluto's atmosphere. One possible explanation that initially comes to mind is that the tidal forces exerted on Pluto by the close proximity of Charon result in an atmospheric tidal bulge. This explanation is consistent with the Pluto–Charon orientation shown in Figure 5.19. However, the KAO data did not show an asymmetry in the opposite sense, as would be expected from a symmetric tidal bulge. Hubbard et al. (1988) also note that gravitational distortions from spherical symmetry should only be noted at higher altitudes than those probed by stellar occultations.

Because the Pluto atmosphere is comparable in thickness to the radius of the planet itself, the standard stellar occultation theory used for thin atmospheres (Baum and Code, 1953; Bartholdi and Owen, 1972) requires modification. W.B. Hubbard and D.M. Hunten derived a new theory for an isothermal atmosphere, at temperature T, to model the Mt Canopus occultation data (Hubbard et al., 1988). The isothermal assumption was used since it is the simplest to model and should be adequate over the small height range that controls the optical light curve. The Hubbard et al. model assumes that Pluto's atmosphere is composed of a single molecular species with

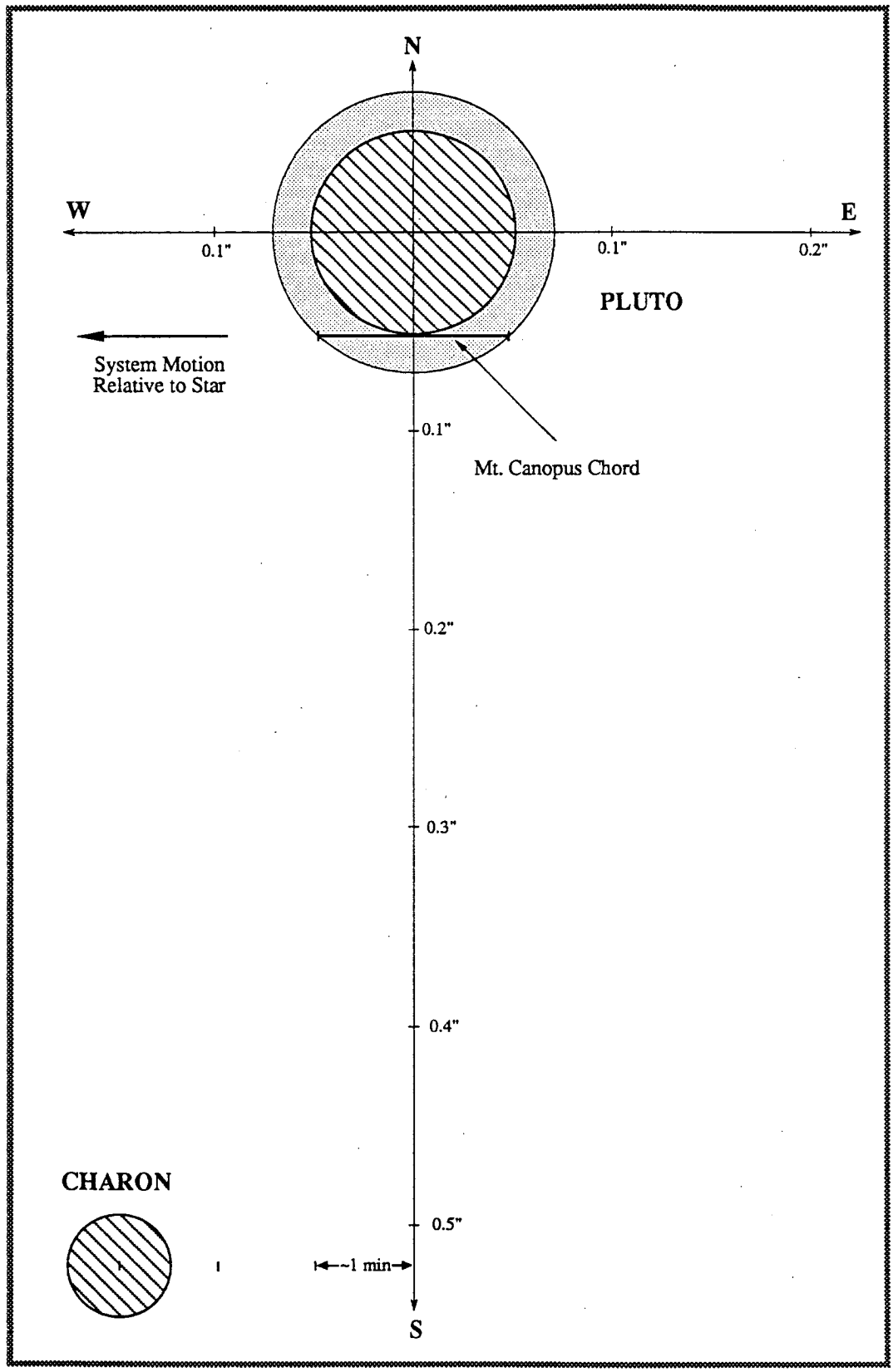

Figure 5.19
A schematic of the Pluto-Charon configuration at the time of the P8 occultation event. The extent of Pluto's atmosphere probed by the Mt Canopus chord is also shown.

molecular mass m. The ratio of gravitational potential energy to thermal energy, defined by a parameter λ, is given by

$$\lambda = \frac{G\ M\ m}{r\ K_b\ T}\ , \qquad 5.4$$

where G is the gravitational constant, M is Pluto's mass ($M=1.29 \times 10^{25}$ g, Elliot et al., 1989), r is the distance from the centre of Pluto, and K_b is Boltzmann's constant. A likely candidate for the major atmospheric molecule is methane, whose ice absorption features appear in the planet's spectrum (Cruikshank et al.,1976; Buie and Fink, 1987). For hydrostatic equilibrium, the number density of molecules in Pluto's atmosphere, as a function of λ, is given by

$$n(r)= n_0\, e^{(\lambda-\lambda_0)}\ , \qquad 5.5$$

where n_0 is the molecular number density at the surface, and λ_0 is λ at $r=a_0$, with a_0 being Pluto's radius. For a spherical atmosphere, the observed stellar flux described by the model is related to four parameters. These are λ_0, which has already been defined, and three others, y_0, t_0, and K_0. The parameter y_0 is the minimum distance between the chord and the optical axis. The optical axis is the line connecting the centre of Pluto and the star. The parameter t_0 is the time at which the minimum distance y_0 occurs. The final parameter, K_0, is defined by the product $D \times N_0$, where D is the observer's distance from Pluto, and N_0 is the refractivity of the gas at $r=a_0$. For methane, the refractivity N is 4.41×10^{-4} at STP. Hence, $K_0 = D \times N_0 = 5.1 \times 10^7 \times \frac{P_0}{T}$, where P_0 is the surface pressure in ubar, T is in °K, and D is in cm. Plausible surface temperatures for Pluto lie in the range 46 °K to 64 °K, depending on the rate of heating by sunlight and on the planet's thermal properties (Tafton, 1980). This temperature range is consistent with a methane atmosphere produced by sublimation of Pluto's surface ice. Two model atmospheres were considered, corresponding roughly to the likely temperature range. The *cold* atmosphere model assumed pure methane at T=50 °K (λ_0=28), and the *warm* atmosphere model assumed pure methane at T=61 °K (λ_0=23). To fit each model to the Mt Canopus data, λ_0 was held fixed and K_0, y_0, and t_0 were adjusted, using least squares, for the best fit . Figure 5.20 shows the results of the *warm* atmosphere fit to the data. Normalised stellar flux is plotted as a function of position x along the chord. Here x=0 corresponds to closest approach. The fit yielded y_0=1168 km, which is ~26 km above the limb of the planet, and P_0=5 μbar. The plot also shows the predicted stellar flux for chords in the range y_0= 0 to 1335 km, in steps of 167 km. The squares

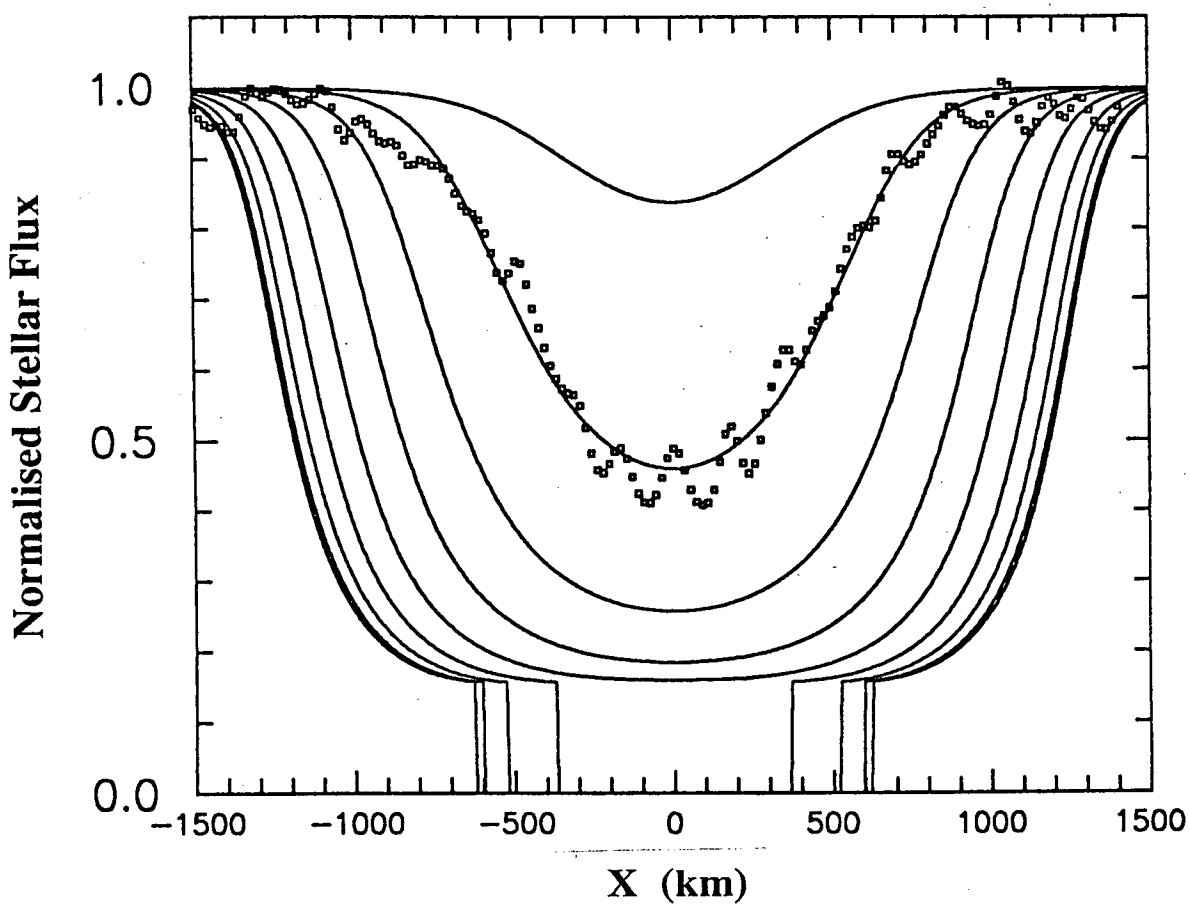

Figure 5.20
Stellar flux plotted against position along the chord, for nine chords in the *warm* atmosphere model (from Hubbard et al. 1988). The chords range from y_0 = 0 km to y_0 = 1,335 km, in steps of 167 km. The Mt Canopus chord, fitted by least squares, is at y_0 = 1,168 km, approximately 26 km above the limb of the planet. The squares mark the Mt Canopus data, smoothed by a Gaussian window with a 2 s characteristic width.

mark the data, smoothed by a Gaussian window with a 2 s characteristic width. The *cold* model was fitted in a similar manner, giving y_0=1234 km, about 92 km above the planetary limb, and P_0=18 ubar. Both the *warm* and *cold* atmosphere models are fitted equally well by the data. The maximum surface pressure consistent with spectroscopic measurements is 25 μbar (Buie and Fink, 1987; Sykes et al., 1987). Hence, the resultant surface pressure obtained from both fits is compatible with the earlier work.

The *cold* and *warm* atmosphere models do, however, predict different light curves for chords more central than the Mt Canopus one. In the *cold* atmosphere model, the transmitted star light never falls to zero, since P_0 is sufficiently high that the star light is never fully obscured by the planet. For near central chords the star light is enhanced due to focussing, and the light curves exhibit a central flash. In contrast, the *warm* model predicts that the star light will drop rapidly to zero for the more central chords. The model predicts that the transition from a central bright spot to a dark spot occurs near P_0=7 μbar. The two near central light curves, from Darling Downs and Mt Tamborine, support the *warm* model, in that neither show an enhancement of the star light near the central passage of the shadow. Also, the value of y_0 for the *warm* model is more consistent with preliminary astrometric solutions for the location of the Mt Canopus chord with respect to the shadow's centre (Elliot et al., 1989). Figure 5.21 is a schematic of Pluto's atmosphere, as determined by the Hubbard et al. (1988) model. It also illustrates the atmospheric temperature and density profiles for both the *warm* and *cold* models in the region probed by the occultation light curves. The dashed lines, connecting the isothermal curves, represent a possible modification to the constant temperature assumption very near to the surface. The exobase lies at 3,200 km and >5,000 km for the *cold* and *warm* models respectively.

Finally, it is worth commenting on the light curves from sites that probed deeper into Pluto's atmosphere than did the Mt Canopus chord. An interesting feature of these light curves is an abrupt drop in the signal just after the half–light level. The effect was seen in the Charters Towers, KAO and Auckland data, but could not be clearly identified in the Darling Downs and Mt Tamborine data because of their low signal–to–noise ratio. The effect is most clearly seen in the KAO data (Elliot et al., 1989), and is reproduced here as Figure 5.22. Elliot et al. (1989) successfully fitted the KAO data with an isothermal atmosphere, plus an extinction layer to produce the abrupt drop in signal. Their model is consistent with $T/\mu = 4.2 \pm 0.4$ °K/amu. For a pure methane atmosphere the corresponding temperature would be 67 ± 6 °K. However, Elliot et al. point out that their data is not inconsistent with other molecular species. For example, a

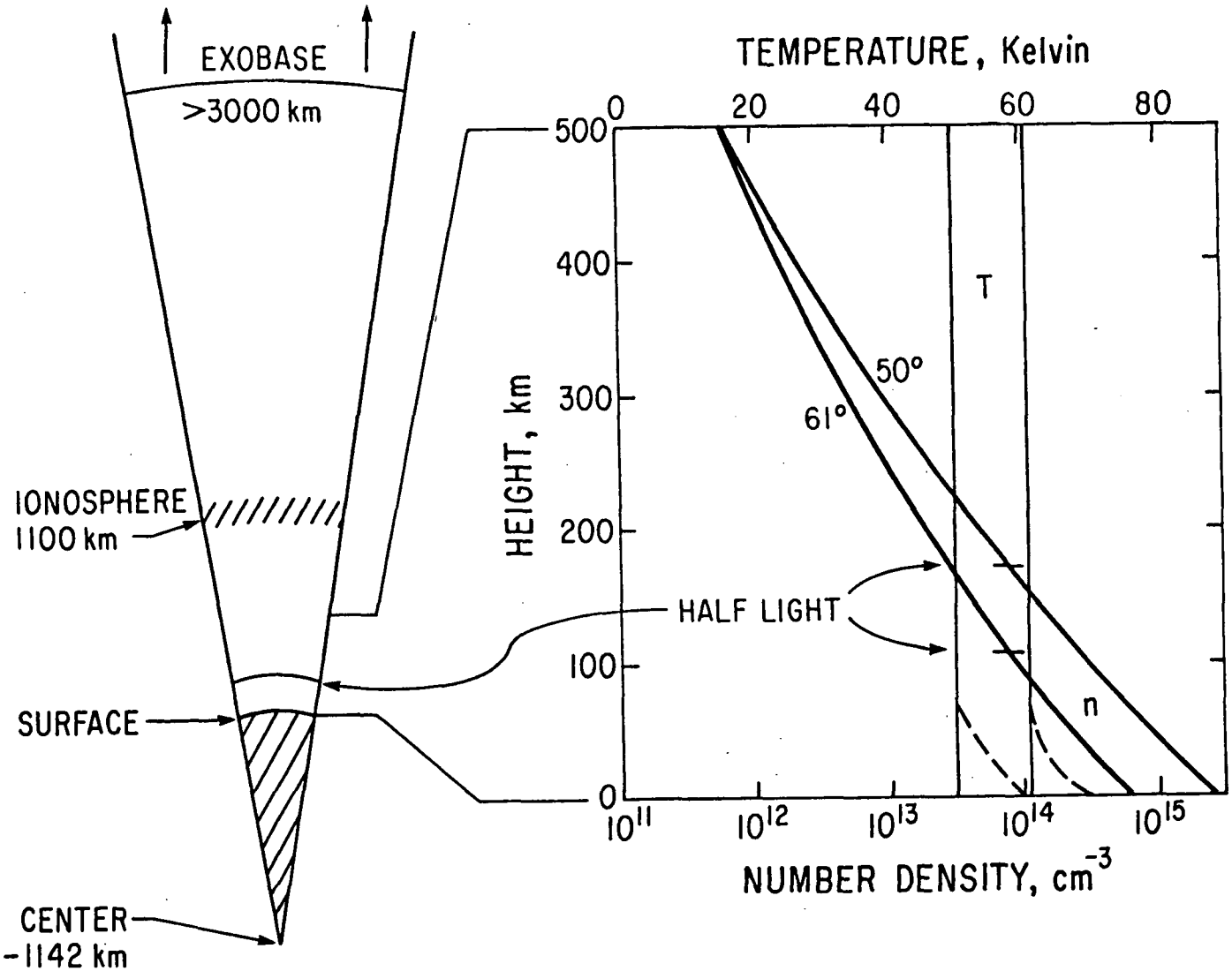

Figure 5.21
A schematic of Pluto's atmosphere showing the temperature and density profiles, assumed for the *warm* and *cold* models (from Hubbard et al., 1988). The curvature of the density profile is due to variation of gravity with height. The dashed lines represent a possible modification of the isothermal profiles.

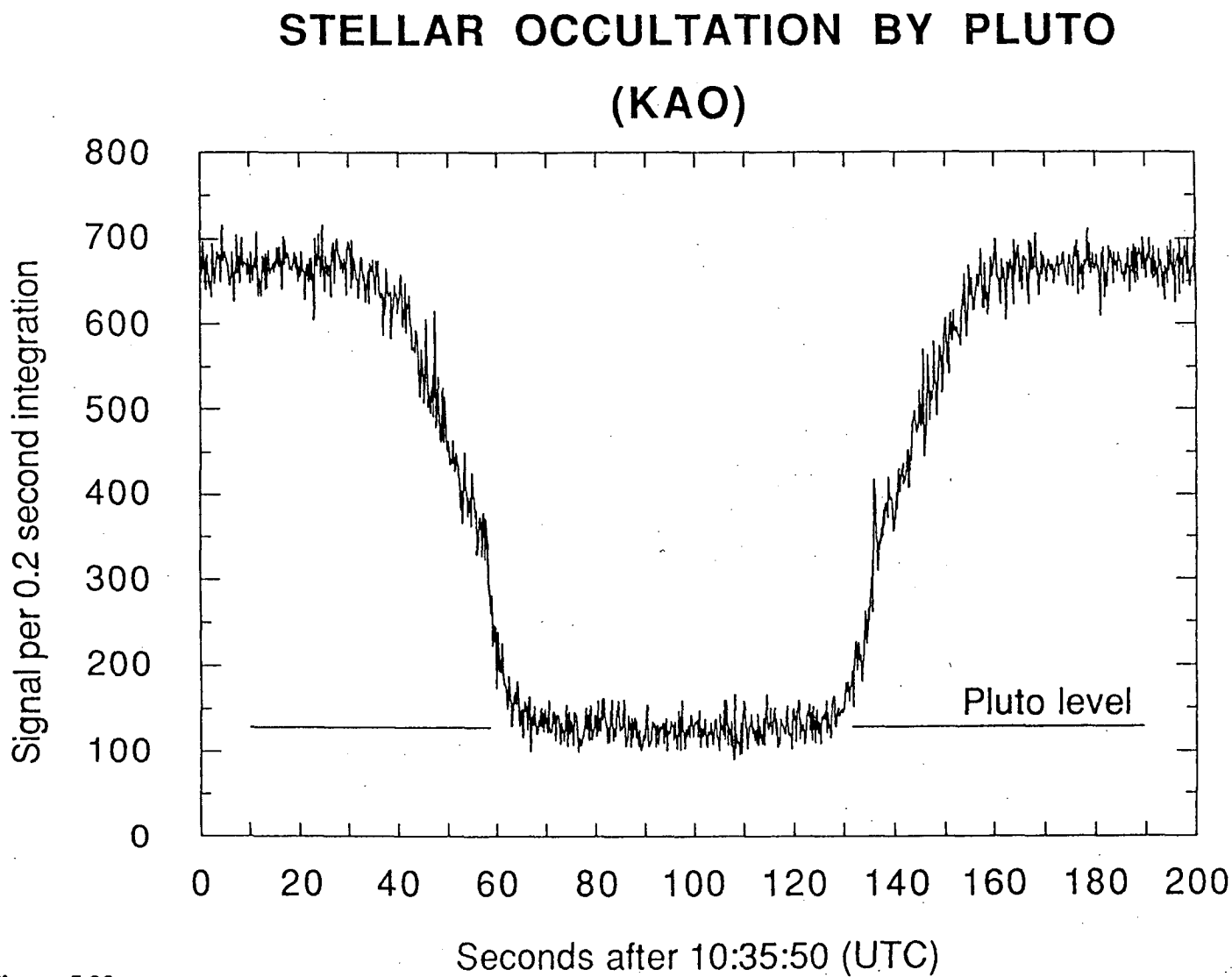

Figure 5.22
The Pluto occultation light curve for the P8 event on 9th of June 1988, obtained using the KAO (from Elliot et al., 1989). This particular chord probed deeper into the atmosphere than did the Mt Canopus chord. The sharp drop in light just after half-light lead Elliot et al. to suggest the presence of an extinction layer at low altitudes.

substantial nitrogen atmosphere at 117 °K would also fit their data. Recently, Hubbard et al., (1989) have modelled Pluto's atmosphere using non–isothermal temperature profiles and a methane atmosphere containing an appreciable fraction of molecules heavier than methane (CO and N_2). The temperature in this model varied from 106 °K in the high atmosphere to ~55 °K at its base. They note that similar effects to the haze layer postulated by Elliot et al. could be produced by a strong temperature gradient near the surface.

A combined analysis of the data from all of the sites listed in Table 5.4 is currently being undertaken by R.L. Millis, and will provide more information on the size of the planet and will hopefully reveal any variation from spherical symmetry in the planet or its atmosphere. No doubt future occultations by Pluto will be sought in order to verify the present results and obtain new data with a higher signal–to–noise ratio.

5.7 Conclusion

Data integrity is of foremost importance in any observing system and considerable effort has been expended to ensure that the Mark II photometric data acquisition system behaves as it was intended. From the results of the tests described in Section 5.1, it can be concluded that the Mark II option performs correctly and provides the user with a very useful and sensitive instrument. This has been illustrated with the results of observations of the Crab pulsar, short-timescale structure in the light from geostationary AUSSAT satellites, together with the limits placed on the Middleditch et al. (1989) pulsar candidate in SN1987a and the measurements of the Pluto occultation event P8.

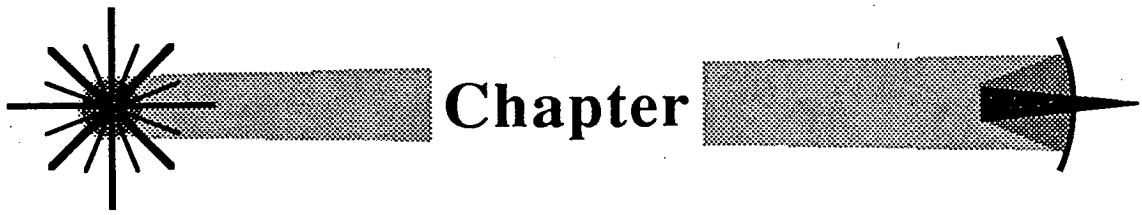

Chapter 6

CONCLUSIONS

A sensitive fast-photometer system has been successfully evolved, within over-riding budgetary constraints. It permits continuous acquisition of data, for up to ~69 min at a maximum sample rate of 9.8 kHz, while providing a real time display of the counts. The system has been thoroughly tested with a pulsing LED source and with observations of the Crab pulsar. This latter observation certainly represents the most southerly ground-based optical detection of the Crab's 33 ms pulsation. Future development of this photometer system should include the addition of a third photometric channel, to convert it into a '2-star' instrument, thus permitting transparency corrections on non-photometric nights. This could be achieved as a modification of the current photometer setup, either using an optical fiber, mounted in the offset guider x-y stage, to pipe the light from the comparison star to a third photomultiplier tube, or by mounting a photo-diode in the offset guider x-y stage, since comparison star measurements would not be required at high-time resolution.

Using the Mark I version of the fast-photometer system, an extensive photoelectric study program on the eclipsing DQ Her type cataclysmic variable EX Hya was undertaken. This program demonstrated the continued secular decrease in the period of the 67 min modulation in EX Hya, with $P/\dot{P} = -3.8 \times 10^6$ yr^{-1}. This $P/\dot{P}$ term is consistent with a white dwarf primary, and is interpreted as being due to angular momentum acquired from material when it couples to the magnetosphere of the white dwarf. The observed rate of change of period implies a mass transfer rate of the order

of ~$3x10^{-11}$ $M_\odot$ yr^{-1} and a magnetic moment around $8x10^{31}$ G cm^3. Two variations in the eclipse timings were identified. Firstly, one sees a long-term variation that has been fitted with an ~20 yr period sinusoid and which is consistent with solar-type cycles in the secondary star. Secondly, one sees a short-term variation which is correlated with the phase of the 67 min cycle. This second variation has been interpreted in terms of the eclipse of an accretion column or arc in the region above the magnetic pole of the white dwarf.

High time resolution spectroscopic data from EX Hya during an eclipse were obtained with the Anglo-Australian telescope on the 21st February 1987, to supplement the photometric data. These data are consistent with the general spectral characteristics noted by other workers. The V/R ratio of the spectral lines, around orbital phase $\Phi_{98}=0$, is consistent with the eclipse of an accretion disk. A sharp peak in the equivalent width of the Balmer lines is seen at the time of the eclipse. It is comparable in width to the X-ray eclipses, and narrower than the optical eclipses. This feature is attributed to the inner region of the eclipsed structure, where there is a stronger optical continuum emission and/or weaker Balmer line emission. Finally, the accretion curtain model of EX Hya has been shown to accommodate, in a qualitative sense, all the observational constraints that must be imposed on any model of the system.

The high temporal resolution attainable with the Mark II photometer system has been amply demonstrated with observations of geostationary spin-stabilised AUSSAT satellites A1 and A2, where temporal features of the order of 1 ms were detected. The satellites were found to exhibit many periodic features. Namely, a basic $f_o \approx 0.95$ Hz attributed to the satellites spin period, modulations at ~90 Hz and ~95 Hz associated with the placement of the solar cells on the spacecraft, and an ~266 Hz reflection from thermal radiator mirrors around their circumference. These features were only detected during the satellites' *on* states, which occur near the passage of the equinoxes, and last about one week. The exact time of the *on* state depends on the observers' latitude on the Earth. When the satellites are in their faint *off* state, no modulation was evident. However, future observations with longer data runs, and smaller apertures, to reduce the sky background, may provide enough sensitivity to detect their spin period in the *off* state. The satellites may be useful as occasional astronomical calibration sources, or in measuring some aspects of the transmission of the Earth's upper atmosphere during their eclipse by the Earth's shadow. The spin rate of the satellites can be easily measured to a few parts in 10^6 (Section 5.3.2), which may allow some study of the perturbing forces on the spacecraft. Long-term measurements of the reflected solar

spectrum may even provide a way of measuring the degradation of the solar cells. In all, these objects have provided a new and very interesting source for study.

The sensitivity attainable with the Mark II system was demonstrated in a program of monitoring SN1987a. An upper limit of 19^{th} magnitude was placed on any sinusoidal component in the light from SN1987a, from three observations in 1989 (February, March and April). This is fainter than the magnitude of the pulsations detected by Middleditch et al. (1989), which would indicate that the pulsation has weakened and now lies below our detection threshold. What was the source of the pulsations? Was the source seen through a transient hole in the surrounding debris? Was the pulsation really due to a rotating neutron star, or was some other mechanism responsible? These questions will probably remain unanswered unless the Middleditch et al. source can be re-observed. Hence continued fast-photometric monitoring of SN1987a is of vital importance. If the source strength turns out to vary irregularly for some reason, observations with a telescope as small as 1 m may provide useful information.

Finally, using the Mark II system, observations of a grazing stellar occultation by Pluto have shown that it possesses an extended atmosphere, whose thickness is comparable to the radius of the planet itself. This fact alone makes Pluto a unique object in the solar system. The occultation light curve has been successfully modelled by W.B. Hubbard and D.M. Hunten from the Lunar and Planetary Laboratory of the University of Arizona, and was found to be consistent with the effects produced by refraction in an isothermal atmosphere of methane at a temperature of 61 °K. The data from sites with more central chords in this occultation event have led to the suggestion that the isothermal assumption may not be valid at low altitudes, and an appreciable temperature gradient may exist near the surface (Hubbard et al. 1989). As a consequence, heavier molecules such as CO and N_2 may also be present in Pluto's atmosphere.

The Mt Canopus Mark II photometer system has thus been shown to be a valuable tool in the study of a diverse range of phenomena in optical astronomy.

APPENDIX 1

Following the announcement by Middleditch et al. (1989), of the detection of an ~1968 Hz modulation in the light from SN1987a, a means was sought to increase the sample rate of the Mark II photometer data acquisition system, in an effort to detect that signal. The increase in time resolution was achieved with only minor software and hardware changes, and at little cost. The modification of the acquisition system was in two parts. Firstly, the counts were stored as 4 bit numbers instead of 8 bit numbers. This change halved the number of bits that had to be written to the disk, and doubled the maximum length of a continuous data run. However, it also meant that the largest number of counts per sample would be 15. This was considered to be acceptable, as is shown by the following calculation. A typical SN1987a count rate in early 1989 of $\sim 10^4$ c s^{-1}, and a sample frequency of 5.0 kHz, would result in a mean count rate of 2 counts per sample. Since the counts follow a Poisson-distribution, with mean x, the probability of exceeding n counts is given by

$$P(n) = 1 - \sum_{i=0}^{n} x^i \frac{e^{-x}}{i!}, \qquad \text{A.1}$$

Thus the probability of exceeding 15 counts with a mean count rate of 2 per sample is only $\sim 4.8 \times 10^{-10}$, or once in every ~4.8 d at 5 kHz. This figure is naturally better at higher sample rates. Hence, four bits is more than adequate with a count rate of 2 counts per sample or less.

The second change involved some additional hardware as follows. The high speed mode would only use the sky+star channel (SSC) photomultiplier tube; hence the counter for the sky channel would not be in use. If the SSC was switched between the two counters then this would halve the number of interrupts required to read the accumulated counts. The first clock pulse would gate the counts from the SSC into counter A. The next clock pulse would gate the counts from the SSC into counter B. The following clock pulse would initiate the usual interrupt sequence (Section 2.6.1), causing both counters to be latched and cleared, and this clock pulse would also begin

repeating the sequence again by gating the SSC counts into counter A. The setup and timing of this hardware modification is illustrated in Figure A.1.

The modified system was successfully tested with sample rates as high as 9.8 kHz. It allows continuous data streams of up to ~74 min to be acquired at a sample rate of 9 kHz. Higher sample rates would be attainable by disabling the real time display of the data. However, such a course of action would probably result in a loss of data quality because of undetected guide errors and so has not been implemented. No doubt higher sample rates could also be achieved by re-designing the counters, so that the data were transferred into the computer using direct memory access (DMA) rather than interrupts. However, this course of action would be reasonably expensive, and is not warranted with the present computer system. Should higher time resolution photometry be required, then a better solution, costing probably only marginally more, would be to develop a system based around an 80286 or 80386 machine with their more readily available, and less expensive, off-the-shelf peripherals. At the present time the current system is quite adequate, with its main disadvantage being its relatively high maintenance costs.

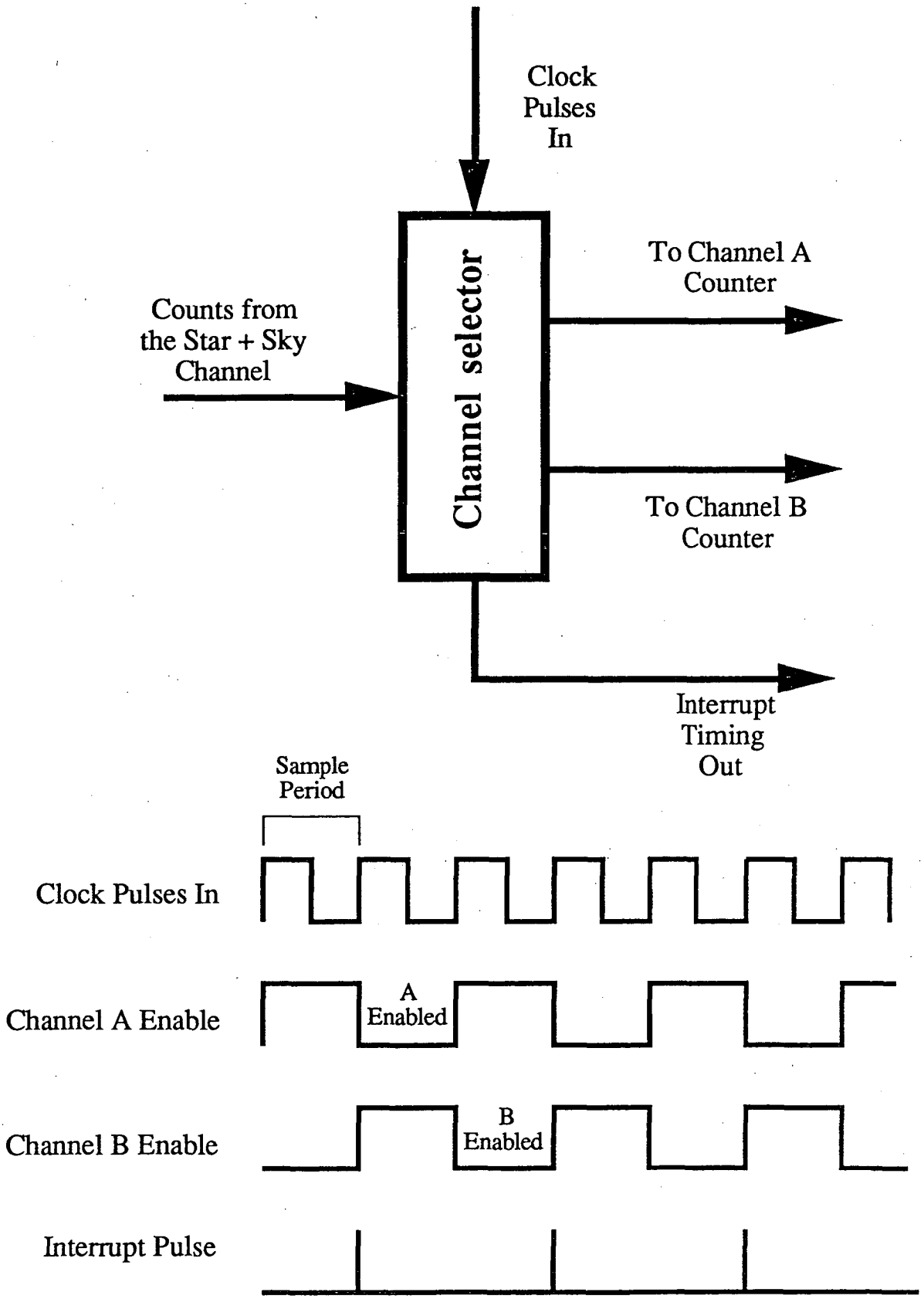

Figure A.1
A schematic diagram showing the single channel dual counter setup and its associated timing diagram.

References

Arnett, W., (1987), Astrophys. J., **319**, p. 136.

Bailey, J., (1975), J. Br. astr. Assoc., **86**, p. 30.

Bailey, J., (1980), Mon. Not. R. astr. Soc., **190**, p. 119.

Bartholdi, P., Owen., F., (1972), Astron. J., **77**, p. 60.

Bateson, F.M., (1979), in "Changing Trends in Variable Star Research", IAU Coll. No. 46, p. 89., eds., F.M. Bateson, J. Smak, J Ulrich, pub. D. Reidel.

Bateson, F.M., Goltz, W., Jones, A.F., McIntosh, R., (1986), Publ. Var. Star Sect. R. astr. Soc. New Zealand, **14**, p. 52.

Bath, G.T., Pringle, J.E., Whelan, J.A., (1980), Mon. Not. R. astr. Soc., **190**, p. 185.

Bath, G.T., Edwards, A.C., Mantle, V.J., (1983), in "Cataclysmic Variables and Related Objects", p. 55., eds., M. Livio., G. Shaviv., pub. D. Reidel.

Bath, G.T., (1984), Astrophys. and Space Sci., **99**, p. 127.

Bath, G.T., Pringle, J.E., (1985), in "Interacting Binary Stars", p. 177.,eds. J.E. Pringle, R.A.Wade, Cambridge University Press.

Baum, W.A., Code, A.D., (1953), Astron. J., **58**, p. 108.

Becker, R., Marshall, F., (1981), Astrophys. J., **244**, L93.

Bergland, G.D., Doland, M.T., (1987), in "Programs for Digital Signal Processing", p. 1.2-1, eds. Digital Signal Processing Committee IEEE Acoustics, Speech, and Signal Processing, pub. John Wiley New York.

Berki, G., Cramer, N., Burnet, N., Rufener, F., Pernier, B., Richard, C., (1989), The Messenger, No 55., p. 51.

Berriman, G., Beattie, D.H., Gatley, I., Lee. T.J., Mochnacki, S.W., Szkody, P., (1983). Mon. Not. R. astr. Soc., **204**, p. 1105.

Beuermann, K., Osborne, J.P., (1984), in "X-ray Astronomy '84, International Symp. on X-ray Astronomy", Bologna Italy., p. 23., eds., M. Oda, R. Giacconi, Institute of Space and Astrophysical Science, Tokyo.

Beuermann, K., Osborne, J.P., (1985), Space Sci. Rev., **40**, p. 117.

Beuermann, K., Osborne, J.P., (1988), Astron. Astrophys., **189**, p. 128.

Blow, G.L., (1988), private communication.

Bond, I.A., Freeth, R.V., Marino, B.F., Walker, W.S.G., (1987), Info. Bull. Var. Stars., No. 3037.

Bond, I.A., Freeth, R.R., (1988), Mon. Not. R. astr. Soc., **232**, p. 753.

Breysacher, J., Vogt, N., (1988), Astron. Astrophys., **87**, p. 349.

Buie, M.W., Fink, U., (1987), Icarus, **70**, p. 483.

Cannizzo, J.K., Wheeler, J.C., Ghosh, P., (1985), in "Cataclysmic Variables and Low-Mass X-ray Binaries", p. 307., eds., D.Q. Lamb, J. Patterson. , pub. D.Reidel.

Cannizzo, J.K., Kenyon, S.J., (1987), Astrophys. J., **320**, p. 319.

Cannizzo, J.K., Pudritz, R.E., (1988), Astrophys. J., **327**, p. 840.

Cohen, J.G., (1987), in "Instrumentation for Ground–Based Optical Astronomy", p. 448, ed. L.B. Robinson, pub. Springer-Verlag.

Cordova, F.A., Riegler, G.R., (1979), Mon. Not. R. astr. Soc., **188**, p. 103.

Cordova, F.A., Mason, K.O., (1983), in "Accretion Driven Stellar X-raySources", p. 147., eds. W.H.L. Lewin, E.P.J. Van Den Heuvel, Cambridge University Press.

Cordova, F.A., Mason, K.O., Khan, S.M., (1985), Mon. Not. R. astr. Soc., **212**, p. 447.

Cowley, A.P., Hutchings, J.B., Crampton, D., (1981), Astrophys. J., **246**, p. 489.

Cropper M., Mason, K.O., Allington–Smith, J.R., Branduari–Raymont, G., Charles, P.A., Mittaz, J.P.,D., Mukai, K., Murdin, P.G., Smale, A.P., (1989), Mon. Not. R. astr. Soc., **236**, p. 29p.

Cruikshank, D.P., Pilcher, C.B., Morrison, D., (1976), Science, **194**, p. 835.

Edwards, A., (1987), AUSSAT Pty. Ltd., private communication.

Edwards, A., Hope D., (1987), The Third National Space Engineering Symposium, Canberra, Australia, p. 94.

Elliot, J.L., Dunham, E.W., Bosh, A.S., Slivan, S.M., Young, L.A., Wasserman, L.H., Millis, R.L., (1989), Icarus, **77**, p. 148.

Elsner, R.F., Lamb, F.K., (1977), Astrophys. J., **215**, p. 897.

Frank, J., King, A.R., Sherrington, M.R., Giles, A.B., Jameson, R.F., (1981), Mon. Not. R. astr. Soc., **196**, p. 921.

French, R.G., Elliot, J.L., Gierasch, P.J., (1978), Icarus, **33**, p. 186.

Freeman, K.C., Lynga, G., Astrophys. J., **160**, p. 767.

Friend, M.T., Martin, J.S., Connon Smith, R., Jones, D.H.P., (1988), Mon. Not. R. astr. Soc., **233**, p. 451.

Gallagher, J.S., Holm, A.,V., (1974), Astrophys. J. Lett., **189**, p. 303.

Gallagher, J.S., Starfield, S., (1978), Ann. Rev. Astron. Astrophys., **16**, p. 171.

Geisel, S.L., Kleinmann, D.E., Low, F.J., (1970), Astrophys. J. Lett., **161**, p. L101.

Ghosh, P., Lamb, F.K., (1979), Astrophys. J. **234**, p. 296.

Gilliland, R.L., (1982), Astrophys. J., **258**, p. 576.

Glasby, J.S., (1970), "The Dwarf Novae", Pub Constable and Co. London.

Goldsmith, D.W., (1963), Icarus, **2**, p. 341.

Gorian, P., Henry, D., (1986), The Second National Space Engineering Symposium, Sydney, Australia, Vol 2, 7B.1.

Heise, J., Mewe, R., Kruszewski, A., Chlebowski, T., (1987), Astron. Astrophys., **183**, p. 73.

Hellier, C., Mason, K.O., Rosen, S.R., Cordova, F.A., (1987), Mon. Not. R. astr. Soc., **228**, p. 463.

Hellier, C., Mason, K.O., Smale, A.P. ,Corbet, R.D.H., O'Donoghue, D., Barrett, P.E., Warner, B., (1989), Mon. Not. R. astr. Soc., **238**, p.1107.

Hill, K.M., Watson, R.D., (1984), Proc. astr. Soc. Aust., **5**, p. 532.

Hill, K.M., Sharma, D.P., Watson, R.D., (1986), in "Instruments and Research Programs for Small Telescopes", IAU Symp. **118**, p. 289., eds, J.B. Hearnshaw, P.H. Cottrell, pub., D. Reidel.

Hoffmeister, C., Richter, G., Wenzel, W., (1984), in "Variable Stars",p. 79.,pub. Springer-Verlag.

Hope, W., Edwards, A., Poynton, B., Hope, W., (1986),The Second National Space Engineering Symposium, Sydney, Australia, Vol 1, 1.3.

Hubbard, W.B., Hunten, D.M., Dieters, S.W., Hill, K.M., Watson, R.D., (1988), Nature, **336**, p. 452.

Hubbard, W.B., Yelle, R.V., Lunine, J.I., (1989), Icarus, submitted.

Hunten, D.M., Watson, A.J., (1982), Icarus, **51**, p. 665.

Jablonski, F., Busko, I.C., (1985), Mon. Not. R. astr. Soc., **214**, p. 219.

Jensen, K.A., (1985), in "Cataclysmic Variables and Low-Mass X-ray Binaries", p. **407**, eds., D.Q. Lamb, J. Patterson., pub. D.Reidel.

Kaitchuck, R.H., Hantzois, P.a., Kakaletris, P., Honeycutt, R.K., Schlegel, E.M., (1987), Astrophys. J., **317**, p. 765.

King, A.R., (1983), in "Cataclysmic Variables and Related Objects", p. 181., eds., M. Livio., G. Shaviv., pub. D. Reidel.

Kitchin, C.R.,(1982), in "Early Emission Line Stars", p. 77., ed., A.J. Meadows, pub. Adam Hilger Ltd., Bristol.

Kovalevsky, J., Link, F., (1969), Astron. Astrophys., **2**, p. 398.

Kraft, R.P., (1962), Astrophys. J., **135**, p. 408.

Kraft, R.P., Krzeminski, W., (1962), Annual Report of the Director Mt. Wilson and Palomar Observatories, 1961-1962., p. 20.

Kristian, J. Pennypacker, C.R., Middleditch, J., Hamuy, M.A., Imamura, J.N., Kunkel, W.E., Lucinio, R., Morris, D.E., Muller, R.A., Perlmutter, S., Rawlings, S.J., Sasseen, T.P., Shelton. I.K.,Steiman-Cameron, T.Y., Tuohy, I.R., (1989), Nature, **338**, p. 234.

Kruszewski, A., Mewe, R., Heise, J., Chlebowski, T., Van Dijk, W., Bakker,R., (1981), Space Sci. Rev., **20**, p. 221.

Kruszewski, A., Mewe, R., Heise, J., Chlebowski, T., Van Dijk, W., Bakker,R., (1982), in "Binary and Multiple Stars as Tracers of Stellar Evolution", p. 457., eds., Z. Kopal, J. Rahe, pub. D.Reidel.

Lamb, D.Q., (1985), in "Cataclysmic Variables and Low-Mass X-ray Binaries", p. 151., eds., D.Q. Lamb, J.Patterson.,pub. D.Reidel.

Lamb, D.Q., Melia, F., (1987), Astrophys and Space Sci., **131**, p. 511.

Lewin, W.H.G, van Paradijs, J., van der Klis, M., (1988), Space Sci. Rev., **46**, p. 273.

Liebert, J., Stockman, H.S., (1985), in "Cataclysmic Variables and Low-Mass X-ray Binaries", p. 151., eds., D.Q. Lamb, J.Patterson., pub. D.Reidel.

Lomb, N.R., (1975), Astrophysics and Space Science., **39**, p. 447.

MacDonald, J., (1983), in "Cataclysmic Variables and Related Objects", p. 77., eds., M. Livio., G. Shaviv., pub. D. Reidel.

Mantle, V.J., Bath, G.T., (1983), Mon. Not. R. astr. Soc., **202**, p. 151.

Mantle, V.J., (1985), in "Cataclysmic Variables and Related Objects", p. 301., eds., M. Livio., G. Shaviv., pub. D. Reidel.

Marsh, T. R., Horne, K., Shipman, H.L., (1987), Mon. Not. R. astr. Soc., **225**, p. 551.

Mason, K.O., (1985), Space Sci. Rev., **40**, p. 99.

Meyer, F., Meyer-Hofmeister, E., (1981), Astron. Astrophys., **104**, p. L10.

Middleditch, J., Pennypacker, C., Morris, D.E., Muller, A., Perlmutter, S., Sasseen, T., Kristian, A., Kunkel, W.E., Hamny, M.A., Imamura, J.N., Steiman–Cameron, T.Y., Shelton, I.K., Tuohy, I.R., Rawlings, S., (1989), IAU Circ, No. 4735.

Mink, D.J., Klemola, A., (1985), Astron., J., **90**, p. 1894.

Mumford, G.S., (1964), Pub. Astron. Soc. Pacific, **76**, p. 57

Mumford, G.S., (1967), Astrophys. J. Suppl., **15**, p. 1.

Nather, R.E., (1970), Astron. J., **75**, p. 583.

Oke, J.B., (1982), Astrophys. J. Suppl., **27**, p.31.

Oke, J.B., Gunn,J.E., (1983), Astrophys. J., **266**, p. 713.

Papaloizou, J., Pringle, J. E., (1977), Mon. Not. R. astr. Soc., **181**, p. 441.

Paterson, J., (1984), Astrophys. J. Suppl., **54**, p. 443.

Paterson, J., Raymond, J.C., (1985A), Astrophys. J., **292**, p. 535

Paterson, J., Raymond, J.C., (1985B), Astrophys. J., **292**, p. 550

Payne–Gaposchkin, C., (1957) "The Galactic Novae", eds. J.H.Oort M.G.J. Minnaert, H.C. van der Hulst ,pub. North-Holland Publishing Co. Amsterdam.

Petterson, J.A., (1980), Astrophys. J., **241**, p. 247.

Press, W.H., Flannery, P., Teukolsky. S.A., Vetterling, W.T., (1986) in "Numerical Recipes: The Art of Scientific Computing", p. 428, pub. Cambridge University Press.

Pringle, J.E., (1975), Mon. Not. R. astr. Soc., **170**, p. 633.

Pringle, J.E., Savonije, G.J., (1979), Mon. Not. R. ast. Soc., **187**, p. 777.

Pringle, J.E., (1981), Ann. Rev. Astron. Astrophys., **19**, p. 137.

Ritter, H., (1984), Astron. Astrophys., **57**, p. 385.

Ritter, H., (1985), Astron. Astrophys., **148**, 207.

Ritter, H., (1986), in "The Evolution of Galactic X-ray Binaries", p. 271.,eds. J.Truemper,W.H.G.Lewin,W.Brinkmann, pub. D.Reidel.

Robinson, E.L.,(1975), Astron. J. **80**, p. 515.

Robinson, E.L.,(1976),Ann. Rev. Astron. Astrophys., **14**, p.119

Rosen, S.R., Mason, K.O., Cordova, F.A., (1988), Mon. Not. R. astr. Soc., **231**, p. 549.

Sahade, J.,Wood, F.B., (1978), in "Interacting Binary Stars", p.101 , ed. D. Ter Haar, pub.Pergamon Press.

Shafter, A.W., Szkody, P., Thorstensen, J.R., (1986), Astrophys. J., **308**, p. 765.

Sherrington, M.R., Lawson, P.A., King, A.R., Jameson, R.F., (1980), Mon. Not. R. astr. Soc., **191**, p. 185.

Smak, J., (1971), Acta Astron., **21**, p. 15.

Smak, J., (1983), Astrophys. J., **272**, p. 234

Smak, J., (1984), Publ. Astr. Soc. Pacific, **96**, p. 5.

Smak, J., (1987), Astrophys. and Space Sci., **131**, p. 497.

Starrfield, S., Sparks, W.M., (1979), Astrophys and Space Sci., **131**, p. 379., pub. D. Reidel.

Starrfield, S., Sparks, W.M., Truran, J.W., (1985), Astrophys. J., **291**, p. 136.

Sterkin, C., Vogt, N., Freeth, R., Kennedy, H.D., Marino, V.F., Page, A.A., Walker, W.S.G., (1983), Astron. Astrophys., **118**, p. 325.

Sykes, M.V., Cutri, R.M., Lebofsky, L.A., Binzel, R.P., (1987), Science, **237**, p. 1336.

Taylor, G.E., (1983) J. B. astr. Assoc., **93**, p. 146.

Taylor, G.E., (1986), Sky and Telescope, **76**, p. 557.

Tholen, D.J., Buie, M.W., (1988), Astron J., **96**, p. 1977.

Trafton, l., (1980), Icarus, **44**, p. 53,

van der Klis, M., (1988), EXOSAT preprint, No. 81.

Vogt, N., (1980), Astron. Astrophys., **88**, p. 66.

Vogt, N., Krzeminski, W., Sterken, C., (1980), Astron. Astrophys., **85**, p. 106.

Wade, R.A., (1985) in "Interacting Binary Stars", p. 289., eds. P.P.Eggleton, J.E.Pringle, pub. D.Reidel.

Wade, .R.A., Ward, M.J., (1985), in "Interacting Binary Stars", p. 129.,eds. J.E.Pringle,R.A.Wade, Cambridge University Press.

Warner, B., Robinson, E.L., (1972), Mon. Not. R. astr. Soc., **159**, p. 101.

Warner, B., (1976), in "The Structure and Evolution of Close Binary Systems" ,I.A.U. Symp. 73., p. 85., eds. P.Eggleton,S.Mitton,J.Whelan, pub. D.Riedel.

Warner, B., McGraw, J.T., (1981), Mon. Not. R. astr. Soc., **196**, p. 59p.

Warner, B., (1983), IAU Colloq. No. 72., p.155, eds M. Livio, G. Shaviv, pub. D.Riedel.

Warner, B., (1986), Mon. Not. R. astr. Soc., **219**, p. 347.

Warner, B., (1988), Nature, **336**, p. 129.

Wasserman, L.H., Veverka, J., (1973), Icarus, **20**, p. 322.

Wasserman, L.H., Millis, R.L., Franz, O.G., Klemola, A.R., Dahn, C.C., (1988), Bull. Amer. Astron. Soc., **20**, p. 806.

Waterworth, M.D., (1980), Proc. astr. Soc. Aust., **4**, p. 14.

Watson, M.G., Sherrington, M.R., Jameson, R.F., (1978), Mon. Not. R. astr. Soc., **184**, p. 79p.

Webbink, R.F., Livio, M., Truran, J.W., Orio, M., (1987), Astrophys. J., **314**, p. 653.

Williams, G., (1983), Astrophys. J. Suppl., **53**, p. 523.

Wood, J., Horne, K., Berriman, G., Wade, R., O'Donoghue, D., Warner, B., (1986), Mon. Not. R. astr. Soc., **219**, p. 629

Woosley, S.E., Phillips, M.M., (1988), Science, **240**, p. 750.

Young, P.J., Schneider, D.P., (1980), Astrophys. J., **238**, p. 955

Young, P.J., Schneider, D.P., Shectman, S.A., (1981), Astrophys. J., **245**, p. 1035.